SCHOOL OF CHEMICAL AND BIO ENGINEERING

ADDIS ABABA INSTITUTE OF TECHNOLOGY

ADDIS ABABA UNIVERSITY

Biopolymer Based Hydrogel for Adsorption of Heavy Metal Ions from Aqueous Solution: Experimental and Theoretical Investigation

Leta Lemma

Dissertation Submitted to School of Chemical and Bio Engineering for Partial Fulfillment of the Requirements for the Doctor of Philosophy in Chemical Engineering (Environmental Engineering).

April, 2024

Addis Ababa, Ethiopia

SCHOOL OF CHEMICAL AND BIO ENGINEERING, ADDIS ABABA INSTITUTE OF TECHNOLOGY, ADDIS ABABA UNIVERSITY

Biopolymer Based Hydrogel for Adsorption of Heavy Metal Ions from Aqueous Solution: Experimental and Theoretical Investigation

Leta Lemma Sherbe

A dissertation submitted to the School of Chemical and Bio Engineering for the partial fulfillment of the requirements for the Degree of Doctor of Philosophy in Chemical Engineering (Environmental Engineering).

April 25, 2024

Addis Ababa, Ethiopia

Declaration

I, Leta Lemma Sherbe (GSR/2273/11), hereby declare that this PhD dissertation on "Biopolymer based hydrogel for adsorption of Cr^{6+}, Pb^{2+} and Cd^{2+} ions from aqueous environment: experimental and theoretical investigation" has been developed by me and has not been submitted, to Addis Ababa University or any other University for the fulfillment of any degree and is, except where otherwise mentioned the original work of the author. The whole dissertation's content is original, and other works have been incorporated, properly cited.

Leta Lemma Sherbe Signature: …… Date: …….

SCHOOL OF CHEMICAL AND BIO ENGINEERING, ADDIS ABABA INSTITUTE OF TECHNOLOGY, ADDIS ABABA UNIVERSITY

Biopolymer Based Hydrogel for Adsorption of Heavy Metal Ions from Aqueous Solution: Experimental and Theoretical Investigation

Leta Lemma Sherbe

A PhD. Dissertation Submitted

To

School of Chemical and Bio Engineering

Addis Ababa Institute of Technology

Addis Ababa University

Approved by Board of Examiners

This is to certify that we have read this PhD research work and that in our opinion; it is adequate, in scope and quality, as a PhD dissertation for the Degree of Doctor of Philosophy in Chemical Engineering (Environmental Engineering).

Advisor		
Prof. Zebene Kiflie	Signature: ……	Date:……...
Co – advisor		
Dr. Shimelis Kebede (Asso. Prof.)	Signature:……	Date:……
Internal Examiner		
Prof. Nigus Gabbiye	Signature: …….	Date:……
External Examiner		
Prof. M. Rajasimman	Signature:……	Date:……
Chair Person		
Dr. Shimelis Kebede (Asso. Prof.)	Signature:……	Date:……

This work is dedicated to researchers who scarify their time and energy for safe guard of our environment.

Acknowledgment

Lensa Fikru, you are not simply my wife; you are also my soul mate, my closest friend. I appreciate your endurance, caring of me and my beloved children while I studied. Atinaf and Elellan, my son and daughters; I did not forget your funny moment, which evaporate those anxieties and reduce work tensions.

My dad – Lemma Sherbe and mom – Bizunesh Muluneh: Thank you in advance for letting me go to school, though you missed such a chance. I could not be here without your kind support. May God rest your soul in peace. Your legacy is always with me. My brother – Biya Lemma, thank you for the sacrifice you paid for me, especially during my undergraduate study is unforgettable. I believe such sacrifice is not only to discharge your responsibility as any mother did but rather your kindness.

My gratitude and appreciations go to my supervisors namely Professor Zebene Kiflie and Dr. Shimelis Kebede. I share many experiences with you all. Thank you for your guidance throughout my study. You also invested more time in editing and commenting on my entire work. Mr. Yossan Teshome, and Mr. Hintsa, your help during my laboratory work is so special and highly appreciated. I have gratitude for the AAiT community especially for School of Chemical and Bio Engineering.

I kindly appreciate the financial support I got from AAiT during my study. Above all, I thank the almighty God, the Lord of all creatures, for his assistance in all corner of my life. Thank you Lord for this achievement and for everything. Thank you Jesus.

Leta Lemma

Executive Summary

Contamination of water by heavy metal ions, in particular, hexavalent chromium (Cr^{6+}) ion, lead (Pb^{2+}) ion and cadmium (Cd^{2+}) ion, has become one of the most serious issues threatening human health and thus remedial measure have to be taken. Adsorption–based research toward biodegradable polymers for heavy metal ions remediation has received much attention in recent years due to environmental concerns. Polysaccharides in this domain are interesting starting materials for the preparation of novel adsorbents. In this work, novel type of biopolymer–based hybrid hydrogel such as PPSgCG, PCCFG, and CZVI–CS–PVA were designed for removal of Cr^{6+}, Pb^{2+}, and Cd^{2+} ions from aqueous solution. Polyvinyl alcohol (PVA), polyvinylpyrrolidone (PVP), acrylamide–grafted native starch (*Coccinia abyssinica*) (S–g–AAm), chitosan (CS), and graphene oxide (GO) were used to prepare PVA–PVP–S–g–AAm–CS–GO (PPSgCG) hydrogel. L-cysteine–functionalized graphene oxide (CFG), chitosan, and polyvinyl alcohol were used to synthesis polyvinyl alcohol–chitosan–cysteine–functionalized graphene oxide (PCCFG) hydrogel. L–cysteine stabilized zero–valent iron (CZVI), chitosan, and polyvinyl alcohol were used to prepare L–cysteine–zero–valent iron–chitosan–polyvinyl alcohol (CZVI–CS–PVA) hydrogel. Physiochemical properties of freeze–dried hydrogel were characterized by Fourier transform infrared spectroscopy (FTIR; Spectrum 65, PerkinElmer), zetasizer (3000HS), scanning electron microscopy (SEM; JCM-6000 Plus, Japan), energy dispersive X–ray spectroscopy (EDX; JSM–IT 100, JEOL), X-Ray Diffractometer (XRD; XRD–7000, Shimadzu, Japan), and thermogravimetric analysis (TGA/DTA; HCT–1, China). Adsorptions of Cr^{6+} ion onto PPSgCG and CZVI–CS–PVA hydrogel, and Pb^{2+} and Cd^{2+} ions onto PCCFG hydrogel as functions of initial heavy metal ion concentration, pH, time, hydrogel dose, and temperature have been studied by following a one–factor–at–a–time approach. The Cr^{6+} ions concentration in solution was determined by UV–vis spectrophotometer (Human, X–ma 1200). The Pb^{2+}, Cd^{2+}, and Cu^{2+} ions concentration in the solution after adsorption was determined by atomic adsorption spectroscopy (AAS; ZEEnit 700p, Analytikajena).

The adsorption of Cr^{6+} onto PPSgCG hydrogel, at optimum conditions: 2, 100 mg l^{-1}, 120 minutes, 3 g l^{-1}, and 25^{o}C of pH, initial Cr^{6+} ion concentration, hydrogel dose and temperature, respectively; were obtained considering both adsorption capacity and removal efficiency. The adsorption data agree with Langmuir (R^2 = 0.99) isotherm at 25°C and follow

pseudo–second–order kinetic model (R^2 = 0.999) at pH of 2. The maximum adsorption capacity of the PPSgCG hydrogel towards to Cr^{6+} was 93 mg g^{-1}. The obtained negative standard Gibb's free energy ($\Delta G° = -1.120$ kJ mol^{-1}) and negative enthalpy ($\Delta H° = -2.360$ kJ mol^{-1}) reveal the spontaneity and exothermic nature of Cr^{6+} ion adsorption onto the hydrogel. Moreover, the adsorption thermodynamics shows enthalpically favoring host–guest complexion along with decrease in entropy. Furthermore, the effect of common competing ions such as sulfate (SO_3^{2-}), phosphate (PO_4^{3-}), nitrate (NO_3^-), and chloride (Cal^-) ions on adsorption efficiency and selectivity of Cr^{6+} ion on the hydrogel were investigated and the result shows that sulfate ion has a significant effect on the Cr^{6+} ion adsorption, which might be related to identical chemical properties and geometrical configuration.

The adsorption of Cr^{6+} onto CZVI–CS–PVA hydrogel, at optimum conditions: 3, 45 mg l^{-1}, 90 minutes, 4 g l^{-1}, and 25°C of pH, initial Cr^{6+} ion concentration, hydrogel dose and temperature, respectively; were obtained considering both adsorption capacity and removal efficiency. The adsorption data agree with Langmuir isotherm (R^2 = 0.99) at 25°C and follow pseudo–second order (R^2 = 0.999) model at pH of 3. The maximum adsorption capacity of the PPSgCG hydrogel towards to Cr^{6+} was 15.86 mg g^{-1}.

The adsorption of Pb^{2+} and Cd^{2+} onto PCCFG hydrogel, at optimum conditions: 5, 225 mg l^{-1}, 50 minutes, 2 g l^{-1}, and 25°C of pH, initial Pb^{2+} and Cd^{2+} ion concentration, hydrogel dose and temperature, respectively; were obtained considering both adsorption capacity and removal efficiency. The experimental data well described by a pseudo–second–order kinetic model (R^2 = 0.99 for Pb^{2+} and R^2 = 0.98 for Cd^{2+}) and Langmuir isotherm (R^2 = 0.980 for Pb^{2+} & R^2 = 0.978) with maximum adsorption capacities of 250 and 192 mg g^{-1} at 25°C for Pb^{2+} and Cd^{2+}, respectively. The adsorption capacity of the PCCFG hydrogel increased with the increase in temperature. The value of $\Delta G°$ was negative, which shows the spontaneity of the reaction (electron exchange or ion exchange) between the metal ion and electron–rich atoms (–N, –S, –O). The positive $\Delta H°$ shows that the adsorption reaction consumes energy and the positive $\Delta S°$ shows the strong affinity of PCCFG toward the Pb^{2+} and Cd^{2+} ions. Pb^{2+} had better affinity and less spontaneity than Cd^{2+}. The effect of competing ions was studied in batch adsorption experiments in the solution containing the three metal ions (Pb^{2+}, Cd^{2+}, and Cu^{2+}) and the result shows that the coexistence of metal ions in the solution inhibits the adsorption capacity of the hydrogel compared to solutions containing a single metal ion.

Theoretical investigation of adsorption mechanism of Cr^{6+} and Pb^{2+}: Gauss View 6.0.16 interface were employed to construct the modeled system. The ground state geometry optimization of modeled system were first optimized by Molecular Mechanics (MM) method with aid of Universal Force Field (UFF) followed by *Hartree fock* (HF) and Density Functional Theory (DFT) method, using Gaussian 09 software package. Moreover, frequency, Natural Bond Orbital (NBO), and energy calculation were done by DFT method with aid of Gaussian 09. Hybrid–generalized gradient approximation (hybrid–GGA), B3PW91–D3 level of theory, where D3 denotes the third–generation dispersion correction by Grimme and basis set, the Stuttgart–Dresden–Boon (SDD) basis set was employed for heavy metal ions, and the 6–31G(d) basis were used for C, N, O, S, and H atoms during geometry optimization, frequency and NBO calculation. Single–point energy calculations were performed using the ωB97XD functional where basis set 6-311+G (d, p) was employed for C, N, O, S, and H atoms, and SDD basis set was employed for heavy metal ions. Solvation effect (H_2O) was evaluated with polarizable continuum model (PCM) to mimic the real aqueous solution. The Gaussian simulation result shows that mainly the –N and –O atoms of amine ($–NH_2$), amide ($–CONH_2$), and carboxyl (–COOH) functional group of the hydrogel were responsible for binding of heavy metal ions via electron sharing/covalent bonding.

Keywords: Acrylamide; Adsorbent; Adsorption; Cd^{2+} ions removal; Chitosan; Cr^{6+} ions removal; DFT; Graphene oxide; Hybrid hydrogel; L–cysteine; Pb^{2+} ions removal; PVA; PVP; Starch; Starch grafting; Zero–valent iron

Table of Contents

List of Figures

List of Tables

Acronyms

APHA	=	American Public Health Association
AWWA	=	American Water Works Association
BD	=	Bonding orbital
BD*	=	Anti-bonding orbital
CZVI–CS–PVA	=	Cysteine–zero–valent–iron–chitosan–polyvinyl alcohol
CNT	=	Carbon Nano Tube
CR	=	Core pair
DFT	=	Density Functional Theory
GGA	=	Generalized gradient approximation
GO	=	Graphene oxide
HF	=	Hartree Fock
IARC	=	International Agency for Research on Cancer
LP	=	Lone pair
MEP	=	Molecular Electrostatic Potential
MM	=	Molecular Mechanics
MO	=	Molecular Orbital
NBO	=	Natural Bond Orbital
ONIOM	=	Our own N-layered Integrated molecular Orbital and Molecular mechanics
PCCFG	=	Polyvinyl alcohol–chitosan–cysteine–functionalized graphene oxide
PPSgC	=	Polyvinyl alcohol–polyvinylpyrrolidone–acrylamide–grafted starch–chitosan
PPSgCG	=	Polyvinyl alcohol–polyvinylpyrrolidone–acrylamide–grafted starch–chitosan–graphene oxide
PPSg	=	Polyvinyl alcohol–polyvinylpyrrolidone–acrylamide–grafted starch
PPSgG	=	Polyvinyl alcohol–polyvinylpyrrolidone–acrylamide–grafted starch–graphene oxide
PVA	=	Polyvinyl alcohol
PVP	=	Polyvinyl pyrrolidone
QM	=	Quantum Mechanics
Ry*	=	Ant-Rydberg
SDD	=	Stuttgart–Dresden–Boon
UFF	=	Universal Force Field

CHAPTER ONE

INTRODUCTION

1.1. Background

Water is one of the most important components of life support in our ecosystem. Sustainability of life is dependent on the quality of water, which is closely related to our health. However, discharge of untreated effluent from industries such as leather tanning, electroplating, mining and smelting, battery manufacturing, phosphate fertilizers, pigments and alloys to the water bodies has become a serious issue (Preethi, Prabhu, and Meenakshi 2017). Pollutant, in particular heavy metals from such activities are transported by runoff and end up accumulating in soil, and sediments of water bodies.

Heavy metals can be found in trace in water bodies, and still be very toxic, and impose serious health problems to human and other ecosystem. Toxicity level of metals depends on type of organisms exposed, nature of metal and period at which the organisms are exposed to the metal. It is shown from the toxicological studies that long term effects of heavy metal damage liver, kidney, and lung. Hence, their maximum concentration level (MCL) in drinking water should be 0.05 mg $l^{-1}$for Cr, 0.01 mg l^{-1} for As, 0.001 mg l^{-1} for Hg, 0.003 mg l^{-1} for Cd, 0.01 mg l^{-1} for Pb, 0.02 mg l^{-1} for Ni, 3.00 mg l^{-1} for Zn and 2.00 mg l^{-1} for Cu or less (Edition 2011). In case of Ethiopia, in particular, studies have revealed that the levels of some heavy metal exceed these limits. For instance, the concentration of Cr and Pb at some location along the Little Akaki River were found to violate the drinking water quality criteria set by Ethiopian Standards and World Health Organization (WHO) (Aschale et al. 2015). Besides, the river water also found to be inappropriate even for irrigation use. Owing to toxic and carcinogenic character of heavy metals, release of them to aqueous solution should be controlled.

Heavy metals such as lead (Pb), cadmium (Cd), arsenic (As), chromium (Cr), mercury (Hg), nickel (Ni), zinc (Zn), cobalt (Co), and copper (Cu) are highly toxic even in minor quantities. Ions of these metallic species are found in industrial wastewater and they are important environmental problems. According to WHO, long term ingestion of these metals polluted water could induce the risk of damage and cancer to liver, lung, kidney, and bladder (Edition 2011).

Lead, chromium, cadmium, and arsenic have received much attention among others because of their high toxicity, and carcinogenic effect. They are classified as carcinogenic to humans (Group 1) by IARC, which means that there is sufficient evidence for their carcinogenicity in humans (Cancer 2012b). These metals become toxic when they are not metabolized by the body and accumulated in soft tissues. They may enter into the human body through food, water, air, or by adsorption through the skin when they encounter human.

Contamination of water by heavy metal ions, in particular, hexavalent chromium (Cr^{6+}) ion, lead (Pb^{2+}) ion, cadmium (Cd^{2+}) ion, has become one of the most serious issues threatening human health because of their toxicity, non–biodegradability, persistence, bio–accumulation tendency, and their bio–magnification through food chain (Lee et al. 2019; Zhitkovich 2005). They do not undergo microbial activities or chemical degradation, and consequently their total concentration can last for a long time after their release to the environment. The biodegradation rate of organic pollutants was decreased by the presence of heavy metal ions in the environment, which doubles the environmental pollution. Their contamination is a major problem of the environment especially in developing countries due to uncontrolled pollution level driven by industrial growth, addition of fertilizers and metal based pesticides (Radwan and Salama 2006).

The toxicity of Cr^{6+} ions to humans is primarily attributed to the chemical structure similarity between Cr oxyanions (CrO_4^{2-}) and sulfate ions (SO_4^{2-}), making the oxyanions to cross the cell membrane through the sulfate routes (Suwalsky et al. 2008). The Pb^{2+} ion is the most toxic heavy metal ion. Pb^{2+} can form stable complexes with anionic molecules (containing –N, –S, and –P ligands) in the natural environment (Town and Filella 2002), which rarely degrade in the environment because of their single–atom–metal property (Liu et al. 2020).

Owing to toxic and carcinogenic character of these heavy metal ions, release of them to aqueous environment should be controlled. The Cr^{6+}, Pb^{2+}, and Cd^{2+} ions can be removed from industrial effluents by means of chemical precipitation (Aziz, Adlan, and Ariffin 2008), ion exchange (Lalmi et al. 2018; Nekouei et al. 2019), membrane filtration (Smara et al. 2005), coagulation (Liu et al. 2013), bio–sorption (Ahamad et al. 2019; Donner et al. 2019), and adsorption (Ali et al. 2021; Hu et al. 2018). However, most of these conventional methods, except adsorption, have many limitations including high investment, complicated

operation, low efficiency, and secondary pollution problems (Table 1.1). Secondary pollution problems related to the chemical used or intermediate pollutant or byproduct generated during the treatment processes and released to the environment, which cause additional pollution in addition to the original pollutant. In case of adsorption phenomena, the adsorbate after adsorption were desorbed from the surface and the concentrated, small volume pollutant were dumped in appropriate damping site without causing additional pollution.

Adsorption is typically a preferable method owing to its relatively low cost, simple synthesis, and ease of operation. It can remove pollutants with extremely low concentrations and in a cost–effective manner (Vellingiri et al. 2018). Moreover, it can be applied for in *situ* removal of numerous organic and inorganic compounds with ease of recycling (Dichiara, Weinstein, and Rogers 2015). In this domain, adsorbents, including biopolymer (chitosan and starch in this case), biopolymer derivatives, macro–porous resins, graphene oxide, and Metal–Organic Framework (MOF), have been thoroughly studied for removal of heavy metal ions from aqueous waste streams.

Biopolymer–based adsorption is generally considered as sustainable and cost effective technique for heavy metal removal owing to its unique properties including biodegradability, non–toxicity, good water absorptive, good gel strength and stability, high efficiency, selectivity, easy synthesis and operation, improved chemical stability, and mechanical strength (Musa, Musa, and Suleiman 2019). Biopolymer based hydrogel (bio–hydrogel) adsorbents, which have three–dimensional (3D) hydrated hydrophilic polymeric network demonstrate high swelling capacity and potential in heavy metal removal through adsorption maintaining their physical structure without dissolving (Ma et al. 2017).

They are natural, biodegradable, and relatively low cost polymers that can be used as adsorbent (bio–hydrogel in this case) of toxic heavy metal ions from aqueous environment. They can possess amine ($–NH_2$), amide ($–CONH_2$), hydroxyl (–OH), thiol (–SH) and carboxyl (–COOH) functional groups in their bulk structure after optimum modification. They combined with synthetic polymers (PVA and PVP in this case) and graphene oxide (GO) to produce functional adsorbent for removal of heavy metal ions from aqueous solution (T. Li et al. 2019; Pooresmaeil and Namazi 2020).

Table 1.1 Comparison of adsorption with other water treatment technologies.

Characteristics	Adsorption	Membrane	Ion-exchange	Chemical precipitation	Coagulation
Scope (removal)	Wide-range	Wide range	Pure-water	Wide range	Suspended-particles
Down-stream processing	Not required	Not required	Not required	Required	Required
Mechanism of separation	Affinity	Pressure differences	Affinity	Affinity	Neutralizing the forces
Application(scale)	Large	Large	Small	Large	Large
2^{o} pollutants	No	No	Yes	Yes	Yes
Sensitivity	High	Low	High	Low	Low
Cost	economical	Economical	Moderate	High	Moderate

1.2. Statement of the Problem

Industrial wastewater is the major contributors to contamination of aquatic ecosystems with toxic heavy metals like lead, chromium, cadmium, arsenic, and mercury whose hazardous bio–accumulative nature in aqueous solution is attributed to their high solubility. They can be found in trace in water bodies, and still be very toxic, and impose serious health problems to human and other ecosystem. It is shown from the toxicological studies that long–term effects of these heavy metal ions (Cr^{6+}, Pb^{2+}, Cd^{2+} in this case) damage liver, kidney, and lung. Their maximum concentration limit in drinking water should be less than the permissible levels. Therefore, always been a need for the removal of these toxic, non–biodegradable, and persistent heavy metals from the industrial wastewater. For several decades, extensive investigation have been performed for easy, efficient, and economic removal of heavy metals with a varying degree of success. Membrane filtration, adsorption, chemical precipitation, ion floatation, ion – exchange, electrochemical and coagulation/flocculation methods have been the most readily available conventional methods for the removal of these heavy metals. These methods however have posed some serious shortcomings such as high sludge production, low removal efficiency, high energy requirements and high operational cost. In the present years, newer more efficient, more economic and innovative technologies are being investigated. Recently, hydrogel, membrane filtration/separation, photocatalysis and electrodialysis

technique and introducing newer adsorbents have been developed and adopted for better adsorption.

In spite of aforementioned achieved progresses in remediation of heavy metal ions polluted waste stream, in recent years, still there are crucial drawbacks. These drawback includes non–biodegradability, low regeneration for further use, long adsorption processing time, instability and aggregation in aqueous solution and causing additional pollution during recovering. A possible solution to aforementioned problem stated is using biodegradable adsorbents hydrogel as scaffolds to generate new composite in an adsorbent1–@adsorbent2–@adsorbent3–@adsorbent4@–@adsorbent... fashion.

This work addresses the problem stated above. In this work, biopolymer–based hydrogel: polyvinyl alcohol–polyvinylpyrrolidone–acrylamide grafted starch–chitosan–graphene oxide (PPSgCG), L-cysteine functionalized graphene oxide–chitosan–polyvinyl alcohol (PCCFG), and L-cysteine stabilized zero valent iron–chitosan–polyvinyl alcohol (CZVI-CS-PVA) hydrogel were synthesized by instantaneous gelation (physical cross–linking) method, which avoids cytotoxicity. PPSgCG hydrogel was synthesized from PVA, PVP, S–g–AAm, CS and GO. PCCFG hydrogel was synthesized from L–cysteine functionalized GO, chitosan and PVA. CZVI–CS–PVA hydrogel was synthesized from L–cysteine stabilized zero–valent iron, chitosan and PVA. These hydrogels possess unique functional groups such as thiol, amine, amide, carboxyl and hydroxyl, which have ability to scavenge heavy metals from waste stream. To the best of our knowledge, there is no report on such novel composite hybrid hydrogel employed for heavy metal decontamination from aqueous solution. The result of this work can be an excellent model to decontaminate heavy metal ions from wastewater by biodegradable materials, which avoids additional environmental pollutions.

1.3. Objective

1.3.1. Main Objective

The main objective of this work is to synthesis biopolymer–based adsorbent hydrogels and adopt for Cr^{6+}, Pb^{2+} and Cd^{2+} ions removal from aqueous solution.

1.3.2. Specific Objective

This work is try to achieve the following specific objectives. These are:

i. To synthesis and characterized PPSgCG, PCCFG, and CZVI–CS–PVA adsorbent hydrogel.
ii. To investigate the adsorption capacity of PPSgCG and CZVI–CS–PVA adsorbent hydrogel towards Cr^{6+} ions in single and competitive environment.
iii. To investigate the adsorption capacity of PCCFG adsorbent hydrogel towards to Pb^{2+} and Cd^{2+} ions in single and competitive environment.
iv. To investigate the adsorption mechanism of Cr^{6+} ion onto PPSgCG and Pb^{2+} ion onto PCCFG by using DFT.

1.4. Scope of the Study

The scope of this work is to synthesized biodegradable adsorbent hydrogel and used for removal of Cr^{6+}, Pb^{2+} and Cd^{2+} ions through adsorption from aqueous solution by batch modes of operation. The adsorption capacity of PPSgCG and CZVI–CS–PVA hydrogel towards Cr^{6+}, and PCCFG hydrogel towards Pb^{2+} and Cd^{2+} in a single environment were studied. Due to robust active adsorption sites they possess, these hydrogels may have high adsorption performance towards these heavy metals. The adsorption capacity of the hydrogel also studied in competitive environment, i.e., adsorption capacity of PPSgCG hydrogel towards Cr^{6+} ion in presence of sulfate (SO_3^{2-}) ion, phosphate (PO_4^{3-}) ion, nitrate (NO_3^-) ion, chloride (Cl^-) ion; and adsorption capacity of PCCFG hydrogel towards Pb^{2+} and Cd^{2+} ions in presence of Cu^{2+} ion. The synthesized PPSgCG was also applied to remove Cr^{6+} ion from Batu Tannery effluent by batch modes of operation. The removal capacity of this hydrogel adsorbent was compared with other similar reported adsorbents. Furthermore, the adsorption mechanism of Cr^{6+} onto PPSgCG and Pb^{2+} onto PCCFG were studied by DFT. The conclusion was drawn based on the result and from observation of this work and further work were recommended.

1.5. Significance of the Study

These days, heavy metals in particular Cr^{6+}, Pb^{2+} and Cd^{2+} ions can be found in trace in water bodies, and still be very toxic, and impose serious health problems to human. Toxicological study shows that long–term effects of these heavy metal ions damage liver, kidney, lung and bladder. According to WHO, the maximum concentration level in drinking water should be

less than 0.05 mg l^{-1}, 0.01 mg l^{-1} and 0.003 mg l^{-1} for Cr^{6+}, Pb^{2+} and Cd^{2+} ions, respectively. However, most of the effluents from wastewater treatment plant did not met the standard set by concerned organizations. For instance, the concentration of Cr and Pb at some sites along the Little Akaki River were found to violate the drinking water quality criteria set by WHO and Ethiopian Standards. Discharge of these effluents to the surrounding environment resulted in bioaccumulation tendency and bio–magnification through food chain. This level should be reduced to permissible level by using high technologies but it incurs cost, complicated treatment processes, high–energy consumption, and additional pollution during regeneration, and required skilled human power. Therefore, developing low cost technologies from biodegradable materials is recommended. The output of this dissertation will be an alternative source of data for anyone interested in heavy metal ions removal from wastewater by adsorption and mechanism of adsorption using biopolymer based adsorbent hydrogel, which was synthesized from biodegradable materials.

1.6. Dissertation Structure

This dissertation includes five main chapters:

- Chapter one: this chapter intended to deliver a general overview of this study. It comprises the background of the study, statement of the problem, objectives (both main and specific objectives), the scope of the study, and the significance of the study.
- Chapter two: detailed literature review on the subject matter of the dissertation. It includes adsorption isotherms, kinetics and thermodynamics, Cr^{6+}, Pb^{2+} and Cd^{2+} ions removal mechanisms (both experimental and theoretical investigation by using DFT), reported Cr^{6+}, Pb^{2+} and Cd^{2+} hydrogel adsorbents (in single and competitive environment).
- Chapter three: this section is all about the materials and experimental design used to conduct the experimental work. Detail chemicals, equipment, and software used, characterization methods, concentration analysis methods, experimental set–up, and data analysis are included.
- Chapter four: this chapter discusses the results observed from the experimental and theoretical work. All results observed during the specific objectives investigation are discussed in detail.
- Chapter five: conclusion and recommendations are provided briefly here.

CHAPTER TWO

LITERATURE REVIEW

2.1. Industrial Wastewater

Water used for industrial purposes can be contaminated at any stages by heavy metals, toxic chemicals, fertilizers, and more. Lead, chromium, mercury, cadmium, arsenic, nitrates, phosphates, oils, and petrochemicals are just a few of the substances that can be found in industrial wastewater. Some are carcinogenic, poisonous to animals and aquatic life, and non–biodegradable, making them extremely difficult to clear from ecosystems. When these pollutants find their way into aqueous environment, they kill animals and flora, and disrupt important environmental processes. Eutrophication is one of these results, in which algae forms in response to changes in the nutrients in water, and over time deplete oxygen, killing other aquatic life and leading to dead zones.

Products like metals, textiles, and food contribute the most to hazardous wastewater through contaminants like dyes and plastics as well as the chemicals used to treat those products. The proliferation of water pollution prompted the Environmental Protection Agency (EPA) to propose the Clean Water Act in 1972, which finally allowed for regulations on the proper treatment of wastewater. Now, many manufactures have on–site treatment facilities for their wastewater, or send their water to municipal treatment plants. However, these treatment options are sometimes inefficient, costly and not practical for smaller facilities.

Chemical industries with their rapid growth have increasingly created nuisances for living beings and the environment. One of these nuisances is the generation of large volumes of wastewater contaminated with heavy metals whose high solubility in the aquatic environment poses serious threats to all living organisms. Several industries have contributed to this problem, with the most prevalent contaminants being lead (Pb), chromium (Cr), cadmium (Cd), arsenic (As) and mercury (Hg). These heavy metals are known to be toxic and are usually generated by electroplating, printed circuit boards manufacturing industries, wood processing industries, and tanning industries.

2.2. Heavy Metal Removal Technologies

Removal of pollutants in particular heavy metal ions from wastewater is of prime importance for a clean environment and human health. Different reported technologies were devoted to heavy metal ions removal from various industrial wastewater sources. These technologies could be classified into conventional and modern technologies. The physical and chemical conventional techniques that have been employed for decent amounts of removal of heavy metals include precipitation, adsorption, ion floatation, ion exchange, coagulation/flocculation and electrochemical processes. Conventional techniques produce large amount of toxic sludge that needs treatment with chemical stabilization followed by proper disposal and selectivity encountered in the conventional methods.

Chemical precipitation and coagulation/flocculation while being among the simplest and least expensive technology requiring easily operable equipment, are not quite effective for treating wastewater with high acid content. Most metals are precipitated as hydroxides, however other methods such as sulfide and carbonate precipitation also in common use(Wang, Hung, and Shammas 2005). Use of MgO as a precipitating agent produce grainy, dense and easily settleable and dewatered sludge than using lime as precipitating agent (BrbootI, Abid, and Al-ShuwaikI 2011). Calcium hydroxide used as a precipitating agent for removal of Pb and optimum removal efficiency was found at pH 5 (Wu 2019). Chemical precipitation is characterized by production of a high water content sludge and expensive disposal process. Besides, chemical precipitation process can be ineffective in the removal of metal ions of low concentration.

Since the introduction of adsorption in the 1940s, activated carbon has been the important and prime choice for the treatment and recycling of industrial wastewater to potable quality water because of its good adsorption capacity due to small particle size, active free valences and high surface area. However, large–scale utilization of activated carbon for wastewater treatment is not feasible because of its high cost of production and regeneration (Cheremisinoff and Ellerbusch 1978).

Ion flotation is one of the most accepted techniques in metal removal from industrial wastewater. Various lab scale and industrial scale removal of metals from wastewater have been reported with various efficiencies. Bodagh et al. studied the removal of cadmium from

aqueous solution by foam flotation with rhamnolipid bio-surfactant as an ion collector (Bodagh et al. 2013). Taseidifar et al., reported that low–level removal of Cr, As, Pb, Cd and Hg ions form aqueous solution have been achieved using cysteine reacted with octanoyl, decanoyl and dodecanoyl chloride (Taseidifar et al. 2017). Ion flotation characterized by its simplicity, flexibility, low energy consumption, small volume sludge production, and acting selectively in industrial applications. However, metal ions are difficult to be separated from the collectors due to they remain still in the form of complexion, which limits its large–scale application (Peng et al. 2019).

Ion exchange is another classical method for heavy metal removal from industrial wastewater with a solid capable of exchanging cations/anions. Advantages of using this method are that it can remove the parts per billion (ppb) levels while managing the relatively large volume. However, it cannot be effective in the case of using concentrated metal solution due to exchange matrix gets easily fouled by the organic and other solids in the waste (Bai and Bartkiewicz 2009).

Electrochemical treatment of industrial wastewater is based on direct passage of current through an aqueous solution containing metal ions between the cathode plates and insoluble anodes. The reduction of hexavalent chromium to trivalent chromium, electrochemically precipitation in an alkaline medium was mostly studied (Chaudhary, Goswami, and Grimes 2003; Cheballah et al. 2015). Electro–chemical processes treatment of industrial wastewater offers the following advantages: high removal efficiency, metal selectivity, lower level of produced sludge and no additional chemicals required. However, it has some limitation, such as pH–sensitive process, high–cost electrode and its subsequent electrical energy requirement, which make it relatively higher cost technologies (Abdel-Raouf and Abdul-Raheim 2017b).

Membrane separation process is a modern technique in which wastewater is forced through a semi–permeable membrane at high pressure to separate specific heavy metal from the solution. Membrane separation process mainly be governed by adsorption, sieving and electrostatic basic principles. The cost–effective analysis and selectivity of materials are the most important parameters that need to be analyzed for use of these materials (Shrestha et al. 2021). Electrodialysis (ED) is among the most economic in recent technology of membrane

type that can be applied for the removal of metal ions through electrically driven ion – exchange membrane (Rodrigues et al. 2008). The method further has the advantage of producing effluent water that can be reused besides removing even lower concentrations of metal ions from the effluents.

The other efficient solution for the treatment of wastewater is the use of super adsorbent polymers. Dutta et al. prepared graft copolymers of polyacrylonitrile onto Arabic gum and employed for removal of Pb^{2+}, Cd^{2+} and Cu^{2+} from the wastewater (Dutta and De 2017). The maximum super adsorbent capacities were found to be 1017, 396 and 413 mg g^{-1} for Pb^{2+}, Cd^{2+} and Cu^{2+} respectively. A large variety of materials has been observed recently for fabricating the membranes and the adsorbents to find the best removal efficiency. Novel chelating, membrane, the PVA/poly(ethyl–eneimine) (PEI) has been prepared and studied for the removal of Pb^{2+}, Cd^{2+} and Cu^{2+} with maximum adsorption capacities of 0.729, 0.525 and 0.692 mmol g^{-1} for Pb^{2+}, Cd^{2+} and Cu^{2+} respectively . Algureiri et al. prepared spiral bound RO membrane and used for removal of Ni^{2+}, Pb^{2+} and Cu^{2+} from industrial wastewater with removal efficiencies of 98.5, 97.5 and 96%, respectively (Algureiri and Abdulmajeed 2016). Wei et al. fabricate hollow fiber membrane with polyamide film on the inner side and employed for removal of Cr, Cu and Ni from electroplating wastewater with removal efficiencies of 95.76, 95.33 and 94.99%, respectively (Wei et al. 2013).

Although previously studied adsorbents have shown good retention and almost complete removal of heavy metals, they have some limitations, such as higher mixing rates needing higher energy, lower removal rates, high limiting capacity and slower reduction, fouled by other pollutant (e.g. Ion–exchange technology), highly pH and temperature dependence (e.g. Ion floatation technology) and high cost operation (e.g. Electrochemical method). To fulfill the need for better technology, recent studies have focused on a particular method for heavy metal ions removals, such as adsorption using synthetic and natural adsorbents, hydrogel, nano–particles and nanotechnology, advanced oxidation processes, electrodialysis, and membranes filtration. Adsorption–based separation of heavy metal ions from wastewater used different adsorbents, such as carbon–, biopolymer–, mineral–, magnetic–, and metal–organic frameworks –based adsorbent. Several polymeric materials and variety of nanomaterial's and hydrogel have been developed to enhance the removal efficiency of the heavy metals.

Carbon–based adsorbent is extensively used in the applications of heavy metal removal owing to their tremendous surface area (500 – 1500 m^2 g^{-1}) (Karnib et al. 2014). The carbon surface charges can be enhanced by surface functional groups functionalization to improve the heavy metal uptake. However, the current surface modification techniques demand high heat/pressure, strong acid/base, or intensive oxidation/reduction reactions. This complex preparation process makes the carbon–based adsorbents expensive, burdening their widespread use in industrial applications.

2.3. Adsorption

Adsorption is surface phenomenon of accumulation of species onto a liquid or solid phase from a bulk phase is termed as adsorption. The development of isotherm models by Langmuir and Freundlich, and the kinetic models developed by *Lagergren* and Ho were some pioneer significant contributions in adsorption. Adsorption on solid phase is a process in which adsorbate adsorbed on to the surface of adsorbent through physical and/or chemical processes from bulk solution phase. These processes involve transfer of metal ion from bulk solution to the surface of adsorbent, pore diffusion (internal mass transfer) from the surface to inner surface of adsorbent pore structure and adsorption of adsorbate onto active site of adsorbent. The adsorption may be through *van der Waals* forces, electrostatic attraction, ion exchange, ion–pair interaction, cation–Π, and hydrophobic hydration (Bhatt, Sreedhar, and Padmaja 2017). The adsorption is affected by nature and dosage of adsorbent and adsorbate, metal ion concentration, co–ions concentration, pH and temperature of aqueous solution, isotherm and kinetics of adsorption, contact time or adsorption rate, and presence of ionic salts and surfactants.

2.3.1. Adsorption Kinetics

To predict the adsorption mechanism, rate of adsorption and rate–determining steps of the adsorption process, adsorption kinetics models were used to interpret the experimental data. Adsorption kinetics provides insight into the reaction rate and the sorption mechanism involving mass transfer, diffusion, and reaction on the adsorbent surface during adsorption. Adsorption kinetics involve the changes in the sorption properties with time for the system, where the degree of surface coverage provides insight on the rate of a process. Both sorption and desorption processes are time-dependent, and it is essential to evaluate the rates of adsorption for the design and regeneration of the adsorbent. Hence, an understanding of

adsorption and desorption kinetics and their kinetic parameters are important since such parameters enable characterization of the movement of the sorbet within and onto the surface sites of the sorbent. Knowledge of adsorption kinetics has gained much attention because the surface chemistry and the adsorption mechanisms contribute to practical applications in wastewater treatment.

Kinetic adsorption studies provide information about optimum conditions (contact time, temperature, adsorbent dosage and pH), mechanism of sorption, and possible rate-limiting step. In order to investigate the mechanism of the adsorption process, kinetic models are used to test the experimental isotherm results. Kinetic studies of this type provide information on the rate at which the process occurs and insight on the non equilibrium steps of the adsorption mechanism (Tan and Hameed 2017). The contact time between the adsorbent and the adsorbate is an important parameter governing the extent of an adsorption process. This is because it provides information on the sorption kinetics of the adsorbate for a given initial dosage of the adsorbent (Singh, Tang, and Tachiev 2013). Hence, it is necessary to study the effect of the contact time on the adsorption ability of biopolymer adsorbents with model species of interest such as heavy metals. The most common kinetic models used to monitor the kinetics of adsorption processes are *Lagergren's* pseudo-first-order model and Ho's pseudo-second-order model, while interfacial and particle diffusion models are most commonly used to determine the mechanism of adsorption. Details of the equations used for each model are given in Chapter 3.

2.3.2. Adsorption Isotherms

The adsorption isotherm models, such as the Langmuir, Freundlich, Temkin, and Dubinin–Radushkevich (D–R) isotherms, describe the interaction between the amount of adsorbate adsorbed and left in the solution at equilibrium. The Langmuir isotherm, is based on constant surface activity during adsorption and no lateral adsorbate interaction, hence monolayer coverage assumption. The Freundlich model equation is an empirical equation that describes multilayer adsorption with the interaction between the adsorbent and adsorbate. The Temkin isotherm, assumes that the heat of adsorption of all the molecules in the layer decreases linearly with coverage due to adsorbent–adsorbate interactions. Details of the equations used for each model are given in Chapter 3.

2.3.3. Adsorption Thermodynamics

The thermodynamic parameters, typically Gibbs free energy change (ΔG^o), standard enthalpy change (ΔH^o), and standard entropy change (ΔS^o) can predict the nature and direction of adsorption. These parameters are important to understand nature of adsorption and to design specific adsorbent at different temperature. The spontaneity and nature of adsorption of adsorbate onto adsorbent also determined from these parameters.

Negative value of ΔG^o indicates spontaneity of adsorption processes. The absolute value of ΔG^o decreases as temperature increases shows the degree of reaction decreases and decreases with temperature indicating the adsorption process is favorable at high temperatures (Liu et al. 2019). A positive ΔH^o value shows that the process of adsorption is endothermic (Yana Bagbi et al. 2017). The negative value of ΔH^o indicates the exothermic nature of the adsorption process. The entropy of the adsorbate is related to the degrees of freedom associated with the adsorbent–adsorbate interactions. A positive ΔS^o value shows that randomness is enhanced whereas a negative value indicates a decrease in randomness at the adsorbent surface during the adsorption process (Liu, Han, and Chen 2002). Details of the equations used for each model are given in Chapter 3.

2.3.4. Adsorption Mechanism of Heavy Metal

Understanding the processes of heavy metal ions removal from aqueous solution is highly dependents on the understanding of the mechanism of adsorption on the surface of adsorbent (through functional groups). However, it is very complicated, and time consuming work to identify the adsorption mechanism of heavy metal ions by the adsorbent. Researchers have made some efforts to identify the mechanism through different methods such as XPS, XRD, SEM–EDX, FTIR, and computational quantum mechanism. Generally, the adsorption mechanism is through electrostatic attraction, complexation and chelation, ion exchange, ion–pair, cation–Π, Van der Waals force, and hydrophobic hydration. Electrostatic attraction, and chelation and complexation mechanism plays a great role in removal of heavy metal ions.

i. Electrostatic attraction

Electrostatic attraction refers to the electrostatic force of long–range interaction occurring between the attractive electrostatic adsorption in an aqueous solution with differently charged particles or uncharged particles (Yu, Shao, and Hou 2017). An electrostatic attraction is a

physical adsorption, which includes *Van der Waals* interactions between the adsorbent and adsorbate. Physical adsorption is an exothermic process with low adsorption enthalpy, which is normally favored at low temperature. Physical adsorption is characterized with low adsorption or binding energy, which shows weak bonding between the surface of adsorbent and adsorbate. Electrostatic attraction between heavy metal ions and functional groups of adsorbent is based on the protonation and de–protonation of the functional groups in aqueous solution, which depend on the solution pH.

Adsorption of Cr^{6+} on the adsorbent is mainly through electrostatic attraction (Yuan et al. 2019), adsorption and reduction (Ren et al. 2017) or plain adsorption (Nasseh et al. 2017). Reduction of Cr^{6+} to Cr^{3+} is mandatory for effective removal of chromium. Acidic conditions and existence of electrons causes the reduction of Cr^{6+} to Cr^{3+}at the surface it was adsorbed. The conversion (reduction) takes place directly or indirectly (Park et al. 2008). In direct conversion the Cr^{6+} are attached to adsorbent sites that can donate electrons such as O –atom, N –atom, and S –atom. Whereas in indirect conversion the Cr^{6+} attached on the adsorbent site is reduced by the electrons from the adjacent functional groups. In aqueous solution, Cr^{6+} oxyanions is mainly present in the form of chromate ion (CrO_4^{2-}), dichromate ion ($Cr_2O_7^{2-}$), chromic acid (H_2CrO_4), and hydrogen chromate ion ($HCrO_4^-$) depending on the solution pH (Mukhopadhyay, Sundquist, and Schmitz 2007). A variation in pH is a determinant factor and plays an important role in the Cr removal from aqueous solution.

Protonation of the nitrogen, sulfur and oxygen–containing functional groups in adsorbent at low pH (strong acidic condition) result in a large amount of H^+. Low removal efficiency were observed at lower pH due to the competition of H_3O^+ or H^+ ions with Pb^{2+} and Cd^{2+} in the solution and repulsion of Pb^{2+} and Cd^{2+} and the protonated functional group (Ahmad et al. 2017). When pH increased (weak acidic condition), the negative charges of the adsorbent and the active site increased, which enhanced the complexation between the adsorbent and Pb^{2+} and Cd^{2+} via electrostatic attraction and/or chelation. However, in adsorption processes, the adsorption efficiency is decreased as pH increases further even if the deprotonation of the hydrogel surface increased as Pb^{2+} and Cd^{2+} convert to a hydroxide form and precipitate (Moradi et al. 2017). It was reported that the negative charge due to –NH (Ghaedi et al. 2018; Yin et al. 2016), –S (Zhang et al. 2016), and –O (Yu et al. 2017) present at the surface of the

adsorbents can attract Pb^{2+} and Cd^{2+} ions via coordination interactions and electrostatic attractions.

ii. Coordination–complexation or chelation

Complexation or chelation is chemisorption phenomena, which is characterized with high enthalpy of adsorption and favors at high temperature. Moreover, the activation energy is high during adsorption of pollutant via chelation due to chemical bonding formed between the adsorbent and pollutant. Complexation occurred through electron sharing between the metal ions and functional groups, which bears electron reach elements such as O, N and S atoms. This phenomenon was explained by the decrease in electron cloud density of electron reach element and the increasing of binding energy (He, Lu, and Luo 2014). Adsorbent–metal complex occurs through a coordinated covalent bond. Chelation mechanism was more elaborated based on bridge and pendant model (Ogawa, Oka, and Yui 1993). Bridge model supposed that metal ions are bounded to several amine or thiol groups from the same chain or from different chains, via intra– or intermolecular complexions. Pedant model proposed that the metal ions bonded to amine or thiol groups in pedant fashion.

2.3.5. Theoretical Investigation of Adsorption Mechanism of Heavy Metal

i. Quantum mechanics

In the early twentieth century Max Planck proposed blackbody radiation which was found to be emitted by microscopic particles. This was limited to certain discrete values, i.e. it was 'quantized'. Bound electrons in atoms, in particular, are limited to discrete energies (levels) as indicated by their ultraviolet and visible line spectra. Thus the promising candidate was wave mechanics, since standing waves are also a quantized phenomenon. Later De Broglie demonstrated that matter can indeed be shown to have wavelike properties. Thus the primary features from their work were that wave function does exist for any (chemical) system, and that appropriate operators (functions) act upon to return the observable properties (such as Energies) of the system. This led to the introduction of quantum mechanics and the basic equation was the Schrodinger Equation as given below (Eq. 2.1):

$$\hat{H}\Psi = E\Psi \qquad (2.1)$$

The wave function or Ψ describes the state of the system as a function of coordinates. This is also known as state function or wave function and contains all the information that can be determined about the system. H is the Hamiltonian (i.e., energy) operator of the system and E

is the energy of that particular state. The equation can be solved approximately where the approximation methods can be categorized as either *ab–initio* or semi empirical. While ab-initio gets its origin from first principles (i.e. at start); semi empirical methods uses parameters that compensate for neglecting some of the time consuming mathematical terms in Schrödinger equation.

ii. Density functional theory (DFT)

The electronic wave function of an n–electron molecule depends on 3n spatial and n spin coordinates. Since the Hamiltonian contains only one– and two–electron spatial terms, the energy can be written in terms of integrals involving only six spatial coordinates. In a sense, the wave function of a many–electron molecule contains more molecular orbital's than is needed and is lacking in direct physical significance. Can the molecular energy be expressed in terms of the first order spinless density matrix (which is a function of the spatial coordinates of one electron) and the second–order spinless density matrix (which is a function of the spatial coordinates of two–electrons)?

Hohenberg and Kohn (Hohenberg and Kohn 1964) proposed that the ground state molecular energy, wave function, and all other molecular electronic properties are uniquely determined by the ground state electron probability density ρ(x, y, z), a function of only three variables. Here electrons interact with one another and with an 'external potential', which is nucleus. A uniform electron gas where the external potential is uniformly distributed as a positive charge is assumed. The Integration of Density should give thus give us the total number of electrons. The final step leads to the solution of the Schrodinger equation (Eq. (2.1)), which is prohibitively difficult due to the electron–electron interaction term. In order to make things simpler, the electron–electron interaction terms the *Hamiltonian* operator for a non-interacting system of electrons is assumed as a sum of one Electron Operator, which is simpler to achieve. Then an external potential is devised for the electron–electron repulsion term. The correction to the kinetic energy deriving from the interacting nature of the electrons, which are simply the entire non–classical corrections to the electron–electron repulsion energy and kinetic energy.

$$E[\rho(r)]=T_{ni}[\rho(r)]+V_{ne}[\rho(r)]+V_{ee}[\rho(r)]+\Delta T[\rho(r)]+\Delta V_{ee}[\rho(r)] \quad (2.2)$$

Where

$$V_{ne}[\rho(r)]=\sum_{k}^{nuclei}\int\frac{Z_k}{|r-r_k|}\rho(r)\,dr \tag{2.3}$$

$$V_{ee}[\rho(r)]=\frac{1}{2}\iint\frac{\rho(r_1)\rho(r_2)}{|r_1-r_2|}dr_1dr_2 \tag{2.4}$$

Here the last two terms indicate the corrections due to the kinetic energy and the electron–electron repulsion energy. We have:

$$E[\rho(r)]=\sum_{i}^{N}\left(\left\langle x_i\left|-\frac{1}{2}\nabla_i^2\right|x_i\right\rangle-\left\langle x_i\left|\sum_{k}^{nuclei}\frac{Z_k}{|r_i-r_k|}\right|x_i\right\rangle\right)+\sum_{i}^{N}\left\langle x_i\left|\frac{1}{2}\int\frac{\rho(r')}{|r-r'_i|}dr'\right|x_i\right\rangle+E_{xc}[\rho(r)] \tag{2.5}$$

Hence

$$\rho=\sum_{i=1}^{N}\langle x_i\,|\,x_i\rangle \tag{2.6}$$

Solve for

$$h_i^{KS}x_i=\varepsilon_i x_i \tag{2.7}$$

$$h_i^{KS}=-\frac{1}{2}\nabla_i^2-\sum_{k}^{nuclei}\frac{Z_k}{|r_i-r_k|}+\int\frac{\rho(r')}{|r_i-r'|}dr'+V_{xc}$$

$$V_{xc}=\frac{\delta E_{xc}}{\delta\rho} \tag{2.8}$$

Exchange–correlation potential V_{xc} is found as the functional derivative of E_{xc}.

$$V_{xc}=\frac{dE_{xc}[\rho]}{d\rho} \tag{2.9}$$

If $E_{xc}[\rho]$ is known, its functional derivative is readily found, and V_{xc} is known. This is similar to a *Hartree-Fock* operator, except that the exchange operators are replaced by V_{xc}. This handles the effects of both exchange (ant symmetry) and electron correlation. The equation above is a first derivative of a function of a single position which depends both on the density and the gradient of the density, also called as Generalized Gradient Approximation (GGA). Hybrid functional, GGA and meta-GGA (Table 2.1) are used to calculate E_{xc} by using Kohn–Sham orbital's.

Table 2.1. DFT Functional

GGA	Meta–GGA	Hybrid–GGA	Hybrid meta–GGA	Range–separated hybrids
PBE	M06–L	B3PW91	PW6B95	ωB97X–D3
OLYP	TPSS	BHLYP	TPSSh	ωB97X
BLYP	revTPSS	PBE0	M06–2X	ωB97
BP86	–	B3LYP	M06	LC–BLYP
–	–	B3LYP/G	–	CAM–B3LYP

iii. Heavy metal adsorption mechanism study by DFT

The adsorption mechanism and kinetic model of biopolymer such as chitosan based adsorbent is still known not clearly. So, further understanding of adsorption mechanism via various characterization methods and theoretical investigation (such as DFT) should be carried out in order to get clues for modification and regeneration strategies. Theoretical investigation by means of *ab initio* quantum mechanics calculations such as DFT is one way of estimating possible adsorption mechanism of heavy metal onto the adsorbent.

Several computational quantum chemical methods with different model chemistry were invoked to investigate mechanism of adsorption of heavy metal ions on adsorbent. Based on interaction distance (bond length) and total binding energy, coordination potential of chelating groups in adsorbent with metal ions were identified. Ribeiro et al., (Ribeiro, Reis, and Pereira 2019) studied the interaction of vanillin monomer with Cd^{2+}, Cu^{2+}, Pb^{2+}, Hg^{2+}, Zn^{2+} and Cr^{3+} by using DFT with hybrid functional wB97X–D. The 6-31+G (d, p) basis set was used for C, N, H and O atoms and the Los Alamos National 2 Double–Zeta effective core potential basis set (LANL2DZ) was used for the heavy metal ions. The effect of water as a solvent was simulated by using the Implicit Solvation Model based on Density (SMD). The reactivity index such as chemical hardness and softness were calculated from HOMO and LUMO energies. Moreover, molecular electrostatic potential (MEP) was used to locate the site of complexation/coordination, and nitrogen of amine group and oxygen of carboxyl group, which has high density of negative charge, is responsible for coordination of metal ions with adsorbent. These regions were very electronegative and susceptible to electrophiles attack. Based on electron density, *Laplacian* of electron density, total energy of the critical

point of connection, and Pearson's theory, Cu^{2+} ions have a favorable interaction with the monomer.

Zhao et al. (Zhao et al. 2014) synthesized magnetic modified polyacrylamide micro composite adsorbent by inverse micro–emulsion polymerization via using N, N'–methylene–bis(acrylamide) as cross–linker for removal of Cd^{2+}, Pb^{2+}, Co^{2+}, and Ni^{2+} from aqueous solution. They also reported that computational methods (DFT) was employed as a tool to understand the adsorption mechanism. Based on the energy of HOMO (of adsorbent) and the point charge, which is calculated with the help of NBO, O–atoms (more negative point charge) of carbonyl and hydroxyl groups is responsible for chelation (O, O'–bi–dentate hydroxamato coordination mode) of metal ions.

Hizhnyi et al. (Hizhnyi et al. 2017) studied chromium adsorption mechanism on graphene and B– or N– doped graphene and CNT and B– or N–doped CNT by *ab initio* computational calculation. Geometry optimization and the adsorption of CrO_4^{2-} on the CNT were investigated by DFT/B3LYP level of theory. The spilt–valance double zeta (6-31G) basis set were used for C –atom and H –atom and correlational consistent polarized valence double–zeta (cc-pVDZ) basis set were applied for Cr –atom and O –atom, and Gaussian 09 software package used as a tool. The adsorbent–CrO_4^{2-} system with optimized geometry was divide into two regions (two level ONIOM approach, low level and high level), the quantum mechanical (QM) and the molecular mechanical (MM) during the calculation. The whole adsorbent, which comprised of C–atom and H–atoms treated by MM, while the CrO_4^{2-}, which comprised of Cr–atom and O– atom treated by QM. To account the electrostatic interaction between QM and MM, the electronic embedding was used. Exited electronic state of CrO_4^{2-} anion and in adsorbed configuration were studied by time–dependent DFT (QM region). Single energy calculation was carried out by the same model chemistry used in geometry optimization. Change in charge density, $\Delta q = -2e - q$, where $q = q_{O1} + q_{O2} + q_{O3} + q_{O4} + q_{Cr}$ of CrO_4^{2-} in adsorbed state were calculated using Mulliken population analysis. Electronic charge was transferred from the CrO_4^{2-} to adsorbent because Δq is negative and ranging from –0.60e to –1.12e, which indicate Chemisorption mechanism of adsorption, transferred from anion to the adsorbent. Bond formation occurs between one O–atom of CrO_4^{2-} and either C, B, or N atoms of the adsorbent. Doping the adsorbent with B –atom reduces the binding energy (E_b) as well as the Δq, weakening the chemical bonding (weaker distortions) between

anions and the adsorbent. Whereas doping with N–atom strengthens (stronger distortions) the bonding between the anions and the adsorbent.

Wang et al. (Wang, Chen, and Yang 2015) studies sorption mechanism of Pb^{2+} ions onto GO by DFT. The interaction of Pb^{2+} with –COOH and –COC were calculated, and Pb^{2+} ions prefer to bind with –COOH groups on GO surfaces (i.e., the binding energy of Pb^{2+} with –COOH is higher than that of –COC). Arshid B. et al. (Bashir et al. 2020) studied the selective adsorption of Zn^{2+}, Pb^{2+}, Cd^{2+}, and Hg^{2+} ions onto potato starch phosphate polymer with both experimental and DFT calculation. Based on a Mulliken charge analysis, oxygen atoms of phosphate group carry more negative partial charges than terminal or glyosidic oxygen, and hence responsible for adsorption of these heavy metal ions. Jiling Zhao et al. (Zhao et al. 2020) studies the selective adsorption mechanism of Pb^{2+} ions by UiO-66-NH_2 (MOF) modified with 1,8-dihydroxyanthraquinone by DFT. Geometry optimization were performed by the B3PW91-D3 functional, and Stuttgart-Dresden-Bonn basis set for Pb^{2+} and the 6–31G (d) basis for other atoms. $PbNO_3$ was used as the model of Pb^{2+} and Solvation effect (H_2O) was evaluated with polarizable continuum model (PCM). Based on the bond distance (i.e., with shortest bond distance) and binding energy (i.e., with greater binding energy), Pb^{2+}–N interaction (mono–dentate coordination) was more favorable than the Pb^{2+}–O (bi–dentate coordination) of C–O and O–H group for adsorption of Pb^{2+}.

2.4. Adsorbents for Heavy Metal Removal

Biopolymers (chitosan and starch in this case) based adsorbent hydrogel are active area of research and promising candidate for heavy metal removal from aqueous environment. The attention has been focused more on the production of adsorbents from renewable and abundant resources like chitosan and starch. Hydrogel synthesized from these biopolymers have attracted great attention in the removal of pollutants because of their intrinsic properties, including biodegradability, biocompatibility, and non–toxicity. Bio–hydrogel are biocompatible, biodegradable, possess lower toxicity, high degree of flexibility, and they have good transport properties. The advantage of using hydrogel as adsorbents based on biopolymer is due to their environmentally friendly nature, ease to modify their structure, or to functionalize with polymerizable groups according to the nature of the pollutant.

In their natural form, bio–sorbents are soft and have a tendency to agglomerate in an aqueous solution or form gel, and the chelating groups are not readily available for sorption in their natural form. To overcome these limitations and to improve the adsorption performance, modification with organic–inorganic materials has been reported. It is possible to make functional modification by specific functional groups on the surface of polymeric matrix to improve their selectivity, adsorption capacity, and reusability (F. Ge et al. 2012). The physical properties of inorganic materials with the intrinsic chemical reactivity of organic materials perform better. Adsorbents are modified by cross–linking, grafting or by changing their chemical form or by engineered composite materials. Researchers employed cross–linking, grafting and/or impregnation methods to obtain composite materials, which was superior in adsorption performance than the native adsorbent.

The mechanical properties and adsorption performance of adsorbent also can be improved through the incorporation of synthetic polymer (PVA and PVP in this case) and graphene oxide into the structures as well as through the formation of composites. Moreover, the formation of composites improves thermal stability and the surface area of biopolymer. This literature review section includes adsorption, adsorption isotherm, kinetics, and thermodynamics, PVA, chitosan, grafted starch, functionalized graphene oxide, and stabilized zero–valent iron adsorbent, Cr^{6+}, Pb^{2+} and Cd^{2+} ions removal mechanism, and DFT based adsorption mechanism studies.

Adsorbents with remarkable adsorption capacity towards Cr^{6+}, Pb^{2+} and Cd^{2+} ions have been designed and developed by different researchers. A wide verities of adsorbent such as biopolymer based hydrogel (Ahamad et al. 2019; Gokila et al. 2017; Habiba et al. 2017; T. Li et al. 2019; Prakash and Vendan 2016; Yuvaraja et al. 2019; Zhou et al. 2016), activated carbon (Valentín-Reyes et al. 2019), metal–organic framework (Ghaedi et al. 2018; Jamali et al. 2016; Vellingiri et al. 2018; Yu et al. 2017), carbon nano–tubes (Hayati et al. 2017; Zhang et al. 2012), silica (Li et al. 2011), smart nano–materials and nano engineered material (Pandey and Ramontja 2016), GO and GO–derivatives (Daneshmand et al. 2018; Mondal and Chakraborty 2020; Nuengmatcha, Mahachai, and Chanthai 2015; Sahraei, Pour, and Ghaemy 2017; Yap et al. 2020) have been reported for the removal of Cr^{6+}, Pb^{2+} and Cd^{2+} ions from aqueous waste streams.

2.4.1. Biopolymer Based Adsorbent

Biopolymers (natural polymers) based adsorbents are active area of research and promising candidate for heavy metal removal from aqueous environment. They are remained attractive as they offer feature sustainability, easy availability, minimum chemical needed, non–toxicity, low cost, regeneration opportunities, potentially degradability and bio–compatibility in nature. Moreover, in their bulk structure they possess functional groups like amine, hydroxide, carboxyl, xanthate groups, aldehydes, ketones, alcohols, ethers, and esters (Ahamad et al. 2019). However, direct use is not sustainable and practical because low surface area, low adsorption capacity, poor mechanical properties, low chemical stability and thermal resistance and difficulty of regeneration for reuse.

In their natural form, bio–sorbents (adsorbent from biopolymer) are soft and have a tendency to agglomerate in an aqueous solution or form gel. Besides, the chelating groups are not readily available for sorption in their natural form. To overcome these limitations and to improve the adsorption performance, modification with organic–inorganic materials has been reported. It is possible to make functional modification by specific functional groups on the surface of biopolymer matrix to improve their selectivity, adsorption capacity, stability, and reusability (F. Ge et al. 2012). The physical properties of inorganic materials with the intrinsic chemical reactivity of organic materials perform better during the adsorption.

Chitosan and starch are the most abundant biopolymer (plant polysaccharides) and potential candidates accepting chemical modification by various reactions such as amidation, carboxy methylation, ethoxylation, etc. Generally, biopolymers are good adsorbent for heavy metals. However, their industrial application is limited since it is difficult to separate after use. Some literature revealed that incorporation of magnetic nano–particles will facilitate separation and recovery after heavy metal adsorption from aqueous environment (Dahlan et al. 2017). But magnetic recovery entails the use of strong magnets, which is uneconomical.

Bio–sorbent or sorbent containing biopolymer is mainly prepared by cross–linking reactions via hydroxyl or amino functional groups and chains with a cross linker (to form gels), and immobilization of biopolymer on insoluble support by coupling or grafting reactions (to get hybrid or composite materials) (Abdel-Raouf and Abdul-Raheim 2017a). For instance, chitosan and starch modification is mainly by chemical methods where grafting functional

groups or cross–linking is carried out or by physical methods where changing from flakes to adsorbents occurred (Dahlan et al. 2017). Both the structural and the functional group modification help chitosan and starch to perform better in adsorption (Kahu et al. 2016). Ahamad et al., fabricate cobalt ferrite dispersed egg albumen–formaldehyde bio–based polymer metal complex ($CoFe_2O_4$) novel adsorbent for removal of Cd^{2+} ion (182 mg g^{-1} at pH of 6) and methyl blue (480 mg g^{-1} at pH of 12) from aqueous environment (Ahamad et al. 2019). According to the author, the egg albumen behaves as a source of N–doped carbon as well as the capping agent, and adsorption occurs via electrostatic complexation. The bi–metallic cobalt ferrite offers the adsorbent fast magnetic separation for further use. The adsorption follows pseudo–second order kinetics and Langmuir isotherm for both pollutants.

Incorporation of magnetic nano–particles to the composite adsorbent is not only offered easy and quick separation with the aid of external magnet after use but also they foster the adsorption due to their adsorption capacity and intrinsic large surface area (Fatehi et al. 2017). Leaching of nano–particles during their use should be considered during the inclusion in the adsorbent.

Dax et al., synthesized cationic hemicelluloses (methacrylate inserted O–acetyl galacotoglucomannan, GGM) based hydrogel by trans–esterification reaction for removal of As^{5+} and Cr^{6+} from aqueous environment (Dax et al. 2014). Methacrylate monomer bearing a quaternary ammonium group was responsible for charge (+ve) of the adsorbent. Higher sorption was determined for As^{5+} for an increasing swelling rate because of increased amount of quaternary ammonium groups available for ion exchange with arsenic oxyanions. The maximum sorption was 48.17 mg of As^{6+} per gram of hydrogel. For Cr^{6+}, sorption was higher for lower swelling rate. Moreover, the sorption is pH dependent and maximum sorption for both metals occurs at pH of 9.

Zhao et al., synthesized magnetic modified polyacrylamide micro composite adsorbent by inverse micro–emulsion polymerization via using N, N'–methylene–bis(acrylamide) as cross–linker for removal of Pb^{2+}, Cd^{2+}, Cu^{2+}, and Ni^{2+} from aqueous solution (Zhao et al. 2014). Hydroxamic acid group surface modification/functionalization of magnetic polyacrylamide was applied to lower swelling property and to from stable chelation with heavy metal ions. Swelling rate of magnetic–polyacrylamide (ZPC = 5.26) was decreased

with increasing pH of solution. At low pH, protonation of amide groups causes cation–cation repulsion resulting in high swelling rate and the inverse is true at higher pH. Whereas the swelling rate of Hydroxamic functionalized magnetic polyacrylamide (ZPC = 4.01) increased with pH because of ionization of Hydroxamic groups (–CONHO–) resulting in electrostatic repulsion among themselves. The adsorption for single metal follows the order of: $Cd^{2+}>Co^{2+}>Ni^{2+}>Pb^{2+}$, which is the inverse of hydration number to hydrated radius ratio. But Pb^{2+} is easily captured by the adsorbent under competitive adsorption because of highest stability constant it forms with hydroxamate in aqueous solution, and the adsorbent is more selective to Pb^{2+} for multi metal adsorption.

Zhou et al., developed bio–based polymeric adsorbent for the removal of Pb^{2+} from wastewater. The adsorbent synthesized by graft polymerization reaction between surface modified biomass cyclosorusinterruptus (CI), which serve as a support and acrylonitrile (AN), followed by amidoxime ($NH_2OH.HCl$) functionalization (Zhou et al. 2016). The protonation and de–protonation of amino groups of amidoxine highly dependent on the pH of solution and maximum sorption capacity (78.76 mg g^{-1} at 298 K) was obtained at pH of 5.5. Since the first order hydrolysis constant of Pb^{2+} is 6.3 x 10^{-8}, hydrolysis of Pb^{2+} occurred above pH of 5.5. Moreover, they report that the adsorbent forms a bi–dentate ligand Pb^{2+} and stable five–membered chelating ring can occur between one Pb^{2+} and one amidoxime group. The adsorption follows pseudo second order and Langmuir isotherms.

Boddu et al., prepared composite bio–sorbent (chitosan coated on alumina) characterized by SEM, XPS, and BET, for removal of Cr^{6+} from aqueous solution (Boddu et al. 2003). Oxalic acid is used to form bridge between chitosan and alumina. Chelating groups such as –CH_2OH, –CO, and –NH_2 are responsible for adsorption of Cr^{6+} and the maximum adsorption capacity was 153.8 mg Cr^{6+} per gram of chitosan at pH of 4.

i. Chitosan based adsorbent

One of the recent developments to remove pollutants from aqueous environment is the use of modified chitosan as adsorbents (Table 2.2). However, low adsorption performance of pristine chitosan adsorbents limits their application in wastewater treatment. For instance, pristine chitosan has been widely studied and frequently applied for heavy metal removal due to its good gale forming ability, biodegradability, and richness in the amine functional group

(Yuvaraja et al. 2019). However, low surface area, poor chemical stability, and weak mechanical strength limit its performance and application in wastewater treatment.

Chitosan blended with carbonaceous materials, such as graphene oxide (GO), is considered as sustainable and cost effective for heavy metal ion removal owing to its unique properties including better chemical stability and improved mechanical strength. However, non–selectivity, weak affinity, relatively intermediate adsorption performance, and slow kinetic adsorption limit its wide application in heavy metal treatment.

Chitosan is easily amenable to chemical modification and activation due to the presence of reactive amino and hydroxyl functional groups. The reactive amino and hydroxyl functional group in chitosan are responsible for easily chemical modification of chitosan (Wang and Zhuang 2017). Grafting (i.e., N –atom or O –atom reach groups such as amino, quaternary ammonium, thiol, and carboxyl groups and cross–linking (H. Ge, Chen, and Huang 2012) are widely used in chemical modification of chitosan. Moreover, introduction of materials containing hetero atoms such as N, P, and S atoms into the backbone increases adsorption performance of chitosan. Cross–linking is used to reinforce the chemical stability of chitosan, which increases the chemical stability and physical strength. However, cross–linking consume the reactive functional groups of chitosan. To overcome these problems and to get adsorbent with better selectivity and adsorption, different functional groups, such as carboxyl groups, sulfur groups, amino groups, alky groups and β–cyclodextrininto (Alsbaiee et al. 2016) are grafted on the back bone of chitosan (Yu et al. 2016). Some report shows that mechanical strength, thermal stability, and adsorption performance of chitosan were enhanced by inclusion of carbon nano–materials, such as CNT (Gopi et al. 2014) and GO nano–particles (Luo et al. 2019). Adsorption performance also enhanced by using targeted pollutant as a template (Tang et al. 2017).

Chitosan based adsorbents have attracted increasing attention in wastewater treatment in the past few years because it’s reactive amino and hydroxyl functional groups, it is easily modified through physical and/or chemical methods, it is biodegradable polymer, it is non–toxic, it is environmental friendly and it is cheap and abundant (Appuhamillage et al. 2019; Gokila et al. 2017; Paulino et al. 2011; Prakash and Vendan 2016; Shaker and Yakout 2016; Yuvaraja et al. 2019; Zhang et al. 2019; Zhao et al. 2013). Luo et al., synthesis GO/CMC

composite aerogel for removal of heavy metals from water, and maximum adsorption capacities were 249.38 mg g^{-1} for Pb^{2+}, 151.30 mg g^{-1} for Ag^{2+}, and 95.37 mg g^{-1} for Cu^{2+} (Luo et al. 2019). The aerogel was synthesized by using vacuum–assisted self–assembly, and freeze–drying method. GO incorporation to CMC (decomposition temperature up to 300^{o}C) increases thermal stability of aerogel (decomposition temperature up to 900^{o}C). Wu et al., synthesis hemi–cellulose cross–linked CMC for removal of toxic heavy metals from aqueous environment, and the maximum adsorption capacity were 909.10 mg g^{-1} for Cd^{2+}, 363.3 mg g^{-1} for Ni^{2+}, 333.3 mg g^{-1} Cu^{2+}, 28.2 mg g^{-1} for Hg^{2+} and 49 mg g^{-1} for Cr^{6+} (Wu et al. 2017).

Yuvaraja et al., prepared ZnO incorporated terephthalaldehyde and thiosemicarbazide modified chitosan for Pb^{2+} ion removal from aqueous environment (Yuvaraja et al. 2019). Chitosan modification (*Schiff's* based formation) may occur through the free amino groups of chitosan with an active aldehydes group of terephthalaldehyde. ZnO nano–particle employed to offer stability and mechanical strength. This complex adsorbent contains sulphur functional group in addition to hydroxyl and amine functional group and adsorption of Pb^{2+} occur through these sites. This result shows that Pb^{2+} removal mechanism might be complexation/coordination, electrostatic attraction, ionic exchange and/or precipitation. The maximum removal was achieved at pH of 5.0. The adsorption follows PSO kinetics and Langmuir adsorption isotherms.

Prakash et al., prepared nylon6 and montmorillonite clay blended chitosan by casting processes (Prakash and Vendan 2016). They also add starch to facilitate binding effect, binding of silk with chitosan, and glutaraldehyde were used as cross–linking agent. According to the report, blending with clay and nylon foster the porosity, which facilitates faster diffusion of ions. This novel adsorbent was employed for adsorption of Cu^{2+}, and Cd^{2+} ions, and they reported that Cu^{2+} has better recoveries when compared to Cd^{2+}. Moreover, maximum adsorption of both metal ions occurs near to potential of zero charge (PZC) of chitosan. They also reported that the adsorption follows Langmuir isotherms and PSO kinetics, which is an indicator of concentration of both metal ions and adsorbent are participating in the rate determining step.

Zhao et al., investigated adsorption of Cd^{2+} and Pb^{2+} on EGTA functionalized chitosan adsorbent in aqueous solution (Zhao et al. 2013). EGTA immobilization on chitosan was

characterized by FTIR spectroscopy. EGTA–chitosan contains six sites; four carboxyl oxygen and other one oxygen of EGTA and one nitrogen atom in amine of chitosan, which might participate in chelation. Six of these sites involved in binding Cd^{2+} and Pb^{2+} forming octahedral structure. They recommend for further studies to understand the complexation by theoretical calculations such as theoretically calculated natural bond orbital (NBO) to predict exact site of adsorption. They tried to locate point charge (both negative and positive) of each atom by FTIR and concluded that EGTA–chitosan form octahedral structure with divalent metal ions. The maximum of uptake of Cd^{2+} and Pb^{2+} was 0.74 mmol g^{-1} and 0.50 mmol g^{-1}, respectively and adsorption kinetics followed PSO model but the rate of adsorption was affected by intra–particle diffusion.

Gokila et al., studied the removal of Cr^{6+} from aqueous solution by chitosan–alginate nano–composites novel adsorbent prepared by ionic gelation method (Gokila et al. 2017). Sodium tripolyphosphate and glutaraldehyde used as cross linker of chitosan nano–particle and chitosan–alginate composite respectively. Alginate, water soluble linear polysaccharide, was used as film forming property of chitosan, which is reduced upon cross–linking. The active site on the adsorbent can either be protonated or deprotonated based on the pH of the solution and maximum adsorption (147.15 mg g^{-1}) takes place at pH of 5. The decrease in adsorption at high pH is due to the formation of soluble hydroxyl complexes. The adsorption follows PSO kinetic model and Freundlich isotherms.

ii. Starch based adsorbent

Starch has wide application in industries due to its low cost, biodegradable, and renewable with specific physic–chemical properties (X.-M. Li et al. 2019). It is a widely used material for making biodegradable plastics. However, pure starch properties such as relative high solubility, instability at high temperature, poor processability, and poor mechanical strength or high brittleness limit its industrial application including wastewater treatment (Kan et al. 2017).

To improve some of these drawbacks, starch was often blended with some biodegradable synthetic polymers such as polyvinyl alcohol (PVA). Physical modification is achieved by using hydrothermal processing (gelatinization). Chemical modification is achieved by incorporation of suitable functional groups into the starch structure using etherification,

esterification, cross–linking, and grafting, acid or oxidation and enzymatic hydrolysis. Chemical modification is mostly used method for improving starch physico–chemical properties.

The hydroxyl group of starch is responsible for chemical modifications. They are chemically bonded to various functional groups resulting in starch based composite with improved physic–chemical properties. Cross–linked carboxymethyl starch (CMS) were used for removal of Pb^{2+} (80 mg g^{-1}), and Cd^{2+} (47 mg g^{-1}) from wastewater (Chen, Zhong, and Fang 2012). Carboxymethyl sago starch hydrogel was used for removal of Pb^{2+} (109.89 mg g^{-1}), Cu^{2+} (21.93 mg g^{-1}), and Cd^{2+} (14.58 mg g^{-1}) from aqueous environment (Basri et al. 2016) (Table 2.3). Result from TGA shows that the formation of hydrogel resulted in improvement of thermal stability of carboxymethyl saga starch. Manganese ferrite nano–particle covered with thin layer of CMS also used for removal of Pb^{2+} from wastewater (Perez et al. 2019). Functionalization by cross–linking is other ways of enhancing the physico–chemical properties of CMS.

Magnetic hydrogel adsorbents–polyvinyl alcohol–CMS grafted with polyvinyl imidazole was employed as an adsorbent for removal of Cu^{2+} (83.60 mg g^{-1}), Pb^{2+} (65.00 mg g^{-1}), and Cd^{2+} (53. 20 mg g^{-1}) in aqueous environment (Pour and Ghaemy 2015). This hydrogel has high porosity, and BET surface area due to incorporation of the magnetite nano–particles. Starch and starch derivatives adsorbent has been used for heavy metal remediation (Table 2.3).

2.4.2. Graphene Oxide based Adsorbents

Low adsorption performance of pristine GO adsorbents limits their application in wastewater treatment. Pristine GO with hydrophilic polar functional groups (–OH, –COOH) and large surface area has unique adsorption properties towards heavy metals. However, hydrophobic surfaces and toxicity, and un–recoverability after use (restacking) limit the application of GO. The restacking and agglomeration problem of pristine GO in aqueous solutions can be improved by covalent functionalization with electron rich atoms bearing materials or non–covalent modification/blending with polymers, such as chitosan, starch, PVA and PVP. Blending GO with chitosan – PVA (L. Li et al. 2015; T. Li et al. 2019), and surface modification through functionalization with electron reach atom–bearing materials (Daneshmand et al. 2018) improves the adsorption capacity as well as the selectivity of GO.

However, mono–functional group (amine or thiol) surface modification limit the application in wastewater treatment due to the presence of the multi–valent oxidation state of heavy metal ions in wastewater.

Pristine GO contains an epoxide group on the basal plane and a hydroxyl group on the edge, which easily react with other materials to form carboxylic functional groups (Javidparvar, Naderi, and Ramezanzadeh 2020). For instance, hydroxyl and amine functional groups available on chitosan can establish effective interaction with GO to synthesizes new environmentally friendly novel adsorbents for heavy metal removal (Table 2.4). In addition to this, carboxylic functional groups of GO easily react with amine ($–NH_2$) (Huang et al. 2020; T. Li et al. 2019) and thiol (–SH) (Javidparvar et al. 2020; Yap et al. 2020) functional groups during functionalization with other materials such as L–cysteine. The nitrogen, oxygen, and sulfur atoms are preferable in scavenging heavy metal ions owing to their strong interaction. For instance, in Pb^{2+} capturing, Pb–S > Pb–N > Pb–O during interaction with materials such as L–cysteine based on their softness–hardness nature (Ali et al. 2021).

L–cysteine, which contains amine, thiol, and carboxylic functional groups is an amino acid and a typical example of heavy metal scavengers in aqueous solution. The thiol functional group has excellent selectivity and a strong affinity for heavy metal ions. It shows remarkable binding capacity with heavy metal ions through metal–ligand interactions. The strong coordinate covalent bond formation with heavy metal ions via soft–Lewis acid–base interaction makes L-cysteine suitable for heavy metal removal form aqueous solution.

Recently, research shows that supporting amine and thiol functional group–bearing materials on solids, such as carbon nano tubes (Zhang et al. 2012), graphene oxide (Zhang et al. 2012), silica gel (Li et al. 2014), and alumina (Xia et al. 2017), improves their adsorption performance. For instance, surface modifications of GO with amine and thiol rich functional group provides better selectivity, strong affinity, and improved adsorption capacity in binding and removing heavy metal ions. In this regard, Daneshmand et al., showed synthesis of L-cysteine functionalized GO that can be used for Hg^{2+} removal (Daneshmand et al. 2018). Huang et al., studied the adsorption properties of amino functionalized GO towards Pb^{2+}, Cd^{2+}, Cu^{2+}, and Cr^{6+} (Huang et al. 2020). Seenivasan et al., researched the synthesis of L-cysteine functionalized GO/polypyrrole for nanocomposite film for Pb^{2+} detection in water

(Huang et al. 2020). Muralikrishna et al., studied the synthesis of L-cysteine reduced GO for simultaneous electrochemical determination of Pb^{2+}, Cd^{2+}, Cu^{2+}, and Hg^{2+} in the solution (Muralikrishna et al. 2014). Nuengmatcha et al., researched the synthesis of thiol–functionalized GO adsorbent and studied its adsorption properties for Hg^{2+} removal (Nuengmatcha et al. 2015).

2.4.3. Zero–Valent Iron based Adsorbent

The application of nano–zero valent iron (nZVI) in *situ* remediation of toxic heavy metal ions in particular Cr^{6+} and Pb^{2+} polluted aqueous solution has attracted extensive attention (Qian et al. 2019) (Table 2.5). nZVI have unique properties such as large surface area, fast reaction speed, a strong reduction ability, eco–friend, strong adsorption ability and an ideal cost–effectiveness (Fang et al. 2011), which makes them a promising candidates for a broad range of pollutants. The nZVI was prepared, mostly in *nano* scale by reducing iron with $NaBH_4$. However, because of their advanced dispersive properties, these nano–adsorbents with small dimensions are difficult to recycle and may lead to loss of the adsorbent and bring about secondary pollution to the environment (Guan et al. 2011; Miao et al. 2012). Moreover, nZVI often aggregates and easily gets oxidize resulting in decrease in adsorption efficiency due to decreases in surface area and producing a less negative oxidation–reduction potential (Y Bagbi et al. 2017). For unmodified nZVI, high surface energy and strong magnetic interactions accentuated the self–aggregation phenomenon, which becomes the main difficulty in synthesizing the stabilized, well-dispersed nZVI suspensions that limits the practical applications of nZVI in a variety of environmental systems. To over come such limitation, nZVI have been supported on different materials such as chitosan, starch, carboxymethyl cellulose, polyvinylpyrrolidone (PVP–K30), PVA, polyacrylic acid (PPA), and zeolite. Zhang et al., prepared carboxymethyl cellulose–stabilized nZVI for in *situ* remediation of Cr^{6+} contaminated soil (Zhang, Zhang, and Fang 2018). Kustove et al., synthesized chitosan stabilized nZVI for toxic heavy metal polluted wastewater remediation (Kustov et al. 2011). Divya Chauhan et al., prepared chitosan/PVA/ZVI biopolymeric nanofibers and employed for arsenic removal from wastewater (Chauhan, Dwivedi, and Sankararamakrishnan 2014). Horzum et al., prepared chitosan fiber–supported nZVI particles and used for the removal of arsenic from water (Horzum et al. 2013). Pei et al., employed Vinegar residue–supported nZVI for remediation of Cr^{6+}–contaminated soil in which Cr^{6+} adsorbed onto nZVI and react with the surface containing nZVI to be reduced to Cr^{3+} (Pei et

al. 2020). Esfahani et al., synthesized polyacrylic acid stabilized nZVI to remove Pb^{2+} from aqueous solution (Esfahani et al. 2013). Zhang et al employed kaolinite–supported nZVI for Pb^{2+} removal from aqueous solution (Zhang et al. 2011). Kim et al., used zeolite–nZVI composite for Pb^{2+} remediation (Kim et al. 2013).

2.5. Summary of Literature Review

In recent years, with more strict environmental regulations, there has been a need for an improved quality of treated industrial wastewater. Technologies like adsorption, membrane filtration, electrodialysis, ion exchange, bio–sorption, chemical precipitation and coagulation/flocculation have been used to treat the wastewater containing heavy metals.

Adsorption by low–cost adsorbents and bio–sorption is identified to be efficient and low cost–effective even applicable for lower concentrations of heavy metals. Bio–sorption has been given high importance keeping the environment–friendly nature of the bio–sorbents in mind but stability is a problem.

Even though extensive research on adsorbents have been done and adopted, most of them lack selectivity and fast adsorption kinetics. Recent studies have focused on biopolymer-based adsorption for removal of heavy metals from industrial wastewater due to good affinity and better overall removal efficiencies compared to other adsorbents. However, high retention time, slow adsorption kinetics, non – selectivity and cycling stability of adsorbents limit its wider application in industrial wastewater treatment.

Based on aforementioned limitations, synthesis of adsorbent form biodegradable materials with better selectivity, fast adsorption kinetics and cycling stability should be considered for remediation of industrial wastewater. The synthesis adsorbent should also reduce the retention time of adsorption and it should have fast adsorption kinetic in order to minimize operational costs.

Table 2.2 Chitosan based adsorbent for Cr^{6+}, Pb^{2+}, and Cd^{2+} removal

Adsorbent	Pollutant	C_o(mg L^{-1})	q_m (mg g^{-1})	pH	Kinetics	Isotherms	Reference
GO–CMC	Pb^{2+}	500	249.38	–	–	–	(Luo et al. 2019)
Arginine cross-linked chitosan–CMCL adsorbent	Pb^{2+}	325	182.5	–	–	–	(Manzoor et al. 2019)
CMC–sewage sludge bio-char composite	Pb^{2+}	100	594.17	–	–	–	(Ifthikar et al. 2018)
Tannic acid modified Chitosan bio–sorbent	Pb^{2+}	450	117.75	6	PSO	Freundlich	(Badawi et al. 2017)
Chitosan–MA–DETA	Pb^{2+}	300	239.2	5	PSO	Langmuir	(Zhang et al. 2017)
Chitosan/PEG/PAA	Pb^{2+}	300	431.7	4.8	PSO	–	(Yu et al. 2016)
Lead-ion imprinted chitosan	Pb^{2+}	–	577	6	PSO	–	(Li, Qiu, and Xu 2013)
CMC	Cd^{2+}	–	121.00	3	–	–	(Borsagli and Borsagli 2019)
Arginine cross-linked chitosan–CMCL adsorbent	Cd^{2+}	300	168.50	–	–	–	(Manzoor et al. 2019)
CMC–hemicelluloses resin composite	Cd^{2+}	100	909.10	–	–	–	(Wu et al. 2017)
Chitosan-MA-DETA	Cd^{2+}	–	201.60	5	PSO	Langmuir	(Zhang et al. 2017)
Chitosan-Iron oxide nanocomposite	Pb^{2+}	100	214.9	5	PSO	Langmuir	(Ahmad and Mirza 2018)
	Cd^{2+}		204.3				
CMC	Cd^{2+}	200	121.00	3	–	–	(Hayati et al. 2017)
	Cr^{6+}		147.20	8.5	–	–	

Chitosan–GO/ CMCL aerogel	Cr^{6+}	127.40	–	–	–	(Huang et al. 2019)
CMC–hemicelluloses resin composite	Cr^{6+}	49.00	–	–	–	(Wu et al. 2017)
Chitosan cross-linked with DETAA	Cr^{6+}	192.30	3	PSO	Langmuir	(Bhatt, Sreedhar, and Padmaja 2015)

Table 2.3 Starch based adsorbent for Pb^{2+}, and Cd^{2+} removal

Adsorbent	Pollutant	C_o(mg L^{-1})	q_m(mg g^{-1})	pH	Kinetics	Isotherms	Reference
Manganese ferrite nano-particles CMS	Pb^{2+}	300	46	5.5	PSO	Sips	(Perez et al. 2019)
CM sago starch–acid hydrogel	Pb^{2+}	100	109.89	–	–	–	(Basri et al. 2016)
	Cd^{2+}		14.58				
Magnetic hydrogel-PVA/ CMS-g-PVI	Pb^{2+}	200	65.00	–	–	–	(Pour and Ghaemy 2015)
	Cd^{2+}		53.20				
Cross linked CMS	Pb^{2+}	–	80.00	–	–	–	(Pour and Ghaemy 2015)
	Cd^{2+}		27.00				
CMS grafted with N-VI	Cd^{2+}	–	68.00	–	–	–	(El-Hamshary et al. 2014)

Table 2.4 Graphene oxide based adsorbent for Pb^{2+}, and Cd^{2+} removal

Adsorbent	Pollutant	q_m (mg g^{-1})	pH	Kinetics	Isotherms	Reference
Amino-functionalized GO	Pb^{2+}	71.89	5	PSO	Langmuir	(Huang et al. 2020)
	Cd^{2+}	10.04	5	PSO	Langmuir	
	Cu^{2+}	26.25	4	PSO	Freundlich	
	Cr^{6+}	280.1	2	PSO	Freundlich	
GO	Cr^{6+}	1.22	4	PFO	Langmuir	(Mondal and Chakraborty 2020)

Table 2.5 ZVI based adsorbent for heavy metal ions removal

Adsorbent	Pollutant	q_m	pH	Isotherms	Reference
Chitosan–nZVI	As^{3+}	0.02 mmol g^{-1}	6	Langmuir	(Horzum et al. 2013)
	As^{5+}	0.03 mmol g^{-1}		Freundlich	
Chitosan/PVA/ZVI	As^{3+}	142.9 mg g^{-1}	7	Langmuir	(Chauhan et al. 2014)
	As^{5+}	200 mg g^{-1}		Freundlich	
Vinegar–nZVI	Cr^{6+} (soil)	–	5.5	–	(Pei et al. 2020)
PAA–nZVI	Pb^{2+}	–	5	–	(Esfahani et al. 2013)
Kaolinite–nZVI	Pb^{2+}	–	5.1	–	(Zhang et al. 2011)
Zeolite – nZVI	Pb^{2+}	96.2 mg g^{-1}	4	–	(Kim et al. 2013)

CHAPTER THREE

MATERIALS AND METHODS

3.1. Research Framework

The experimental work required to attain planned general and specific objective of this dissertation work is conceptually designed (Fig. 3.1). First, the locally available tuber plant, 'anchote' (*Coccinia abyssinica*) were collected, pre–treated and ready for the starch extraction. The starch was extracted and grafted with acrylamide for hydrogel synthesis. The synthesized hydrogel adsorbent PPSgCG, PCCFG, and CZVI-CS-PVA were characterized before the adsorption of heavy metal ions. Using a one–factor–at–a–time approach, batch experiments were conducted using hydrogel adsorbent containing synthetic water and real wastewater. Isotherms, kinetics, thermodynamics, and effect of co–existing ions were studied based on the maximum values obtained from a one–factor–at–a–time approach. The batch experiments were also conducted using Batu Tannery wastewater effluent as real wastewater.

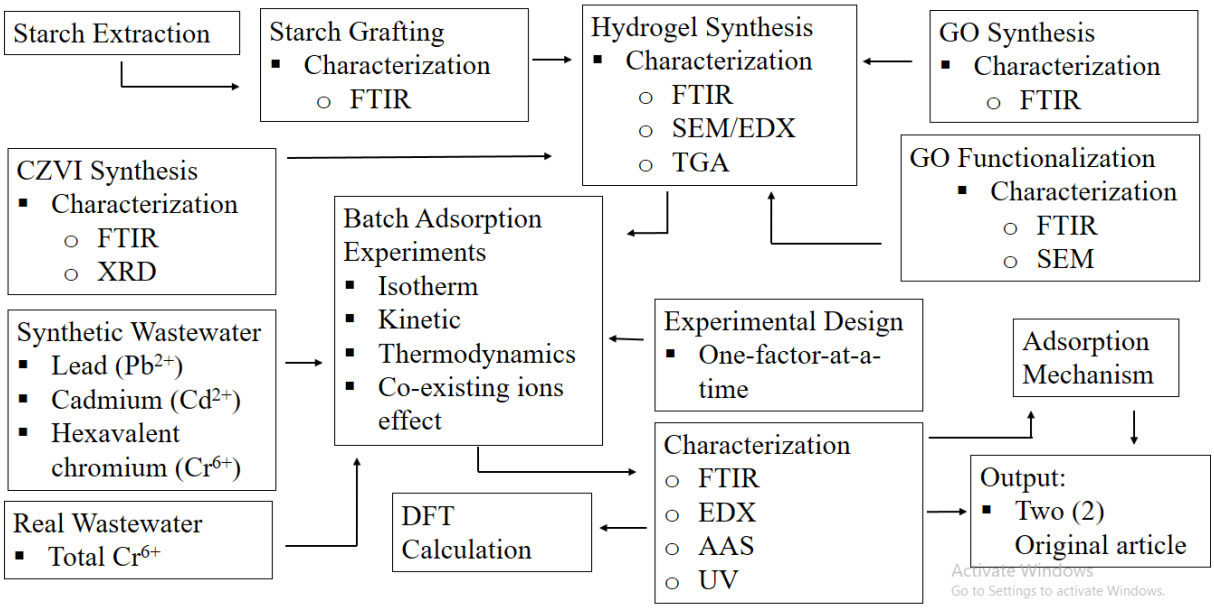

Fig. 3.1 Experimental workflow design.

PPSgCG hydrogel were synthesized from PVA, PVP, S–g–AAm, chitosan and graphene oxide. PCCFG hydrogel were synthesized from PVA, chitosan and L–cysteine functionalized graphene oxide. According to FTIR and EDX analysis results, the $CONH_2$ of S–g–AAm, amine ($–NH_2$) of chitosan, –COOH of graphene oxide and thiol group of L-cysteine were involved in chelation of Cr^{6+} and Pb^{2+}. Based on this, one possible model of schematic

drawing of PPSgCG (Fig. 3.10(a)), which includes structure of S–g–AAm, chitosan and graphene oxide were built by Chem Draw 20.1.1. Similarly, the PCCFG (Fig. 3.11(a)), which includes structure of chitosan and L–cysteine functionalized graphene oxide were built by Chem Draw 20.1.1. The possible adsorption site sections of PPSgCG (hereafter PPSgCG–I) (Fig. 3.10(b)) and PCCFG (hereafter PCCFG–I) (Fig. 3.11(b)), which was built by Gauss View 6.0.16 were first optimized by MM (using UFF) and low level of theory (HF/3–21G) followed by high level of theory (DFT), using Gaussian 09. Geometry optimization, frequency, and NBO calculation were performed by the B3PW91–D3 functional with the 6-31G (d, p) basis set for C, N, O, S and H atoms, and SDD basis set for heavy metal ions. Single–point energy calculation was performed using the wB97XD functional with the 6-311+G(d, p) basis set for C, N, O, S and H atoms, and SDD basis set for heavy metal ions.

3.2. Real Wastewater

Real wastewater samples were taken from the effluent of primary treatment (chemical precipitation) of the Batu Tannery, which is located in Addis Ababa, Ethiopia. The sample were collected, treated, stored and analyzed according to APHA–Colorimetric method (3500–Cr. B) standard (23rd Edition). The collected wastewater sample was treated with 1N NaOH to pH = 9 for total hexavalent chromium (Cr^{6+}) determination, and stored at 4^{o}C before analysis. Prior to the analysis, this wastewater sample was filtered using 0.45–µm filter. The procedure for measuring of total hexavalent chromium were made according Standard Methods: 3500-Cr B: Chromium by Colorimetry (APHA, AWWA 2023).

3.3. Chemical Used

Sulfuric acid (H_2SO_4, 360 ml), phosphoric acid (H_3PO_4, 40 ml), potassium permanganate ($KMnO_4$, 18 g), graphite powder (3 g), hydrochloric acid (HCl, 37%) and hydrogen peroxide (H_2O_2, 30%) were used to synthesis GO. 40 ml thionyl chloride were used for GO surface activation and 0.2 g of L–cysteine dissolved in 50 ml DMF were used for GO functionalization. APS (0.08 g) and TEMED (0.4 ml) were used for starch grafting. Ferric chloride ($FeCl_3.6H_2O$, 14.2 g), sodium borohydride ($NaBH_4$, 7.2 g), and L–cysteine (6.0 g) were used for synthesis of L–cysteine stabilized nZVI. Polyvinylpyrrolidone (PVP k–30, M.W. 40000), polyvinyl alcohol (PVA, degree of polymerization: 1,500), chitosan (CS, degree of deacetylation: 75%, viscosity: min 200 cps.), and sodium alginate (assay: 91%) with GO and grafted native starch were used to synthesis PPSgCG hydrogel. PVA, CS, and

sodium alginate with L–cysteine functionalized GO were used to synthesis PCCFG hydrogel. L–cysteine stabilized nZVI, chitosan, and PVA were used to synthesis CZVI-CS-PVA hydrogel. $CaCl_2$ solution (boric acid saturated) were used to engulf the mixture of chitosan, grafted starch, PVA, PVP, CFG and CZVI during the hydrogel preparation. Potassium dichromate (KCr_2O_7), sodium di–hydrogen phosphate ($NaH_2PO_4.2H_2O$, 99%), sodium sulphate (Na_2SO_4, 99%), sodium chloride (NaCl, 99%), potassium nitrate (KNO_3, 99%), $Pb(NO_3)_2$, $Cd(NO_3)_2$ and $Cu(NO_3)_2$ were dissolved in deionized water to prepare hexavalent chromium, phosphate, sulphate, chloride, nitrate, lead, cadmium, and copper stock solutions (1000 mg l^{-1} each), respectively. During the experimental work, the pH was adjusted using diluted (0.1 M) HCl and (0.1 M) NaOH.

3.4. Apparatus Used for Analysis

The concentration of Cr^{6+} (both in synthetic water and real wastewater), and Pb^{2+} and Cd^{2+} in the solution after adsorption were determined by UV–vis spectrophotometer (x – human) at 350 nm wavelength (for linear range from 0.5 to 100 mg Cr^{6+} L^{-1}) and AAS, respectively. The concentration of total Cr^{6+} in real wastewater before and after adsorption in a solution of pH of 2 and 9 were determined at 350 nm, and 373 nm wavelength (for linear range from 0.5 to 25 mg Cr^{6+} L^{-1}), respectively. A calibration curve (Annex 1) (R^2=0.999) of Eq. (3.1) was obtained from seven standard solutions for the Cr^{6+} measurements by UV–vis spectrophotometer. This calibration curve was used for measurement of Cr^{6+} concentration in synthetic water and real wastewater.

$$C(ppm) = 78.49 * A - 0.396 \quad (3.1)$$

Where C is Cr^{6+} concentration and A is absorbance.

3.5. Hydrogel and Intermediate Product Synthesis

3.5.1. Acrylamide Grafted Starch Synthesis

Starch was extracted from 'anchote' (*Coccinia abyssinica*), an indigenous tuber plant according to the method reported (Abera et al. 2019). White powder extracted starch was grafted with acrylamide according to the method used elsewhere with some modification (Lanthong, Nuisin, and Kiatkamjornwong 2006; Musa et al. 2019). In a typical procedure (Annex 2): starch (4 g) was mixed with 60 ml of distilled water in three necked round bottom flask. The solution was mechanically stirred (300 rpm) under heating at 82°C in nitrogen environment for 60 min to form gelatinized white paste starch. Then the gelatinized starch was cooled to 47°C. Hence, a 100 ml solution containing 8.0 g of AAm (starch to monomer ratio of 1:2), 0.08 g of ammonium per sulfate (APS, 1.0 wt%) and 0.4 ml of TEMED was added to gelatinized starch and stirred for 40 minutes under nitrogen environment. The reaction product was precipitated in 300 ml methanol for 12 h and dried at 65°C. Afterwards, the dry grafted starch powder (11 g) was placed into 300 ml distilled water and vigorously stirred for 24 h at room temperature in order to remove free polymer. The solution was centrifuged (6000 rpm) for 30 min and the supernatant (free polymer) was decanted away and the filtrate was dried at 65°C for 12 h. Finally, 6.10 g of acrylamide grafted pristine starch (S–g–AAm) was obtained. The grafting efficiency (GE) and grafting percentage (GP) were calculated by using Eq. (3.2) and Eq. (3.3), respectively. The reaction of starch with acrylamide was shown in Schematic–I.

$$GE(\%) = \frac{w_{gs} - w_{st}}{w_m} * 100\% \tag{3.2}$$

$$GP = \frac{w_{gs} - w_{st}}{w_{gs}} * 100\% \tag{3.3}$$

Where, w_{st}, w_{gs} and w_m denote mass of pristine starch, grafted pristine starch and monomer, respectively.

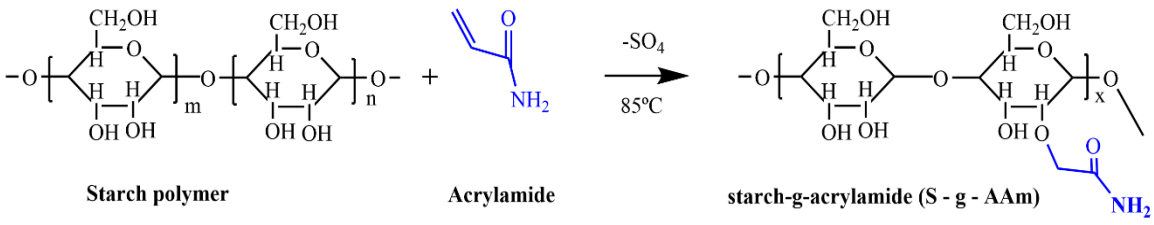

Schematic–I

3.5.2. Graphene Oxide Synthesis

Graphene oxide was synthesized from graphite powder according to improved Hummer's method (Marcano et al. 2010) with some modification (Annex 3). Briefly, 18.0g of KMnO4 and 3.0g of graphite powder (6:1) was added to mixture of 360 ml of H_2SO_4 and 40 ml of H_2PO_4 (9:1) strong acid in ice both and stirred for 30 minutes. Then, this mixture was reacted for 10 hour at constant temperature of 50 ^oC (in water bath) under continues mixing at 250 rpm. After 10 hour of reaction, the slurry added to 500 ml of iced distilled water, followed by addition of 3ml H_2O_2 (30%), and washed repeatedly with excess distilled water and allowed to settle for 24 hour. The settled gray solid was filtered by polyester fiber and the filtrate was centrifuged (4000rpm, 2h). The supernatant were decanted away and the remaining solid washed with 200ml of distilled water and filtered by polyester fiber and centrifuged repeatedly to remove unreacted graphite powder. The remaining solid after filtration and centrifugation was treated with 200ml of HCL (30%) and 200 ml of pure ethanol (99.9%) sequentially. Then the obtained solid materials were coagulated with 200 ml of ether and resulting in suspension, which was filtered over PTFE membrane. The solid materials obtained on the filter were vacuum dried for 2 hour at room temperature and oven dried at 60 ^oC for 20 hour. Finally, 1.0g of grapheme oxide (GO) were obtained.

3.5.3. Graphene Oxide Functionalization with L-cysteine

The L–cysteine functionalized GO was prepared according to a previous method (Daneshmand et al. 2018; Javidparvar et al. 2020; Milenković et al. 2021) with some modification (Annex 4). Briefly, 0.2 g of GO powder was added to 10 ml of dimethylformamide (DMF) under ultra–sonication for 1h and transferred to an oil bath maintained at 85^oC. After 20 min, 40 ml of thionyl chloride was added to the GO solution for surface activation (covalent modification) under a nitrogen environment (Fig. 3.2). During the activation of GO surfaces, the carboxylic acid of GO was converted to acyl chloride. After 24 h of reaction, the black solid activated GO was removed from the solvent, dried, and dissolved in 50 ml of DMF at 85^oC. Simultaneously, 0.2 g of L-cysteine dissolved in DMF solution was added drop–wise to the activated GO solution and left to react for 24 h. Finally, the black precipitate was centrifuged and washed with ultra–pure water and DMF several times to remove any un reacted thionyl chloride and L-cysteine, and then dried at 60^oC.

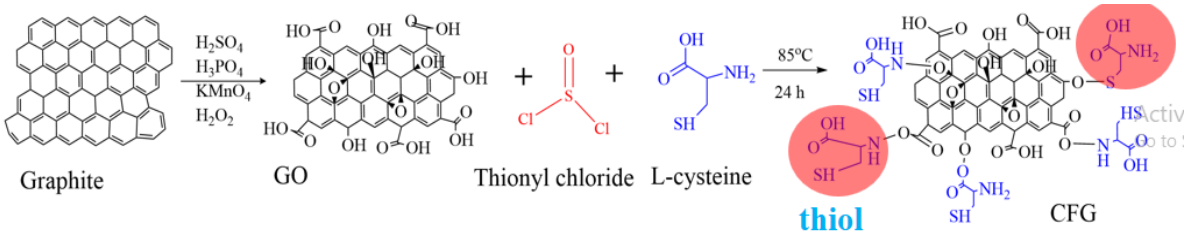

Fig. 3.2 Schematic diagram showing **CFG** synthesis.

3.5.4. PPSg Hydrogel Synthesis

The PPSg hydrogel was synthesized as follows (Fig. 3.3): 1.2 g PVA, 0.8 g PVP (3:2 PVA/PVP ratio), and 0.26 g sodium alginate powder were placed in ultrapure water (90°C) and blended using magnetic stirrer (300 rpm) for 3 h. Then, 1.6 g of S-g-AAm powder were added to the white paste mixture in 30 min intervals and stirred for 5 h. Following this, the mixture was added to 2% $CaCl_2$ solution (boric acid saturated) drop wise to form cylindrical hydrogel. After 72 h immersion, the hydrogel were washed with ultrapure water several times to remove excess calcium ions and preserved in ultrapure water until further use.

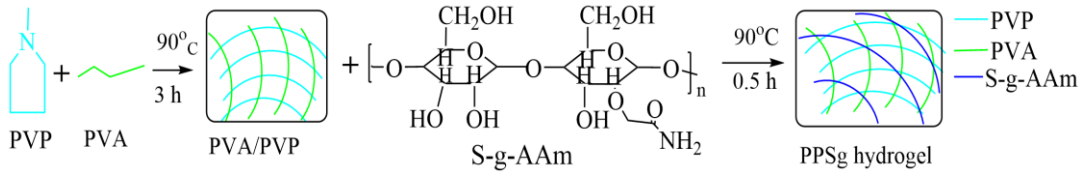

Fig. 3.3 Schematic diagram showing PPSg hydrogel synthesis.

3.5.5. PPSgC Hydrogel Synthesis

The PPSgC was synthesized as follows (Fig. 3.4): 1.2 g PVA, 0.8 g PVP (3:2 PVA/PVP ratio), and 0.26 g sodium alginate powder were placed in ultrapure water (90°C) and blended using magnetic stirrer (300 rpm) for 3 h. Then, 1.6 g of S-g-AAm and 0.4 g of CS powder were added to the white paste mixture in 30 min intervals and stirred for 5 h. Then the mixture was cooled to room temperature. Following this, the mixture was added to 2% $CaCl_2$ solution (boric acid saturated) drop wise to form cylindrical hydrogel. After 72 h immersion, the hydrogel were washed with ultrapure water several times to remove excess calcium ions and preserved in ultrapure water until further use.

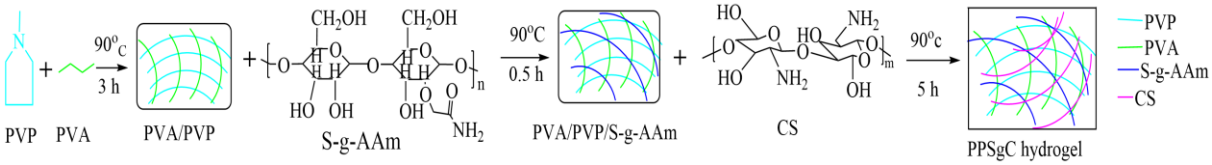

Fig. 3.4 Schematic diagram showing PPSgC hydrogel synthesis.

3.5.6. PPSgG Hydrogel Synthesis

The PPSgG was synthesized as follows (Fig. 3.5): 1.2 g PVA, 0.8 g PVP (3:2 PVA/PVP ratio), and 0.26 g sodium alginate powder were placed in ultrapure water (90°C) and blended using magnetic stirrer (300 rpm) for 3 h. Then, 1.6 g of S–g–AAm powder were added to the white paste mixture in 30 min intervals and stirred for 5 h. Then the mixture was cooled to room temperature. The 2 mg ml^{-1} GO dispersed solution was added to this mixture and blended using magnetic stirrer. This blend was dispersed by ultra–sonication for 40 min at room temperature. Following this, the mixture was added to 2% $CaCl_2$ solution (boric acid saturated) drop wise to form cylindrical hydrogel. After 72 h immersion, the hydrogel were washed with ultrapure water several times to remove excess calcium ions and preserved in ultrapure water until further use.

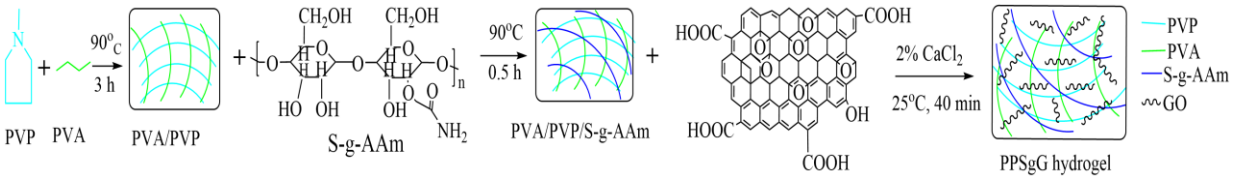

Fig. 3.5 Schematic diagram showing PPSgG hydrogel synthesis.

3.5.7. PPSgCG Hydrogel Synthesis

The PPSgCG was synthesized as follows (Annex 5 & Fig. 3.6): 1.2 g PVA, 0.8 g PVP (3:2 PVA/PVP ratio), and 0.26 g sodium alginate powder were placed in ultrapure water (90°C) and blended using magnetic stirrer (300 rpm) for 3 h. Then, 1.6 g of S–g–AAm and 0.4 g of CS powder were added to the white paste mixture in 30 min intervals and stirred for 5 h. Then the mixture was cooled to room temperature. The 2 mg ml^{-1} GO dispersed solution was added to this mixture and blended using magnetic stirrer. This blend was dispersed by ultra-sonication for 40 min at room temperature. Following this, the mixture was added to 2% $CaCl_2$ solution (boric acid saturated) drop wise to form cylindrical hydrogel. After 72 h immersion, the hydrogel were washed with ultrapure water several times to remove excess calcium ions and preserved in ultrapure water until further use. The adsorbent was engulfed

in the network formed by the reaction between the carboxylic groups present in the alginate backbone and Ca^{2+}, forming ionic cross–link hence no cytotoxicity.

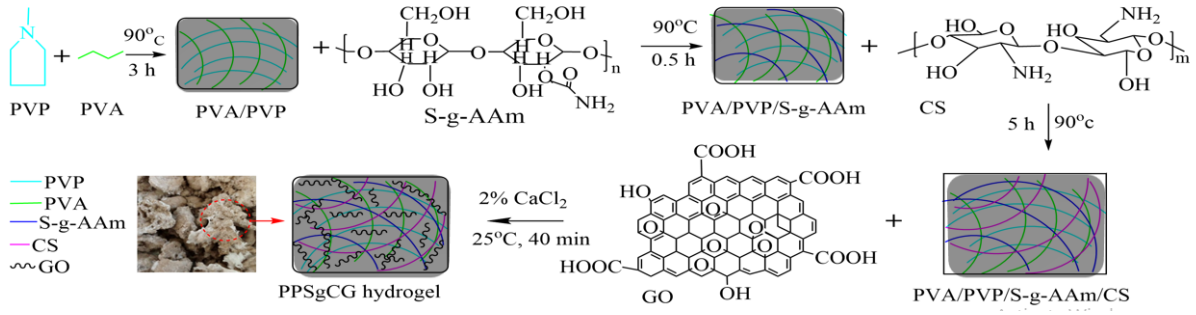

Fig.3.6 Schematic diagram showing PPSgCG hydrogel synthesis.

3.5.8. PCCFG Hydrogel Synthesis

The PCCFG hydrogel was synthesized according to the method reported elsewhere (T. Li et al. 2019) with some modification (Annex 6 and Fig. 3.7). Briefly: 2 g of PVA and 0.25 g of sodium alginate powder were added to 60 ml of hot (90°C) ultrapure water and mixed vigorously (350 rpm) for 2 h in water bath. 2g of chitosan (CS) was added to 30 ml of 1% (v/v) glacial acetic acid and stirred for about 2 h. The chitosan solution was added to a PVA–sodium alginate gel and mixed vigorously at 80°C for 6 h, which produced a white gel. Then, 20 ml of 1.0 mg mL^{-1} of CFG solution was sonicated for 30 min and added to the CS–PVA mixture at room temperature. The CS–PVA–CFG mixture was stirred and sonicated for 2 h at room temperature. Finally, the resulting slurry was added to a gently stirred 2% boric saturated $CaCl_2$ solution drop wise and immersed in ultra–pure water for 72 h for stable cross–linking. At the end, the CS–PVA–CFG (PCCFG) hydrogel was washed with ultra–pure water several times and freeze–dried for further use. The interaction among the polymers depends on the type of functional groups they possessed in their bulk structure, molecular size and compatibility mode. These polymers (PVA and CS) and CFG at least possess an –OH functional group, which favors inter–molecular and intra–molecular hydrogen bonding during the interaction. Hydroxyl functional groups of both PVA and CS are responsible for the strong interactions between them (Sandoval et al. 2005). The hydroxyl group and amine group favor the interaction of chitosan with amine, thiol, and carboxylic groups of CFG.

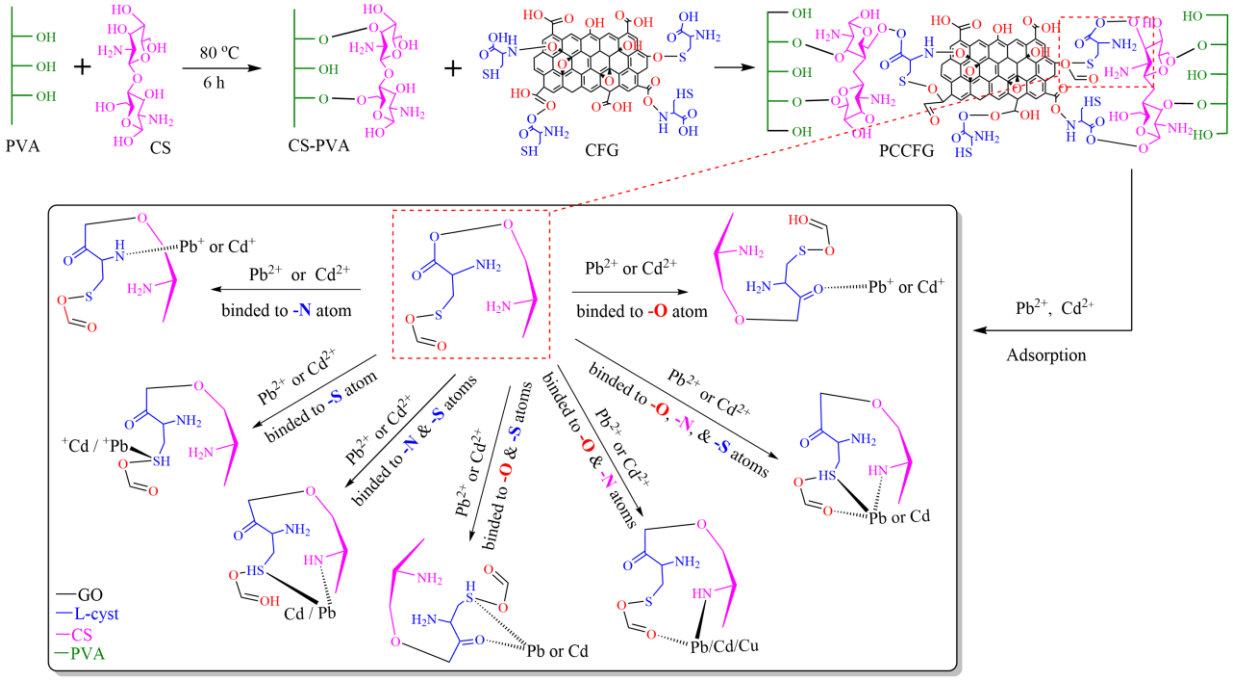

Fig.3.7 Schematic diagram showing synthesis of PCCFG hydrogel and possible Pb^{2+} and Cd^{2+} binding site

3.5.9. L–Cysteine Stabilized Zero –Valent Iron Synthesis

L–cysteine stabilized zero–valent iron (CZVI) was synthesized in conical flask with three open necks at room temperature in a closed chamber with nitrogen gas environment to avoid oxygen interference (Fig. 3.8). Borohydride ($NaBH_4$) was used to reduce ferric ion to zero–valent iron (Eq. (3.4)). Briefly, 14.2 g of $FeCl_3.6H_2O$ was dispersed in a solution containing 35 ml absolute ethanol and 15 ml distilled water and stirred (500 rpm) for 3 h. Similarly, 7.2 g of $NaBH_4$ was dissolved in 100 ml distilled water and added to ferric ions solution. Slowly the yellowish–red color solution turned black color and formed zero–valent iron slurry. The mixtures was continuously stirred for more 30 minutes and 4.2 g of L–cysteine was then added slowly into the slurry. This mixture was continuously stirred for 50 minutes, the stabilized ZVI was separated from the liquid phase via vacuum filtration, and the residue was washed several times with ethanol. The resulting black solid was dried at room temperature in desiccators for 36 hrs and store for CZVI-CS-PVA hydrogel synthesis.

$$4F_e^{3+} + 3BH_4^- + 9H_2O \rightarrow 4F_e^0 \downarrow + 3H_2BO_3^- + 12H^+ + 6H_2 \qquad (3.4)$$

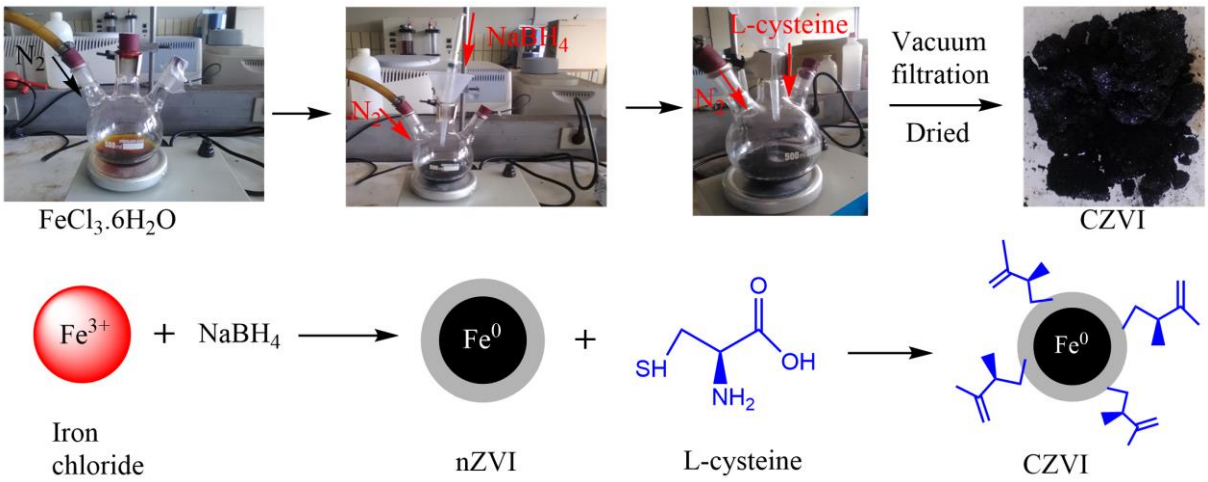

Fig. 3.8 L–cysteine Stabilized Zero–Valent Iron Synthesis

3.5.10. CZVI-CS-PVA Hydrogel Synthesis

Chitosan (2 g) were dissolved in 100 ml of 2 % acetic acid solution at room temperature with magnetic stirring for 24 h. The PVA solution (5 g in 100 ml distilled water) was prepared in water at 90^{o}C under magnetic stirrer, and then cooled to room temperature. Then, the chitosan solution prepared was mixed with the PVA solution prepared to obtain chitosan – PVA gel. Finally, 100 ml of chitosan–PVA white gel were mixed (500 rpm) with 2 g ml^{-1} of synthesized L–cysteine stabilized ZVI solution to get CZVI-CS-PVA (Annex 7 & Fig. 3.9). This gel was added to a gently stirred 2% boric saturated $CaCl_2$ solution drop wise and immersed in ultra–pure water for 72 h for stable cross–linking. At the end, the CZVI–CS–PVA hydrogel was washed with ultra–pure water several times and freeze–dried for further use.

The thiol group of L–cysteine reacted with the iron oxide of nZVI forming strong chemical bond. The –OH of chitosan and PVA form strong intra–hydrogen bonding with –OH of L–cysteine stabilized zero–valent iron. The amine of chitosan may react with amine of L–cysteine stabilized ZVI, which form strong chemical bonding between CS–PVA and CZVI during dispersion of CZVI in CS–PVA. Biodegradable polymers (e.g., chitosan, PVA) are regarded as an attractive candidates for changing surface charges and steric stabilization to enhance stability due to large molecular weights, the abundance of charged functional groups and their environmental friendliness. In addition to L–cysteine stabilization of ZVI, incorporation of CS–PVA provides inter–particle and electrostatic repulsion that reduces

magnetic forces between magnetic particles, thereby reducing agglomeration and enhances water dispersibility.

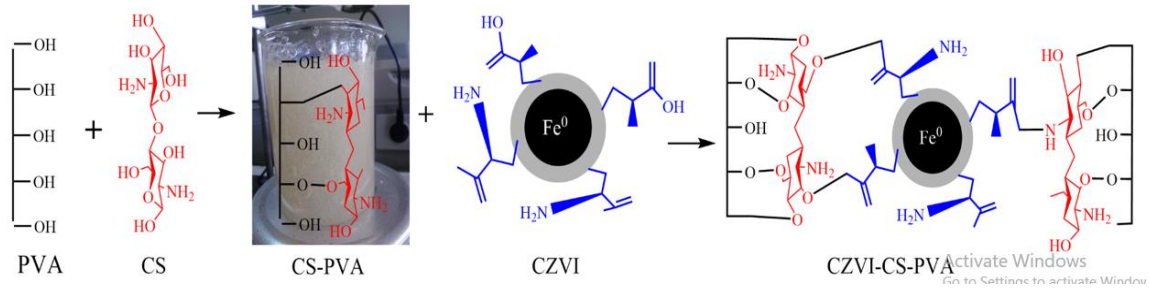

Fig.3. 9 CZVI–CS–PVA Hydrogel Synthesis (schematic diagram)

3.6. Synthesized Intermediate Product and Hydrogel Characterization

The functional group of GO, pristine starch (S), grafted pristine starch (S–g–AAm), PPSgCG hydrogel before and after Cr^{6+} ion adsorption, and PCCFG hydrogel before and after Pb^{2+} loading were analyzed by Fourier spectrometer (FTIR; Spectrum 65, PerkinElmer) in the wave number range of 4000 to 400 cm^{-1}. Morphology analysis was performed using a scanning electron microcopy instrument (SEM; JCM-6000 Plus, Japan) operated at high acceleration 10 kV voltage. Elemental composition analysis was performed using energy dispersive x–ray spectroscopy (EDX; JSM–IT 100, JEOL) before and after adsorption of Pb^{2+}. The sample was coated (Sputter Coater; SCD 050) with an alloy of gold and palladium (80 % Au, and 20 % Pd). The hydrogel sample was freeze–dried before imaging. Thermal stability and decomposition behavior of as–prepared PPSgCG and PPSgC hydrogel was performed using TGA (HCT–1, China) in the temperature range of 25 to 800^{o}C at hating rate 20^{o}C min^{-1}. The structures and crystalline size of synthesized L–cysteine ZVI was obtained using X–ray Diffractometer (XRD–7000, SHIMADZU–Japan with CuKα radiation at λ = 1.5406 Å). The crystallographic analysis of samples in diffraction patterns was recorded from 10˚ to 80˚ counting at scan speed of 3˚ min^{-1} with an accelerating voltage of 40.0 kV. The zeta potential of the sample were measured by a Zetasizer instrument (3000HS). The Cr^{6+} ions concentration in solution was determined by UV–vis spectrophotometer (Human, X–ma 1200) by direct method (Sanchez-Hachair and Hofmann 2018). The Pb^{2+}, Cd^{2+}, and Cu^{2+} ions concentration in the solution after adsorption was determined by atomic adsorption spectroscopy (AAS; ZEEnit 700p, Analytikajena).

3.7. Hydrogel Swelling Ratio

The freeze–dried hydrogel with known mass was put into a tea bag and immersed in beaker containing ultrapure water at room temperature. The swollen hydrogel was continuously taken out from the solution and its weight was recorded until it was constant. The swelling ratio (SR) of hydrogel was calculated using Eq. (3.5).

$$SR(\%) = \left(\frac{w_s - w_d}{w_d}\right)*100\% \quad (3.5)$$

Where, w_s and w_d are mass of swollen and dry hydrogel, respectively.

3.8. Batch Adsorption Experiments

Adsorption experiments were conducted to investigate the adsorption properties of the designed hydrogel. In particular, the effects of initial solution pH, heavy metal ions concentration, hydrogel dose, and time were studied by following a one–factor–at–a–time approach. All batch adsorption studies were conducted in 100ml rubber stopped volumetric flasks. The flasks were placed inside incubator shaker (New Brunswick Scientific Edison, USA, EXCELLA E24R) at 120 rpm for specified times. The adsorption capacities (q_t, q_e) and removal efficiency (R) of the freeze–dried hydrogel for Cr^{6+}, Pb^{2+}, and Cd^{2+} ions were calculated using Eq. (3.6), Eq. (3.7) and Eq. (3.8), respectively.

$$q_t = \frac{(C_o - C_t)*V}{m} \quad (3.6)$$

$$q_e = \frac{(C_o - C_e)*V}{m} \quad (3.7)$$

$$R = \frac{(C_o - C_e)*100\%}{C_o} \quad (3.8)$$

Where; q_t and q_e are the amounts of Cr^{6+} or Pb^{2+} or Cd^{2+} ion adsorbed at time t and at equilibrium (mg g^{-1}), respectively. C_o, C_t and C_e are concentrations of Cr^{6+} or Pb^{2+} or Cd^{2+} ion in the solution (mg l^{-1}) at time 0, t and equilibrium, respectively. V is the volume of heavy metal ion solution used (liter) and m is the mass of the freeze–dried hydrogel used (g).

3.8.1. Adsorption of Cr^{6+} onto PPSgCG Hydrogel

A stock solution (1000 mg l^{-1}) of Cr^{6+} ion was prepared by dissolving appropriate amount of KCr_2O_7 in ultrapure water. The Cr^{6+} ion solution ranging from 20 to 120 mg l^{-1} were prepared by serial dilution of the respective stock solutions and 25 ml of the prepared

solutions were used for the batch adsorption experiments. The effect of initial Cr^{6+} ion concentration (20–100 mg l^{-1}), pH (2–6), time (30–240 minutes), and hydrogel dose (2–4 g l^{-1}) on adsorption of Cr^{6+} onto PPSgCG were studied. The coexisting ions (PO_4^{3-}, SO_4^{2-}, NO_3^-, and Cl^-) competing for the adsorption on the PPSgCG hydrogel during Cr^{6+} ion adsorption were examined at the initial concentration of 100 mg l^{-1} (20 ml) keeping other factors constant. The kinetic adsorption experiments were conducted at pH of 2, 100 mg l^{-1} initial Cr^{6+} ion concentration, 3 g l^{-1} hydrogel dose, 25°C temperature and in time range of 20 – 120 minutes. The isotherm experiments were conducted at pH of 2, 120 minute, 3 g l^{-1} hydrogel dose, and various temperatures (25, 35, 45°C). After adsorption, the hydrogel was separated and the remaining Cr^{6+} concentration in the solution was determined by UV–vis spectrophotometer by direct method. Absorbance at 350 nm wavelength of standard solutions of 10, 20, 50, 80, 100, and 120 mg l^{-1} of Cr^{6+} ion in acidic condition (at pH of 2) was used for calibration.

3.8.2. Adsorption of Cr^{6+} onto CZVI-CS-PVA Hydrogel

A stock solution (1000 mg l^{-1}) of Cr^{6+} ion was prepared by dissolving appropriate amount of KCr_2O_7 in ultrapure water. The Cr^{6+} ion solution ranging from 5 to 100 mg l^{-1} were prepared by serial dilution of the respective stock solutions and 25 ml of the prepared solutions were used for the batch adsorption experiments. The effect of initial Cr^{6+} ion concentration (5–100 mg l^{-1}), pH (2–8), time (10–150 minutes), and hydrogel dose (1–5 g l^{-1}) on adsorption of Cr^{6+} onto CZVI–CS–PVA were studied. The kinetic adsorption experiments were conducted at pH of 3, 45 mg l^{-1} initial Cr^{6+} ion concentration, 4 g l^{-1} hydrogel dose, 25°C temperature and in time range of 20–100 minutes. The isotherm experiments were conducted at pH of 3, 90 minute, 4 g l^{-1} hydrogel dose, and 25°C temperature. After adsorption, the hydrogel was separated and the remaining Cr^{6+} concentration in the solution was determined by UV–vis spectrophotometer by direct method.

3.8.3. Adsorption of Pb^{2+} and Cd^{2+} onto PCCFG Hydrogel

A stock solution (1000 mg l^{-1}) of Pb^{2+}, Cd^{2+} and Cu^{2+} ions was prepared by dissolving appropriate amount of $Pb(NO_3)_2$, $Cd(NO_3)_2$ and $Cu(NO_3)_2$ in ultrapure water. The Pb^{2+} and Cd^{2+} ions solution ranging from 100 to 350 mg l^{-1} were prepared by serial dilution of the respective stock solutions and 25 ml of the prepared solutions were used for the batch adsorption experiments. The effect of initial Pb^{2+} and Cd^{2+} ions concentration (50–350 mg l^{-}

^{1}), pH (1–8), time (5–100 minutes), and hydrogel dose (1–8 g l^{-1}) on adsorption of Pb^{2+}, and Cd^{2+} ions onto PCCFG were studied. The competitive adsorption experiments of heavy metal ions adsorption onto PCCFG hydrogel conducted in a combined solution containing Pb^{2+}, Cd^{2+} and Cu^{2+}, after the freeze–dried hydrogel was immersed in 25 mL of combined solutions. The kinetic adsorption experiments were conducted at pH of 5, 225 mg l^{-1} initial Pb^{2+} and Cd^{2+} ion concentration, 2 g l^{-1} hydrogel dose, 25^{o}C temperature and in time range of 5–350 minutes. The isotherm experiments were conducted at pH of 5, time of 50 minute, 2 g l^{-1} hydrogel dose, and 25^{o}C temperature. After adsorption, the hydrogel was separated and the remaining Pb^{2+} and Cd^{2+} ions concentration in the solution was determined were measured by AAS.

3.8.4. Adsorption Isotherm

Adsorption equilibrium is a fundamental property in adsorption studies, which describes the phenomena prevailing in the retention of the adsorbate from aqueous solution to an adsorbent at constant pH and temperature. It describes the interaction between the adsorbate and adsorbent. Many isotherm models are often used to describe the interaction phenomena between the adsorbate and adsorbent.

i. Langmuir adsorption isotherm

The Langmuir model is based on the assumption that molecules are adsorbed on fixed sites, which have the same energy with no lateral interaction (Langmuir 1918). The linear form of Langmuir isotherm (Eq. (3.9)) was used to fit experimental data for the adsorption of heavy metal ions onto the hydrogel adsorbents. In Langmuir isotherm, favorability of adsorption is expressed by separation factor, R_L, which is expressed by Eq. (3.10).

$$\frac{1}{q_e} = \frac{1}{bq_m C_e} + \frac{1}{q_m} \tag{3.9}$$

$$R_L = \frac{1}{1+bC_o} \tag{3.10}$$

Where q_e is the amount of heavy metal ions adsorbed at equilibrium (mg g^{-1}), C_e is concentration of solution at equilibrium (mg L^{-1}), q_m is the maximum adsorption capacity of the hydrogel (mg g^{-1}), and b is the Langmuir adsorption constant (l mg^{-1}).

From the plot of $1/q_e$ versus $1/C_e$, k and q_m are determined from the slope and y-intercept, respectively. The model applicability is evaluated from a linear fit of data (R^2). R_L value varied between 0 and 1. $R_L > 1$ suggests unfavorable adsorption, $0 < R_L < 1$ suggests favorable adsorption, $R_L = 0$ suggests irreversible adsorption, and $R_L = 1$ suggests linear adsorption. The Langmuir constant referred to as b, indicates the level of interaction between the surface and the adsorbate. If the value of b is larger, it indicate a strong interaction between the adsorbent and the adsorbate. On the other hand, b having a smaller value indicates a weaker interaction between the surface and the adsorbate.

ii. Freundlich adsorption isotherm

Freundlich model is known to describe the non–ideal and reversible adsorption, which was not restricted to the formation of monolayer. It is applied to multilayer adsorption over heterogeneous surface. The linear form of Freundlich model (Eq. (3.11)) is based on the assumption that the sites of adsorption are heterogeneous.

$$\log q_e = \log k_F + \frac{1}{n}\log C_e \qquad (3.11)$$

Where k_F is the Freundlich isotherm constant (l g^{-1}) and it implies that the energy of adsorption on a homogeneous surface is independent of surface coverage. Moreover, K_F related to the adsorption capacity on heterogeneous sites level and adsorbent–adsorbate affinity. The surface heterogeneity, which ranges between 0 to 1, is characterized by a heterogeneity factor of 1/n, where n indicates linearity between adsorbate solution and adsorption processes. The value of n gives an indication of the favorability and capacity of the adsorbent/adsorbate system. For $1/n < 1$, adsorption process with chemical interaction is suggested. But if the value of 1/n (adsorption intensity) is above one, then it is an indication of the cooperative process. From the plots of $\log q_e$ versus $\log C_e$, n and k_F were determined from y-intercept and slope, respectively.

iii. Tempkin adsorption isotherm

Tempkin isotherm assumes that the heat of adsorption of all the molecules in the layer decreases linearly with coverage due to adsorbent–adsorbate interactions, and that the adsorption is characterized by a uniform distribution of the binding energies up to some maximum binding energy. Tempkin isotherm assumes that adsorbent–adsorbate interaction exist and the adsorption temperature of the molecules in the layer decreases linearly with the

surface coverage of the molecules due to adsorbate–adsorbent repulsion, i.e., heat of adsorption of all molecules in the layer decreases linearly as a result of increase surface coverage. The linear form of Tempkin isotherm is expressed by Eq. (3.12).

$$q_e = \frac{RT}{b} \ln k_T + \frac{RT}{b} \ln C_e \qquad (3.12)$$

Where k_T is the equilibrium binding constant (l mol^{-1}), b is related to adsorption heat, R is the universal gas constant (8.314K^{-1} mol^{-1}), and T is temperature (K). After linear plot q_e versus $\ln C_e$, k_T, and b obtained from y-intercept and slope, respectively. These values of RT/b>0 for adsorption processes indicate that the adsorption of adsorbate on to adsorbent is endothermic processes in nature.

iv. Dubinin-Radushkevich isotherm

Dubinin–Radushkevich (D–R) model is based on the assumption that the adsorbent size is equivalent to the micro pore size and for the given adsorbate-adsorbent; the adsorption combination could be given independently of temperature using the adsorption Polanyi potential (ε, kJ mol^{-1}). The D–R model is expressed by Eq. (3.13).

$$\ln q_e = \ln q_s - \beta\varepsilon^2 \qquad (3.13)$$

Where q_s is D–R constant (mole g^{-1}), and is the free energy of adsorption per adsorbate molecule at the moment of its transfer to the solid surface from the bulk solution. According to this model, E< 8kJ mol^{-1} indicates the adsorption is physical, and 8<E<16 kJ mol^{-1}, indicates the adsorption is due to the exchange of ions. The values of q_s and β could be determined by plotting $\ln q_e$ versus ε^2 from the y-intercept and slope, respectively.

3.8.5. Adsorption Kinetics

Adsorption phenomena such as rate of adsorption, rate–determining steps (mass transport, chemical reactions), and mechanisms of adsorption were evaluated by kinetic models, such as pseudo–first order (PFO), pseudo–second order (PSO), and Elovich. These kinetic models were employed to simulate the experimental data of heavy metal ions adsorption onto the hydrogel.

i. Pseudo–first order

Pseudo–first order (PFO) kinetic model proposed by Lagergren (Lagergren 1898) was used to follow adsorption kinetic, which proceeds by diffusion through a boundary, and the linear and non–linear form of the PFO model is given by Eq. (3.14) and Eq. (3.15):

$$\ln(q_e - q_t) = \ln q_e - k_1 t \quad (3.14)$$

$$q_t = q_e(1 - e^{-k_1 t}) \quad (3.15)$$

Where, k_1 (min^{-1}) is PFO rate constant, q_e (mg g^{-1}) and q_t (mg g^{-1}) are the amounts of heavy metal ions adsorbed at equilibrium, and t is time (minutes).

ii. Pseudo–second order

The pseudo–second order (PSO) kinetic model describes the adsorption processes achieved via chemical binding of adsorbate onto the surface of adsorbents, i.e., the rate–limiting step during adsorption is the chemical reaction expressed by linear (Eq. (3.16)) and non–linear (Eq. (3.17)):

$$\frac{t}{q_t} = \frac{1}{k_2 q_e^2} + \frac{t}{q_e} \quad (3.16)$$

$$q_t = \frac{q_e^2 k_2 t}{1 + q_e k_2 t} \quad (3.17)$$

Where q_e (mg g^{-1}) and q_t (mg g^{-1}) are the amounts of heavy metal ions adsorbed at equilibrium and at any time t, respectively, and k_2 (g mg^{-1} min^{-1}) is PSO rate constant.

iii. Intra-particle diffusion

During the adsorption processes, the adsorbate molecules might diffuse into the interior of the pores of the adsorbent. The most widely applied intraparticle diffusion equation for adsorption system is given by linear (Eq. (3.18)) and non–linear (Eq. (3.19)):

$$\log q_t = \log k_i + \frac{1}{2}\log t \quad (3.18)$$

$$q_t = k_i t^{1/2} \quad (3.19)$$

Where k_i is intraparticle diffusion rate constant (g mg^{-1} min^{-1}) and qt (mg g^{-1}) is the amount of heavy metal ions adsorbed at any time.

iv. Elovich kinetic model

The Elovich model, which is an extension of the PSO, and assumes the surface of adsorbent is energetically heterogeneous and increasing activation energy with increasing adsorption time expressed by linear (Eq. (3.20)) and non–linear equation (Eq. (3.21)).

$$q_t = \frac{1}{\alpha}\ln(\alpha\beta) + \frac{1}{\alpha}\ln t \quad (3.20)$$

$$q_t = \frac{1}{\alpha}\ln(1+\alpha\beta t) \quad (3.21)$$

Where, α (mg g^{-1} min^{-1}) is the initial adsorption rate and β (g mg^{-1}) is the desorption constant related to the extent of surface coverage and the activation energy in Chemisorption.

3.8.6. Adsorption Thermodynamics

The thermodynamic parameters, typically Gibbs free energy change (ΔGº), standard enthalpy change (ΔHº), and entropy change (ΔSº) can predict the nature and direction of adsorption. The value of the equilibrium constant (K_d, l g^{-1}) and ΔGº were calculated from Eq. (3.22) and Eq. (3.23), respectively. The equilibrium constant is expressed as the ratio of the amount of adsorbate adsorbed and that remaining in solution at equilibrium. The natural logarithm plot of K_d versus the inverse of temperature (Eq. (3.24)) was used to obtain the value of ΔHº and ΔSº.

$$K_d = \frac{q_e}{C_e} \quad (3.22)$$

$$\Delta G^o = \Delta H^o - T\Delta S^o \quad (3.23)$$

$$\ln K_d = \frac{-\Delta H^o}{RT} + \frac{\Delta S^o}{R} \quad (3.24)$$

Where, ΔG^o and ΔH^o are in kJ mol^{-1}; ΔS^o is in kJ mol^{-1}. K^{-1}, T is temperature (K), and R is universal gas constant (8.314 J K^{-1} mol^{-1}).

3.9. Theoretical Adsorption Mechanism Studies (DFT Calculation)

3.9.1. Geometry Optimization and Single–point Energy Calculation

Geometry optimizations and energy calculations were performed with the aid of Gaussian 09 (Frisch 2009) computational package with Gauss View 6.0.16 interface (Liu, Lu, and Chen 2021). The ground state geometry optimization of modeled system, frequency and NBO calculation were done using the hybrid–GGA, B3PW91–D3 level of theory, where D3 denotes the third–generation dispersion correction by Grimme. For basis set, the Stuttgart–Dresden–Boon (SDD) (T. H. Dunning Jr. and P. J. Hay 1977) basis set was employed for heavy metal ions, and the 6–31G(d) basis were used for C, N, O, S, and H atoms. Single–point energy calculations were performed using the ωB97XD functional (Chai and Head-Gordon 2008), where basis set 6-311+G (d, p) was employed for C, N, O, S, and H atoms, and SDD basis set was employed for heavy metal ions. Solvation effect (H_2O) was evaluated with polarizable continuum model (PCM). To minimize the computational cost, section I of PPSgCG (hereafter PPSgCG–I, which include unit structure of S–g–AAm, chitosan and GO) and PCCFG (hereafter PCCFG–I, which include structure of chitosan and CFG) were used as model for simulation. The PPSgCG–I (Fig. 3.10(a)) and PCCFG–I (Fig. 3.11(a)) model was built by using Gauss View 6.0.16. First, the singular model PPSgCG–I (Fig. 3.10(b)) and PCCFG–I (Fig. 3.11(b)) structure were optimized to obtain the minimum energy surface. Besides the frequency calculation for both regions were carried out to check whether it is at minima or in transition state on potential energy surface (PES). Next, adsorption of Cr^{6+} and Pb^{2+} at the surface of PPSgCG–I and PCCFG–I was investigated by performing additional optimization calculations to obtain the PPSgCG–I@Cr and PCCFG–I@Pb complex model, respectively. In this step, the stabilized model of PPSgCG–I@Cr and PCCFG–I@Pb complex was obtained and the adsorption energy (AE) was measured (Eq. 3.25). To evaluate the electronic features, frontier molecular orbital's including the highest occupied molecular orbital (HOMO) and the lowest unoccupied molecular orbital (LUMO) were calculated to measure their energy levels and energy gap (EG) distances. Moreover, chemical hardness (η), chemical softness (S), and chemical potential (μ) were evaluated from HOMO–LUMO gap for interpreting the reactivity tendency of the models, and calculated by using Eq. (3.26), Eq. (3.27), and Eq. (3.28), respectively. Band/energy gap (E_{gap}, eV) was calculated from Eq. (3.29). Perturbation theory energy analysis for the given surfaces/adsorbent and complexes/adsorbent–adsorbate was computed using Eq. (3.30) for each donor NBO(i) and acceptor NBO(j).

$$E_{adsorption} = E_{complex} - (E_{surface} + E_{metal\ ion}) \quad (3.25)$$

$$\eta = \frac{[E_{LUMO} - E_{HOMO}]}{2} \quad (3.26)$$

$$S = \frac{1}{\eta} \quad (3.27)$$

$$\mu = \frac{[E_{LUMO} + E_{HOMO}]}{2}, \quad \chi = -\mu \quad (3.28)$$

$$E_{gap} = E_{HOMO} - E_{LUMO} \quad (3.29)$$

$$E^2 = \Delta E_{i,j} = -q_i \frac{F^2(i,j)}{\varepsilon_j - \varepsilon_i} \quad (3.30)$$

Where χ is electro negativity, $E_{complex}$ is energy of complex (PPSgCG or PCCFG + heavy metal ion), $E_{surface}$ is energy of PPSgCG or PCCFG, E_{HOMO} is energy of HOMO, E_{LUMO} is energy of LUMO, E^2 is stabilization energy, q_i is the donor orbital occupancy, ε_i is energy of the Lewis NBO, ε_j is the energy of the non-Lewis NBO and F (i, j) is the off-diagonal NBO fock matrix element. The χ differs from Pauling's classical definition of electro negativity, i.e. "the power of an atom in a molecule to attract electrons to itself". It seems to be the natural way to define electron–attracting power.

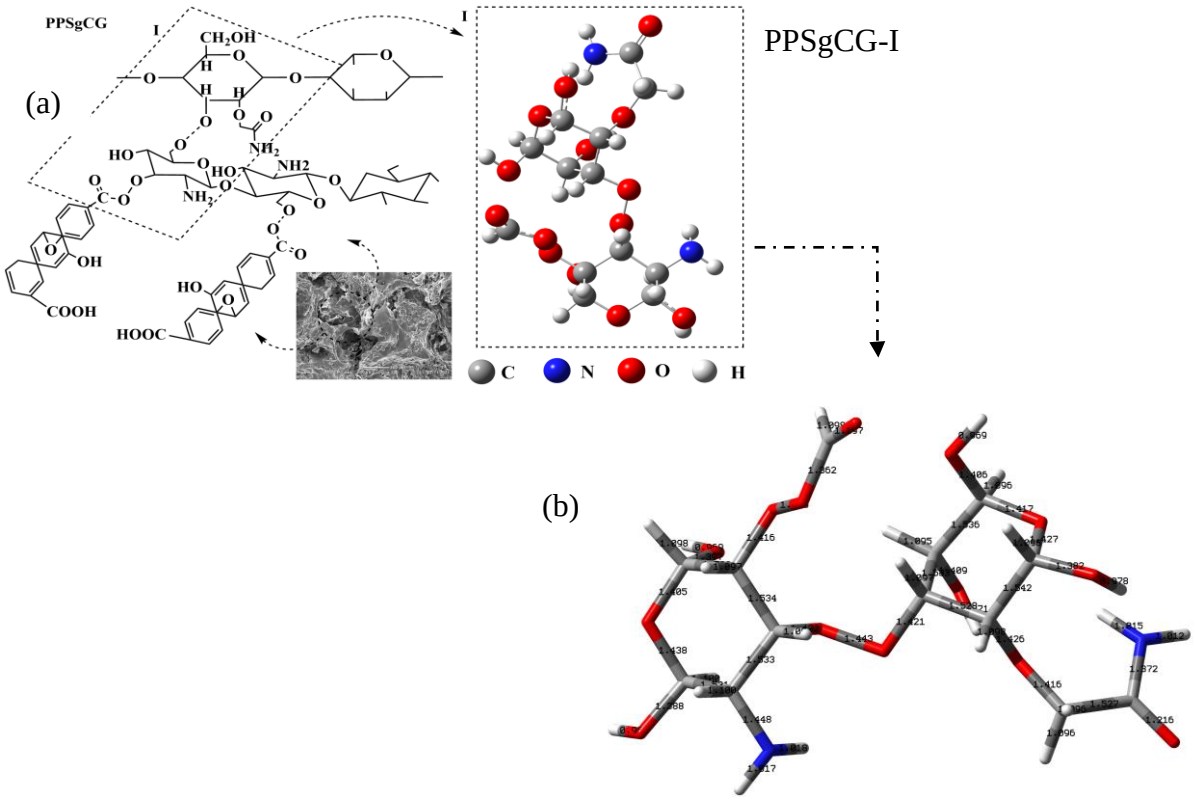

Fig.3.10 (a) PPSgCG–I Schematic representation; (b) optimized PPSgCG–I bond length (Å)

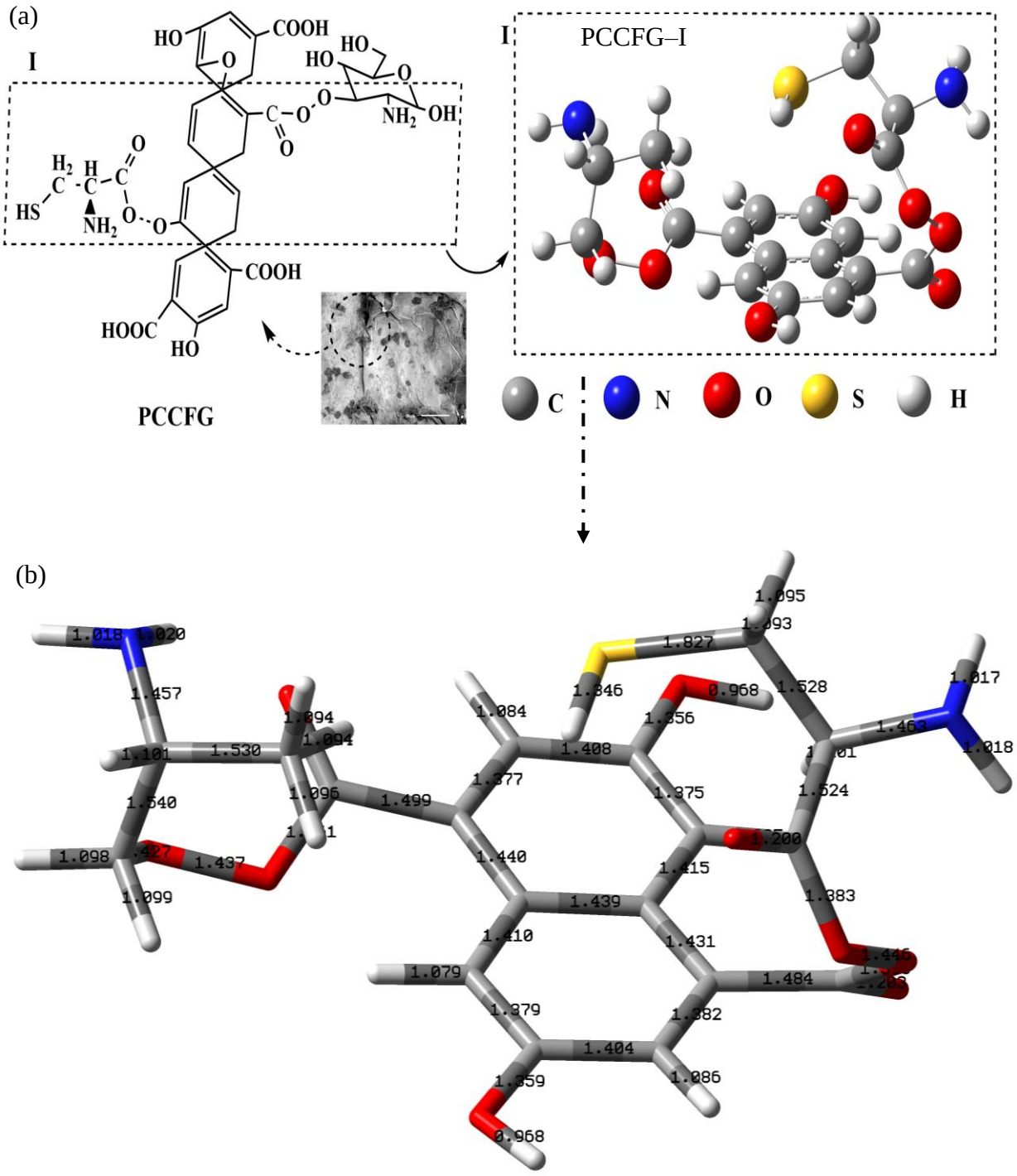

Fig.3. 11 (a) PCCFG–I Schematic representation; (b) optimized PCCFG–I bond length (Å)

CHAPTER FOUR

RESULTS and DISCUSSION

4.1. Acrylamide Grafted Starch Synthesis

In aqueous medium, the efficient redox initiator system is the potassium or ammonium per sulfate for the graft copolymerization of starch. The radical graft copolymerization reactions occur on –OH groups of starch through radical polymerization reaction route with the influence of ammonium per sulfate (APS) redox initiator. The hydroxyl radicals are produced, which abstracted hydrogen atoms from a acrylamide monomer, or from starch, so the free radical sites are produced on the polymer backbone as suggested by the below reaction scheme (Schamatic–1). Schamatic–1 illustrates the characteristic grafting of acrylamide onto starch. At first, the primary radicals are produced because of decomposition of the reaction of the heating solution of APS. The sulfate radical is formed and also many other free radical species. The produced anionic radicals fall down the hydrogen atoms of the –OH groups and initiate the macromolecular chains of the starch for the production of macro radicals, and radical reactive sites are able to initiate the acrylamide for processing of chain propagation. Finally, the reaction terminates with grafting efficiency of 26.25% (Eq. 3.2) and grafting percentage of 34.43% (Eq. 3.3) starch–g–acrylamide (S–g–AAm) produced.

$$S_2O_8^{-} \rightarrow 2SO_4^{-}$$

$$SO_4^{-} + H_2O \rightarrow HSO_4^{-} + OH^{\bullet}$$

$$HO^{\bullet} + M \rightarrow H_2O + M^{\bullet}$$

$$HO^{\bullet} + S\text{-}H \rightarrow S^{\bullet} + H_2O$$

Where M is the monomer, S–H is the starch molecule, and $S^{\bullet}$ is the starch free radical.

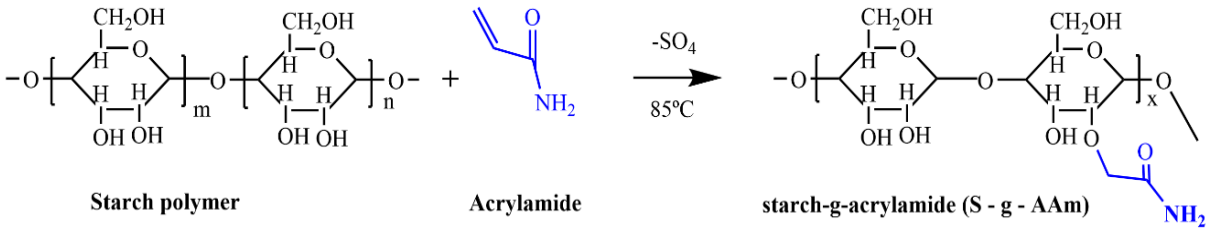

Schamatic–1

The acrylamide monomer free radical or starch free radical can react with more acrylamide producing homopolymer or with starch to produce the grafting copolymer. In this method, significant amounts of homopolymer are usually formed.

4.2. Hydrogel Swelling

As presented in Fig. 4.1, the PPSgCG hydrogel swelled quickly, attaining a swelling of 1100% (swelling degree (SD)/distilled water absorption = 12 g g^{-1}) and the saturation point of 1400% (SD/distilled water absorption = 15 g g^{-1}) in 30 and 150 min, respectively. This degree of swelling is comparable with succinic anhydride–cross-linked potato starch (SD/distilled water absorption = 18 g g^{-1}) (Pathak 2018), graft polymerization of starch–acrylamide (1500–4500% in distilled water) (Luo et al. 2021) and starch grafter with acrylic acid and 2-hydroxy ethyl methacrylate (SD/distilled water absorption = 95 g g-1 at pH of 8) (Sadeghi and Soleimani 2012). Swelling capacity of PPSg is higher than that of PPSgC due to consumption of hydrophilic functional group during cross–linking with chitosan. But the swelling capacity of PPSgG is higher than both PPSg and PPSgC hydrogel because of abundance of –OH and –COOH functional group on basal and edge of GO and high surface area of GO. The PPSgCG hydrogel swell faster than other hydrogel. The fast swelling rate and highest capacity is attributed to the super permeability of GO to water. The –OH group of pristine starch and PVA might have attracted water into the hydrogel microstructure. In spite of this, the vast porous microstructures of the hydrogel provide easy water flow channels, which resulted in fast swelling.

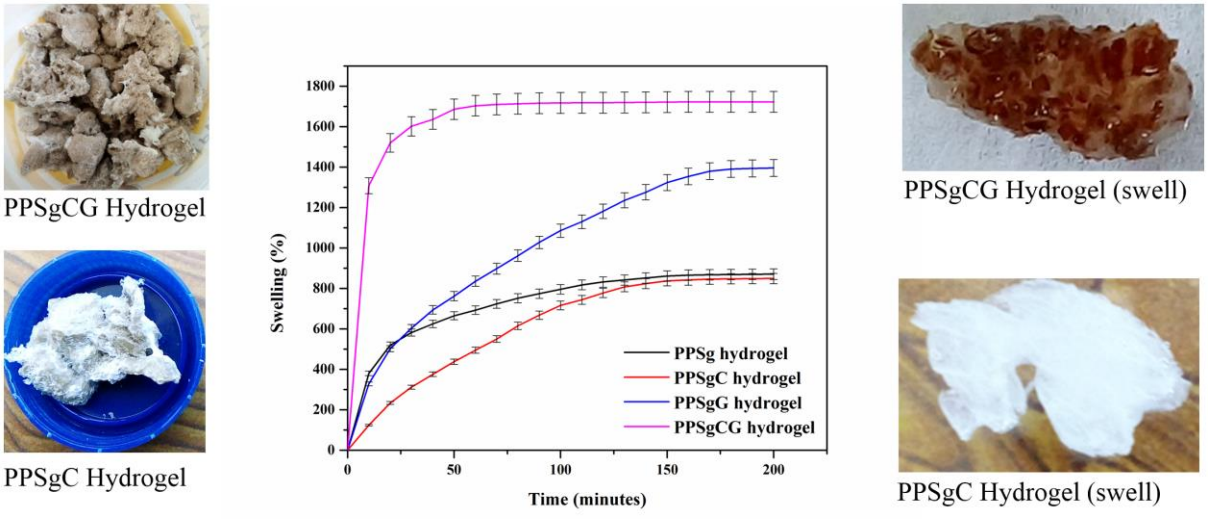

Fig.4. 1 Swelling of Hydrogel. Error bar represent the standard deviations from triplicates.

4.3. Characterization Results

4.3.1. Functional Group Analysis Using FTIR

i. Pristine starch and acrylamide grafted starch

The FTIR spectra of pristine starch (S) and grafted starch (S–g–AAm) are presented in Fig. 4.2(a). As depicted in Fig. 4.2(a), the spectra associated with S, the broadband located at 3520 cm^{-1} was attributed to the stretching of –OH (Spagnol et al. 2012). The band associated with C–H vibrations appeared at 2935 cm^{-1}. The adsorption bands at 1648, 1541, and 1459 cm^{-1} are related to C–OH bending (Leng 2009). Grafting of pristine starch with acrylamide changes the base spectrum of pristine starch, with decrease in vibrational frequencies after grafting. There are new peak formations on S–g–AAm at 2350 cm^{-1}, which are assigned to the adsorption band of C=O moiety of $–C=O–NH_2$ functional group (amide–I) (Setty, Deshmukh, and Badiger 2014; Turan, Demirci, and Caykara 2009). The adsorption bands at 3830 cm^{-1} corresponding to –OH stretching and at 3650 cm^{-1} for N–H amide stretching confirm the grafting of acrylamide on pristine starch. The adsorption bands at 1845, 1665, and 1531 cm^{-1} are attributed to C–N stretching (Zhang, Li, and Kumar 2008).

ii. Graphene oxide

In the GO spectrum (Fig. 4.2(a)), the broadband adsorption peaks observed at 3410–3880 cm^{-1}, which are attributed to –OH stretching mode, indicate the presence of hydroxyl functional group in the prepared GO. The adsorption band observed at 1625 cm^{-1} peak corresponds to the –COOH moiety of –C–COOH functional group. The peak observed at 2935 cm^{-1} indicates the C–H stretching vibration. Adsorption bands observed at 1300 and 1151 cm^{-1} peaks correspond to epoxy C–O and alkoxy C–O vibrational frequencies at the edges, respectively. Moreover, the adsorption bands observed at 1625 and 1846 cm^{-1} are related to the vibrations of C=C and C=O, respectively (Turan et al. 2009).

iii. PPSgCG and PPSgCG + Cr^{6+}

FTIR was employed to further explore the interaction among the components during formation of PPSgCG and the interaction between PPSgCG and Cr^{6+} ion. Fig. 4.2(a) depicts the FTIR spectrum of PPSgCG, and the band at 3785 cm^{-1} is attributed to the stretching vibrations of N–H and O–H. The peak observed at 3425 cm^{-1} attributed to –OH stretching modes indicates the hydrophilic properties of as–prepared PPSgCG. The peak observed at 2930 cm^{-1} indicates the C–H stretching vibration. The peak height of adsorption bands

observed at 1622, 2930, and 3425 cm^{-1} are reduced, showing the formation of composite PPSgCG. The shift and reduction in peak indicates that there is hydrogen bonding via –OH within the functional group. These peaks are also observed in GO in the region of 1620 – 3420 cm^{-1} with better peak height. This indicates successful incorporation of GO into the hydrogel. The interaction between PPSgCG and Cr^{6+} ion (PPSgCG + Cr^{6+}) during adsorption was also analyzed by FTIR. As presented in Fig. 4.2(a), the vibrational frequencies observed on PPSgCG + Cr^{6+} at 1490, 1650, and 3425 cm^{-1} are reduced with respect to that of PPSgCG, indicating the formation of a new compound. Reduction in vibrational frequencies of N–H amide stretching observed in the region of 3250–3800 cm^{-1} may be related to the interaction between Cr^{6+} ion and the –N atoms of amine and amides. The vibrational frequencies described by the adsorption bands in the region 1800–1400 cm^{-1} attributed to C–N stretching also reduced, which may be due to the interaction between –N and Cr^{6+} ion. It was found that N–H and C–N stretch and bend were responsible for the effective removal of Cr^{6+} ions as it can be elucidated from Fig. 4.2(a).

iv. Graphene oxide and L–cysteine functionalized graphene oxide

The FTIR spectra for graphene oxide (GO), and L–cysteine functionalized graphene oxides (CFG) are presented in Fig. 4.2(b). The broadband adsorption peaks observed in region IV indicate the presence of hydroxyl functional groups (-OH) (at v_{oc} =3425 cm^{-1}) in the prepared GO. The swelling or water uptake capacity of hydrogel is directly related to the availability of hydrophilic functional group in particular –OH, which is attached to the polymeric backbone. As the hydrogel takes more water, it opens up and the active adsorption sites are easily accessible to the heavy metal ions. The adsorption band observed in region II illustrate the –C=C, –C=O, and moiety of –C–COOH functional groups in GO (Turan et al. 2009) and formation of amide group (v_{oc}=1645 cm^{-1}) from the reaction between amine of L–cysteine and –COOH of GO (Daneshmand et al. 2018). The peaks related to vibrational frequencies of functional groups observed in region I correspond to epoxy C–O (v_{oc} =1105 cm^{-1}) and alkoxy C–O groups of GO. The peak observed in region IV is related to the stretching of –OH (Spagnol et al. 2012). As shown in region III, there are new peak formations on CFG, which are assigned to the adsorption band of –S–H (Pawlukojć et al. 2005), and C=O moiety of –C=O–NH_2 functional group (Setty et al. 2014). The adsorption bands observed in region IV correspond to –N–H stretching (v_{oc}=3250–3500 cm^{-1}) confirming that GO functionalization with L–cysteine, which is a similar finding to that previously reported

(Muralikrishna et al. 2014). Moreover, the peaks observed in region III are due to presence of –S–H (at v_{oc}=2500 cm^{-1}, 2640 cm^{-1}) and C–N functional groups, which indicate successful functionalization of L–cysteine on to GO.

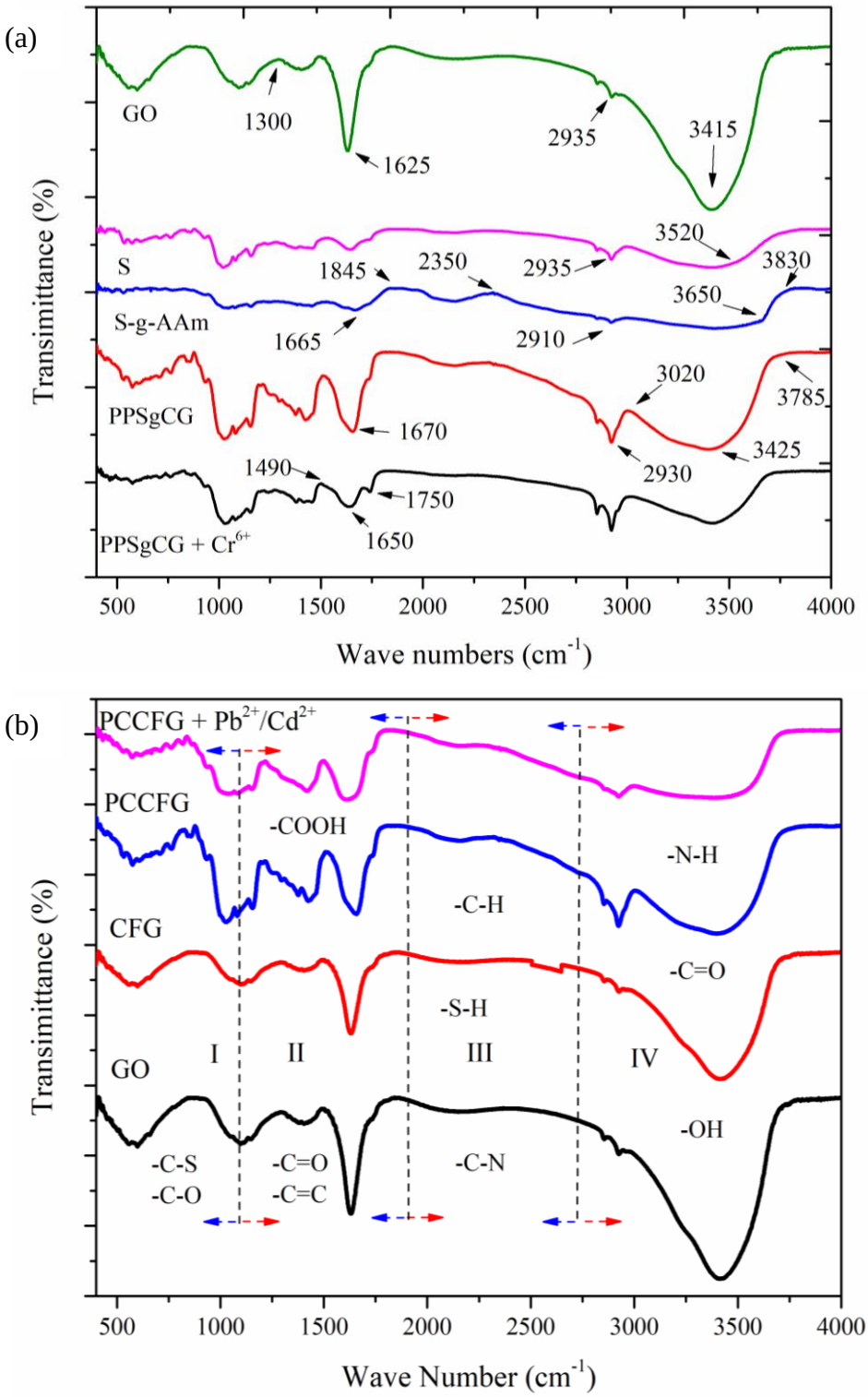

Fig.4. 2 FTIR spectrum of: a) GO, S, S–g–AAm, PPSgCG, and PPSgCG + Cr^{6+}; b) GO, CFG, PCCFG, and PCCFG loaded with Pb^{2+}/ Cd^{2+} (PCCFG + Pb^{2+}/ Cd^{2+}).

v. PCCFG and PCCFG loaded with Pb^{2+}/Cd^{2+}

The FTIR spectra for PCCFG and PCCFG after $Pb^{2+/}Cd^{2+}$ loading (PCCFG + Pb^{2+}/Cd^{2+}) are presented in Fig. 4.2(b). The peak in region IV, which were attributed to the stretching vibrations of –N–H and O–H, indicate the successful incorporation of $–CONH_2$ and $–NH_2$ into the prepared PCCFG hydrogel. The peaks observed in regions II, III, and IV were reduced after Pb^{2+}/Cd^{2+} loading, which illustrate adsorption of Pb^{2+}/Cd^{2+} onto the hydrogel. After adsorption of Pb^{2+}/Cd^{2+}, in particular, peaks of $–NH_2$ and –SH groups were reduced, illustrating the involvement of the amine and thiol groups in the adsorption process. The peaks described by the adsorption bands in regions I and II which were attributed to C–N stretching also reduced. This may be due to the interaction between the –N atom and Pb^{2+}/Cd^{2+}. The above phenomena reveal the successful syntheses of PCCFG hydrogel from CFG, chitosan, and PVA and adsorption of Pb^{2+}/Cd^{2+} on to the hydrogel.

vi. L–cysteine stabilized zero–valent iron (CZVI)

The bonding between the stabilizer L–cysteine and ZVI was confirmed by the FTIR measurements (Fig. 4.3). In the FTIR spectrum of L–cysteine stabilized ZVI, the peak observed at 2917 cm^{-1} is assigned to the anti-symmetric stretching of $–CH_2$. Compared to the FTIR absorption spectrum of pure L–cysteine (Li et al. 2017), the characteristic peak in 2250–2800 cm^{-1}, which is corresponding to the stretching vibration of S–H is completely disappeared after stabilized with ZVI. This shows a chemical bond formation between the thiol group and iron oxide on the surface of ZVI. Moreover, the adsorption peak at 2086 cm^{-1}, which is corresponds to the N–H of L–cysteine stretching also disappeared after stabilization with ZVI. The above-mentioned results shows the successful stabilization L–cysteine with ZVI.

vii. CZVI–CS–PVA hydrogel

The FTIR spectra of CS–PVA and CZVI–CS–PVA is shown in Fig. 4.3. The strong peak around 3422 cm^{-1} corresponds to the axial stretching vibration of O–H superimposed to the N–H stretching band, and inter hydrogen bonds of the chitosan. The band corresponding amide I C=O stretching mode of the chitosan chains were observed at 1625 cm^{-1}. Vibration band at 848 cm^{-1} confirms the presence of Fe–O bond, which is also confirmed in XRD pattern at peak of 28.58˚.

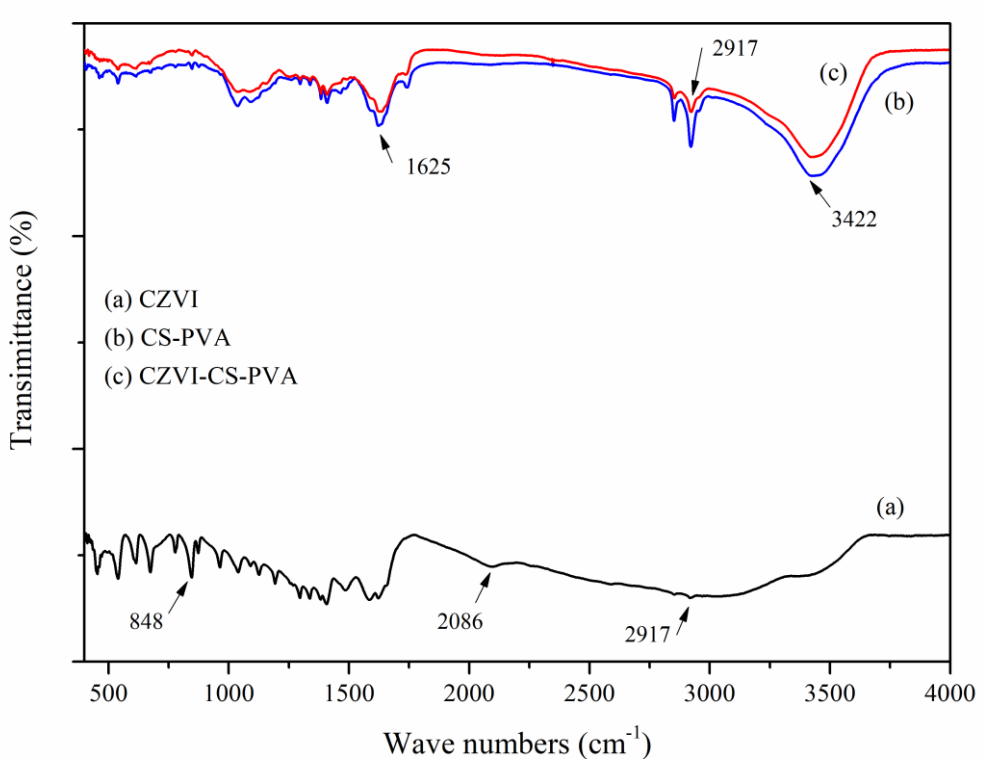

Fig.4. 3 FTIR spectra of L–cysteine stabilized ZVI and CZVI–CS–PVA hydrogel

4.3.2. Morphological Analysis Using SEM

i. PPSgCG hydrogel

The adsorption performance of an adsorbent is influenced by its morphological structure. The morphology of as–prepared PPSgCG hydrogel was observed by SEM, as presented in Fig. 4.4. Here, different SEM images of as–prepared hydrogel were presented for comparison with the PPSgCG hydrogel. As shown on Fig. 4.4(a), the clusters/agglomerates observed on the surface of PPSg are from dome shape with polygonal or irregular geometries of 'anchote' starch (Abera et al. 2019). These irregularities were not observed in the other hydrogel due to addition of CS and/or GO. As depicted in Fig. 4.4(b), instead of cluster/agglomerate, channel like sheet with a few microstructures were observed on PPSgG due to addition of GO. This may be due to successful incorporation of GO in polymer chains. As presented in Fig. 4.4(c), fiber like thin sheet is observed on the smooth surface of PPSgC due to addition of CS. The hydrogen bonding between –OH of PPSgG and –OH of CS forms interconnected and stable polymer chain. The SEM image of the PPSgCG hydrogel (Fig. 4.4(d)) shows formation of interconnected internal structure with heterogeneous macro pores and rough surfaces in the presence of CS and GO, which is not observed on PPSg, PPSgG and PPSgC surfaces. After addition of GO, the microstructure of PPSgCG (Fig. 4.4(d)) shows highly porous and

interconnected structure. This may be due to interaction among the GO and polymer chains which limits agglomeration and restacking of π–π stacking interaction between GO sheets, leading to microstructure formation. The π–π interactions (orbital overlap between the π bonds) occur when aromatic π systems bind face to face with one another and involve a combination of dispersion and dipole – induced dipole interactions leading agglomeration or stacking. This attractive stacking can occur in either a perpendicular T–shaped or a parallel displaced stacking arrangement of GO layer. Layer stacking reduces the surface area of GO and this phenomena can be reduced by dispersing GO in polymer chain or by functionalization of GO surfaces, which reduces dipole–induced dipole interaction. The highly porous microstructures can provide not only large surface area but also easy mass transfer channels, less mass transfer resistance, resulting in high swelling, fast adsorption kinetics and high adsorption capacity. The film like sheet observed especially around the outer surface of macro pores is due to the polymer chains of CS. Besides, the dome shape of 'anchote' starch granule (Abera et al. 2019) is not observed in SEM image of PPSgCG because of interconnected polymer chains of CS and incorporation of GO. The above phenomenon describes the successful formation of the hybrid hydrogel which has a well–connected 3D porous structure.

ii. PCCFG hydrogel

As presented in Fig. 4.5, the morphology of freeze–dried PCCFG hydrogel was observed by SEM. The SEM image of PCCFG shows formation of an interconnected polymer network blended with CFG. The surface of PCCFG hydrogel shows a smooth and interconnected structure. This may be due to interaction among the CFG and polymer chains which limits agglomeration and restacking of π–π stacking interaction between GO sheets which actually was also limited by addition of L–cysteine, leading to the formation of a smooth surface. The SEM image of PCCFG shows flower shaped morphologies, which is the result of cross–linking between PVA and chitosan via hydrogen bonding. A close observation of Fig. 4.5(a) reveals that pores and cavities are visible on the morphology of the hydrogel, which might be related to the action of alkaline on the polymer chain. Overall, blending of CFG in the polymer network is clearly observed in the morphology of PCCFG. The above phenomenon describes the successful formation of the hydrogel composite adsorbent.

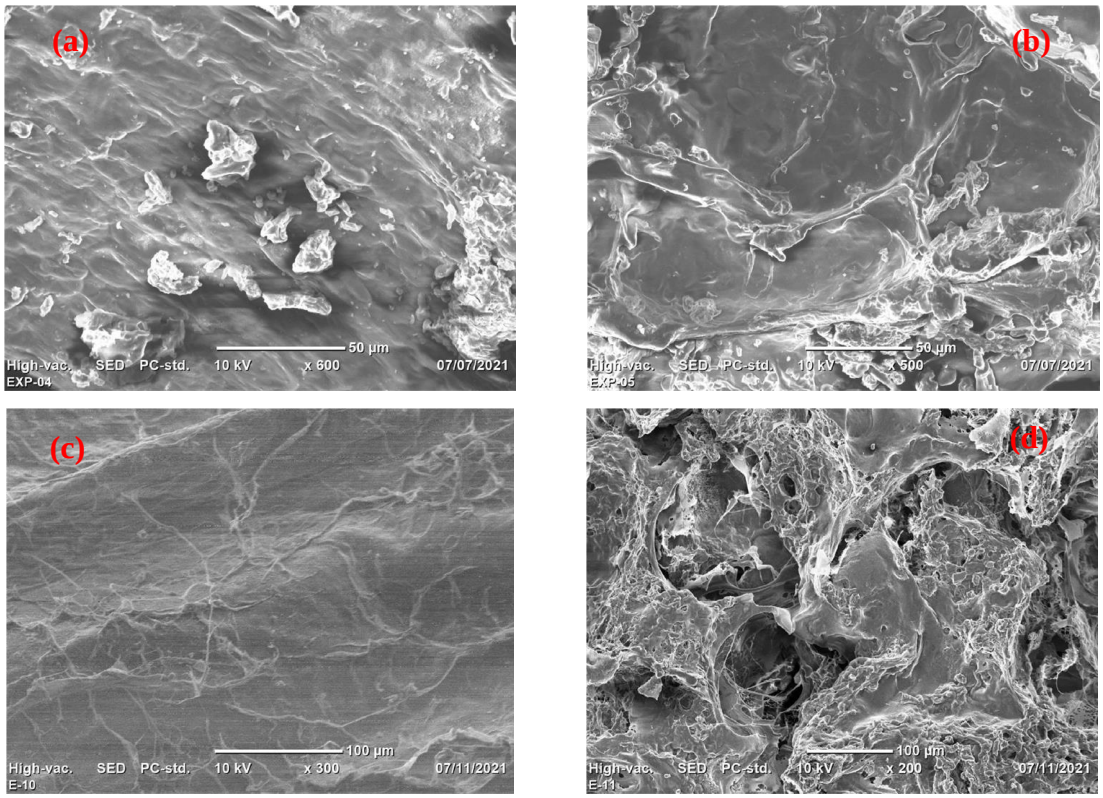

Fig.4. 4 SEM image of hydrogel: a) PPSg (*EXP–04*), b) PPSgG (*EXP–05*), c) PPSgC (*E-10*) and d) PPSgCG (*E–11*).

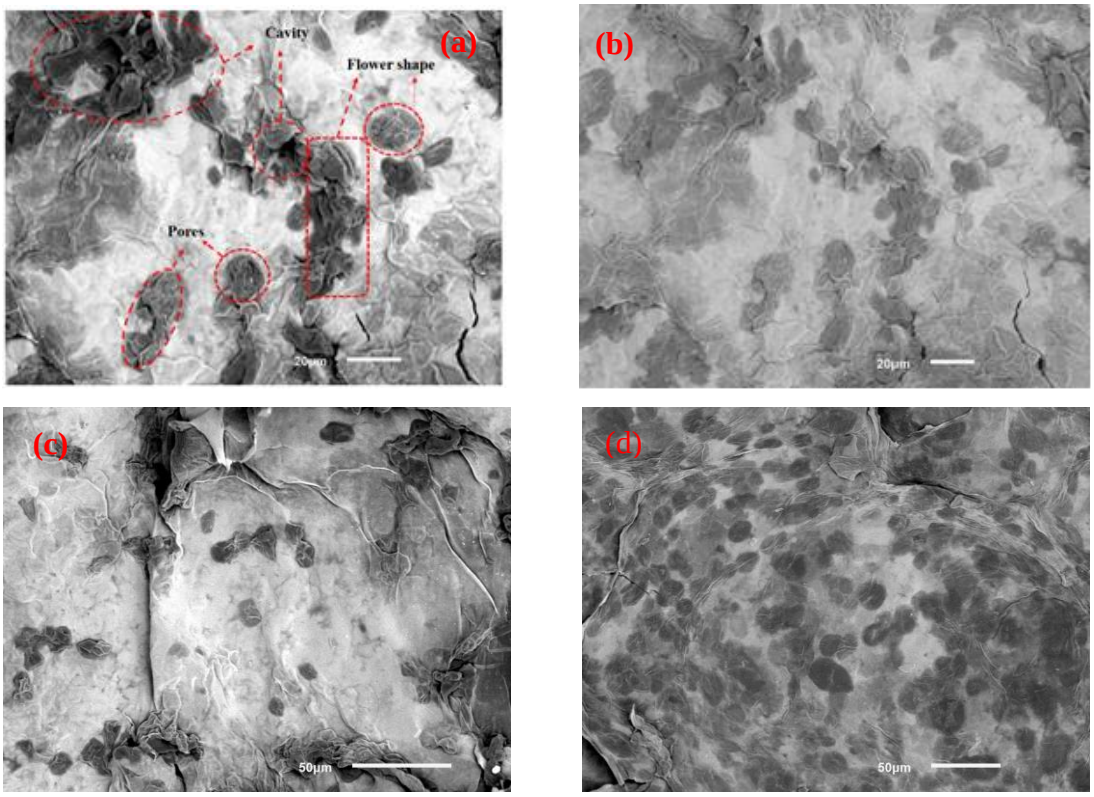

Fig. 4.5 SEM image of PCCFG hydrogel: (a) 20µm & 700x, (b) 20µm & 550x, (c) 50µm & 500x, (d) 50µm & 350x.

4.3.3. Elemental Composition Analysis Using EDX

i. PPSgCG hydrogel before and after Cr^{6+} adsorption

The X–ray spectra emitted by the material under a high–energy beam provides information on the elemental composition of the material under examination. As illustrated in Fig. 4.6, PPSgCG hydrogel contains a high composition of oxygen, carbon, nitrogen, and calcium with naturally occurring aluminum and chloride. The complexation via electrostatic attraction/chelation between the Cr^{6+} and –N atoms are clearly shown in the EDX spectra. This observation reveals the decreases –N atom in the composition and the spectra, and the increase of the Cr^{6+} peak after adsorption (Fig. 4.6). As illustrated in Fig. 4.6, the higher Cr^{6+} peak shows the higher concentration of Cr^{6+} in the hydrogel, which indicate the adsorption of Cr^{6+} on the hydrogel adsorbents. Moreover, disappearance of calcium and the significant change for aluminum after Cr^{6+} adsorption indicate displacement and exchange of ions between Ca^{2+}, Al^{3+}, and Cr^{6+}. The Cr^{6+} adsorbed onto the hydrogel via the ion exchange of Ca^{2+} and Al^{3+}, coordination, electrostatic attraction/chelation with amine functional group. From the above, it can be noted that the EDX results were consistent with the FTIR results. The result of the EDX analysis before and after Cr^{6+} adsorption shows that PPSgCG hydrogel has an ability to remove Cr^{6+} from wastewater.

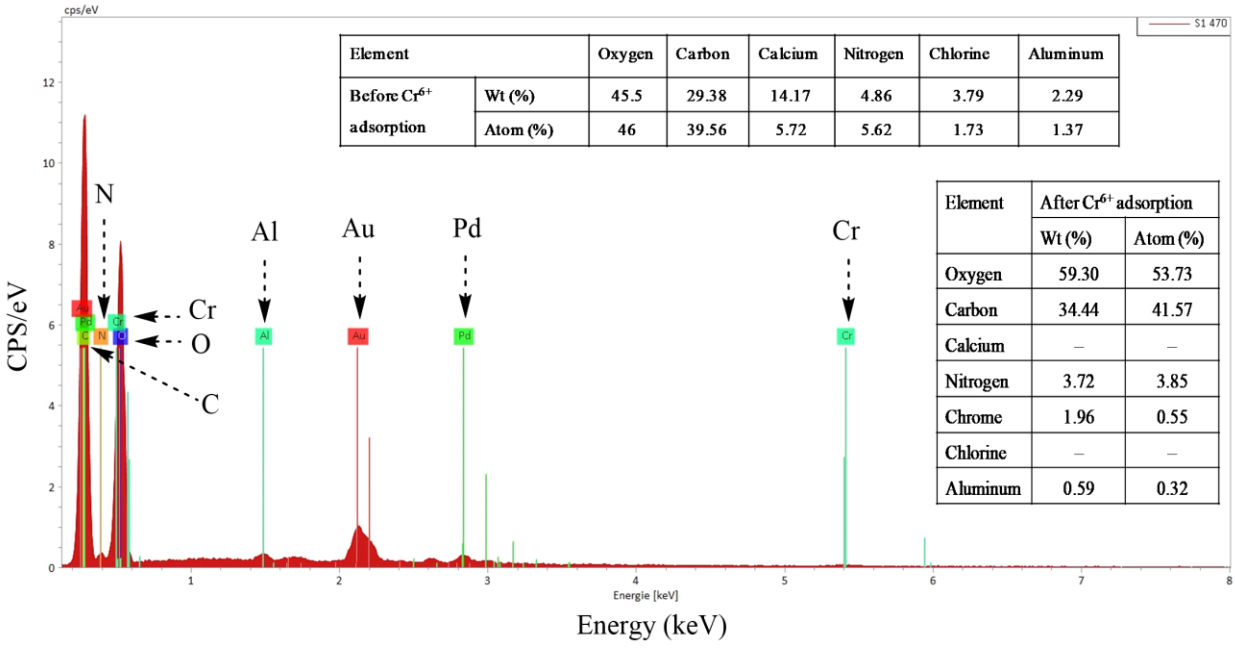

Element		Oxygen	Carbon	Calcium	Nitrogen	Chlorine	Aluminum
Before Cr^{6+} adsorption	Wt (%)	45.5	29.38	14.17	4.86	3.79	2.29
	Atom (%)	46	39.56	5.72	5.62	1.73	1.37

Element	After Cr^{6+} adsorption	
	Wt (%)	Atom (%)
Oxygen	59.30	53.73
Carbon	34.44	41.57
Calcium	–	–
Nitrogen	3.72	3.85
Chrome	1.96	0.55
Chlorine	–	–
Aluminum	0.59	0.32

Fig.4.6 EDX spectra of PPSgCG hydrogel after Cr^{6+} adsorption.

ii. PCCFG hydrogel before and after Pb^{2+} adsorption

In this study, only single Pb^{2+} adsorption on to PCCFG was studied by the EDX to illustrate the adsorption mechanism. As shown in Fig. 4.7(a), PCCFG hydrogel contains a high composition of oxygen, carbon, nitrogen, sulfur, and calcium with naturally occurring aluminum and chloride. The complexation via electrostatic attraction/chelation between the Pb^{2+} and –N and –S atoms is clearly shown in the EDX spectra. This observation reveals the disappearance of –N and –S atom in the composition and the spectra, and the increase of the Pb^{2+} peak after adsorption (Fig. 4.7(b)). As illustrated in Fig. 4.7(b), the higher Pb^{2+} peak shows the higher concentration of Pb^{2+} in the hydrogel, which indicate the adsorption of Pb^{2+} on the hydrogel adsorbents. Moreover, there were significant changes in the composition of oxygen and carbon of PCCFG after Pb^{2+} adsorption, indicating that hydroxyl and carboxylic functional groups of the hydrogel are also responsible for the adsorption of Pb^{2+} (Afolabi, Musonge, and Bakare 2021).

The –N, –S, and –O atoms are responsible for adsorption of Pb^{2+} (Alboghbeish, Larki, and Saghanezhad 2022), and the Pb^{2+} might be coordinated or electrostatically attracted to $–NH_2$, –SH, –COOH and –OH functional groups. Furthermore, disappearance of calcium and the significant change in the amount of aluminum after Pb^{2+} adsorption indicate displacement and exchange of ions between Ca^{2+}, Al^{3+}, and Pb^{2+} (Fig. 4.7(b)). The Pb^{2+} adsorbed onto the hydrogel via the ion exchange of Ca^{2+} and Al^{3+}, coordination, electrostatic attraction/chelation with amine and thiol functional group, and surface precipitation is likely due to the –OH functional group present in the PCCFG hydrogel. Similar results were reported previously (Liang et al. 2020; Yuvaraja et al. 2019). From the above, it can be noted that the EDX results were consistent with the FTIR results. The result of the EDX analysis before and after Pb^{2+} adsorption shows that PCCFG hydrogel has an ability to remove Pb^{2+} and other divalent oxidation state heavy metals from aqueous solutions.

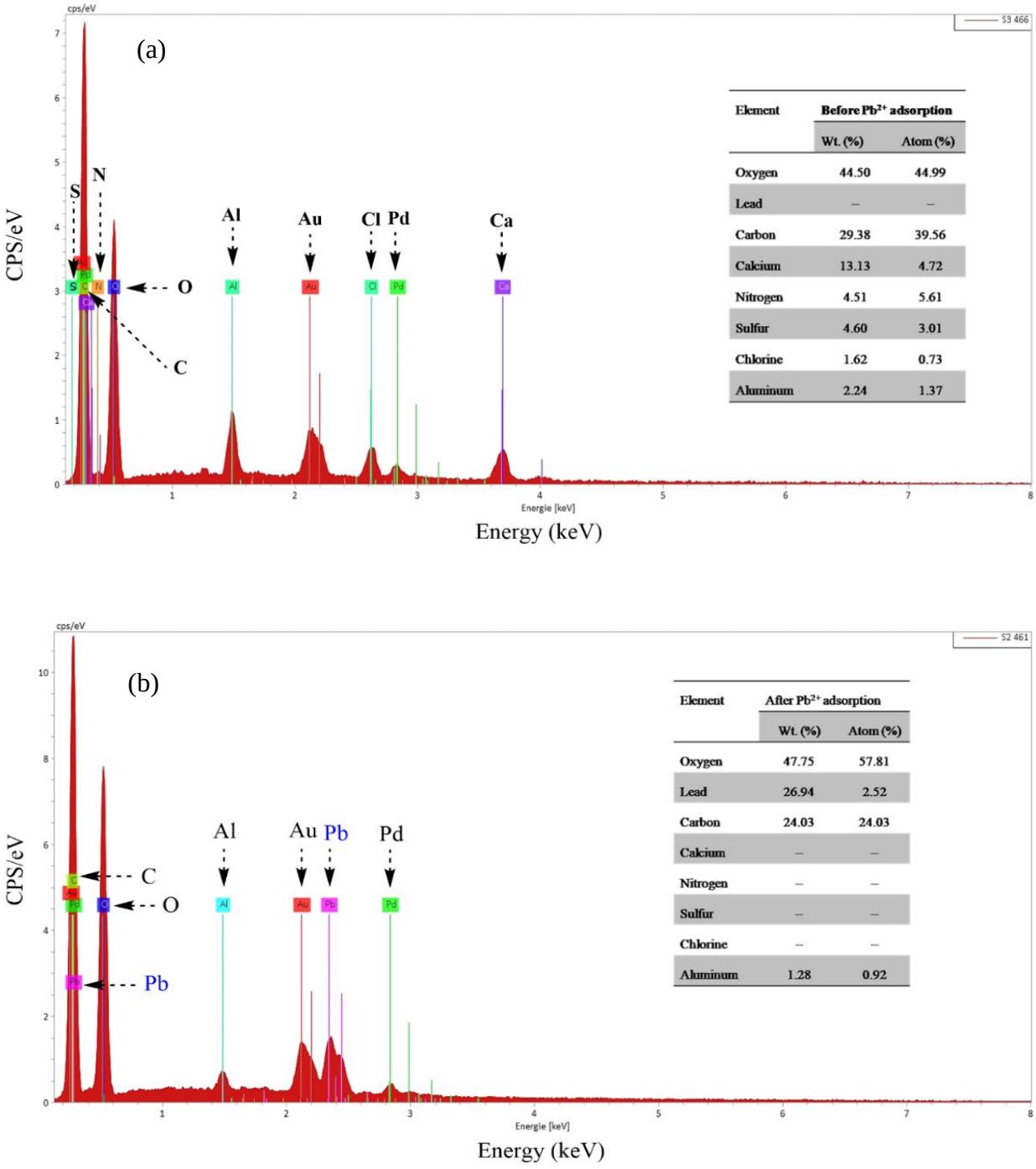

Fig.4. 7 EDX spectra of PCCFG hydrogel: (a) before Pb^{2+} adsorption, (b) after Pb^{2+} adsorption.

4.3.4. Thermal Stability Analysis

i. PPSgC and PPSgCG hydrogel

The thermal stability and decomposition behavior of a composite may depend on the thermal properties of the individual components and their interactions (La Mantia and Valenza 1994). The thermogravimetric analysis (TGA) and differential thermal analysis (DTA) curves of PPSgC and PPSgCG are shown in Fig. 4.8. An endothermic peak observed at 95°C in DTA curves shows the elimination of water molecules. The onsets of weight loss of the PPSgCG and PPSgC are observed at 255 and 235°C, respectively. The PPSgC begins to lose weight earlier than PPSgCG. The PVP exhibited only one mass loss region, which started at 400°C, and its maximum rate of decomposition was observed at 480°C. It is reported that the vinyl pyrrolidone monomer is the main volatile gas involved during the thermal decomposition (Loría-Bastarrachea et al. 2011). A blend of PVA and PVP undergoes three stages of mass loss in the temperature range of 200–500°C (Rao et al. 1999). Addition of PVP to PVA increases initial thermal decomposition. As can be observed in Fig. 4.8, PPSgCG and PPSgC hydrogel exhibited five step degradation. The first stage of degradation (up to 95°C) is attributed to evaporation of water. The second stage (up to 235°C) is due to water elimination from PVA and PVP, decomposition of grafted starch, and cracking of PVA (Taghizadeh and Sabouri 2013), which related to decomposition of unstable oxygen containing functional groups.

The third stage of degradation was predominantly the characteristic of degradation of polymer structure and decomposition of functional groups and the oxidation of GO related to CO, CO_2 (Zhu, Hu, and Wang 2014). The mass loss in the fourth and fifth stages was attributed to the combustion of the graphite region (Aksu and Tunç 2005). Further heating cracks the polymer backbone.

The major mass loss was observed in the third (235–333°C) and fourth stages (333–640°C) and was followed by smaller mass loss in the fifth stage before complete degradation. In the fifth stage, the PPSgC hydrogel was destroyed at lower temperature (about 575°C) than the PPSgCG (about 650°C). As illustrated in Fig. 4.8, the weight loss of PPSgC is observed at lower temperatures than that of PPSgCG, indicating that the latter is thermally more stable. Addition of GO to the hydrogel increases both initial and final decomposition temperature. This indicates that the addition of GO has enhanced the thermal stability of the hydrogel.

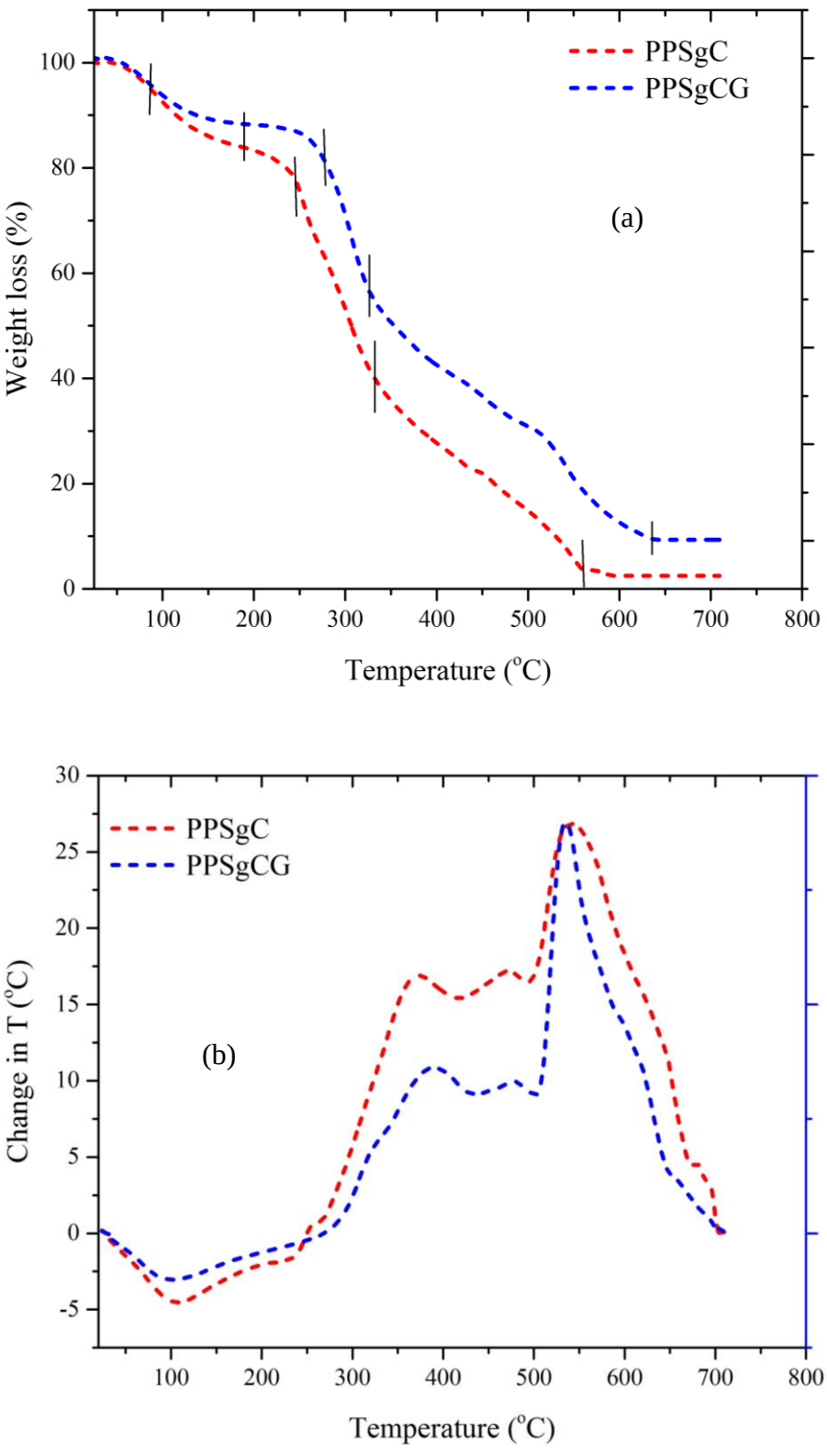

Fig.4. 8 **a**) TGA, **b**) DTA Curves of freeze–dried PPSgC and PPSgCG Hydrogel

4.3.5. XRD Pattern of Synthesized L-cysteine-nZVI

As shown in Fig. 4.9, the dominant peak appear at 28.58˚ corresponds to the plane (111) and interplanar spacing (d = 3.118 Å), confirming the formation of iron in its zero–valent state (Y Bagbi et al. 2017). The minor peak appeared at 59.09˚ corresponds to the (222) plane and interplanar spacing (d = 1.562 Å) of iron oxides existed as a thin shell packing on the surface of ZVI. As illustrated in the figure, no extra peaks were observed in the diffraction pattern confirming there is no impurities present in the sample.

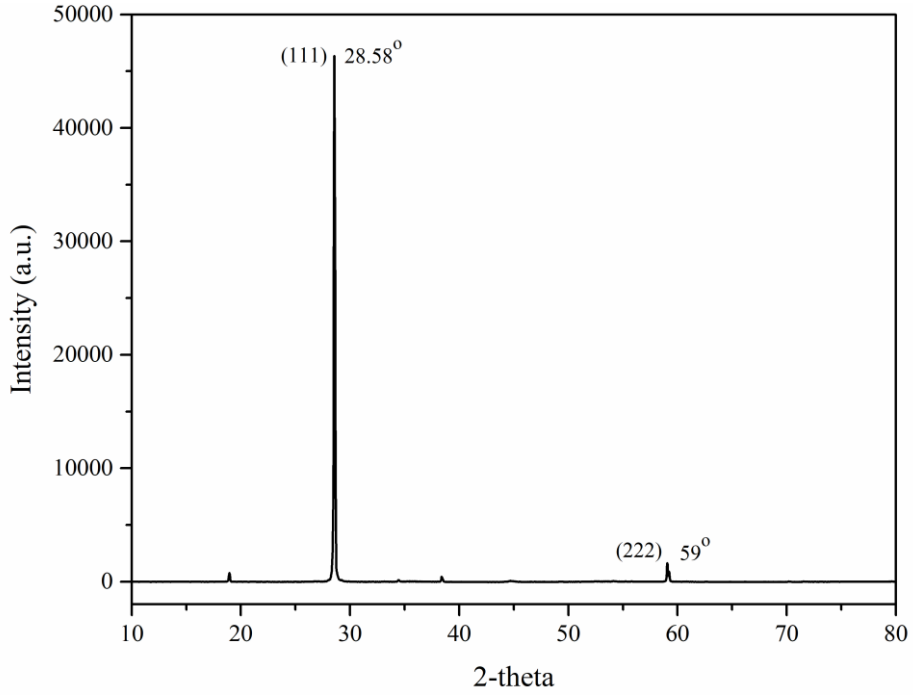

Fig.4. 9 XRD pattern of synthesized L–cysteine–ZVI.

4.4. Removal of Cr^{6+} Ion by PPSgCG Hydrogel

4.4.1. Effect of Adsorption Parameters

i. Zeta Potential and Effect of pH

As shown in Fig. 4.10(a), the zero charge point (pH_{zcp}) of PPSgCG hydrogel was at pH 3.5. The nitrogen atoms of amine and amide functional group of PPSgCG were protonated in the presence of H^+ at lower pH (lower than pH_{zcp}), which make the surface of PPSgCG positively charged. This allowed the surface to interact with $HCrO_4^-$ by electrostatic attraction, thereby improving the ion exchange performance of the hydrogel.

pH is an important factor that affects the swelling capacity of hydrogel and the degree of association–disassociation of heavy metal ions on the adsorbent surfaces. It is a key parameter for the evaluation of adsorption capacity of materials. The effect of the initial pH of Cr^{6+} ion solution was studied in the pH range of 2–6. The pH of the solution was adjusted by using 0.1 M of HCl and NaOH solution as needed. Fig. 4.10(b) shows the effect of pH on the adsorption capacity of the as–prepared PPSgCG. The availability of protonation of amine group at low pH results in complexation with chrome species ($HCrO^{2-}_4$). At low pH, Cr^{6+} ion is present as dichromate anion. Furthermore, the amine groups contained in hydrogel are easily protonated. Thus, the dichromate anion interacts with adsorbent through ion–pair formation. However, at higher pH (higher than pH_{zcp}) there are competitions between –OH and CrO_4^{2-} ion for adsorption on the hydrogel surface, which decrease chrome ions uptake. In addition, as pH increases from 2 to 6, the amine group deprotonates, resulting in electro–static repulsion of $HcrO_4^-$ ions, further contributing to the decrease in the adsorption capacity of the hydrogel. Maximum adsorption was obtained at pH of 2, similar to the result reported in the literature (Kalidhasan et al. 2013).

ii. Effect of adsorption time

The effect of contact time on the adsorption capacity of the PPSgCG was studied at 30, 60, 90, 120, 150, 180, 210, and 240 min, keeping the other variables constant. Cr^{6+} ion adsorption capacity (mg g^{-1}) and removal efficiency (RE %) were measured as a function of time (Fig. 4.11). The adsorption capacity on Cr^{6+} ion sharply increased in the first 120 min and declined afterward. The fast adsorption in the first 120 min may be attributed to the polymer channels and porous microstructure of the as–prepared PPSgCG hydrogel, which affect diffusion of ions into the pore structure.

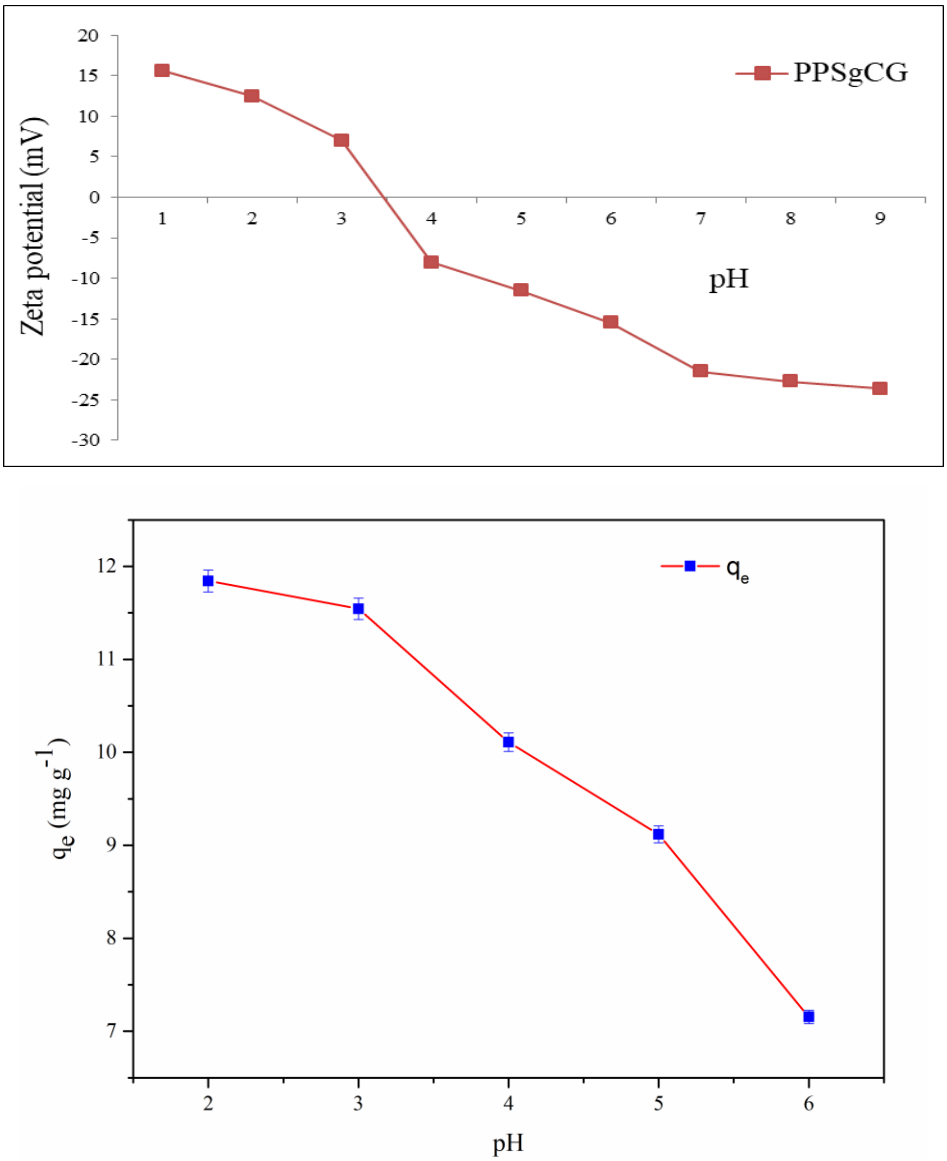

Fig.4. 10 (a) Zeta potential of PPSgCG hydrogel; b) adsorption performance of PPSgCG at different pH (t = 24 h). Adsorption conditions were, C_o = 60 mg l^{-1}, hydrogel dose = 1 g l^{-1}, agitation speed = 120 rpm, T = 25^{o}C). Error bars represent the standard deviation from triplicates.

The decline in adsorption after 120 min may be due to the oxidation–reduction process that occurs at the adsorbent surface (Liu et al. 2018). The electrostatic bonding of Cr^{6+} ion to protonated sites at lower pH and existence of electron–rich hetero atoms (O, N) may oxidize the adsorption sites while the Cr^{6+} gets reduced to Cr^{3+} after adsorption, thus reducing the available adsorption sites for Cr^{6+} ion. Therefore, the equilibrium time of 120 min was chosen as optimum contact time for adsorption Cr^{6+} ion on the PPSgCG hydrogel. The fastest time of

adsorption shows the excellent affinity of as–prepared PPSgCG hydrogel toward Cr^{6+} ion in spite of the complex polymeric network and high degree of cross–linking. Different adsorption experiments have shown a wide range of adsorption equilibrium time. The adsorption equilibrium of trimesic acid–cross–linked CS was 14.5 h for Cr^{6+} ion (Bhatt et al. 2017) and the equilibrium time of MS@APTES@PNIPAm was 6 h for Cr^{6+} ion (Chang, Kim, and Lee 2017).

iii. Effect of Cr^{6+} initial concentration

The effect of Cr^{6+} ion initial concentration on adsorption capacity of the as-prepared PPSgCG hydrogel was evaluated at different initial Cr^{6+} ion concentrations (20 – 100 mg l^{-1}). As shown in Fig. 4.12(a), the adsorption of Cr^{6+} gradually increased with increasing initial concentration. As Cr^{6+} ion concentration increases, the chance of collusion between Cr^{6+} molecule and hydrogel surface increases that tends to increase mass transfer rate from solution to hydrogel surface. The equilibrium adsorption capacity was increased and removal efficiency was decreased with increasing concentration. Considering both the adsorption ability (q_e) and removal efficiency, we chose initial Cr^{6+} ion concentration of 100 mg l^{-1} for the kinetic, isotherm and thermodynamics studies.

iv. Effect of PPSgCG hydrogel dose

The effect of adsorbent dose on the Cr^{6+} ion removal capacity is presented in Fig. 4.12(b). The figure shows that the amount of Cr^{6+} ion removed decreased and the removal efficiency increased with the increase in hydrogel dose. At lower hydrogel dose, the adsorptive sites were easily and quickly saturated, resulting in higher adsorption capacity and lower removal efficiency. The sorption efficiency is fast in the first dose of hydrogel (2–4 g l^{-1}) due to the availability of effective adsorption sites for Cr^{6+} ions, which resulted in sufficient electrostatic attractions between amine–amide of hydrogel and $HCrO_4^-$ ions. Considering both the adsorption ability (q_e) and removal efficiency, we chose hydrogel dose of 3 g l^{-1} for the kinetic, isotherm and thermodynamics studies.

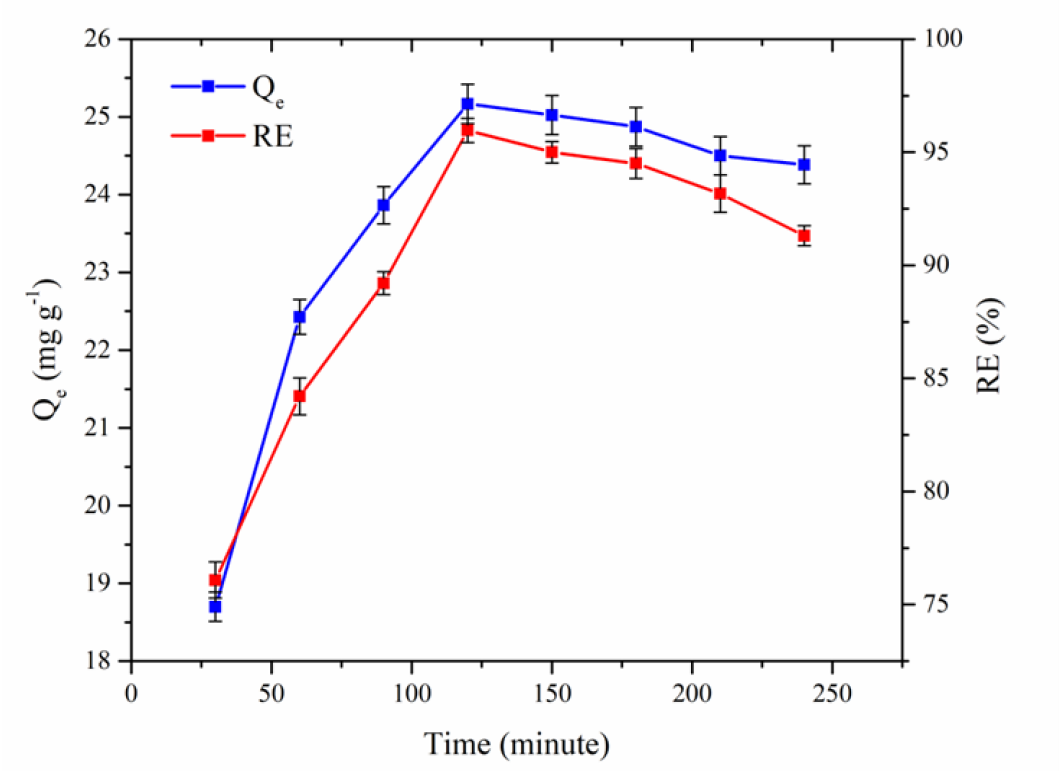

Fig. 4.11 Adsorption capacity of PPSgCG at different times (pH = 2). Adsorption conditions were, C_o = 60 mg l^{-1}, hydrogel dose = 1 g l^{-1}, agitation speed = 120 rpm, T = 25°C). Error bars represent the standard deviation from triplicates.

v. Effect of competing ions

Studying the competitive adsorption of different adsorbate is important in order to know the adsorption performance of the adsorbent in real water samples. Chromate adsorption is affected by the presence of coexisting anions such as phosphate, sulfate, chloride, nitrate, and carbonate in the solution (Tahmasebi 2020). Identical chemical properties and geometrical configuration enhance the competitive adsorption between sulfates and chromate under acidic condition (Lin et al. 2021; Meena and Arai 2016). The effect of common competing ions such as sulfate (SO_3^{2-}), phosphate (PO_4^{3-}), nitrate (NO_3^-), and chloride (Cl^-) on adsorption efficiency and selectivity of Cr^{6+} ion on the hydrogel (PPSgCG) was investigated. The results show that the effect of chlorine ion was not significant compared to that of the control (Fig. 4.13). The effects of phosphate and nitrate ions were somewhat significant compared to the control. As illustrated in Fig. 4.13, sulfate ion has a significant effect on the Cr^{6+} ion adsorption, which might be related to identical chemical properties and geometrical configuration.

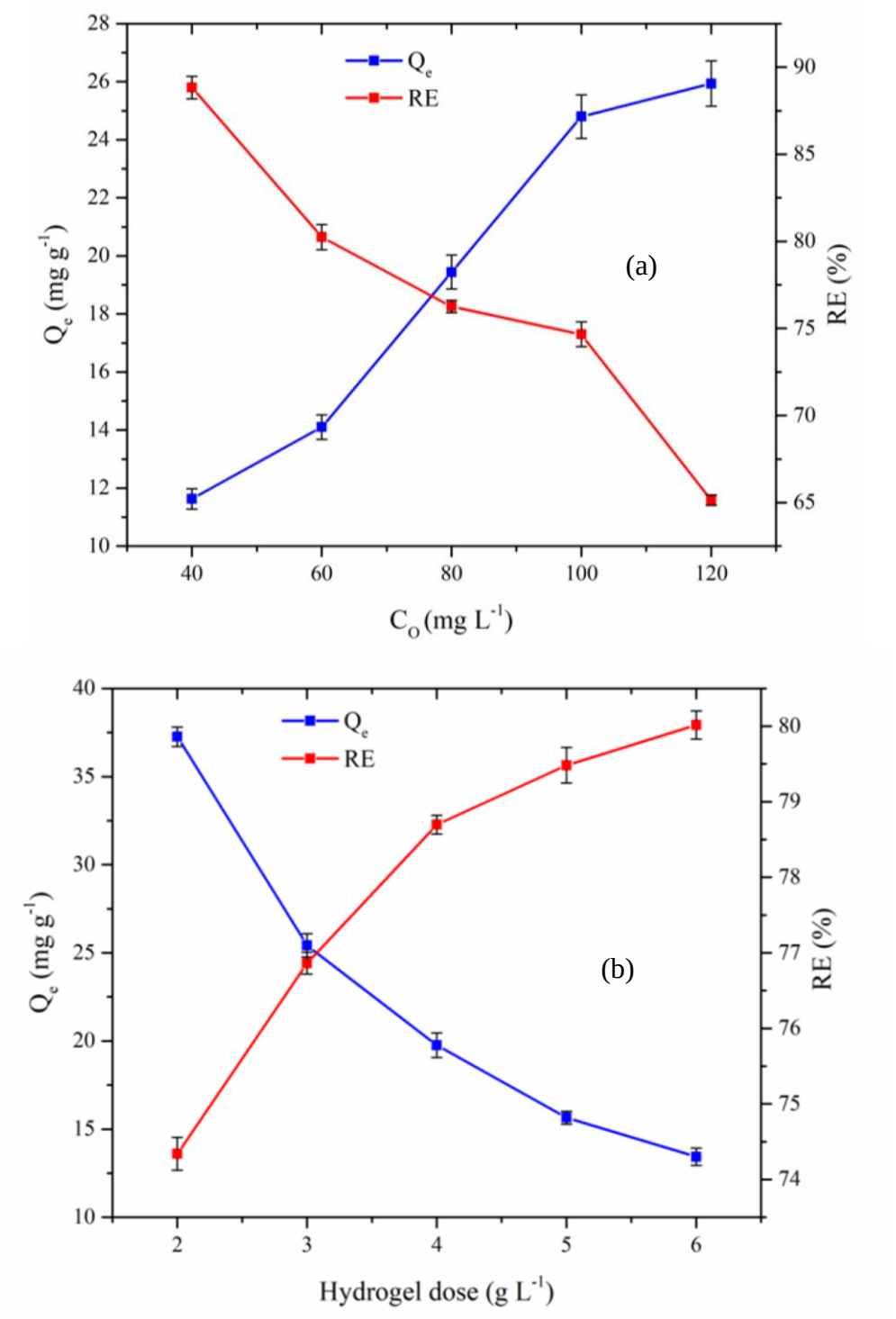

Fig.4.12 Adsorption capacity of PPSgCG: a) at different Cr^{6+} ion initial concentration (hydrogel dose = 1g l^{-1}); b) at different hydrogel doses (C_o = 60 mg l^{-1}). Adsorption conditions were pH = 2, t = 120 min, agitation speed = 120 rpm, T = 25^{o}C). Error bars represent the standard deviation from triplicates.

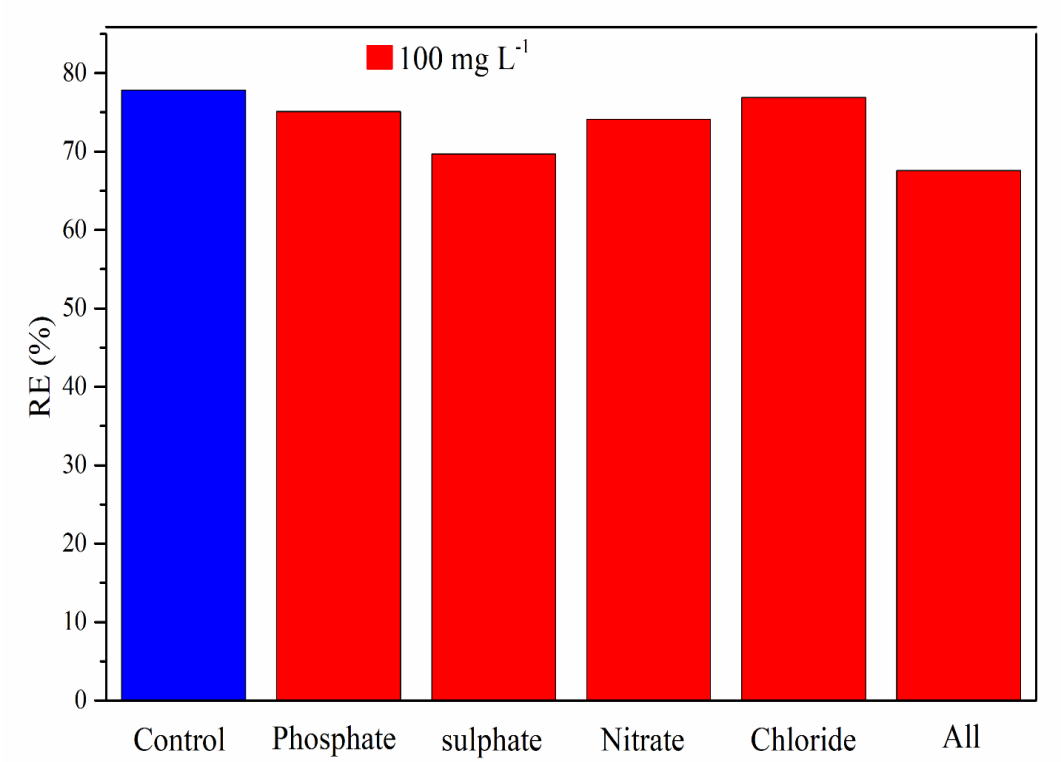

Fig.4.13 Effect of computing ions (t =120 min) for adsorption of Cr^{6+} on PPSgCG. Adsorption conditions were at pH = 2, C_o = 100 mg l^{-1}, hydrogel dose = 3 g l^{-1}, agitation speed =120 rpm, T =25^oC).

4.4.2. Adsorption Kinetic Models of Cr^{6+} Adsorption onto PPSgCG Hydrogel

To predict the adsorption mechanism of the adsorption process, adsorption kinetics models were used to interpret the experimental data. The Cr^{6+} ion removal through synthesized PPSgCG hydrogel was evaluated in terms of the Cr^{6+} ion removal kinetics by measuring removal at different time.

i. Pseudo–first order

Pseudo–first order (PFO) kinetic model is applicable at initial stage of adsorption and if a few active sites exist in the adsorbent (Wang and Guo 2020). It assumes that the adsorption process occurs through a first–order reaction mechanism, where the rate of adsorption is directly proportional to the number of unoccupied sites on the adsorbent surface. As shown in Table 4.1 and Fig. 4.14, the experimental data for adsorption of Cr^{6+} onto PPSgCG is not correlated well by pseudo–first order (R^2 = 0.71). The adsorption of Cr^{6+} onto PPSgCG is not follow the assumption behind the pseudo–first order kinetic model.

Table 4.1 Summary of kinetic model parameters and coefficient of correlation

Pseudo–first order			Pseudo–second order			Intraparticle diffusion	
q_e (mg g^{-1})	k_1	R^2	q_e (mg g^{-1})	k_2	R^2	k_i	R^2
4.68	0.01	0.71	26.62	0.004	0.999	15.65	0.77

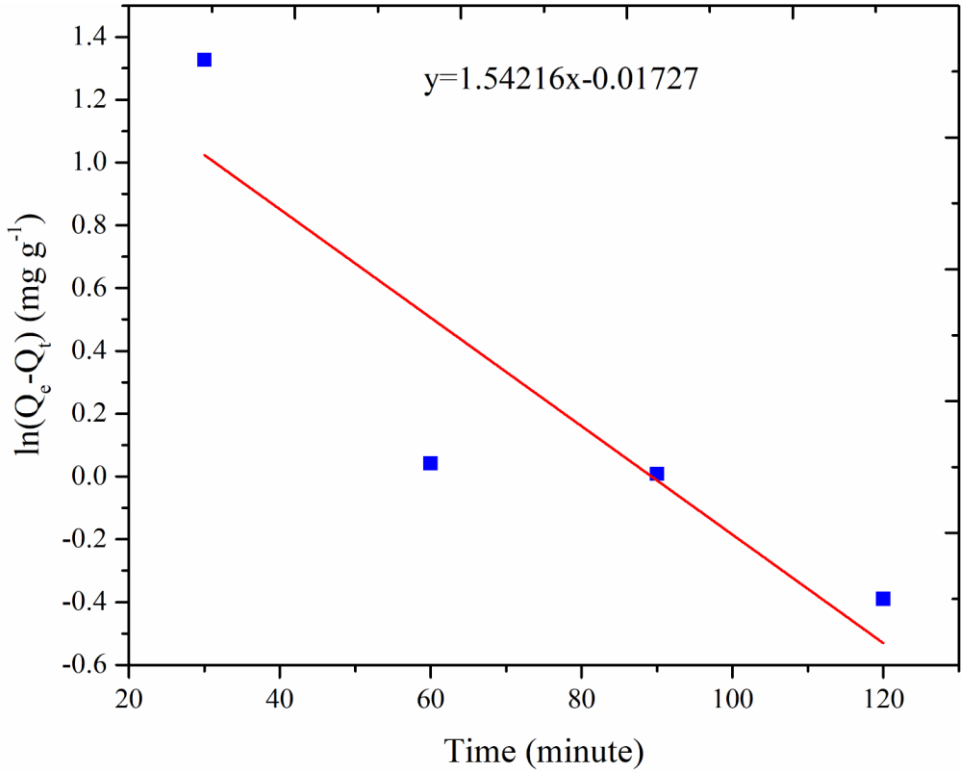

Fig.4.14 PFO model for adsorption of Cr^{6+} on PPSgCG. Adsorption conditions were at pH = 2, C_o = 100 mg l^{-1}, hydrogel dose = 3 g l^{-1}, agitation speed =120 rpm, T =25 ^oC).

ii. Pseudo–second order

Pseudo–second order (PSO) is used to describe adsorption processes that are governed by surface Chemisorption. The PSO model is widely adopted to describe adsorption processes at final stage of adsorption and for adsorbents with abundant active sites, and for adsorption kinetics dominated by the adsorption on to active sites (Wang and Guo 2020). The R^2 is one of the most important parameters that determine which experimental data best fit the model. It is clear from the result (Table 4.1) that the value of R^2 obtained for PSO (R^2 = 0.999) is higher than those obtained for PFO (R^2 = 0.71) and intraparticle diffusion (R^2 = 0.77). Besides, the calculated q_e was close to the experimental value (25.54 mg g^{-1}). Hence, PSO (Fig. 4.15) provides an excellent agreement for the adsorption of Cr^{6+} ion onto the PPSgCG

hydrogel adsorbents, showing that it fits the assumption behind this model. This model assumes that the rate–limiting step might be Chemisorption involving exchange of electrons between the active sites and the Cr^{6+} ions. The adsorption process is controlled by the adsorption on active sites. The Cr^{6+} ions may be adsorbed due to electrostatic interaction (cation adsorption by acid site) with the functional group. The $HCrO_4^-$ electrostatically bonded to two –N atoms in amine of CS and one –N atom in amide of grafted pristine starch and might be followed by reduction to Cr^{3+} (Liu et al. 2018).

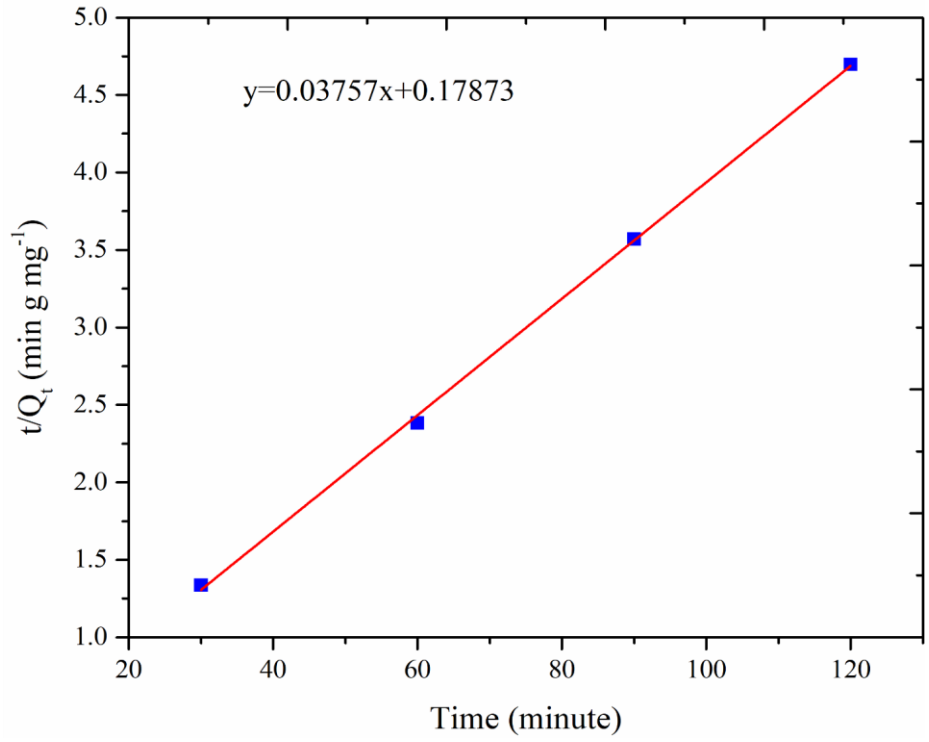

Fig.4.15 PSO kinetic model for adsorption of Cr^{6+} ion on PPSgCG. Adsorption conditions were at pH = 2, t = 120 min, C_o = 100 mg l^{-1}, hydrogel dose = 3 g l^{-1}, agitation speed = 120 rpm, T = 25^oC).

iii. Intra–particle diffusion

In pore diffusion model, diffusion is assumed to take place in the liquid–filled pore. The driving force for intraparticle mass transfer is solute concentration gradient in the pore phase of the particle. For reactions that are pore diffusion controlled, it is recommended to locate the active adsorption site close to the fluid–solid interface in order to decrease the diffusion path of reactants and products. As shown in Table 4.1, the experimental data is well correlated with pseudo–second order kinetic model, which shows pore diffusion is not rate limiting step rather chemisorption controlled the adsorption processes. As we can see from

Table 4.1, the intra–particle diffusion (R^2 = 0.77), internal surface and pore diffusion is not a rate–limiting step. Besides, it is observed that (Fig. 4.16) the plot did not pass through the origin, indicating that intraparticle diffusion was not the rate–limiting step. The formation of microspore structure (Section 4.3.2) might be makes easy for the diffusion of the Cr^{6+} ions to the active sites of the hydrogel.

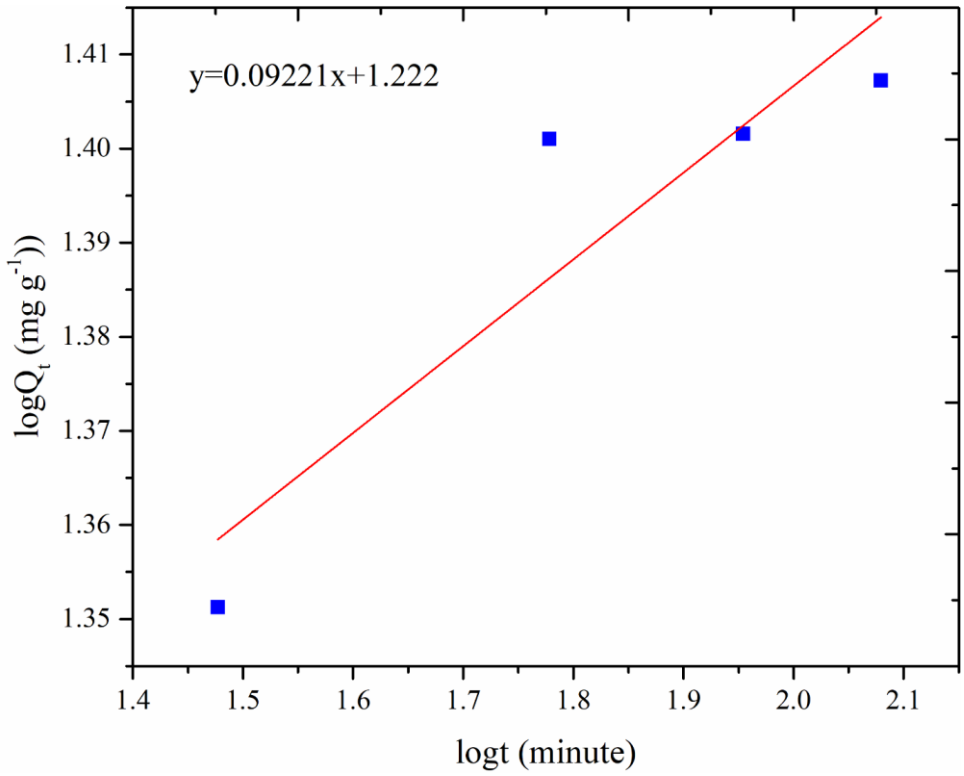

Fig.4.16 Kinetic model for adsorption of Cr^{6+} ion on PPSgCG: a) PSO; b) intra–particle diffusion. Adsorption conditions were at pH = 2, t = 120 min, C_o = 100 mg l^{-1}, hydrogel dose = 3 g l^{-1}, agitation speed = 120 rpm, T = 25^{o}C).

4.4.3. Adsorption Isotherm Models of Cr^{6+} Adsorption onto PPSgCG Hydrogel

Adsorption equilibrium is a fundamental property in adsorption studies, which describes the phenomena prevailing in the retention of the adsorbate from aqueous solution to an adsorbent at constant pH and temperature. It describes the interaction between the adsorbate and adsorbent. Many isotherm models are often used to describe the interaction phenomena between the adsorbate and adsorbent.

i. Langmuir

The Langmuir model is based on the assumption that molecules are adsorbed on fixed sites, which have the same energy with no lateral interaction (Langmuir 1918). The linear form of Langmuir isotherm was used to fit experimental data for the adsorption of Cr^{6+} ion onto the PPSgCG hydrogel adsorbents at 25, 35, and 45°C (Fig. 4.17). The correlation coefficient (R^2) and kinetic parameters are summarized in Table 4.2. The Langmuir isotherm agreed with the experimental data with $R^2 = 0.99$ at 25°C (Table 4.2). The values of q_m, R_L, and R^2 decline while the temperature rises, suggesting that the process is less favorable at higher temperatures. In Langmuir isotherm, favorability of adsorption is expressed by separation factor, R_L. The values of R_L calculated at 25, 35, and 45°C (Table 4.2) are between zero and one suggesting that the adsorption of Cr^{6+} on PPSgCG hydrogel adsorbents is favorable. However, R_L is found to decrease as temperature rises, showing that the adsorption is less favorable at higher temperatures. Hence, 25°C is an optimum temperature for the adsorption of Cr^{6+} ions on PPSgCG hydrogel adsorbents.

Table 4.2 Summary of isotherm parameters and coefficient of correlation.

Langmuir isotherm					Freundlich isotherm			Temkin isotherm		
T(^{o}C)	q_m(mg g^{-1})	b(lmg^{-1})	R^2	R_L	k(lg^{-1})	1/n	R^2	b	k_T	R^2
25	93.00	0.001	0.989	0.92	0.07	1.03	0.98	789.72	0.08	0.86
35	51.47	0.001	0.942	0.89	0.04	1.10	0.91	893.61	0.07	0.75
45	8.86	0.007	0.826	0.59	0.18	0.67	0.49	1524.32	0.10	0.51

ii. Freundlich

Freundlich model is known to describe the non–ideal and reversible adsorption, which was not restricted to the formation of monolayer. It is applied to multilayer adsorption over heterogeneous surface. The linear form of Freundlich model is based on the assumption that the sites of adsorption are heterogeneous. The surface heterogeneity, which ranges zero to one, is characterized by a heterogeneity factor of 1/n, where n indicates linearity between adsorbate solution and adsorption processes. A typical plot of Freundlich isotherm (Fig. 4.18(a)) and the values of k_F, n, and R^2 are listed in Table 4.2. The value of n gives an indication of the favorability and capacity of the adsorbent/ adsorbate system. For $1/n < 1$, adsorption process with chemical interaction is suggested. But if the value of 1/n (adsorption intensity) is above 1, then it is an indication of the cooperative process.

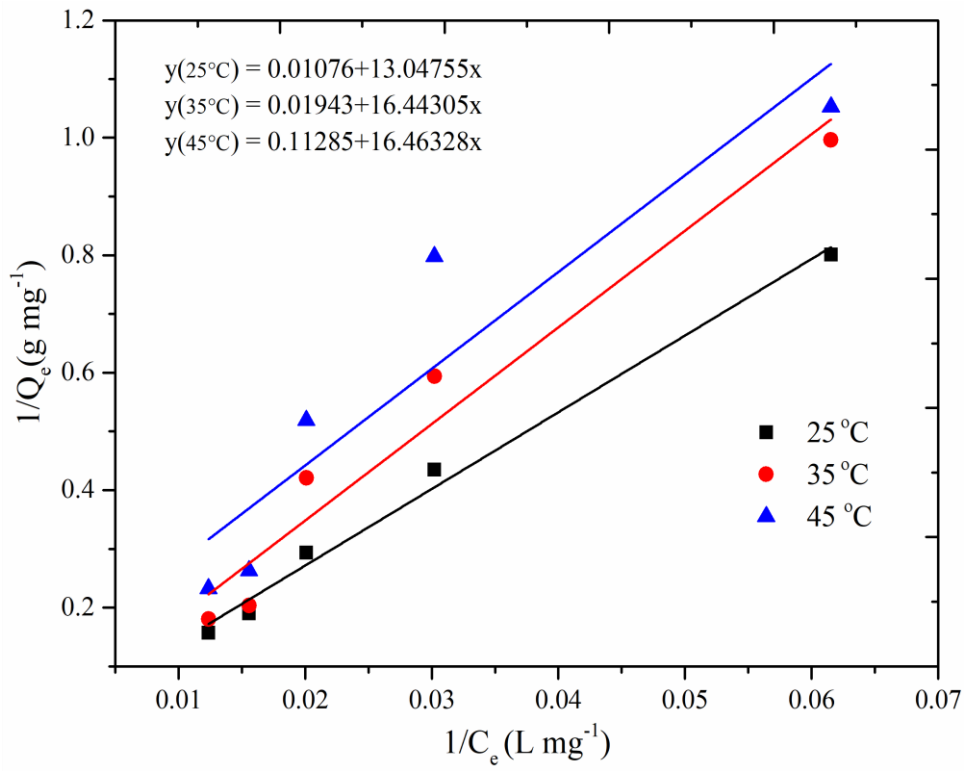

Fig.4.17 Langmuir isotherm for adsorption of Cr^{6+} ions on PPSgCG hydrogel adsorbents. Adsorption conditions were at pH = 2, t = 120 min, C_o = 100 mg l^{-1}, hydrogel dose = 3 g l^{-1}, agitation speed = 120 rpm).

It is quite clear that the value of 1/n is above one (Table 4.2) at 25 and 35°C, suggesting that the interactions between the Cr^{6+} ions in the solution with the PPSgCG hydrogel adsorbents are both physical and chemical.

iii. Tempkin

Besides, the linear form of Tempkin isotherm was used to fit experimental data for the adsorption of Cr^{6+} ions on to PPSgCG adsorbents at different temperatures (Fig. 4.18(b)). It assumes that the heat of adsorption of all the molecules in the layer decreases linearly with coverage due to adsorbent–adsorbate interactions, and that the adsorption is characterized by a uniform distribution of the binding energies up to some maximum binding energy. As shown in Table 4.2, the value of R^2 decreases as temperature rises and the experimental data were not described well by this model (R^2 = 0.86 at 25°C).

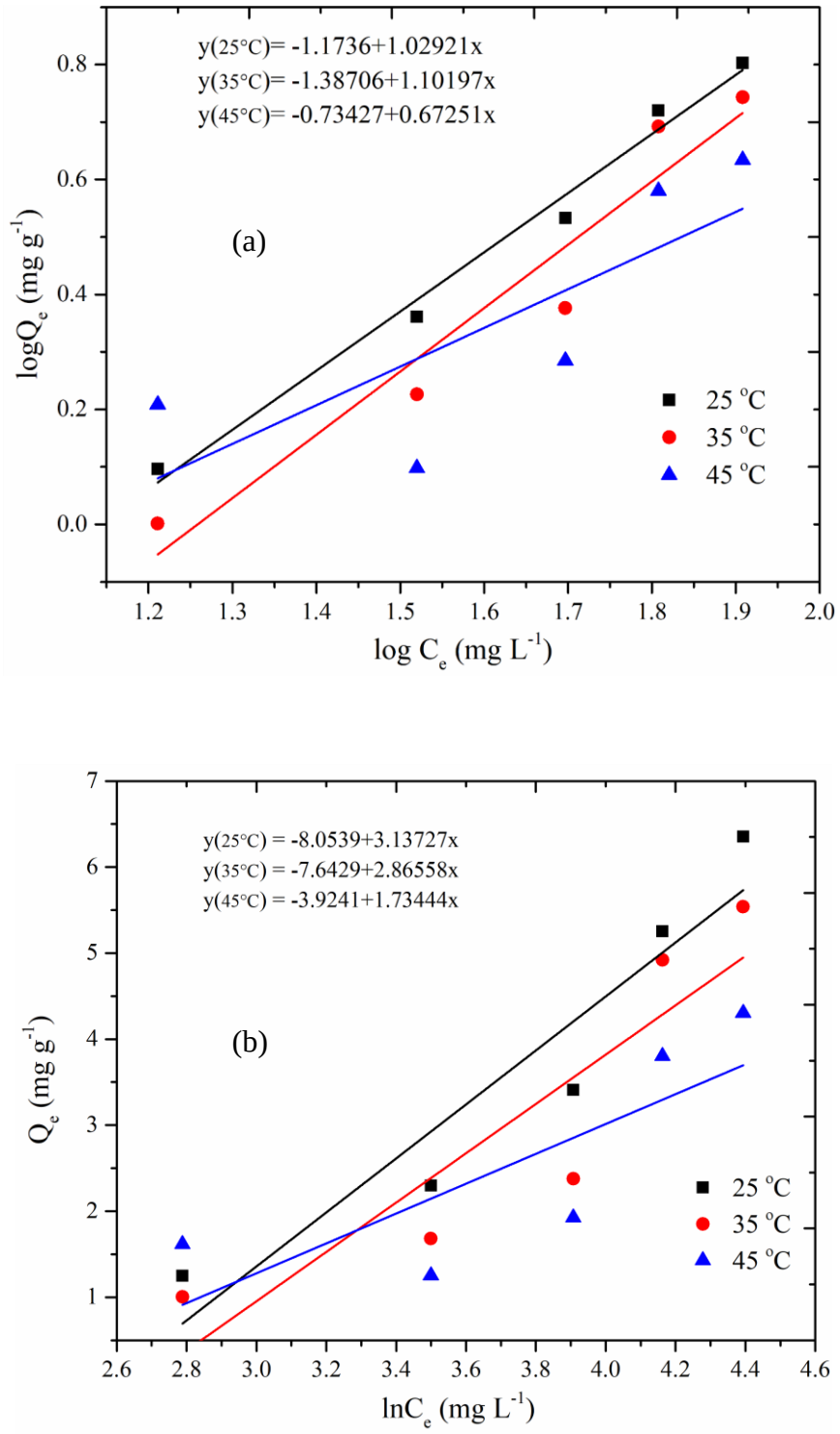

Fig.4.18 Isotherm for adsorption of Cr^{6+} ions on PPSgCG hydrogel adsorbents: a) Freundlich; b) Tempkin. Adsorption conditions were at pH = 2, t = 120 min, C_o = 100 mg l^{-1}, hydrogel dose = 3 g l^{-1}, agitation speed = 120 rpm).

4.4.4. Thermodynamic Parameters

The thermodynamic parameters such as standard enthalpy change (ΔH°), standard entropy change (ΔS°), and Gibbs free energy change (ΔG°) were studied to understand the adsorption performance under different temperatures. The equilibrium constant K_d (l g^{-1}) and ΔG° for the adsorption of Cr^{6+} ion on PPSgCG hydrogel adsorbents was calculated at 25, 35, and 45°C by using Eq. (3.22) and Eq. (3.23), respectively. ΔH° and ΔS° were obtained from the slope and intercept of *Van't Hoff* plot of ln K versus 1/T (Eq. (3.24)), respectively. The values of ΔH°, ΔS°, and ΔG° are presented in Table 4.3. The value of ΔS° is negative, which is similar to Kalidhasan (Kalidhasan et al. 2013). The negative value of ΔG° (Table 4.3) confirms that the adsorption of Cr^{6+} ions on to PPSgCG hydrogel adsorbents is spontaneous but the degree of reaction decreases as temperature rises. The decrease of ΔG° in absolute value observed as temperature increases might be due to growth of film boundary layer near the adsorbent surface and decrease in electron density in the vicinity of adsorption site. The negative enthalpy change shows the attractive van der Waals interaction between the Cr^{6+} ions and PPSgCG hydrogel adsorbents enhanced exothermically. The entropy of the adsorbate is related to the degrees of freedom associated with the adsorbent–adsorbate interactions. The negative change in entropy (decrease in overall entropy) is due to the detachment of water molecules after hydrophobic hydration (guest–host complexion) (Liu et al. 2002). This might be due to localized ion–pair interaction between the $HCrO_4^-$ anion with cation of protonated amine and amide functional group in the hydrogel. Moreover, it might be related to rotational and translational motion of $HCrO_4^-$ anion and cation of functional group restriction in multi polymer matrix that resulted in negative entropy change. The size and orientation of chain length of polymer also affect the randomness of the system here in the PPSgCG hydrogel adsorbents (Valentín-Reyes et al. 2019).

Table 4.3 Thermodynamic parameters for adsorption of Cr^{6+} onto PPSgCG hydrogel adsorbents.

Temperature (oC)	ΔH° (kJ mol^{-1})	ΔS° (kJ mol^{-1} K^{-1})	ΔG° (kJ mol^{-1})
25	-2.36	-0.004	-1.120
35	-2.36	-0.004	-1.067
45	-2.36	-0.004	-1.025

4.4.5. Theoretical Adsorption Studies (DFT) of Cr^{6+} onto PPSgCG Hydrogel

i. Geometry and structural analysis of PPSgCG–I and PPSgCG–I@Cr^{6+}

The geometrical structures of PPSgCG–I are depicted in Fig. 3.10 (Section 3.9.1) and were thoroughly optimized using DFT/B3PW91–D3 at the 6-31G (d) level. The optimization completed with convergence and stationary point found on potential energy surfaces (PES) (Annex 8). The +ve frequency of converged PPSgCG–I shows that the structures are at local minima on PES (Annex 9). The PPSgCG–I@Cr^{6+} were optimized using DFT/B3PW91–D3 at the 6-31G (d)/SDD level. Optimization helps to determine the minimum energies and configuration of system and enables one to evaluate the structural parameters within the system, before and after interactions. As shown in Fig. 4.19, the bond distance of adsorption site (–$CONH_2$) of PPSgCG–I were changed after the adsorption of Cr^{6+} (Annex 10 & 11). It was observed that PPSgCG tends to chelate with Cr^{6+} through a mono–denate nitrogen atom ligand (*Model–1*). On the other hand, the coordination sites were through nitrogen and oxygen atom of amide by bi–dentate coordination as presented in *Model–2*. In *Model–1*, the Cr–N bond distance was 2.005Å and in *Model–2*, Cr–N and Cr–O bond distance were 2.005Å and 2.019Å, respectively. The nitrogen of amide was more closed to Cr^{6+} than the oxygen of amide, suggesting that nitrogen played a more important role in the interaction with Cr^{6+} during the adsorption. This result were agreed with the result from FTIR (Section 4.4.1, sub-section iii.) and EDX (Section 4.4.3, sub-section i.) analysis.

ii. Molecular electrostatic potential of PPSgCG–I and PPSgCG–I@Cr^{6+}

Information about the local reactivity's of a molecule were obtained from molecular electrostatic potential (MEP), due to the density of electrons present from atoms that make up the molecule (Raghi et al. 2018). It is possible to determine the possible site of reaction or formation of complex by analyzing the MEPs (Hakiri et al. 2018). The points of greatest reactivity of the molecule can be identified from MEP.

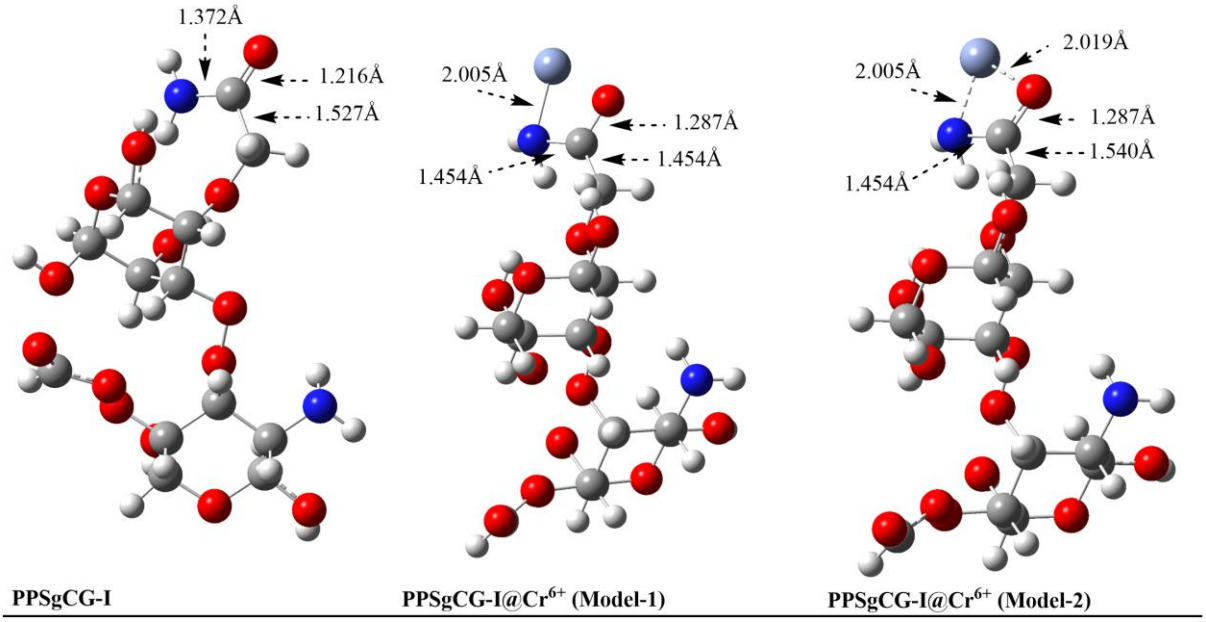

Fig.4.19 Optimized geometries of PPSgCG–I and PPSgCG–I@Cr^{6+}. Calculated at DFT/B3PW91–D3/6-31G(d)/SDD.

From total density mapped with EPS, in the regions with the most intense colors, where more orange or red are partially negative and blue indicates a partially positive region. All surfaces were generated with a density 0.0004 a. u. Fig. 4.20 shows the MEPs of PPSgCG–I and PPSgCG–I@Cr^{6+} and the coloring related to charge density. In the PPSgCG–I, it is possible to observe the presence of two regions (Fig. 4.19(a)) with high density of partially negative region. High density of negative region (more red) were observed in amide (–$CONH_2$) region due to the nitrogen and oxygen atoms, which is the region of interest for adsorption site for Cr^{6+}. These regions is very electronegative and thus susceptible to interactions involving electrophiles.

iii. Frontier molecular orbital's and reactive indices of PPSgCG–I and PPSgCG–I@heavy metals

The molecular orbital (MO) of PPSgCG–I before and after Cr^{6+} interaction and Cr^{6+} where illustrated in Fig. 4.21. In PPSgCG–I (Fig. 4.21(a)), in the HOMO–1, the orbital's have opposite signs, and so they combine to form an anti–bonding Π^* molecular orbital. The HOMO–1, HOMO–2, and HOMO–3 (Fig. 4.21(a – c)) in PPSgCG–I is an orbital formed from *p* orbital's from the two-carbon atom, the nitrogen atom and the oxygen atom. The contributions from the carbon–carbon atoms, and the carbon atoms and the nitrogen atoms

are situated along the single bond where as the contribution from the carbon atoms and the oxygen atoms are situated along the double bond.

To verify the reactivity between the PPSgCG and heavy metal ions, the study of frontier molecular orbital's (FMO) were carried out (Annex 12 & 13) and the reactivity were calculated (Table 4.4) from molecular orbital's (MO). Molecular orbital's are important to analysis the qualitatively as well as quantitatively possibility of reaction from its positioning. After analyzing the results found form the Gaussian output (Table 4.4), it is possible to infer the PPSgCG is relatively soft compound with respect to Pb^{2+}, Cd^{2+}, Cu^{2+} and Hg^{2+}. This is due to the presence of amine, amide, and carboxyl groups, generating an increase of the softness. PPSgCG–I molecule have positive electron affinity (+ve LUMO); that is, energy is not required to force an electron on to the PPSgCG–I molecule.

We can see that Pb^{2+}, Cd^{2+}, Cu^{2+} and Cr^{6+} are more electronegative (*Lewis acid*, electron acceptor, electrophiles) than PPSgCG-I and will accept electrons from PPSgCG-I resulting in a coordinate covalently bonded compound. Molecular orbital interaction of PPSgCG–I and Cr^{6+} were observed in Fig. 4.22. Where as PPSgCG-I is more electronegative (Lewis acid, electron acceptor) than $HCrO^{-}_{4}$ (*Lewis base*, electron donor, nucleophile) and will accept electrons from $HCrO^{-}_{4}$. This is a result of large negative electron affinity (large LUMO). A hard molecule has a large HOMO–LUMO gap and a soft molecule has a small HOMO–LUMO gap. Soft molecules are more polarizable than are hard molecules.

Electrons transfer from HOMO of each molecule to the LUMO of other takes place by mixing of the orbital's (delocalization effect). The Cr^{6+} is the harder acid (high E_{gap}) metal ion, which limits the amount of electron transfer and $HCrO^{-}_{4}$ is the softer (low E_{gap}) ions (Table 4.4). For the metal ions, Cu^{2+} ion was the one with the greatest softness (soft–soft interaction, strongest covalent bonding) and Pb^{2+}, Cd^{2+} and Hg^{2+} (soft acids) were with better softness with respect to PPSgCG. By far $HCrO^{-}_{4}$ is the soft ions with small HOMO–LUMO gap and forms weak interaction (hard–soft interaction) with PPSgCG. It is possible to infer that Cu^{2+}, Pb^{2+}, Cd^{2+} and Hg^{2+} ions tends to have a favorable interaction (covalent bonding, soft–soft interaction) with PPSgCG according to Pearson's theory.

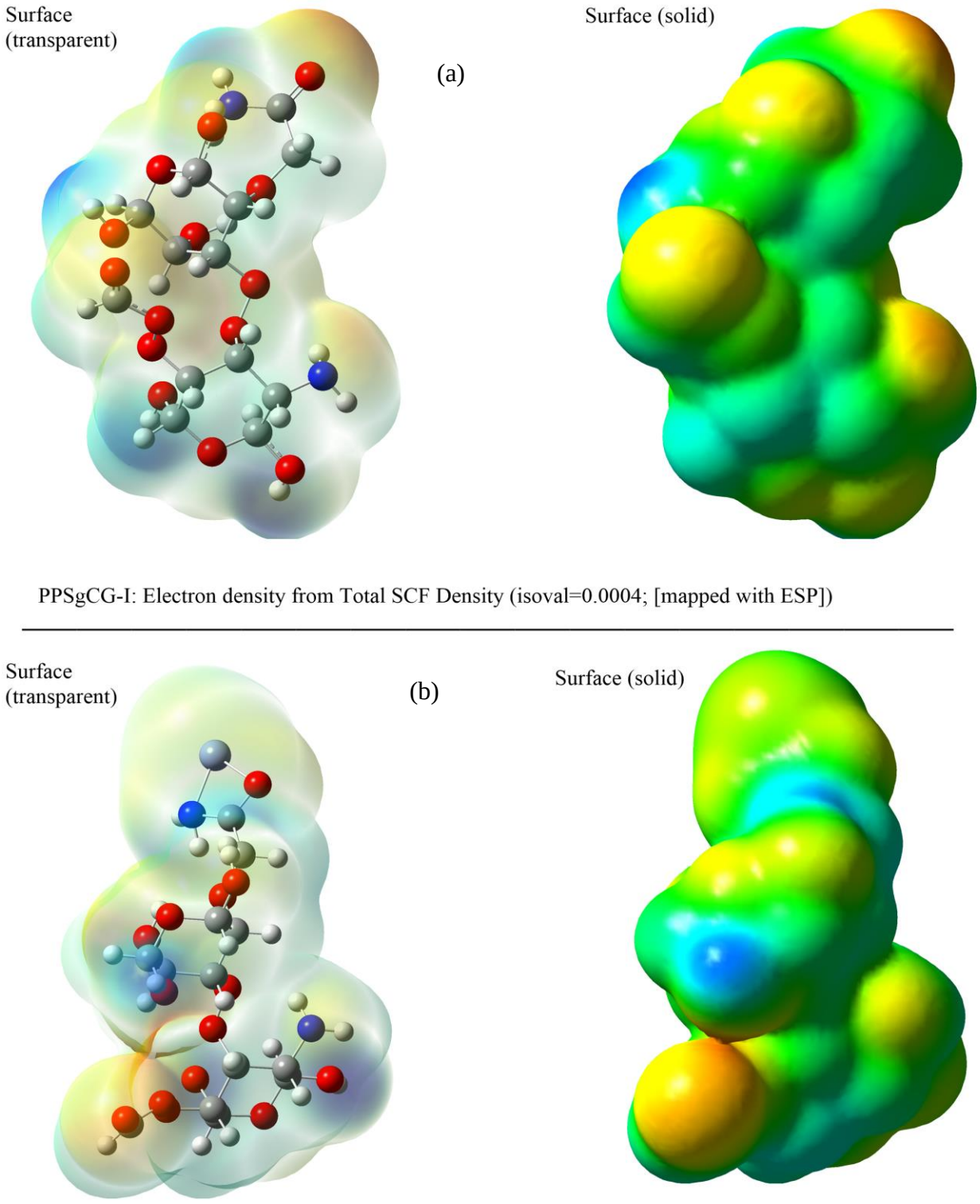

Fig.4.20 Representation of MEP: a) PPSgCG; b) PPSgCG–I@Cr^{6+} (Model-2). Surface Map value: -7.102e^{-2} to 7.102e^{-2}. Calculated at DFT/B3PW91–D3/6-31G(d)/SDD.

From Perturbation theory, there are electron delocalization and polarization-bonding interaction between molecules, which is greatest when energy of HOMO is small for both reactants and the energy of LUMO is large and positive (i.e. both molecules should be soft). The MO diagrams of PPSgCG–I derived from PPSgCG before and after Cr^{6+} adsorption are shown in Fig. 4.22 (a) and (c), respectively. After adsorption of Cr^{6+}, the HOMO–LUMO energy gap of PPSgCG–I is reduced (Table 4.4), which indicate the PPSgCG–I@Cr^{6+} complex was soft compound (high polarity) and stable.

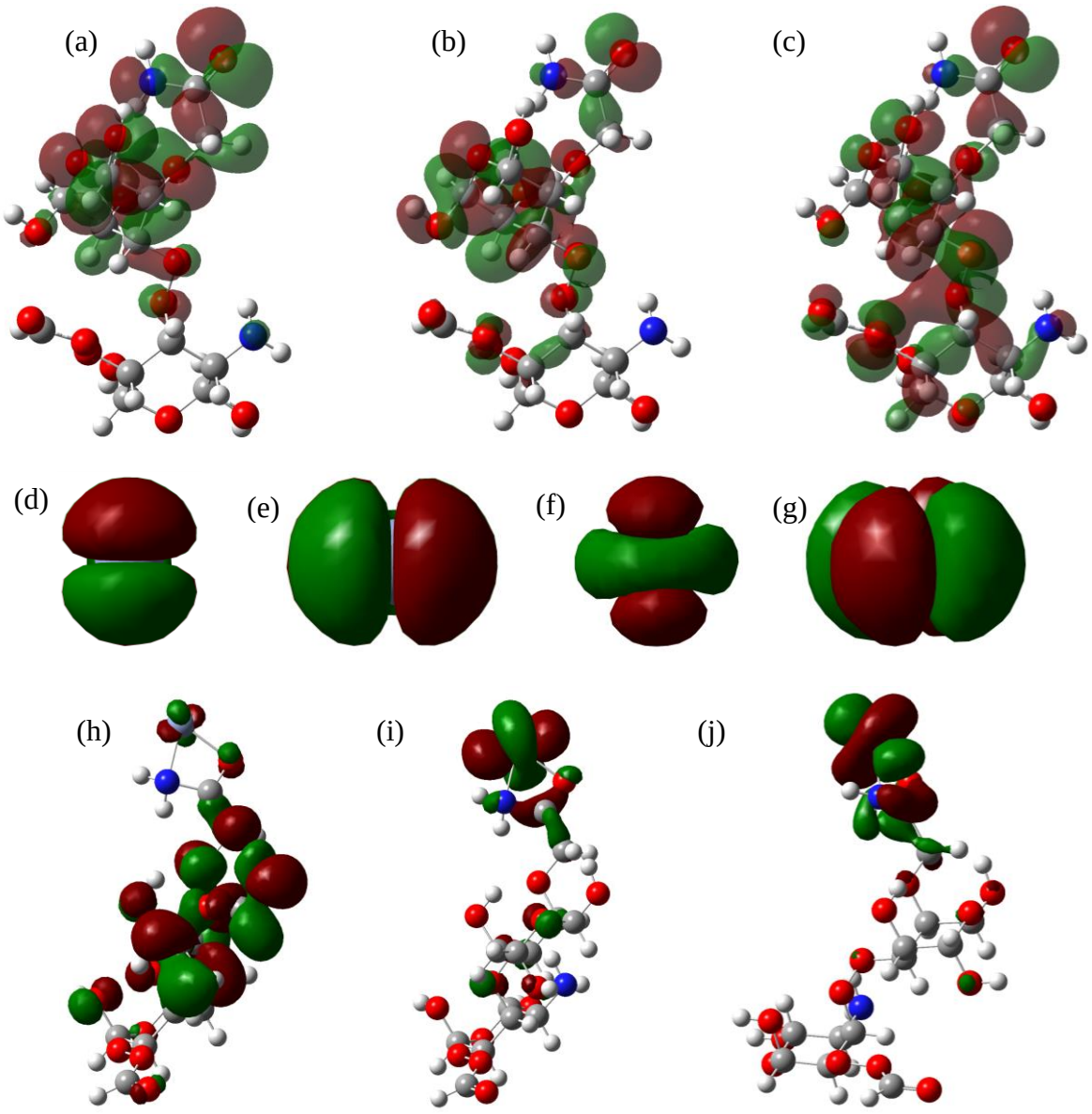

Fig.4.21 MO of PPSgCG–I: a) HOMO–1, b) HOMO–2, c) HOMO–3; MO of Cr^{6+}: d) LUMO+1 (p_z), e) LUMO+2 (p_x), f) LUMO+3 (d_z^2), g) LUMO+4 (d_{xy}); and MO of PPSgCG–I@Cr^{6+}: h) HOMO–2, i) HOMO–5, j) HOMO–6. Calculated at DFT/wB97XD/6-311+G (d, p)/SDD.

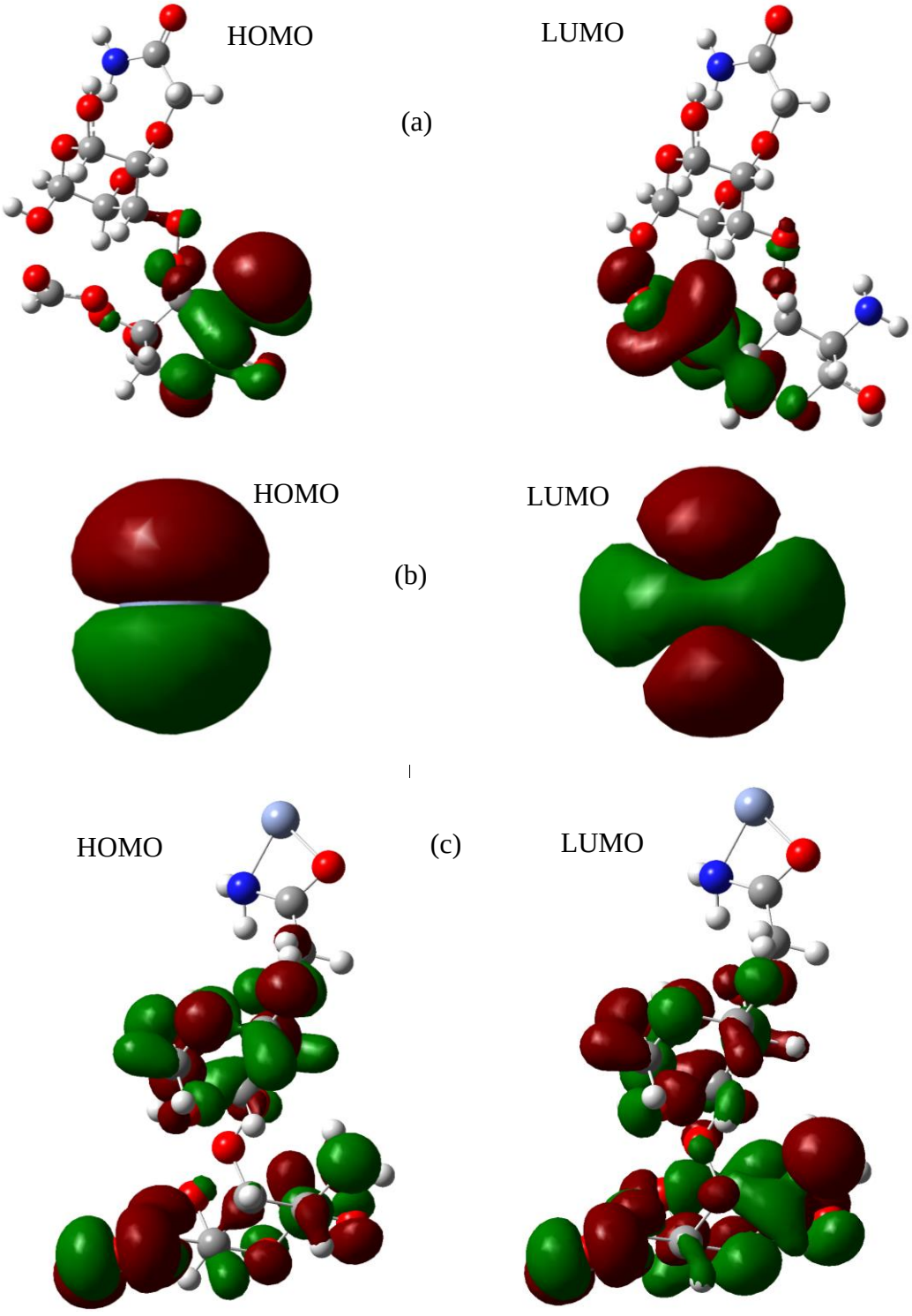

Fig.3.22 HOMO–LUMO diagram of optimized system: a) PPSgCG–I; b) Cr^{6+}; c) PPSgCG–I@Cr^{6+} (Model-2). MO, Isoval = 0.02 (-ve = green, +ve = red). Calculated at DFT/wB97XD/ 6-311+G (d, p)/SDD.

Table 4.4 Energy of HOMO (E_{HOMO}, eV), LUMO (E_{LUMO}, eV), Band/Energy gap (E_{gap}, eV), Softness (S), Hardness (η), Chemical potential (μ) and electronegative (χ) of PPSgCG–I and heavy metals. Calculated at DFT/wB97XD/6-311+G (d, p)/SDD.

Group	E_{HOMO}	E_{LUMO}	E_{Gap}	η	S	μ	χ
PPSgCG-I	-9.170	0.925	10.10	5.05	0.20	-4.12	4.12
Cr^{6+}	-151.65	-99.35	52.30	26.15	0.04	-125.50	125.5
$HCrO_4^-$	-2.90	-0.46	2.44	1.22	0.82	-1.68	1.68
Pb^{2+}	-27.70	-15.86	11.86	5.93	0.17	-21.79	21.79
Cd^{2+}	-32.14	-20.22	11.92	5.92	0.17	-26.18	26.18
Cu^{2+}	-32.05	-21.71	10.34	5.17	0.19	-26.88	26.88
Hg^{2+}	-7.46	-0.52	6.97	3.48	0.29	-4.00	4.00
PPSgCG-I@Cr^{6+}	-25.46	-24.96	0.50	0.25	4.00	-25.21	25.21

iv. Structural and vibrational analysis of PPSgCG–I and PPSgCG–I@Cr^{6+}

Complexes formation between PPSgCG and Cr^{6+} were also confirmed by analyzing the vibrational frequencies of the adsorption site. The vibrational frequencies of –C=O and –C–N of amide in isolated PPSgCG–I and corresponding Cr^{6+} complexes were investigated and presented in Table 4.5. Based on the data output from frequency calculation, vibration frequencies of C-N and C=O of amide of PPSgCG–I are 3544.90 cm^{-1} and 1843.70 cm^{-1}, respectively, which is shifted to lower frequencies after PPSgCG–Cr^{6+} complexes. This result were similar with the FTIR analysis (Section 4.4.1. subsection–iii). The vibrational frequencies of C-N shifted more to lower than that of C-O after complexes (Annex 14 & 15), which shows that Cr^{6+} is more attracted to nitrogen atoms than oxygen atom. This result is similar with bond distance calculated after complexes (Fig. 4.19).

Table 4.5 Vibration frequencies of PPSgCG–I and PPSgCG–I@Cr^{6+}.

Complex	Interaction position	Frequency (cm^{-1})	
		Experimental (FTIR)	Theoretical (DFT)
PPSgCG–I	–amine	3425 – 3785	νC = N/3544.90
	–amide I	1670	νC = O/1843.70
PPSgCG–I@Cr^{6+}	N–Cr^{6+}	3675 – 3370	νC = N/1583.83
	O–Cr^{6+}	1650	νC = O/1347.11

v. Natural bond orbital analysis of PPSgCG–I and PPSgCG–I@Cr^{6+}

NBO analysis is one of many available options (e.g. of QTAIM, Mulliken, graphical maps of electrostatic potential (ESP) etc.) for translating computational solutions of Schrodinger's wave equations into familiar language of chemical bonding concepts. Natural bond orbital (NBO) analysis was used for the study of the charge transfer occurring within the atom, adjacent atom or more remote atom during the interaction/adsorption processes. The charge transfer calculation were carried out with the DFT/B3PW91–D3/6-31G(d)/SDD level of theory. Atoms of potential adsorption site, which has total NBO charges greater than -0.5 were selected for Lewis and non–Lewis NBO analysis (Table 4.6). The calculated Lewis and non–Lewis NBO (from NBO summary of Gaussian output, Annex 16) of these atoms before and after Cr^{6+} adsorption were presented in Table 4.7 and Table 4.8, respectively.

Condensed summary of the principal NBOs, showing the electron occupancy, orbital energy, and the qualitative pattern of delocalization interaction with each and other atoms are presented in Table 4.7. This table allows quickly to observe the principal delocalizing acceptor orbital's associated with each donor NBO and their topological relationships to this NBO. NBO is also used to identified electron occupancy and energy of orbital associated with each atom. As presented in Table 4.7, the adsorption site (-$CONH_2$) of PPSgCG–I atoms, the oxygen lone pair (LP(2)O_{21}) and nitrogen lone pair (LP(1)N22) are seen to be the lowest–occupancy (1.85640 electrons for O21, 1.74773 electrons for N22) and highest–energy (-0.24928 a. u for O21, -0.30184 a. u for N22). The strongest interaction were identified for the interaction of lone pair (LP) orbital NBO of localized on O21 and N22 with the adjacent sigma*(σ^*) (O–C and C–C) and σ^*(C–O and O–H), respectively. At the bottom of table, summary shows that the Lewis NBOs is about 98.74% of the total electron density, with the remaining non–Lewis density found primarily in the valence–shell anti–bonds.

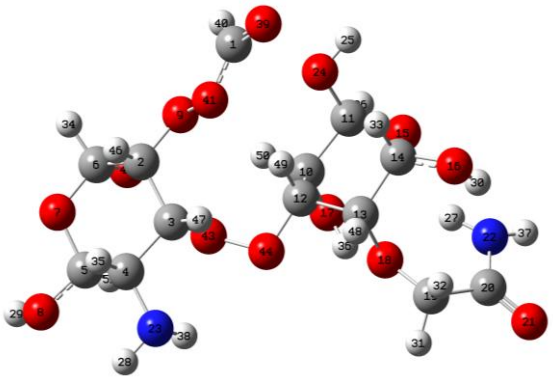

Fig.4.23 Labeled atoms of Optimized PPSgCG-I (used as reference for Table 4.6).

Table 4.6 NBO total charge of PPSgCG-I. Calculated at DFT/B3PW91–D3/6-31G(d)/SDD

Labels (Fig. 4.23)	Atom	NBO charge	Labels (Fig. 4.23)	Atom	NBO charge
7	O	-0.615	21	O	-0.600
8	O	-0.746	22	N	-0.902
15	O	-0.626	23	N	-0.898
16	O	-0.758	24	O	-0.778
17	O	-0.759	39	O	-0.555
18	O	-0.620	42	O	-0.749

Table 4.7 Lewis and non – Lewis NBO (from NBO Summary) of PPSgCG-I. Calculated at DFT/B3PW91–D3/6-31G(d)/SDD.

Surface	Lewis NBO	Occupancy (electrons)	Energy (a. u)	Principal Delocalization (non-Lewis NBO)
PPSgCG-I	$LP(1)O_7$	1.95345	-0.58037	$BD^*_{C-O,}\ BD^*_{C-H}$
	$LP\ (1)O_8$	1.97878	-0.59724	$BD^*_{C},\ BD^*_{C-O}$
	$LP(2)O_{15}$	1.90043	-0.31741	$BD^*_{C-H},\ BD^*_{C-O}$
	$LP(2)O_{16}$	1.92703	-0.31241	$BD^*_{C-O},\ BD^*_{O-H}$
	$LP(2)O_{17}$	1.94664	-0.28569	$BD^*_{C-C},\ BD^*_{O-H}$
	$LP(1)O_{18}$	1.94853	-0.57338	$BD^*_{C-H,}\ BD^*_{O-H}$
	$LP(1)O_{21}$	1.97776	-0.67964	$BD^*_{C-N},\ BD^*_{C-C}$
	$LP(2)O_{21}$	1.85548	-0.24928	$BD^*_{O-C},\ BD^*_{C-C}$
	$LP(1)N_{22}$	1.75119	-0.30184	$BD^*_{C-O},\ BD^*_{O-H}$
	$LP(1)N_{23}$	1.94738	-0.30027	$BD^*_{C-H,}\ BD^*_{O-H}$
	$LP(1)O_{24}$	1.97620	-0.61159	$BD^*_{C-C},\ BD^*_{O-H}$
	$LP(2)O_{24}$	1.93456	-0.32334	$BD^*_{C-H,}\ BD^*_{O-H}$
	$LP(1)O_{43}$	1.98391	-0.69366	$BD^*_{C-C},\ BD^*_{O-H}$
	$LP(2)O_{43}$	1.94914	-0.32575	$BD^*_{C,}\ BD^*_{C-H}$
Total Lewis = 223.15736 (98.7422%)				
Valence non-Lewis = 2.40438 (1.0639%)				
Rydberg non-Lewis = 0.43826 (0.1939%)				

After adsorption of Cr^{6+} onto PPSgCG, it was observed that the electron occupancy and energy were changed in both $LP(1)O_{21}$ and $LP(1)N_{22}$ Lewis NBOs (Table 4.9). Transfer of electrons were observed from oxygen (O21) to chromium (Cr52) ($LP(1)O_{21} \rightarrow BD^{*}_{O\text{-}Cr}$), and from chromium (Cr52) to oxygen (O21) ($LP(2)Cr_{52} \rightarrow BD^{*}_{C\text{-}O}$) and nitrogen (N22) ($LP(1)Cr_{52} \rightarrow \sigma^{*}_{N\text{-}H}$ (Table 4.9). After Cr^{6+} adsorption, the strongest interaction were identified for the interaction of lone pair (LP) orbital NBO of localized on Cr52 with σ^{*}(N–H) and the adjacent σ^{*}(C–C). The second strongest interaction were identified for the interaction of lone pair (LP) orbital NBO of localized on Cr52 with σ^{*}(C–O). This shows Cr is more attracted to –N atom than it is attracted to –O atom. From these results, we can infer that there were chemical bonding between chromium and oxygen and nitrogen atoms, which shows adsorption of Cr^{6+} onto the PPSgCG hydrogel by covalent bonding, which is similar to FTIR and EDX analysis.

Table 4.8 Lewis and Non–Lewis NBO (from NBO Summary) of PPSgCG-I@Cr^{6+}. Calculated at DFT/B3PW91–D3/6-31G(d)/SDD.

Surface	Lewis NBO	Occupancy (electrons)	Energy (a. u)	Non-Lewis NBO
PPSgCG-I@Cr^{6+}	$LP(1)O_7$	1.95495	-1.23755	$BD^{*}_{C\text{-}O}, BD^{*}_{C\text{-}H}$
	$LP(1)O_8$	1.93775	-1.19400	$BD^{*}_{C}, BD^{*}_{C\text{-}O}$
	$LP(1)O_{15}$	1.95442	-1.22316	$BD^{*}_{C\text{-}H}, BD^{*}_{C\text{-}O}$
	$LP(2)O_{16}$	1.74953	-0.93749	$BD^{*}_{C\text{-}O}, BD^{*}_{O\text{-}H}$
	$LP(2)O_{17}$	1.69519	-0.96780	$BD^{*}_{C\text{-}H}, BD^{*}_{O\text{-}H}$
	$LP(1)O_{18}$	1.95804	-1.24989	BD^{*}c-c, $BD^{*}_{O\text{-}H}$
	$LP(1)O_{21}$	1.96019	-1.40766	$BD^{*}_{O\text{-}Cr}$, $BD^{*}_{C\text{-}N}$
	$LP(1)N_{22}$	1.63522	-0.98880	BD^{*}c-c, BD^{*}c
	$LP(1)N_{23}$	1.31042	-0.95086	$BD^{*}_{C\text{-}H}, BD^{*}_{O\text{-}H}$
	$LP(1)O_{24}$	1.96459	-1.23024	$BD^{*}_{C\text{-}H}, BD^{*}_{O\text{-}H}$
	$LP(2)O_{24}$	1.86244	-0.95663	$BD^{*}_{C\text{-}C}, BD^{*}_{O\text{-}H}$
	$LP(1)O_{42}$	1.97971	-1.36665	$BD^{*}_{C\text{-}C}, BD^{*}_{O\text{-}H}$
	$LP(2)O_{42}$	1.88752	-1.00266	$BD^{*}_{C\text{-}C}, BD^{*}_{C\text{-}H}$,
	$LP(1)Cr_{52}$	1.99457	-0.96742	$BD^{*}_{N\text{-}H}, BD^{*}_{C\text{-}C}$
	$LP(2)Cr_{52}$	1.98769	-0.97078	$BD^{*}_{C\text{-}O}$

vi. Perturbation energy analysis

The perturbation energy of active adsorption site, which contains the highest, and the lowest second–order perturbation energy is selected for discussion in this thesis. From Table 4.9, it was observed that the highest stabilization energy were found on O21 (26.70 kcal mol^{-1}) and N22 (23.66 kcal mol^{-1}) of $–CONH_2$ of PPSgCG. Therefore, most effective interacted atoms (O21 and N22) among the atoms with NBO charge greater than –0.5 charge atoms of PPSgCG-I were extracted for discussion in this section. In particular, we focus on active adsorption site ($–CONH_2$) of PPSgCG. The highest and lowest stabilization energy of O21 were observed at interacting orbital's $LP(2)O_{21} \rightarrow BD^*(1)C_{20}–N_{22}$ and $LP(1)O_{21} \rightarrow BD^*(1)C_{20}–N_{22}$ with values of 26.70 and 2.11 kcal mol^{-1}, respectively. The highest stabilization energy of N22 were observed at interacting orbital's $LP(1)N22 \rightarrow BD^*(2)C_{20}–O_{21}$ with values of 23.66 kcal mol^{-1} (Table 4.9). The strongest interaction were identified for the interaction of lone pair orbital NBO localized on O21 and N22 with adjacent sigma*(C–N, C–C) and sigma* (C–O, O–H) bonds, respectively. These shows increased electron density around O21 and indicates possible adsorption site for Cr^{6+}. Among the atoms in PPSgCG–I with higher NBO charges (>–0.5), O21 atom with the highest stabilization energy is perturbed (unstable) due to reactivity (Louis et al. 2022). Moreover, N22 is the second highest stabilization energy (23.66 kcal mol^{-1}) with $LP(1)N_{22} \rightarrow BD^*(2)C_{20}$-$O_{21}$ interacting orbital's, showing increased electron density. Hence, both –O and –N atoms are susceptible to interactions involving electrophiles, which agreed with EPS (Section 4.4.5: ii).

For PPSgCG-I@Cr^{6+}, after Cr^{6+} interacting with O21 and N22, interacting orbital's were observed at $LP(1)O21 \rightarrow BD^*(1)O_{21}–Cr_{52}$, $LP(1)Cr_{52} \rightarrow BD^*(1)C_{19}–C_{20}$, $LP(1)Cr_{52} \rightarrow BD^*(2)N_{22}–H_{51}$, $LP(2)Cr_{52} \rightarrow BD^*(1)C_{20}–O_{21}$, and $LP(2)Cr_{52} \rightarrow BD^*(1)N_{22}–H_{27}$ with stabilization energy of 0.96, 0.73, 0.65, 0.50, and 1.46 kcal mol^{-1}, respectively (Table 4.10). These shows decreases in electron density around O21 and N22 after interacted with Cr^{6+}. These interacting orbital's shows the transfer of electron from –O to Cr with interacting orbital of $LP(1)O21 \rightarrow BD^*(1)O21–Cr52$, which shows the interaction of lone pair orbital NBO of localized on O21 with σ^*(O–Cr) bonds. There are also electron transfer from Cr to –N atoms with interacting orbital's $LP(1)Cr_{52} \rightarrow BD^*(2)N_{22}–H_{51}$ and $LP(2)Cr_{52} \rightarrow BD^*(1)N_{22}–H_{27}$, which shows the interaction of lone pair orbital NBO of localized on Cr52 with adjacent σ^*(N–H) bonds. On the other hand, electron transfer occurred from –Cr to adjacent –C atom with interacting orbital's $LP(1)Cr_{52} \rightarrow BD^*(1)C_{19}–C_{20}$ and $LP(2)Cr_{52} \rightarrow BD^*(1)C_{20}–O_{21}$, which

shows the interaction of lone pair orbital NBO of localized on Cr52 with adjacent σ^*(C–C and C–O) bonds. From these results, we can infer that electron transfer or electron sharing where occurred between the Cr and active adsorption site of PPSgCG.

Table 4.9 Second Order Perturbation Theory Analysis of Fock Matrix in NBO Basis of PPSgCG–I/ DFT/wB97XD/6-311+G (d, p)/SDD. Threshold for printing: 0.50 kcal mol^{-1}

Surface	Donor (i)	Acceptor (j)	E^2 (i, j) (kcal mol^{-1})	E(i)–E(j) (a. u)	F(i, j) (a. u)
PPSgCG-I	LP(1)O_7	$BD^*(1)C_5$ - O_8	3.92	0.90	0.053
	LP(2)O_7	$BD^*(1)C_6$ - O_{42}	12.47	0.61	0.078
	LP (1)O_8	$BD^*(1)C_5$ - H_{51}	3.07	1.04	0.051
	LP(2)O_8	$BD^*(1)C_5$ - O_7	16.04	0.59	0.087
	LP(1)O_{15}	$BD^*(1)C_{14}$ - O_{16}	3.91	0.91	0.053
	LP(2)O_{15}	$BD^*(1)C_{11}$ - O_{24}	13.06	0.61	0.081
	LP(2)O_{16}	$BD^*(1)C_{14}$ - O_{15}	9.55	0.59	0.067
	LP(1)O_{17}	$BD^*(1)C_{10}$ - C_{12}	4.26	0.93	0.057
	LP(2)O_{17}	$BD^*(1)C_{10}$ - C_{11}	8.70	0.65	0.067
	LP(1)O_{18}	$BD^*(1)O_{17}$ - H_{36}	9.19	1.04	0.088
	LP(2)O_{18}	$BD^*(1)C_{19} – C_{20}$	6.90	0.70	0.062
	LP(1)O_{21}	$BD^*(1)C_{20}$ - N_{22}	2.11	1.13	0.044
	LP(2)O_{21}	$BD^*(1)C_{20}$ - N_{22}	26.70	0.70	0.124
	LP(1)N_{22}	$BD^*(2)C_{20}$ - O_{21}	23.66	0.44	0.092
	LP(1)N_{23}	$BD^*(1)C_4$ - C_5	9.83	0.66	0.072
	LP(2)O_{24}	$BD^*(1)C_{11}$ - O_{15}	11.78	0.62	0.076
	LP(1)O_{42}	$BD^*(1)C_6$ - H_{34}	2.35	1.06	0.045
	LP(2)O_{42}	$BD^*(1)C_6$ - O_7	15.16	0.62	0.087

Table 4.10 Second Order Perturbation Theory Analysis of Fock Matrix in NBO Basis of PPSgCG–I@Cr^{6+}/ DFT/wB97XD/6-311+G (d, p)/SDD. Threshold for printing: 0.50 kcal mol^{-1}

Surface	Donor (i)	Acceptor (j)	E^2 (i, j) (kcal mol^{-1})	E(i)–E(j) (a. u)	F(i, j) (a. u)
PPSgCG-I@Cr^{6+}	$LP(1)O_7$	$BD^*(1)C_5 - O_8$	4.13	0.94	0.056
	$LP(1)O_8$	$BD^*(1)C_5 - O_7$	9.10	0.84	0.078
	$LP(2)O_8$	$BD^*(2)C_5 - O_7$	49.66	0.23	0.102
	$LP(1)O_{15}$	$BD^*(1)C_{11} - O_{24}$	4.18	1.01	0.058
	$LP(1)O_{16}$	$BD^*(1)C_{14} - O_{15}$	8.03	0.75	0.070
	$LP(2)O_{16}$	$BD^*(1)C_{13} - C_{14}$	18.35	0.47	0.086
	$LP(2)O_{17}$	$BD^*(1)C_{10} - C_{12}$	9.62	0.58	0.071
	$LP(1)O_{18}$	$BD^*(1)C_{19} - H_{31}$	1.83	1.05	0.039
	$LP(2)O_{18}$	$BD^*(1)C_{13} - C_{14}$	9.97	0.54	0.066
	$LP(1)O_{21}$	$LP^*(5)Cr_{52}$	5.68	0.90	0.064
	$LP(1)O_{21}$	$LP^*(6)Cr_{52}$	0.80	0.89	0.024
	$LP(1)O_{21}$	$LP^*(7)Cr_{52}$	0.52	0.97	0.020
	$LP(1)O_{21}$	$BD^*(1)O_{21} – Cr_{52}$	0.96	0.69	0.023
	$LP(1)N_{22}$	$LP^*(3)Cr_{52}$	0.79	0.21	0.013
	$LP(1)N_{22}$	$LP^*(4)Cr_{52}$	0.73	0.26	0.013
	$LP(1)N_{22}$	$LP^*(6)Cr_{52}$	1.16	0.48	0.023
	$LP(1)Cr_{52}$	$BD^*(1)C_{19} – C_{20}$	0.73	0.59	0.019
	$LP(1)Cr_{52}$	$BD^*(2)N_{22} – H_{51}$	0.65	0.67	0.019
	$LP(2)Cr_{52}$	$BD^*(1)C_{20} – O_{21}$	0.50	0.20	0.01
	$LP(2)Cr_{52}$	$BD^*(1)N_{22} – H_{27}$	1.46	0.65	0.027

4.5. Regeneration of PPSgCG Hydrogel

Desorption and reusability of the adsorbent is an important characteristic from design, practical and economical point of view. In this study, the adsorption capacity of PPSgCG hydrogel towards to Cr^{6+} ion during consecutive adsorption–desorption cycle was investigated. During the adsorption–desorption cyclic process, 0.1 M HNO_3 was used as desorption agent. The effects of reuse time on PPSgCG for Cr^{6+} adsorption from aqueous solution were presented in Fig. 4.24. It can be observed that the adsorption capacity of the hydrogel decreases slowly as the number of cycle of using increase. The adsorption capacity of PPSgCG in removing Cr^{6+} after five–cycle was 90% of its initial capacity. The slight decreases in adsorption capacity during adsorption – desorption cycle is attributed to losses due to rewashing and difficulty to recovery the whole active site form the hydrogel. The above result indicates that the adsorption–desorption cycle did not affect the adsorption capacity of the PPSgCG hydrogel significantly, suggesting that the hydrogel can be considered as an effective adsorbent in decontamination of metal ions form wastewater.

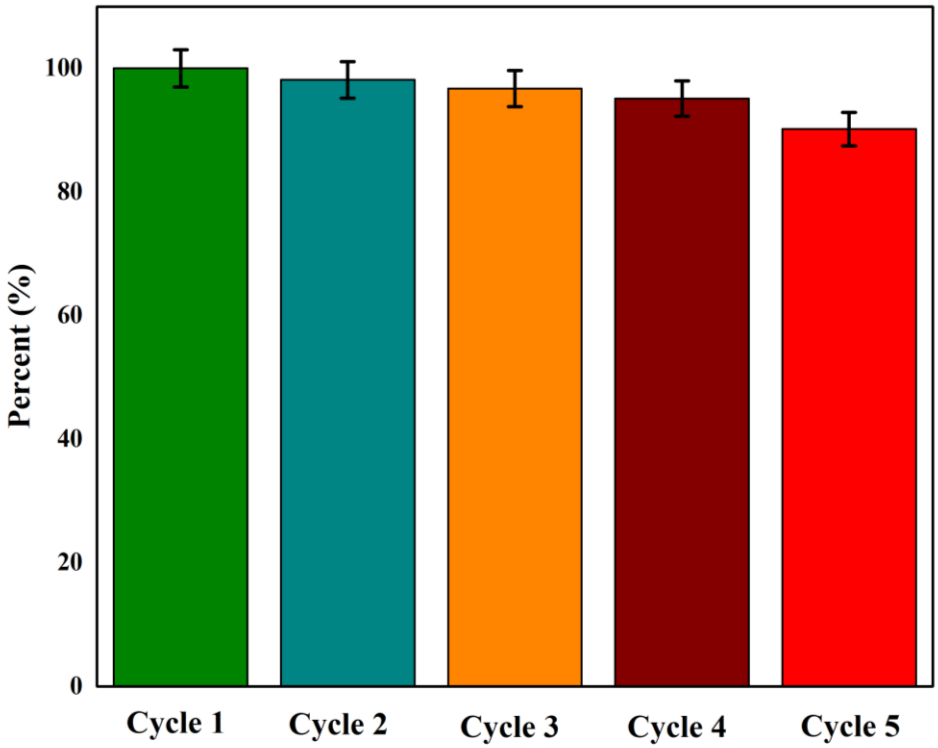

Fig.4. 24 Reuse times and adsorption capacity of PPSgCG hydrogel adsorbents for Cr^{6+} (where, pH = 2, C_o = 100 mg l^{-1}, t = 120 min, hydrogel dose = 3 g l^{-1}, agitation speed = 120 rpm, T = 25°C).

4.6. Characteristics and Removal of Batu Tannery Wastewater

The sample from Batu Tannery wastewater were collected, treated, stored and analyzed according to APHA–Colorimetric method (3500–Cr. B) standard (23rd Edition) (Section 3.2.). Batch adsorption studies were conducted in 100ml rubber stopped volumetric flasks. The flasks (25 ml wastewater) were placed inside incubator shaker (New Brunswick Scientific Edison, USA, EXCELLA E24R) at 120 rpm for 2h. PPSgCG Hydrogel dose of 3.0 g l^{-1} were used for adsorption. The concentration of the total Cr in the solution before and after adsorption were determined by UV–vis spectrophotometer (Section 3.4.). The concentration of total Cr in the Batu Tannery wastewater, which was measure at 350 nm and pH of 2 were 6.86 mg l^{-1}. Where as the concentration of total Cr measured at 373 nm and pH of 9 were 14.89 mg l^{-1}. According to different studies, Cr shows charge transfer absorption bands, which differ in acid and alkaline solution. $HCrO^{-}_{4}$ has a maximum absorption at 350 nm, whereas CrO^{2-}_{4} peaks at 373 nm. In both acidic and basic conditions, the concentration of total Cr were reduced to 5.97 and 9.76 mg l^{-1}, respectively, after adsorption onto the PPSgCG hydrogel adsorbents. The removal efficiency (R %) were calculated using Eq. (3.8) and the result is presented in (Table 4.11). Only 13% at pH of 2 and 34.45 % at pH 9 of total Cr^{6+} were removed from real wastewater by this hydrogel in two hour of contact, which is promising adsorbent for real wastewater remediation. The low performance of PPSgCG at lower pH might be attributed to the competition for adsorption between chromate and sulfate ions. Due to the identical chemical properties and geometrical configuration between sulfate and chromate, they should display not only similar adsorption behavior but also strong competitive adsorption on adsorbent surfaces. Both show strong competitive adsorption under acidic condition. With the increases in pH, the competitive adsorption between sulfate and chromate decreases. Overall, the adsorption performance of PPSgCG was low in real wastewater (effluents from chemical precipitation) treatment, which might be related to large amount of sulfate and other competitive ions, and precipitating agents used during chemical precipitation.

Table 4.11 Characteristics of chromium from Batu tannery wastewater

Chromium (Cr)		pH	Concentration (mg l^{-1})	R (%)
Total Cr^{6+}	Before/ After adsorption	2	6.86/ 5.97	13.6
Total Cr^{6+}	Before/ After adsorption	9	14.89/ 9.76	34.5

4.7. Removal of Cr^{6+} Ion by CZVI–CP–PVA Hydrogel

4.7.1. Effect of Adsorption Parameters

i. Effect of pH

The effect of initial pH in the range of 1–10 on the removal of Cr^{6+} was examined using CZVI–CS–PVA at the concentration of 25 mg l^{-1} and hydrogel dose of 2 g l^{-1} (Fig. 4.25). As illustrated in Fig. 4.25, the adsorbent hydrogel was found to be efficient over the wide range of pH. The mechanism of adsorption could be explained by electrostatic attraction of amine and solution–oxidation adsorption by ZVI (Katsoyiannis, Ruettimann, and Hug 2008). Significant decreases in adsorption capacity were observed in Cr^{6+} sorption beyond pH of 3.0. The underlying reason for the decrease in Cr^{6+} removal was explained by formation of its anionic species that undergoes repulsion by the negatively charged sorbent surface.

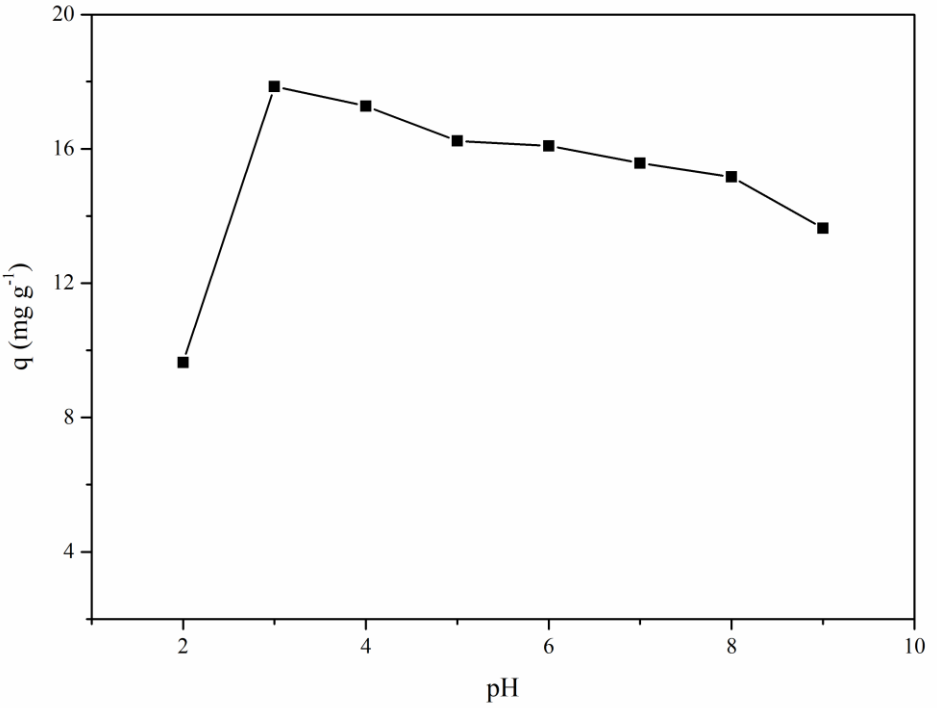

Fig.4. 25 Effect of pH on Cr^{6+} adsorption onto CZVI–CS–PVA

ii. Effect of Cr^{6+} initial concentration and time

The initial concentration of metal ion in the solution and duration of contact between the metal ion and the adsorbent were highly affect the adsorption capacity and the removal efficiency of adsorbent. As illustrated in Fig. 4.26 (a), the adsorption capacity (q_m) of the CZVI–CS–PVA were increased as the initial concentration of Cr^{6+} in the solution were increased. The adsorption capacity were increased during the first 40 minutes contact time and nearly constant for the rest of 120 minutes. The fast adsorption rate during the 40 minutes

might be related the adsorption–reduction of Cr^{6+} to Cr^{3+}. The removal efficiency (R) were decreased as the concentration of Cr^{6+} in the solution increased (Fig. 4.26(b)).

iii. Effect of CZVI–CS–PVA hydrogel dose

The effect of adsorbent dose on Cr^{6+} removal was studied to optimize the exact quantity of hydrogel. The CZVI–CS–PVA adsorption capacity (q) decreased with increasing in CZVI–CS–PVA dosage (Fig. 4.27(a)). The Cr^{6+} removal efficiency (R) increased with increase in CZVI–CS–PVA dosage (Fig. 4.27(b)); thereby indicating that higher is the adsorbent dose, higher will be its binding active sites for Cr^{6+} adsorption.

4.7.2. Adsorption Kinetic Models

The Cr^{6+} removal kinetic date were obtained by CZVI–CS–PVA hydrogel adsorption performance were fitted to pseudo–first order (PFO) (Fig. 4.28(a)), pseudo–second order (PSO) (Fig. 4.28(b)), Elovich (Fig. 4.29(a)) and intra–particle diffusion (Fig. 4.29(b)) kinetic models to select the most appropriate kinetic equation. The obtained kinetic parameters, i.e., the coefficient of determination (R^2) and kinetic rate constant (k) are illustrated in Fig. 4.28 & 4.29. It was observed that the highest coefficient of determination (R^2 = 0.999) belongs to PSO kinetic model that appears to be the best fitted model with the experimental data of Cr^{6+} removal as compared to the rest of models which indicates that the adsorption of Cr^{6+} ions onto the CZVI–CS–PVA hydrogel was controlled by chemisorptions. This model assumes that the rate–limiting step is chemical sorption or chemosorption and predicts the behavior over the whole range of adsorption.

Elovich kinetic model is used to describes the chemical adsorption (chemical reaction) mechanism in nature during the adsorption processes. As seen from Fig. 29 (a), R^2 values is high (0.944) which also indicates that the adsorption process obeys Elovich kinetic model, however, these value is less than the results obtained from PSO kinetic model (0.999). When the kinetic data was analyzed using intraparticle diffusion model, it was observed that the plot (Fig. 29 (b)) did not pass through the origin indicating that intraparticle diffusion was not the only rate–limiting step. This deviation from the origin reveals the existence of some boundary layer effect. The R^2 values are relatively high (0.94) which showed that the adsorption processes fairly obeyed the intraparticle diffusion model, however, it was not the sole rate–determining step.

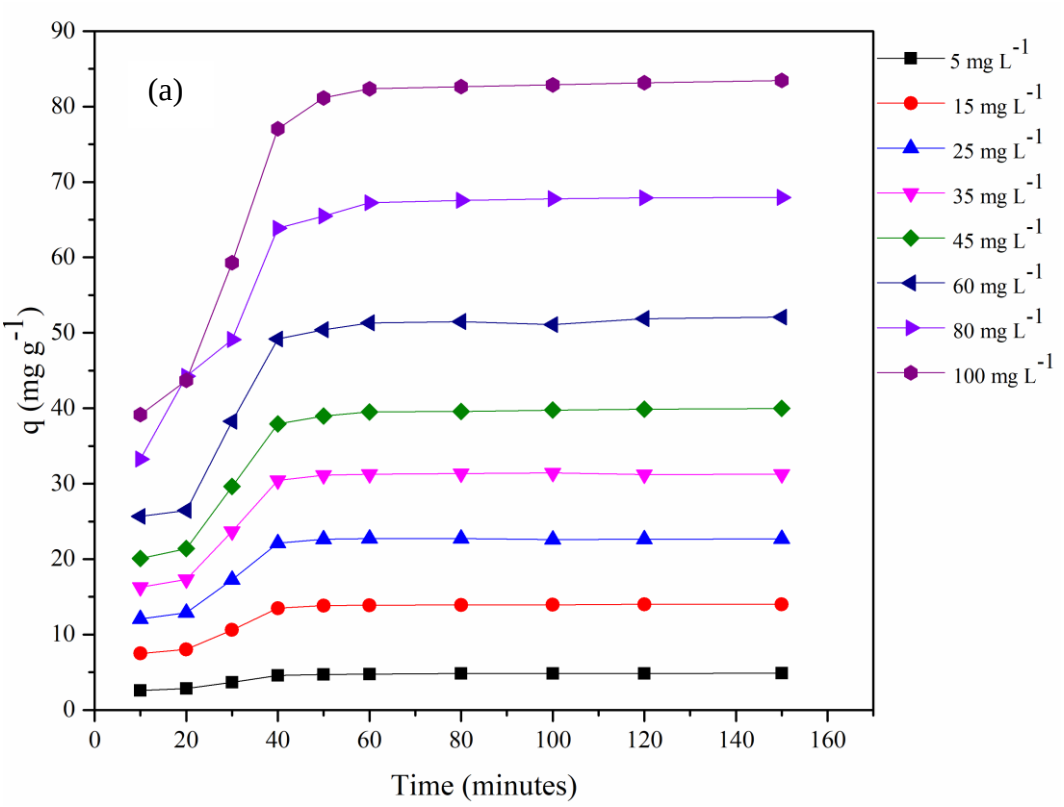

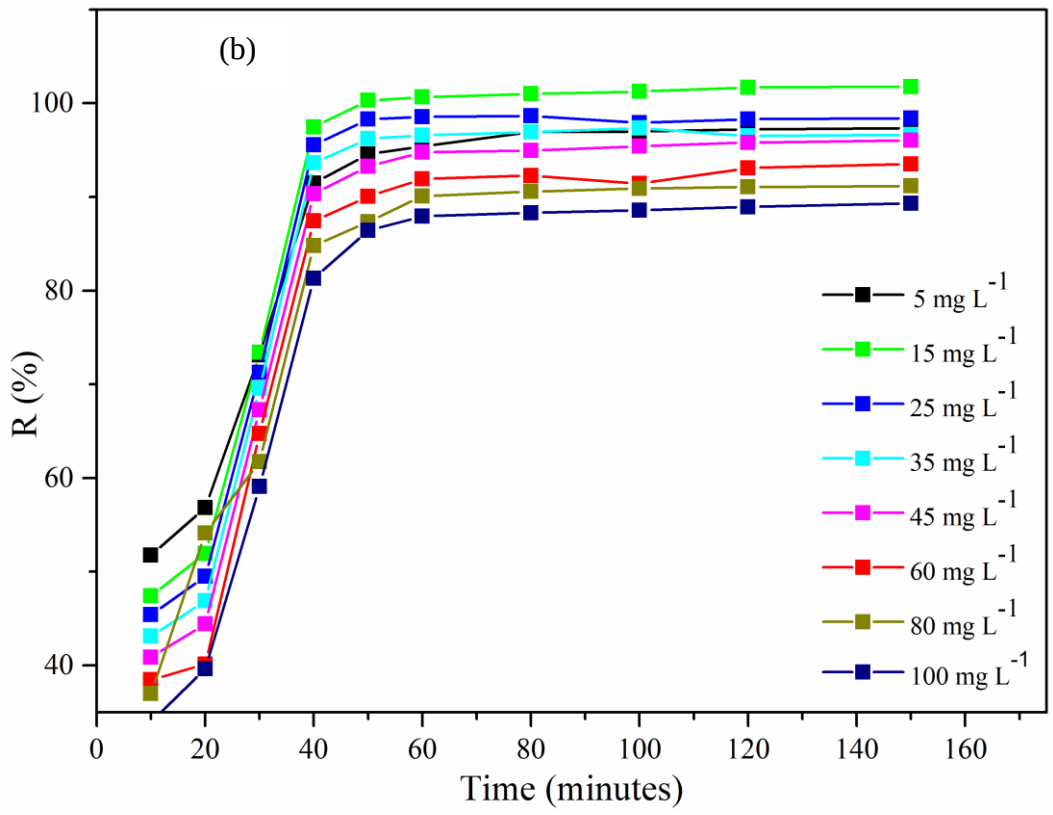

Fig.4. 26 Effect of Cr^{6+} initial concentration and time: a) q (mg g^{-1}); b) R (%).

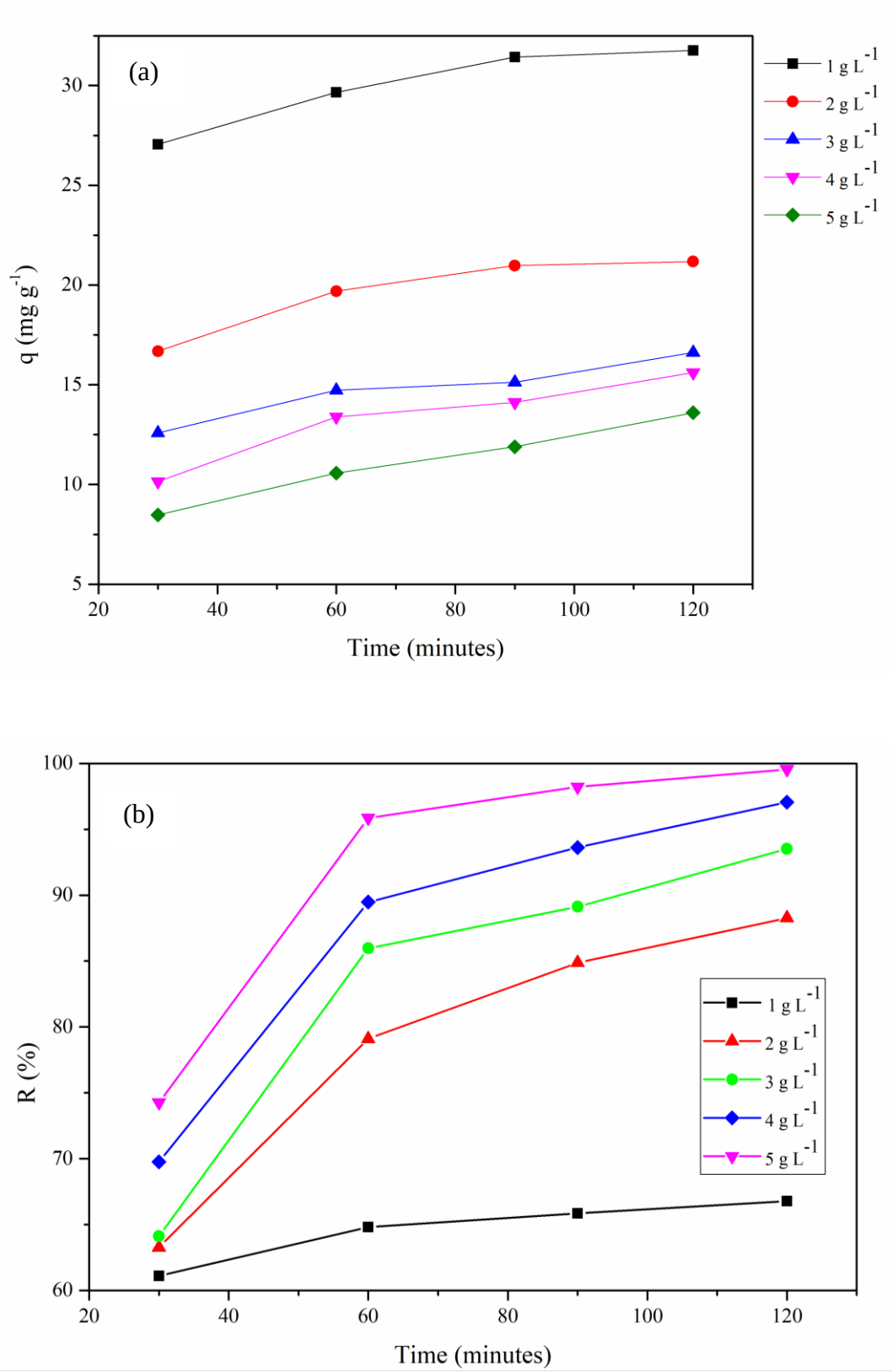

Fig.4. 27 Effect of hydrogel dose: a) q; b) R (%).

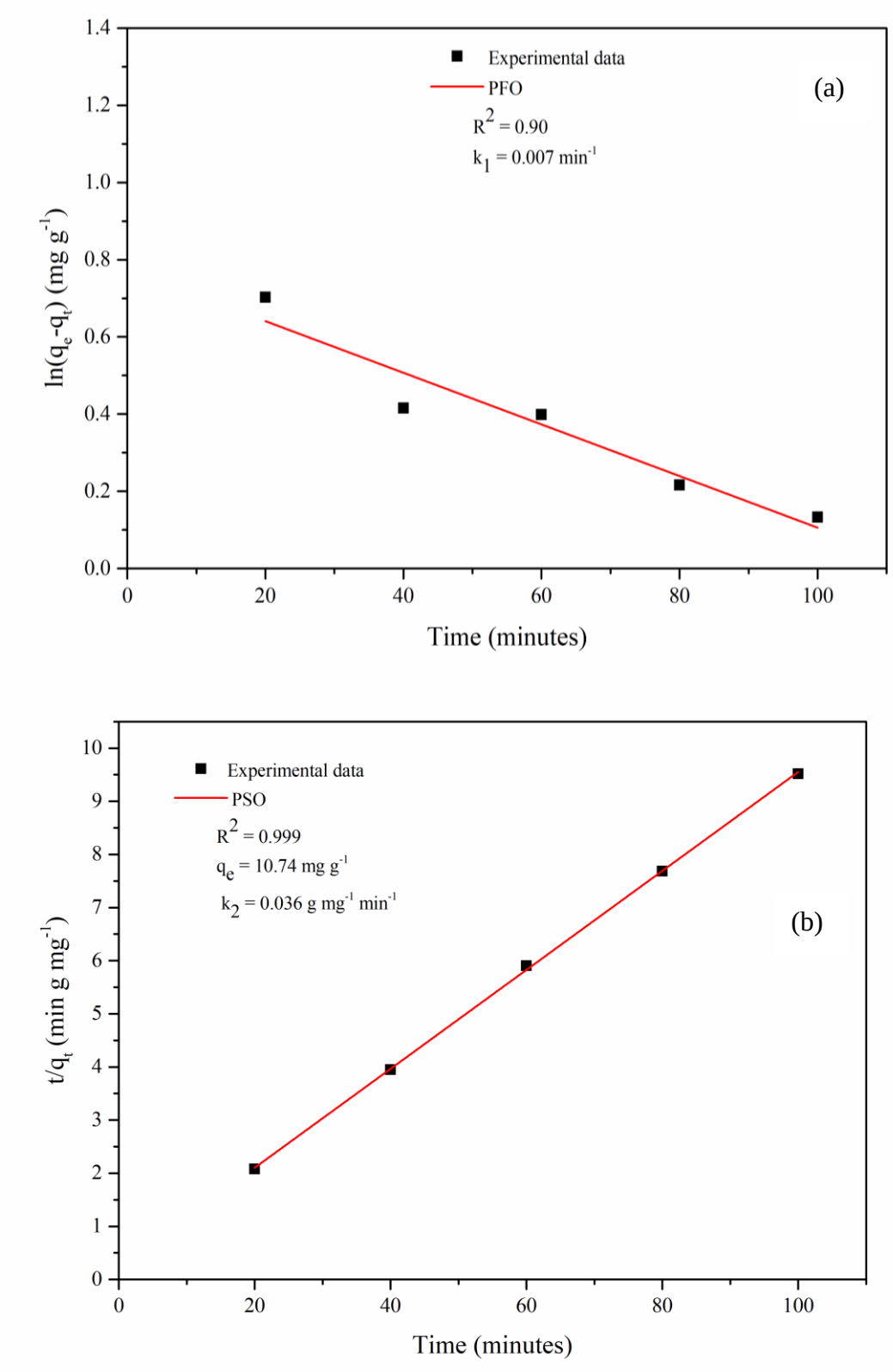

Fig.4. 28 Kinetic models: a) PFO; b) PSO

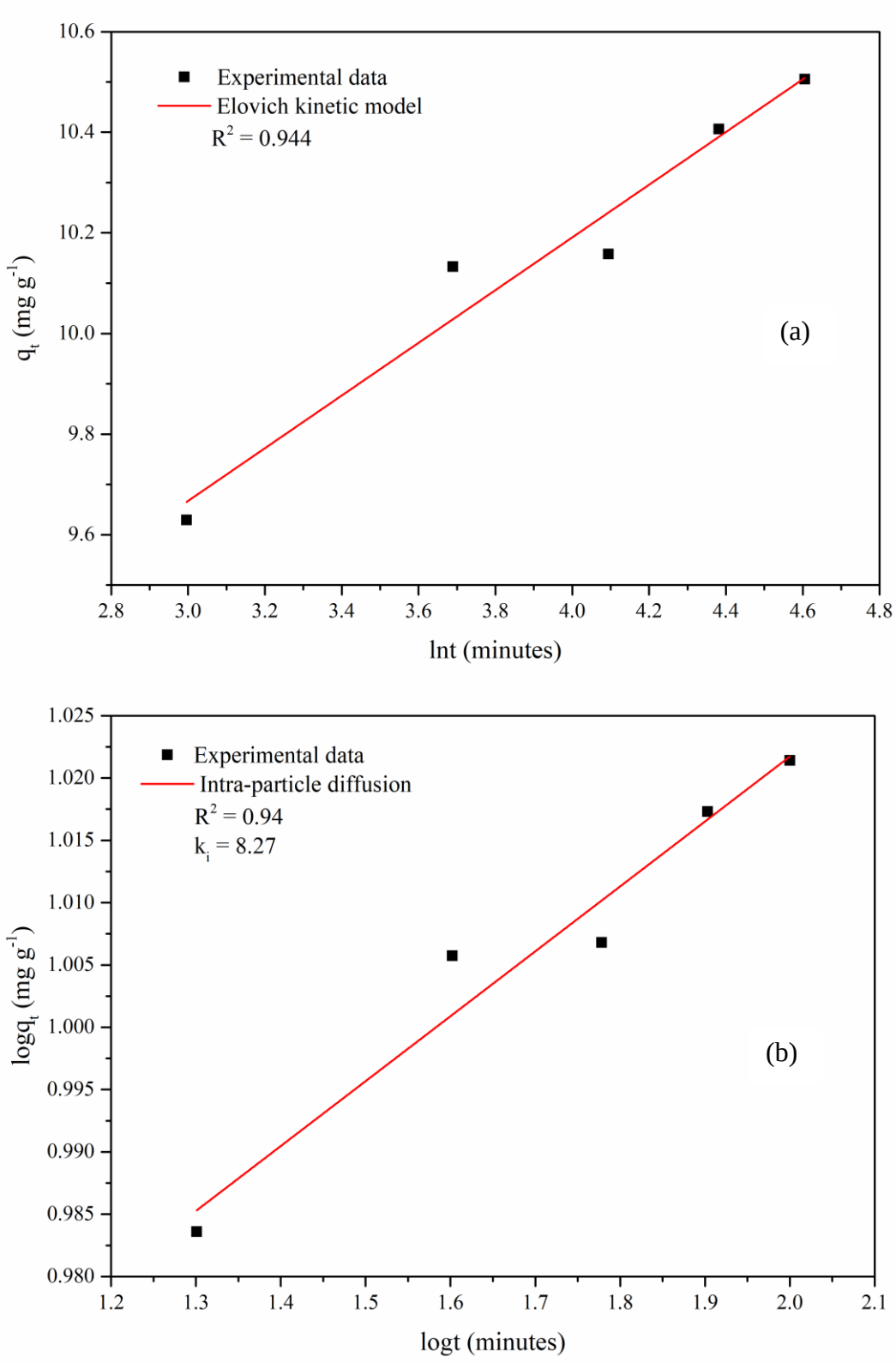

Fig.4. 29 Kinetic models: a) Elovich; b) Intra–particle diffusion.

4.7.3. Adsorption Isotherm Models

i. Langmuir and Freundlich isotherm

The Langmuir isotherm is used to describe the equilibrium between adsorbate and adsorbent system, where the adsorbate adsorption is limited to one molecular layer at or before a relative pressure of unity is reached. Although the isotherm initially proposed by Langmuir in 1918 is generally suitable for describing the chemisorption process when ionic or covalent chemical bonds are formed between the adsorbent and the adsorbate, the equation is obeyed in many systems with moderately low coverage and can be easily extended to describe the behavior of the binary adsorption system. The values of Langmuir and Freundlich constants were obtained from linear fits of the sorption data and shown in Fig. 4.30. Adequate linear correlations was observed for Langmuir isotherm models (Fig. 4.30 (a)). The adsorption capacities (q_{max}) of Cr^{6+} for CZVI–CS–PVA hydrogel adsorbent have been evaluated to be 15.86 mg g^{-1}. The separation factor (R_L) calculated form the Langmuir constant (b) is 0.2, which shows favorability of adsorption of Cr^{6+} onto the CZVI–CS–PVA hydrogel surfaces.

The Freundlich isotherm is employed for non – ideal adsorption that takes place on heterogeneous solid surfaces with non – equivalent and/or independent binding sites as well as for description of multilayer adsorption with interaction between adsorbed molecules. The value of Freundlich constant (1/n) reflects sorption linearity, and it usually varies between zero and one. The corresponding values obtained from linear regression (Fig. 4.30((b)) indicate that sorption is nonlinear, which is a typical behavior for surfaces with fixed and limited sorption capacities. A typical plot of Freundlich isotherm (Fig. 4.30(b)) shows the values of n, and the value of n gives an indication of the favorability and capacity of the adsorbent/adsorbate system. For $1/n < 1$, adsorption process with chemical interaction is suggested. But if the value of 1/n (adsorption intensity) is above 1, then it is an indication of the cooperative process. As we can see from the plot, the value of 1/n is greater than one suggesting a cooperative adsorption processes.

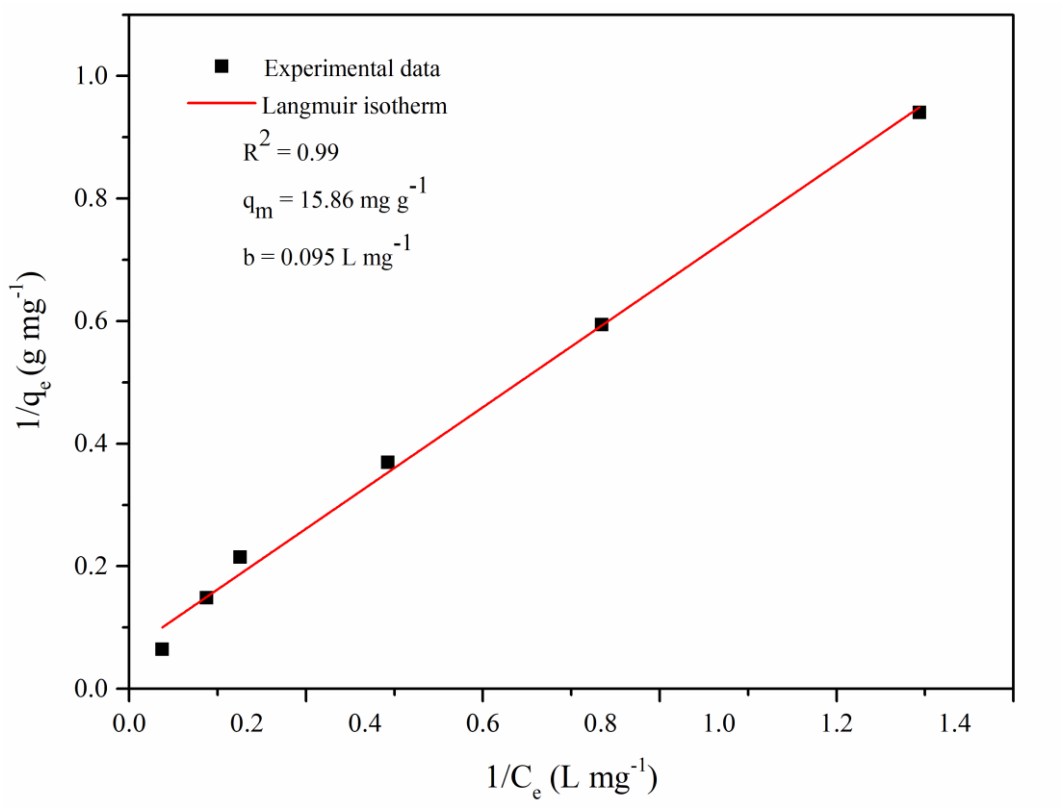

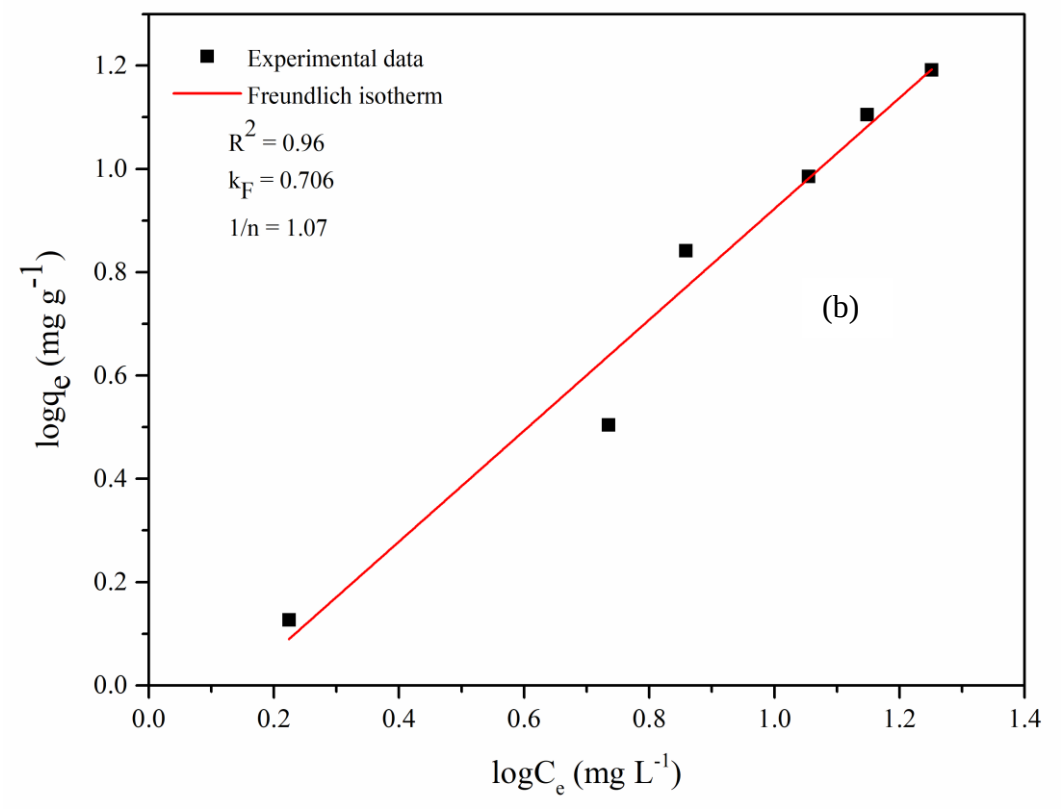

Fig.4. 30 Isotherm models: a) Langmuir; b) Freundlich

4.8. Removal of Pb^{2+} and Cd^{2+} Ions by PCCFG Hydrogel

4.8.1. Effect of Adsorption Parameters

i. Zeta Potential and Effect of pH

As shown in Fig. 4.31(a), the zero charge point (pHzcp) of PCCFG hydrogel was at pH 1.8. The nitrogen atoms of amine functional group of chitosan of PCCFG were protonated in the presence of H^+ at lower pH, which makes the surface of PCCFG positively charged and create repulsion with P^{b2+} those reducing adsorption. Zeta potential of chitosan was positive at lower pH (3–7) and negative at higher pH (7–12). The zeta potential was negative at all pH values for GO due to the massive oxygen containing sites on its surface. The zeta potential of L–cysteine varies with pH. L–Cysteine is negatively charged due to the presence of carboxyl group at lower pH (<5) and positively charged due to the presence of ammonium group at higher pH (>5). As pH increase, the negative surface charge of PCCFG increased due to the presence of oxygen and carboxyl containing functional group. This allowed the surface to interact with Pb^{2+} and Cd^{2+} by electrostatic attraction, thereby improving the adsorption performance of the PCCFG hydrogel.

The effects of initial solution pH on adsorption of Pb^{2+} and Cd^{2+} by PCCFG hydrogel was investigated in the pH range of 1–8 and the results are shown in Fig. 4.31(b). It can be seen from the figure that adsorption of Pb^{2+} and Cd^{2+} increases with increasing solution pH up to a pH of 5. Protonation of the amine functional group and oxygen containing functional groups at low pH ($pH< pH_{zcp}$) result in a large amount of H^+. Therefore, the low adsorption capacity (q) and removal efficiency (R) at lower pH can be attributed to the competition of H_3O^+ or H^+ ions with Pb^{2+} and Cd^{2+} in the solution and repulsion of $Pb^{2+}$and Cd^{2+} and the protonated amine–amide functional group (Ahmad et al. 2017). The significant increases in adsorption efficiency from pH 3 to 5 can be related to the reduction in the amount of H^+ ions in the solution leading to weaker competition. Besides, when pH increased, the negative charges of the adsorbent and the active site increased, which enhanced the complexation between the hydrogel and Pb^{2+} and Cd^{2+} via electrostatic attraction and/or chelation. However, the adsorption efficiency was found to decrease beyond a pH of 5 even if the deprotonating of the hydrogel surface increased as Pb^{2+} and Cd^{2+} convert to a hydroxide form and precipitate (Moradi et al. 2017), eventually reducing the removal efficiency. Precipitation of Pb^{2+} and Cd^{2+} occurred when the pH value was greater than 6 and 8, respectively. Similar results were

reported previously (Afolabi et al., 2021). Hence, an initial pH of 5 was selected as an optimum condition for both sorption of Pb^{2+} and Cd^{2+}.

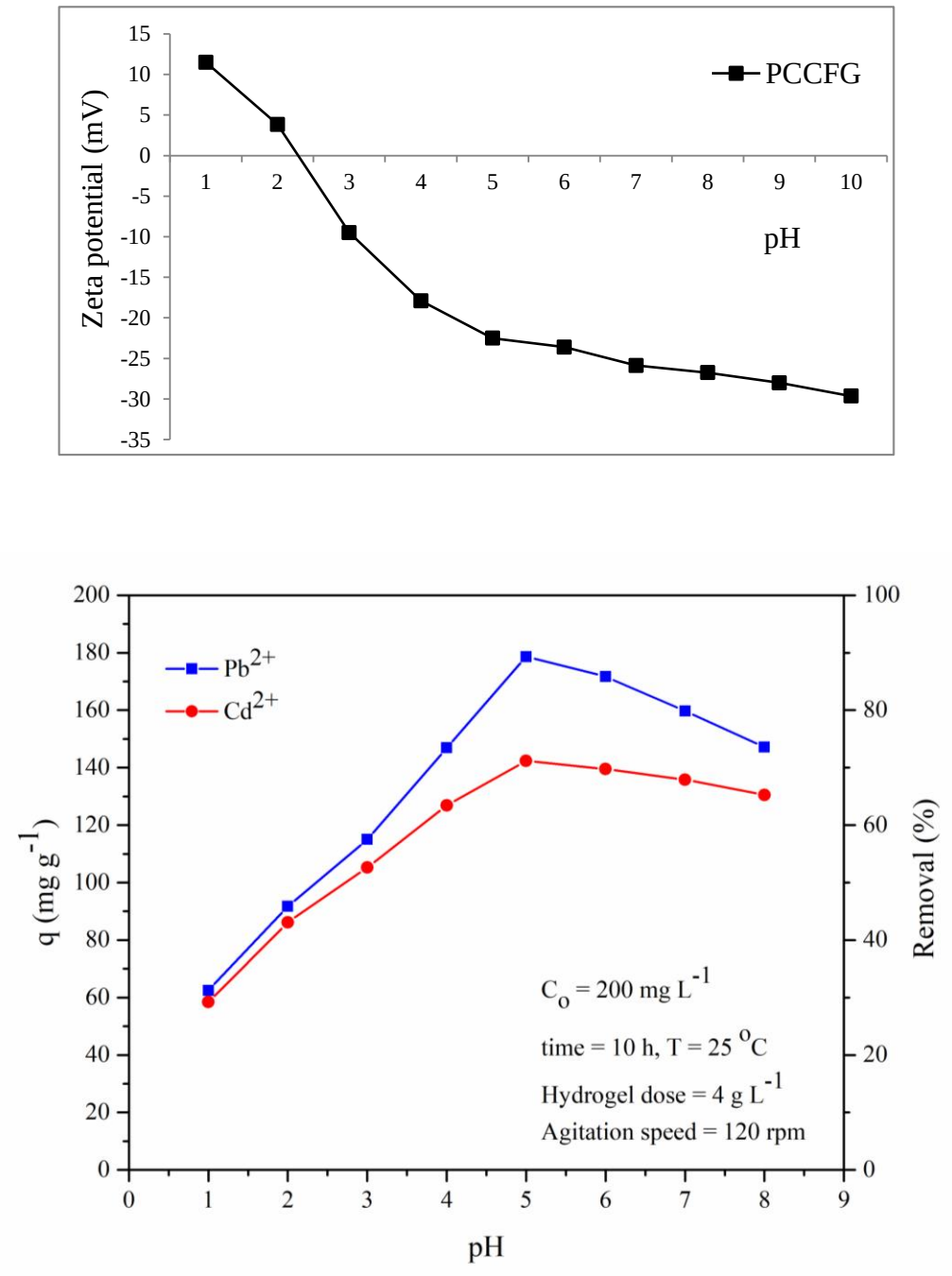

Fig.4. 31 a) Zeta potential; b) Adsorption capacity of PCCFG hydrogel at different pH. Mean of triplicate experimental data were used.

ii. Effect of Pb^{2+} and Cd^{2+} initial concentration

As depicted in Fig. 4.32(a), the removal efficiency (R %) of Pb^{2+} and Cd^{2+} by the hydrogel decreased with increasing concentration of both ions in the solution while the adsorption capacity (q) increased. Initially the removal efficiency was 97% for Pb^{2+} and 85% for Cd^{2+} at 50 mg l^{-1}, which decreased to 92% for Pb^{2+} and 81% for Cd^{2+} when the initial concentrations were increased to 200 mg l^{-1}. The adsorption capacity of the hydrogel increased sharply as the initial concentrations increased due to the availability of high amount of Pb^{2+} and Cd^{2+} in the solution, which has a higher concentration gradient. The adsorption capacity did not further increase beyond the 250 mg l^{-1} concentration increment. This might be related to overcrowding adsorbate at the surface of the adsorbent, which enhances mass transfer resistance and, hence, reduces the diffusion rate. The removal efficiency further decreased as the concentration of both ions in the solution increased, which might be related to quick saturation of the adsorption site and lack of enough space for additional adsorption. Thus, considering both adsorption capacity and removal efficiency, a concentration of 225 mg l^{-1} was chosen for adsorption experiments.

iii. Effect of PCCFG hydrogel dose

Adsorption capacity and removal efficiency of both Pb^{2+} and Cd^{2+} on to the PCCFG hydrogel were studied by varying the adsorbent dose from 1 to 8 g l^{-1} while keeping other adsorption parameters constant. As presented in Fig. 4.32(b), the adsorption capacity (q) of the hydrogel decreased as the hydrogel dose increased. However, the removal (R) increased as the hydrogel dose increased. The increases in removal efficiency as the hydrogel dose increased were attributed to availability of more adsorption sites. The higher adsorbent dose provided more chelating active sites and the metal ions got a higher probability of adsorption, which resulted in higher removal of the metal ions from the solution. The adsorption capacity decreased sharply while removal increased as the dose was increased from 1 to 5 g l^{-1}. As the dose increased further to 8 g l^{-1}, the adsorption capacity decreased slowly and the removal efficiency was almost constant. This may be due to the pore space in the PCCFG becoming completely occupied by Pb^{2+} or Cd^{2+}, and the active sites ($–NH_2$, –SH, –OH, and –COOH) were saturated. Thus, considering both the adsorption capacity and removal efficiency, 2 g l^{-1} of hydrogel dose was optimum for Pb^{2+} and Cd^{2+} sorption.

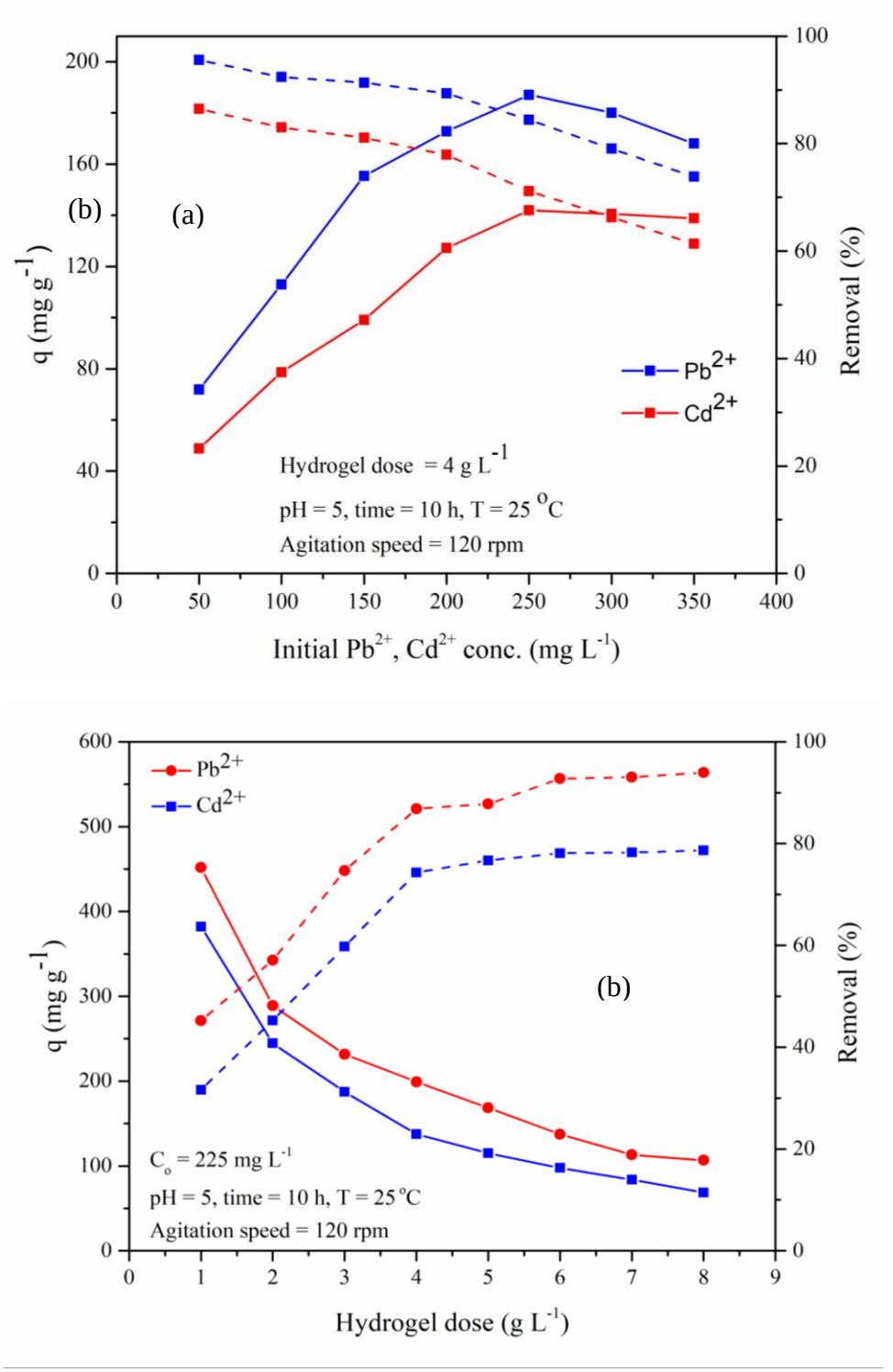

Fig.4. 32 a) effect of initial Pb^{2+} and Cd^{2+} concentration; b) effect of hydrogel dose on adsorption capacity and removal efficiency of PCCFG hydrogel. Mean of triplicate experimental data were used.

iv. Effect of time

As illustrated in Fig. 4.33, the adsorption capacity (q) and removal efficiency (R) of both Pb^{2+} and Cd^{2+} increased sharply as time increased in the first 40 min of adsorption and remained nearly constant as time further elapsed. Generally, the adsorption phenomena involve transportation of metal ions from bulk solution to the adsorbent surface followed by diffusion into pores. The adsorption capacity and removal efficiency were fast during the first 20 min, which can be attributed to availability of plenty of active sites and external surface adsorption. Moreover, the adsorption capacity and removal efficiency increased as the adsorption time increased from 20 to 40 min, which is attributed to availability of abundant adsorption sites and less mass transfer resistance in the internal pores of the adsorbent hydrogel. The maximum removal efficiencies of 90% and 86% were obtained within 40 min for Pb^{2+} and Cd^{2+}, respectively. After 40 min of adsorption time, both adsorption capacity and removal efficiency for both metal ions reached equilibrium, which might be related to saturation of active sites, and increases in mass transfer resistance as the metal ions accumulated at the adsorbent–solution boundary.

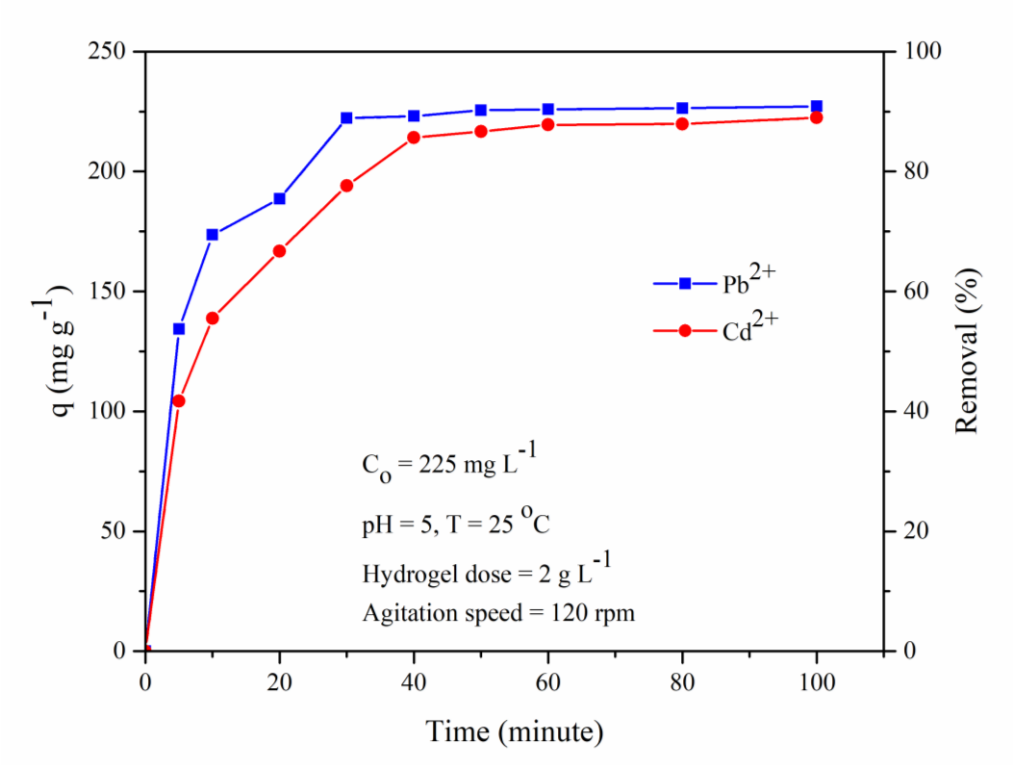

Fig.4. 33 Effect of time on adsorption capacity and removal of PCCFG hydrogel.

v. Effect of temperature and adsorption thermodynamics

The adsorption capacity as well as the removal efficiency of metal ions were also influenced by temperature. The effect of temperature on adsorption performance of PCCFG hydrogel towards Pb^{2+} and Cd^{2+} was studied at 25, 30, and 45°C while keeping other adsorption parameters constant (C_o = 100 mg l^{-1}, pH = 2, t = 120 minutes, hydrogel dose = 3 g l^{-1}). As shown in Fig. 4.34(a), both the adsorption capacity and removal efficiency increased slightly as temperature increased, which is, suggesting endothermic processes (Ali et al. 2016; Yana Bagbi et al. 2017). In the case of Chemisorption, the adsorption increases as temperature increases as the adsorbate molecules gain energy higher than the activation energy (Ren, Wei, and Zhang 2008). Thus, adsorption capacity increases as temperature increases (Yuvaraja et al. 2019). The adsorption capacity as well as the removal efficiency increased slightly during the first course of temperature increases from 25°C to 35°C. As temperature was raised further from 35°C to 45°C, the intensity of adsorption and removal efficiency showed less increment because the increases in temperature increased the energy of the metal ions adsorbed and hence enhanced the rate of desorption.

As presented in Table 4.12, the value of ΔG° is negative, showing the spontaneity of the reaction (electron exchange or ion exchange) between the metal ions and electron reach atoms (–N, –S, –O). These value increased as temperature increased, indicating the adsorption of both Pb^{2+} and Cd^{2+} onto the hydrogel was more favorable at higher temperature. The positive enthalpy change demonstrates that the interaction between the adsorbent and adsorbate is endothermic in nature, that is, the adsorption reaction consumes energy. The positive ΔS° indicates the interaction between the system (PCCFG and the metal ions) and surrounding environment were spontaneous in nature. Moreover, the positive ΔS° shows the strong affinity of PCCFG towards the Pb^{2+} and Cd^{2+}, and the increased randomness at the solution–PCCFG interfaces during the adsorption of both metal ions. The Pb^{2+} has better affinity and less spontaneity than Cd^{2+} due to the fact that Pb^{2+} can form more stable complexes with anionic molecules (those containing –N, –S, and –P ligands) (Town & Filella, 2002).

Table 4.12 Thermodynamic parameters for adsorption of Pb^{2+} and Cd^{2+} on to PCCFG adsorbents

Temp.	Heavy metal ion	ΔH° (kJ mol^{-1})	ΔS° (J mol^{-1} K^{-1})	ΔG° (kJ mol^{-1})
25°C	Pb^{2+}	11.23	41.57	-1.16
	Cd^{2+}	8.02	33.25	-1.89
35°C	Pb^{2+}	11.23	41.57	-1.57
	Cd^{2+}	8.02	33.25	-2.22
45°C	Pb^{2+}	11.23	41.57	-1.99
	Cd^{2+}	8.02	33.25	-2.55

vi. Effect of competing ions

The effect of competing ions was studied in batch adsorption experiments in the solution containing the three metal ions (Pb^{2+}, Cd^{2+}, and Cu^{2+}) using PCCFG hydrogel as the adsorbent. The competitive (q_{mm}) and single (q_{ms}) adsorption capacity of the hydrogel towards the metal ions were calculated and compared. As depicted in Fig. 4.34(b), the PCCFG hydrogel adsorbents could effectively adsorb all three metal ions in the solution simultaneously, showing higher selectivity towards Pb^{2+}. The adsorption capacity of the hydrogel towards single metal ions decreased in a competitive adsorption ($q_{mm} < q_{ms}$) system. This indicates that the coexistence of metal ions in the solution inhibits the adsorption capacity of the hydrogel compared to solutions containing a single metal ion.

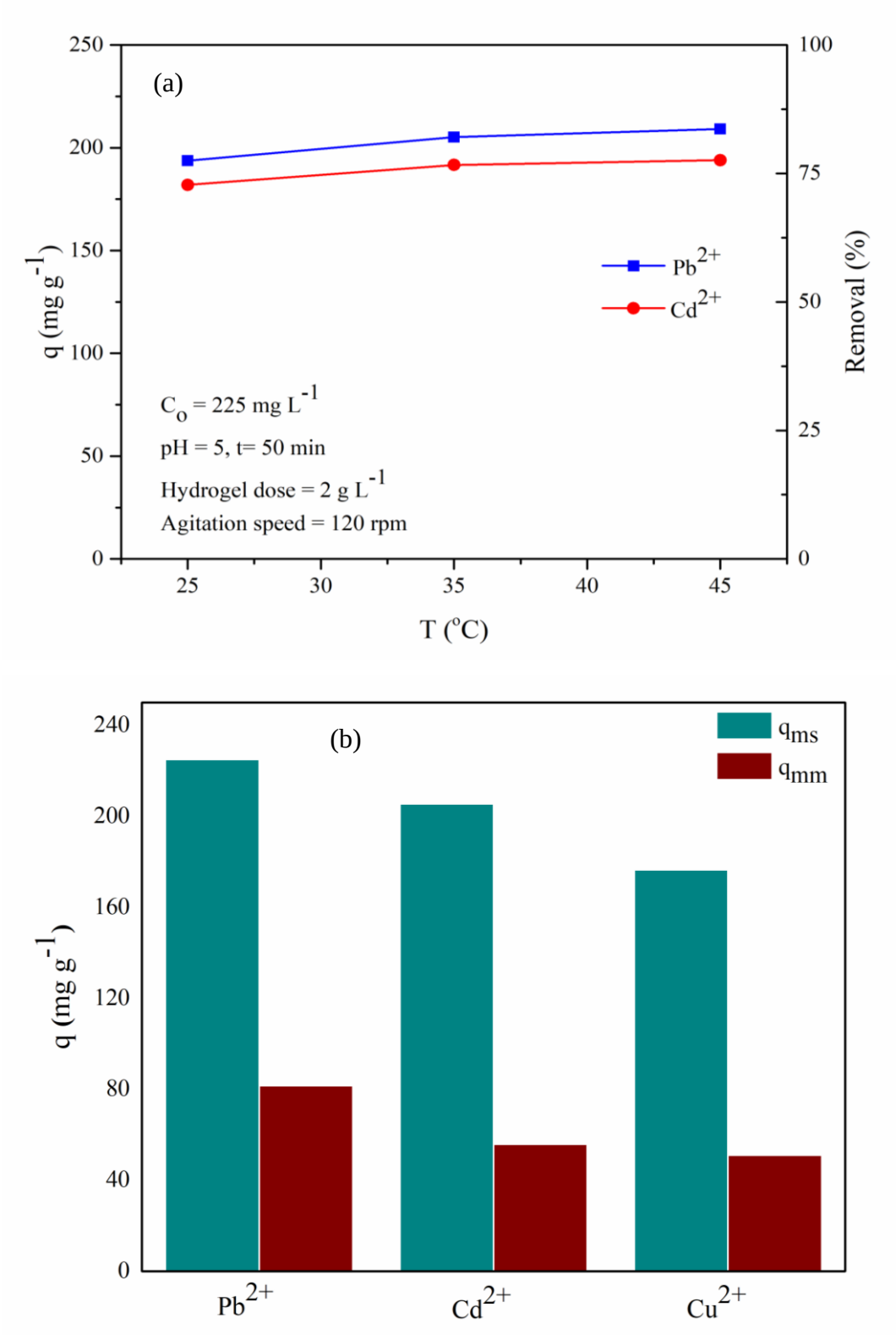

Fig.4. 34 Effect of: a) temperature; b) competing ions (T = 25°C). Adsorption condition, pH = 5, C_o = 225mg l^{-1}, t = 50 min, hydrogel dose = 2g l^{-1}, agitation speed =120rpm).

4.8.2. Adsorption Kinetic Models

i. Pseudo–first order

Fig. 4. 35(a) depicts the PFO kinetic model obtained for adsorption of both Pb^{2+} and Cd^{2+} by PCCFG hydrogel adsorbents. The calculated value of R^2 (Table 4.13) is high but relatively less than the results obtained from PSO and Elovich; there exist a good agreement between q_e (calculated) and q_e (theoretical) for both Pb^{2+} and Cd^{2+}. The rate constant of adsorption (k_1, min^{-1}) of Cd^{2+} is higher than that of Pb^{2+}, indicates more adsorption rate and spontaneity of Cd^{2+} adsorption onto PCCFG, which is agree with thermodynamics properties of adsorption (Table 4.12).

Table 4.13 Summary of kinetic model parameters and coefficient of correlation

Model	Metal	$q_{e,exp.}$ (mg g^{-1})	$q_{e,calc.}$ (mg g^{-1})	Parameters	R^2
PFO	Pb^{2+}	224.36	232	k_1=0.09 min^{-1}	0.96
	Cd^{2+}	174.51	189	k_1=0.1 min^{-1}	0.92
PSO	Pb^{2+}	224.36	227	k_2=0.0004 g mg^{-1} min^{-1}	0.99
	Cd^{2+}	174.51	179	k_2=0.001 g mg^{-1} min^{-1}	0.98
Elovich	Pb^{2+}	224.36	-	α=0.27mg g^{-1} min^{-1}, β=2.6 g mg^{-1}	0.98
	Cd^{2+}	174.51	-	α=0.35 mg g^{-1} min^{-1}, β=3.5g mg^{-1}	0.98

ii. Elovich

The plot of the Elovich kinetic model (Fig. 4.35(b)) and the calculated value of R^2 (Table 4.13) shows the experimental data correlated better with the Elovich model than for the PFO model, but not the PSO model. As seen from Table 4.13, R^2 is high (0.98) which also indicates that the adsorption process obeys Elovich kinetic model. The calculated value of initial adsorption rate (α) and desorption constant (β) (Table 4.13) for Cd^{2+} is higher than that for Pb^{2+}, which indicates that PCCFG hydrogel has less affinity but more spontaneity towards to Cd^{2+} than Pb^{2+}. This phenomenon is also agreed with the thermodynamics adsorption properties of Cd^{2+} and Pb^{2+} onto PCCFG (Table 4.12). This shows the adsorption–desorption of Cd^{2+} is higher and the PCCFG has weak affinity towards Cd^{2+} relative to Pb^{2+}.

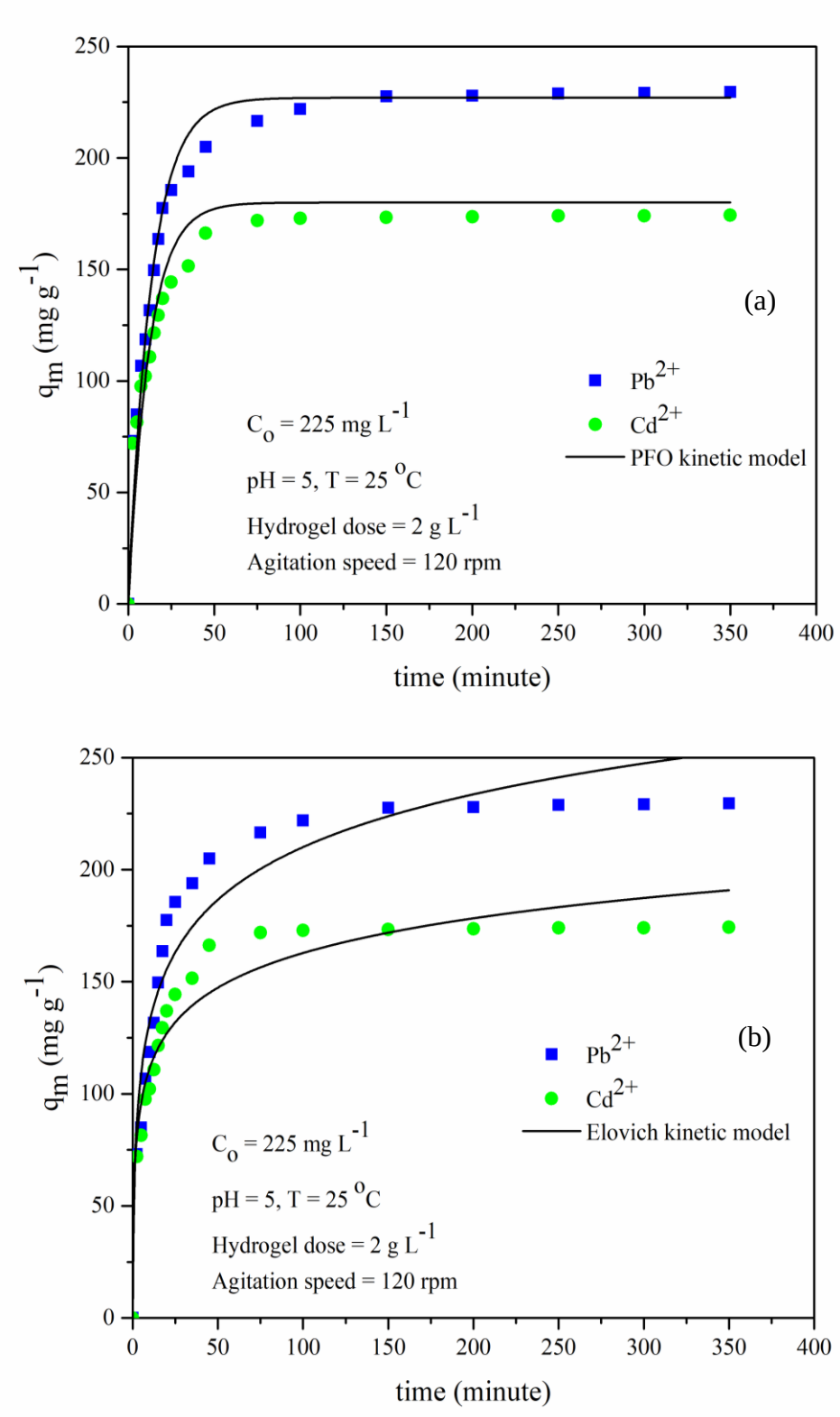

Fig.4. 35 a) PFO; b) Elovich kinetic model for adsorption of Pb^{2+} and Cd^{2+} onto PCCFG hydrogel.

iii. Pseudo–second order

Fig. 4.36 illustrates the PSO kinetic model obtained for adsorption of both Pb^{2+} and Cd^{2+} by PCCFG hydrogel adsorbents. As presented in Table 4.13, the numerical value of R^2 for adsorption of both Pb^{2+} and Cd^{2+} or the PSO model is higher than those for the PFO and Elovich kinetic models. Besides, the calculated values of q_e ($q_{e,calc.}$) (Table 4.13) from the PSO kinetic model for both metal ions were closer to the experimental q_e ($q_{e,\ exp.}$). This clearly shows that the PSO correlated with experimental data better than the PFO and Elovich models. These results show that Chemisorption is the rate–limiting step during the adsorption processes of Pb^{2+} and Cd^{2+} onto the PCCFG. Similar results were reported in the literature (Yana Bagbi et al. 2017; Yuvaraja et al. 2019). These phenomena describe the strong coordinate covalent bond formation between heavy metal ions (Pb^{2+} and Cd^{2+}) and functional groups (–NH_2, –SH, –COOH) of PCCFG via the soft–Lewis acid–base interaction. Furthermore, the calculated values of k_2 of Cd^{2+} were greater than k_2 of Pb^{2+}, which indicate Cd^{2+} has higher Columbus forces than Pb^{2+} towards the PCCFG hydrogel surfaces (Hokkanen, Repo, and Sillanpää 2013).

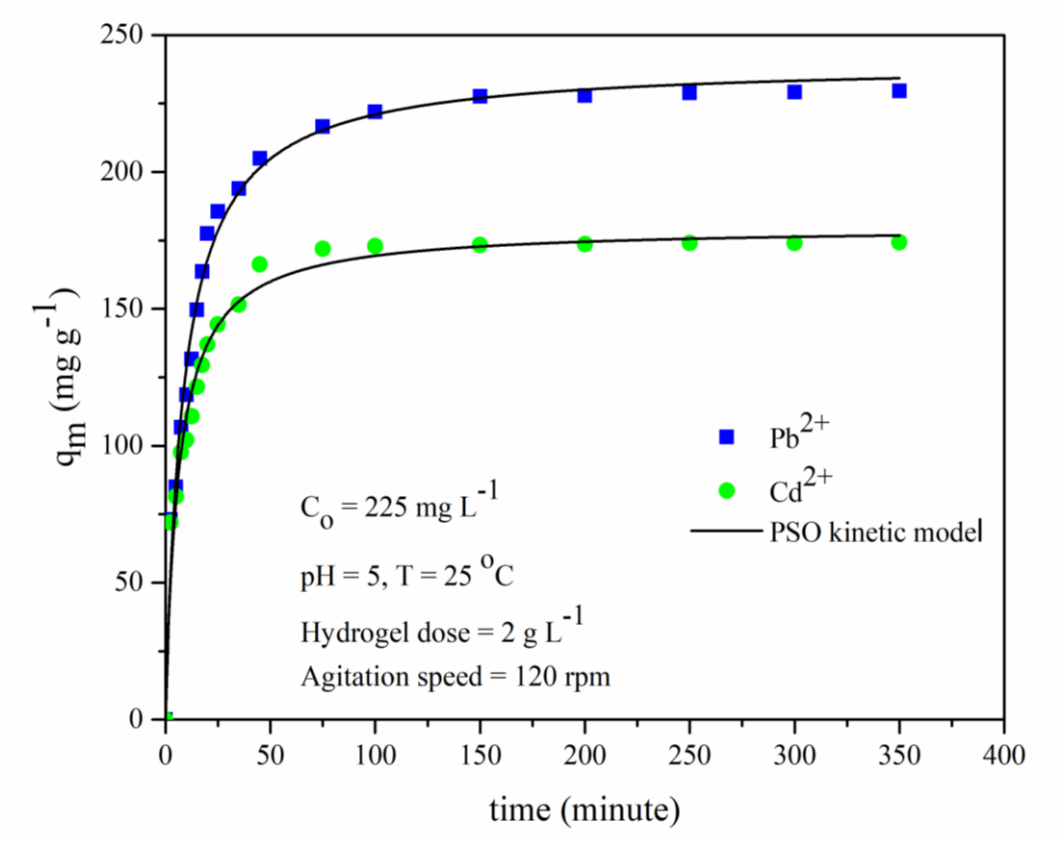

Fig.4. 36 PSO kinetic model for adsorption of Pb^{2+} and Cd^{2+} onto PCCFG hydrogel.

4.8.3. Adsorption Isotherm Models

i. Langmuir

The experimental data of both Pb^{2+} and Cd^{2+} adsorption on to the hydrogel were well described by the Langmuir isotherm (Fig. 4.37(a). The coefficient of determination (R^2) of Langmuir for both metal ions is higher than the R^2 of Freundlich, Temkin, and D–R isotherms (Table 4.14), which indicates the experimental data correlated well with the Langmuir isotherm. As illustrated in Table 4.14, the maximum adsorption capacity (q_m) of the PCCFG hydrogel at 298K was 250 and 192 mg g^{-1} for Pb^{2+} and Cd^{2+}, respectively, which is close to the experimental q_m. The observed values of q_m for Pb^{2+} are higher than the q_m of Cd^{2+}, which indicates the hydrogel has more affinity towards Pb^{2+} as illustrated with positive change in entropy. The calculated values of R_L were 0.043 for Pb^{2+} and 0.034 for Cd^{2+} at the initial concentration of 225 mg l^{-1}, which show favorable adsorption of both Pb^{2+} and Cd^{2+} onto the PCCFG hydrogel adsorbent.

Table 4.14 Summary of isotherm model parameters and coefficient of correlation.

Isotherms	Heavy metal ions	Parameters	R^2
Langmuir	Pb^{2+}	q_m = 250 mg g^{-1}, k = 0.099 L mg^{-1}	0.980
	Cd^{2+}	q_m = 192 mg g^{-1}, k = 0.128 L mg^{-1}	0.98
Freundlich	Pb^{2+}	K_F = 17.30 L g^{-1}, n = 2.03	0.97
	Cd^{2+}	K_F =17.06 L g^{-1} , n = 2.40	0.98
Temkin	Pb^{2+}	K_T = 1.01 L mol^{-1}, b = 49.60 kJ/mol	0.97
	Cd^{2+}	K_T = 1.16 L mol^{-1} , b = 56.75 kJ/mol	0.97
D – R	Pb^{2+}	q_s = 135.7 mg g^{-1}, E = 13.9 kJ mol^{-1}	0.88
	Cd^{2+}	q_s = 125.5 mg g^{-1}, E = 14.3 kJ mol^{-1}	0.88

ii. Freundlich

Fig. 4.37(b) shows the Freundlich isotherm obtained for adsorption of both Pb^{2+} and Cd^{2+} by PCCFG hydrogel adsorbents. The R^2 values are relatively high (0.97 for Pb^{2+} & 0.98 for Cd^{2+}) but less than the R^2 of Langmuir, which showed that the adsorption process fairly obeyed the assumption behind Freundlich isotherm model. The numerical values of n>1 (Table 4.14) for both Pb^{2+} and Cd^{2+} shows a favorable adsorption of both metal ions on to PCCFG hydrogel.

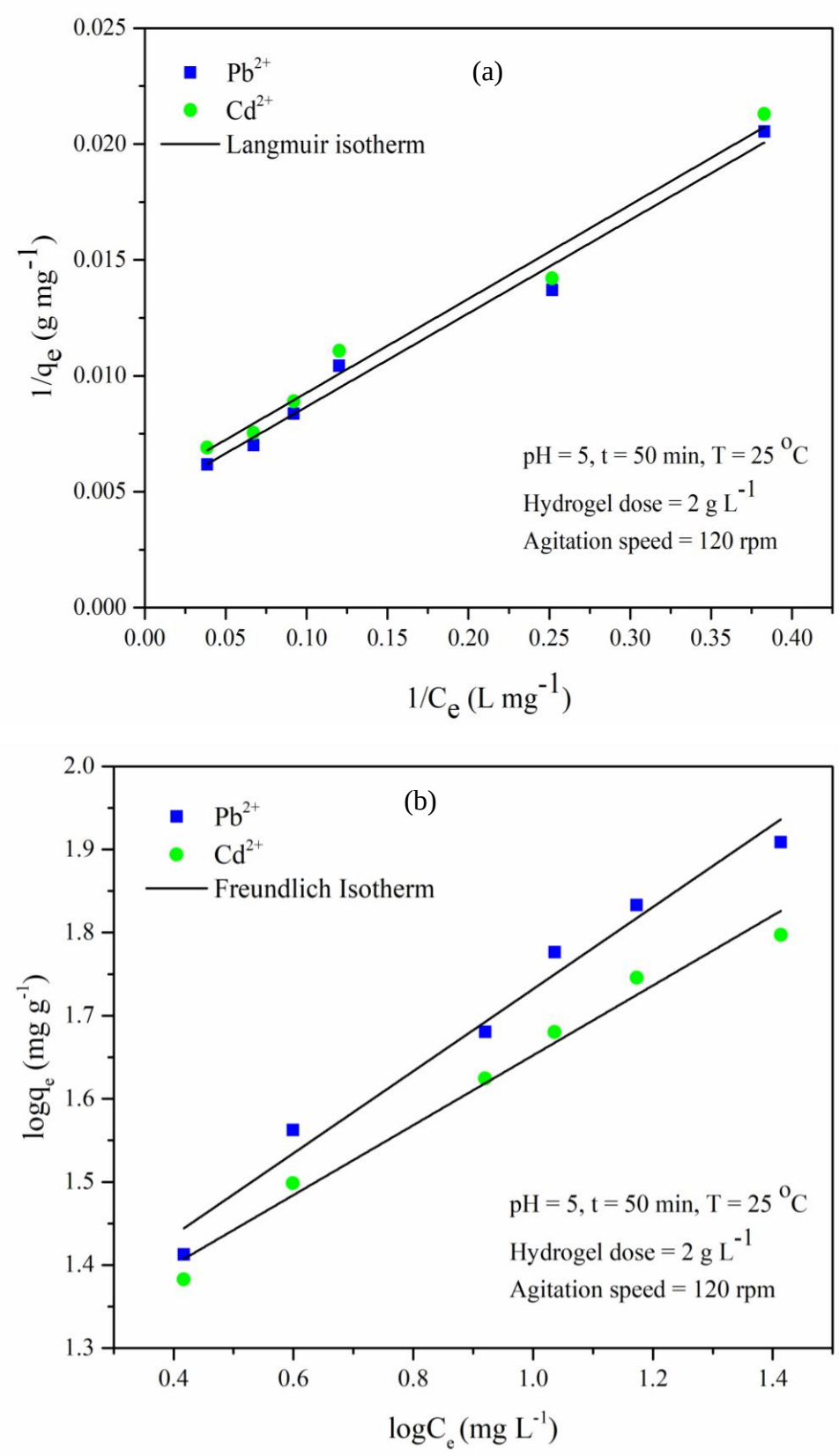

Fig.4. 37 a) Langmuir isotherm; b) Freundlich isotherm for adsorption of Pb^{2+} and Cd^{2+} on to PCCFG hydrogel.

iii. Temkin

The Temkin isotherm model assumes that adsorption free energy is dependent on the coverage of the adsorbent surface and it takes into account the adsorbents interaction with sorbate to be adsorbed. Fig. 4.38(a) shows the Temkin isotherm obtained for adsorption of both Pb^{2+} and Cd^{2+} by PCCFG hydrogel adsorbents. The R^2 values are relatively high (0.97) but less than the R^2 of Langmuir, which showed that the adsorption process fairly obeyed the assumption behind Temkin isotherm model. The higher values of Temkin constant (b = 49.6 kJ mol^{-1} for Pb^{2+} & 56.75 kJ mol^{-1} for Cd^{2+}), which is greater than 8 kJ mol^{-} revealed that the interaction between Pb^{2+} and Cd^{2+}, and PCCFG was strong. The numerical values of adsorption heat constant (RT/b) were 49.95 and 43.66 kJ mol^{-1} for Pb^{2+} and Cd^{2+}, respectively. These values of RT/b>0 for both Pb^{2+} and Cd^{2+} indicate that the adsorption of both metal ions on to PCCFG are endothermic processes. These observations are also supported by the positive enthalpy changes (Table 4.12).

iv. Dubinin–Radushkevich (D–R)

The main feature of this approach is related to the fact that the sorption capacity depends on the adsorbed amount on the surface of the material, differently from Langmuir model. To further understand the nature of the adsorption mechanism (chemisorption or physisorption) of Pb^{2+} and Cd^{2+} onto PCCFG, experimental data were also fitted to the D–R model. The correlated experimental data of the D–R model are depicted in Fig. 4.38 (b). The R^2 values are relatively high (0.88) but less than the R^2 of other isotherm model, which showed that the adsorption process fairly obeyed the assumption behind D–R isotherm model. As presented in Table 4.14, the calculated values of free energy of adsorption (E) are 13.9 and 14.03 kJ mol^{-1} for Pb^{2+} and Cd^{2+}, respectively. These values are in the range of 8–16 kJ mol^{-1}, showing that the adsorption of both metal ions onto the hydrogel were somewhat chemical processes. However, the experimental data was not fully explained by with model with respect to Langmuir isotherm that emphasize on physical adsorption.

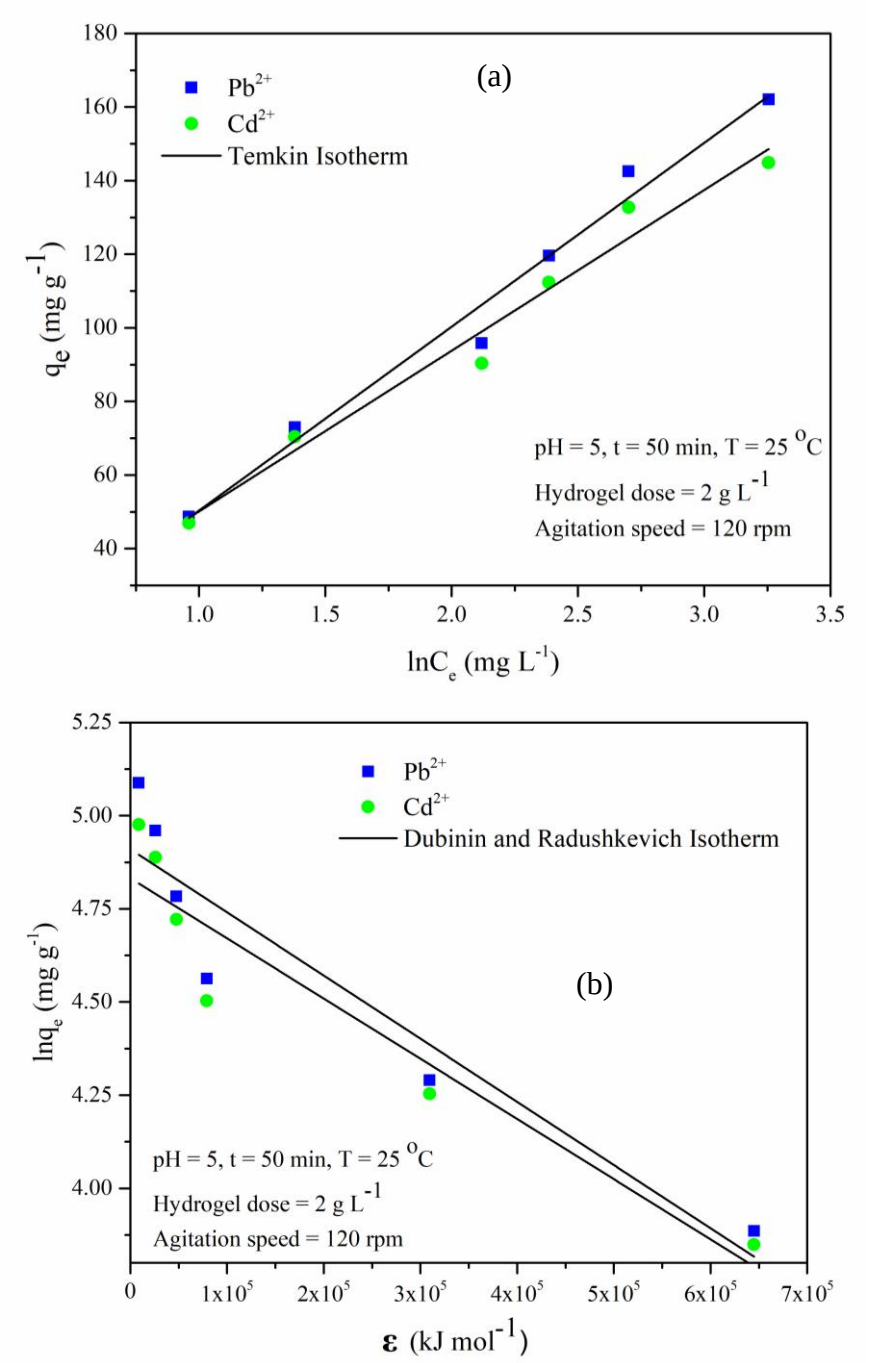

Fig.4. 38 a) Temkin; b) Dubinin and Radushkevich (D-R) isotherm for adsorption of Pb^{2+} and Cd^{2+} on to PCCFG hydrogel.

4.8.4. Theoretical Adsorption Mechanism Studies of Pb^{2+} onto PCCFG Hydrogel

i. Geometry and structural analysis

The geometrical structures of PCCFG–I built by Gauss View 6.0.16 were fist optimized by molecular mechanics (MM) method with UFF. Then geometrical structures were optimized before Pb^{2+} adsorption (a *spin restricted* model: closed shell modeling system) and after Pb^{2+} adsorption (a *spin unrestricted* model: open shell modeling system) thoroughly using DFT/B3PW91–D3 at the 6-31G(d)/SDD level. The optimization completed with convergence and stationary point found on PES (Annex 11 & 19). The +ve frequency of both converged PCCFG–I and PCCFG–I@Pb^{2+} shows that the structures are at local minima on PES (Annex 17 & 20). As shown in Fig. 4.39 (a&b), the bond distance of adsorption site (–NH_2) of PCCFG–I were changed after the adsorption of Pb^{2+}. It was observed that PCCFG tends to chelate with Pb^{2+} through a mono–denate nitrogen atom ligand with binding energy of –62.33 kcal mol^{-1} and bond distance (Pb–N) of 2.159Å (Annex 13 & 14). DFT simulation results shows that the coordination binding between Pb^{2+} and N of amine occurs.

PCCFG–I have an even number of electrons divided into pairs of opposite spin hence calculations on closed shell systems were used (Fig. 4.40(a)). Closed shell systems uses a *spin-restricted* model assumes that all molecular orbital's are doubly occupied, each containing two electrons of opposite spin (force each electron pair into a single spatial orbital). In contrast, PCCFG–I@Pb^{2+} were modeled by a *spin unrestricted*, which separate spatial orbital's for the spin up and spin down electrons, known as α and β orbital's (Fig. 4.40(b)), respectively. The illustration in Fig. 4.40(b) depicts orbital's from open shell system (PCCFG–I@Pb^{2+}). The diagram shows the unpaired electron in orbital 117α.

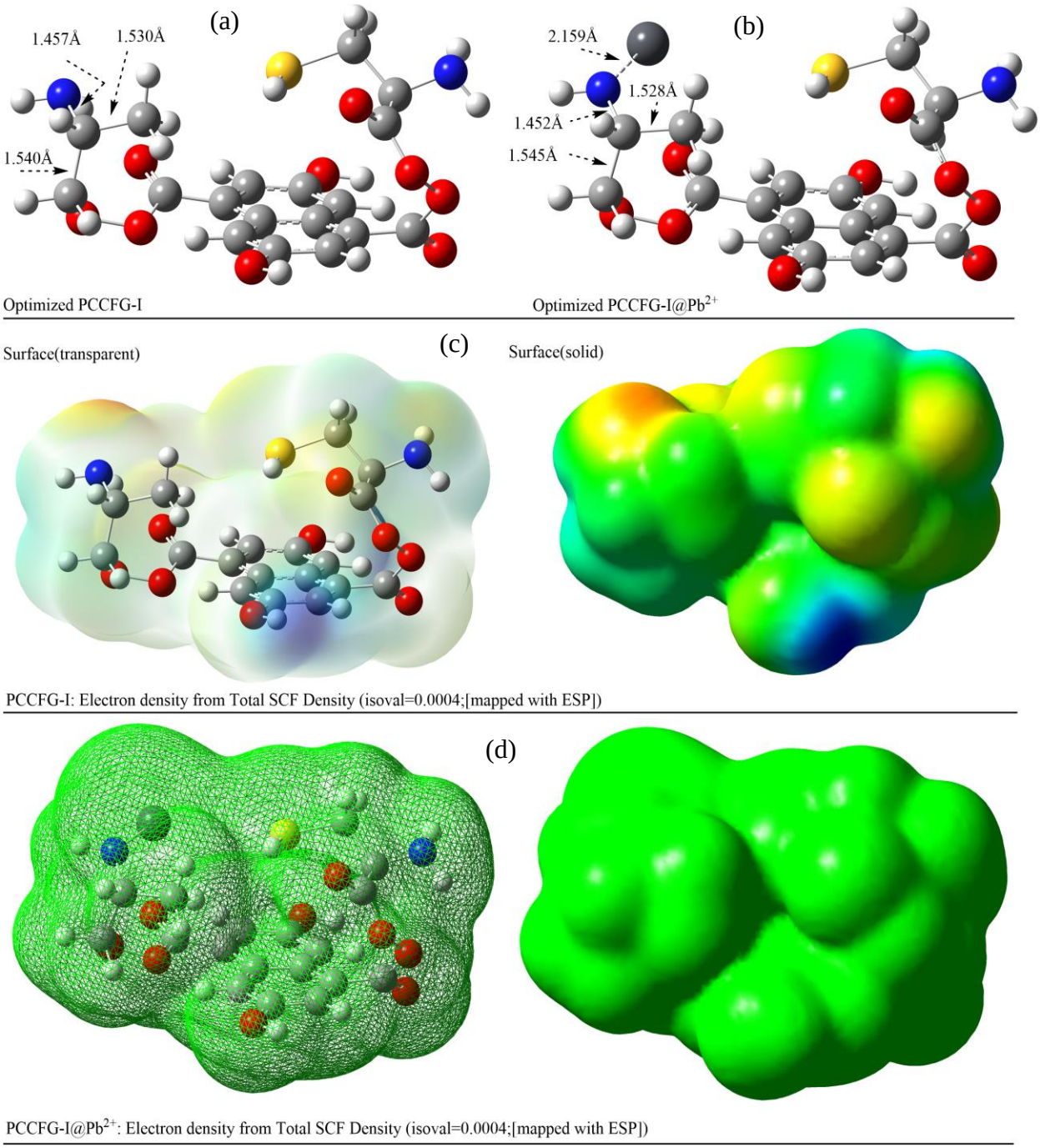

Fig.4. 39 Representation of: a) optimized PCCFG–I; b) optimized PCCFG–I interacting with Pb^{2+}; c) MEP of PCCFG–I; d) MEP of PCCFG–I@Pb^{2+}. Surface Map value: -8.047e^{-2} to 8.047e^{-2}. Calculated at DFT/B3PW91–D3/6-31G(d)/SDD.

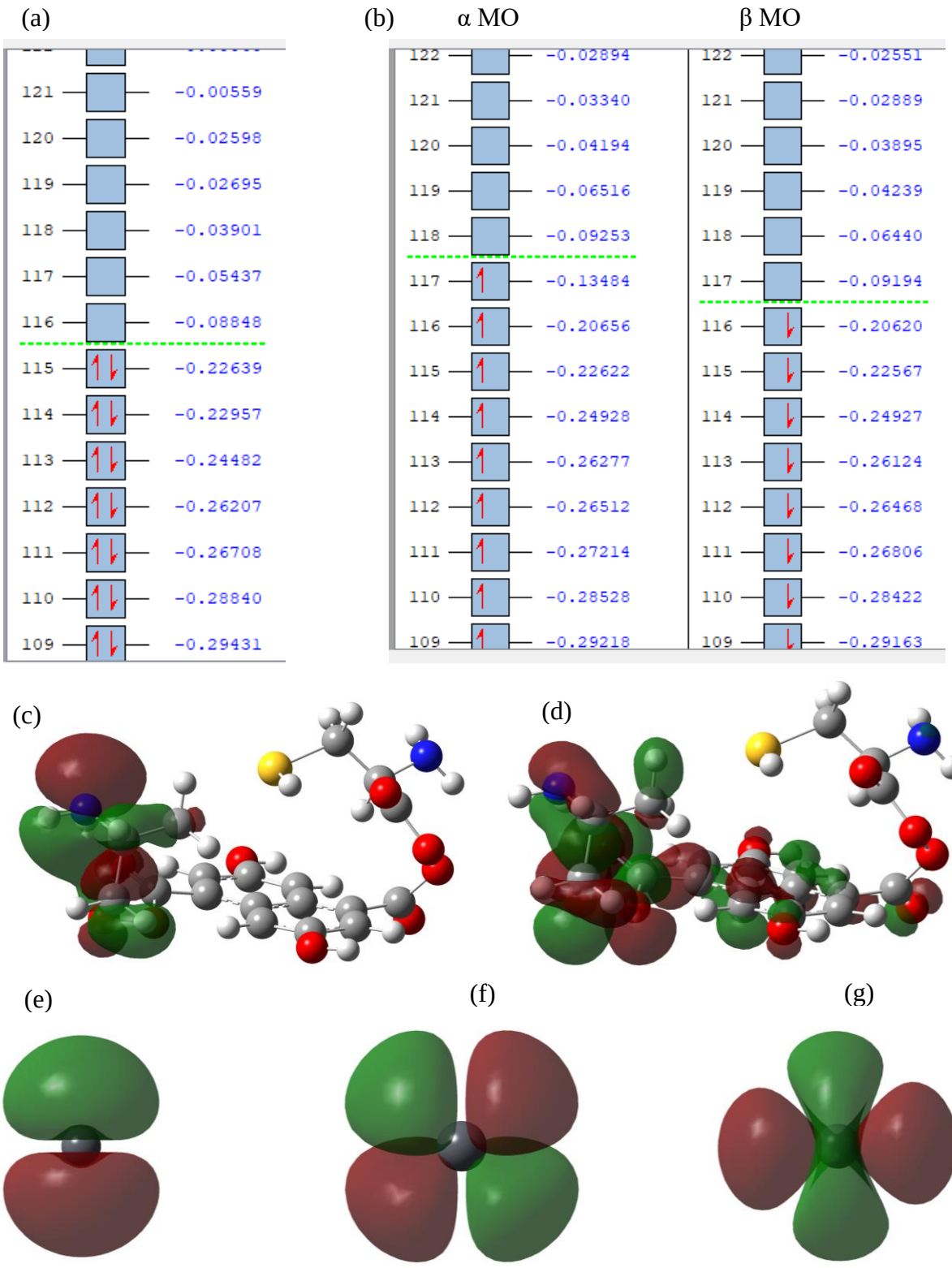

Fig.4. 40 Modeling: a) closed shell (PCCFG–I), b) open shell (PCCFG–I@Pb^{2+}); MO diagram of PCCFG–I: c) HOMO–1 (adsorption site), d) HOMO–5 (adsorption site); MO diagram of Pb^{2+}: e) LUMO + 2 (p_x), f) LUMO + 3 (d_{xy}), g) LUMO + 4 (d_z^2). Isoval = 0.02 (-ve = green, +ve = red). Calculated at DFT/wB97XD/6-311+G (d, p)/SDD.

ii. Molecular electrostatic potential

Fig. 4.39 (c & d) shows the molecular electrostatic potential (MEPs) of PCCFG–I and PCCFG–I@Pb^{2+}, respectively and the coloring related to charge density. All surfaces were generated with a density 0.0004 a. u. In the PCCFG–I, it is possible to observe the presence of two regions (Fig. 4.39(c)) with high density of partially negative region. High density of negative region (more red) were observed in amide (-NH_2) region due to the nitrogen atoms, which is the region of interest for adsorption site for Pb^{2+}. These regions is very electro–negative and thus susceptible to interactions involving electrophiles. After the interaction of PCCFG with Pb^{2+}, MEP were changed to high density of positive region (Fig. 4.39 (d)) which shows the adsorption of Pb^{2+} onto the PCCFG hydrogel.

iii. Frontier molecular orbital's and reactive indices

To verify the reactivity between the PCCFG and heavy metal ions, the study of frontier molecular orbital's (FMO) were carried out and the reactivity were calculated (Table 4.15) from molecular orbital's (MO). Molecular orbital's is a mathematical function that describes the behavior of an electron or pair of electrons within a molecule. Orbital's are actually mathematical conveniences and not physical quantities, despite how real visualization may make them seem. While the optimized geometries, energy, and electron density are physical observables, the orbital's are not. Orbital's are very useful for qualitative descriptions of bonding and reactivity. The MO diagrams of PCCFG-I derived from PCCFG before and after Pb^{2+} adsorption are shown in Fig. 4.40 and 4.41. In PCCFG–I, HOMO-5 (Fig. 4.40 (d)) is an orbital formed from *p* orbital's from the nitrogen atom and the carbon atom and from the *s* orbital on the hydrogen atoms. The contributions from the nitrogen atom and the carbon atom are situated perpendicular to the single bond, which connect the carbon–nitrogen atoms.

After analyzing the results found form the Gaussian output (Table 4.15), it is possible to infer the PCCFG is relatively soft compound. This is due to the presence of amine and carboxyl groups, generating an increase of the softness. For the metal ions, Hg^{2+} ion was the one with the greatest softness and Cu^{2+}, Pb^{2+}, and Cd^{2+} were with better softness, and Cr^{6+} was with greatest hardness or list softness. It is possible to infer that Hg^{2+}, Cu^{2+}, Pb^{2+} and Cd^{2+} ions tends to have a favorable interactions with PCCFG (soft–soft interactions) according to *Pearson's theory*. The electronegative of Cr^{6+}, Cu^{2+}, Cd^{2+} and Pb^{2+} are greater than the

electronegative of PCCFG–I and the Cr^{6+}, Cu^{2+}, Cd^{2+} and Pb^{2+} will accept electron from PCCFG–I.

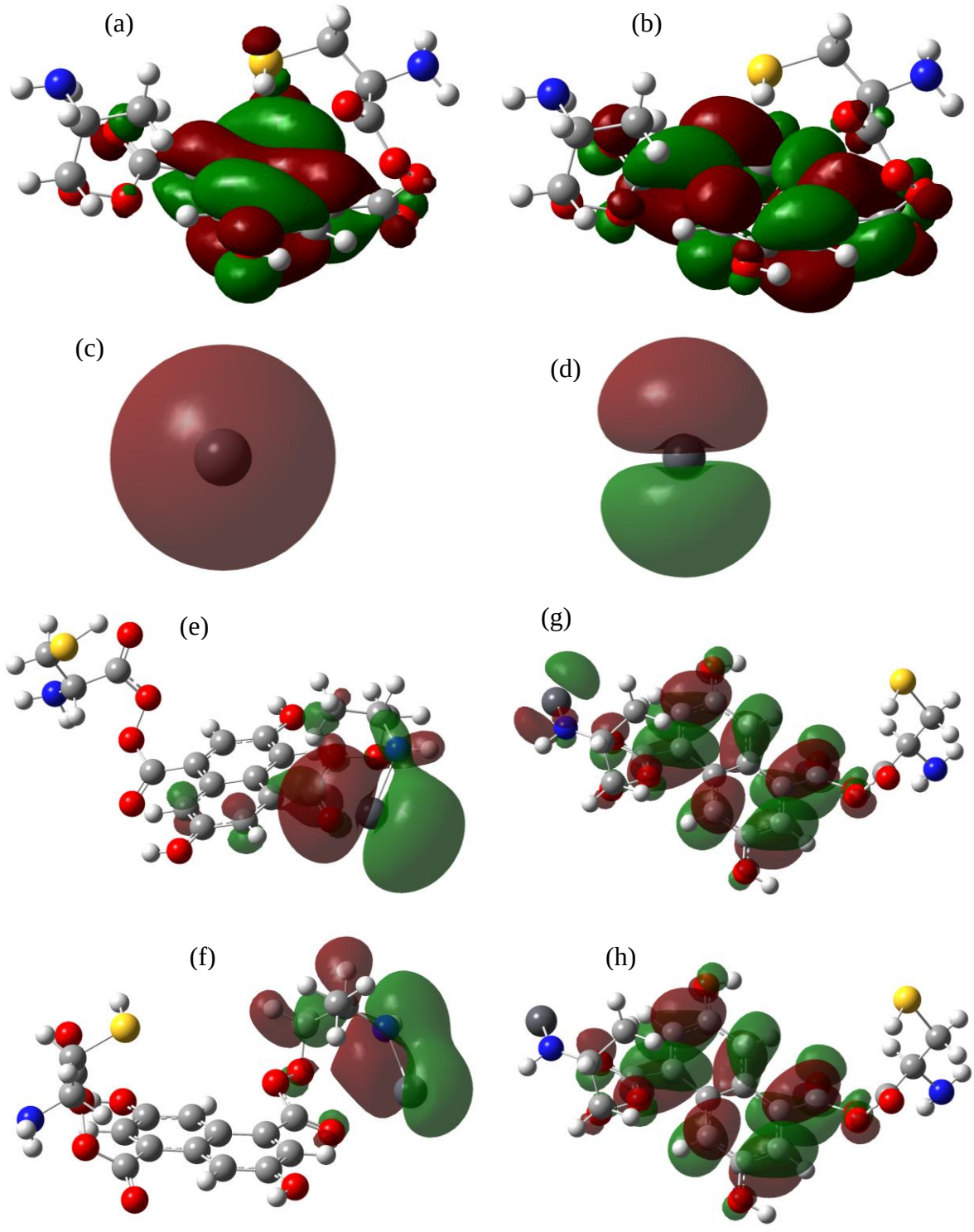

Fig.4. 41 MO diagram of PCCFG-I: a) HOMO, b) LUMO; MO of Pb^{2+}: c) HOMO, d) LUMO; MO of PCCFG-I@Pb^{2+}: e) αHOMO, f) βHOMO, g) σLUMO, h) βLUMO. Isoval = 0.02 (-ve = green, +ve = red). Calculated at DFT/wB97XD/6-311+G (d, p)/SDD.

Hence, during the PCCFG–I and Pb^{2+} interaction, HOMO of PCCFG–I act as *Lewis base* (electron donor) and LUMO of Pb^{2+} act as *Lewis acid* (electron acceptor) (Fig. 4.41). The stability or reactivity of a molecule were depends on the HOMO–LUMO energy gap. Soft molecules are more reactive than harder molecules. The electronegative of PCCFG is greater than the electronegative of Hg^{2+} and the PCCFG–I will accept electron from Hg^{2+}. The direction of spontaneous electron flow will be from PCCFG–I to Cr^{6+}, Cu^{2+}, Cd^{2+}, $Pb^{2+}$and from Hg^{2+} to PCCFG–I. After adsorption of Pb^{2+} on to PCCFG–I, the electronegative and energy gap of the PCCFG–I@Pb^{2+} were decreases and it is more soft showing that it is more stable. Generally, the hardness measures the rate of change of chemical potential with density of electrons. A hard system is one where a small change in electron density produces a large change in chemical potential. The more the hardness of the molecule is the less change in the electron density for a given change in chemical potential. There will be flow of electron density from one system to the other until chemical potential is constant.

Table 4.15 Energy of HOMO (E_{HOMO}), LUMO (E_{LUMO}), Band/Energy gap (E_{gap}), Softness (S), Hardness (η), chemical potential (μ), and electro negativity (χ). Calculated at DFT/wB97XD/6-311+G (d, p)/SDD (Annex 15 & 16).

Group	E_{HOMO}/eV	E_{LUMO}/eV	E_{gap}/eV	η	S	μ	χ
PCCFG-I	-8.26	-1.01	7.25	3.62	0.28	-4.64	4.64
Cr^{6+}	-151.66	-99.35	52.31	26.15	0.04	-125.51	125.51
Pb^{2+}	-27.73	-15.87	11.86	5.93	0.17	-21.80	21.80
Cd^{2+}	-32.14	-20.21	11.93	5.97	0.17	-26.18	26.18
Cu^{2+}	-32.05	-21.71	10.34	5.17	0.19	-26.88	26.88
Hg^{2+}	-7.47	-0.51	6.96	3.48	0.29	-3.99	3.99
PCCFG-I@Pb^{2+}	-5.56	-1.07	4.49	2.25	0.44	-3.32	3.32

iv. Structural and vibrational analysis

Complexes formation between PCCFG and Pb^{2+} were also confirmed by analyzing the vibrational frequencies of the adsorption site. The vibrational frequencies of –C–N of amine in isolated PCCFG, which is part I and corresponding Pb^{2+} complexes were investigated and presented in Table 4.16. Based on the data output from frequency calculation, vibration frequencies of C-N of amine of PCCFG–I is 3478.48 cm^{-1}, which is shifted to lower

frequencies, 542.26 cm^{-1} after PPSgCG–Pb^{2+} complexes. This result is similar with the result from FTIR analysis (Section 4.3.1: v).

Table 4.16 Vibrational frequencies of PCCFG and PCCFG@Pb^{2+}. Calculated at DFT/B3PW91–D3/6-31G(d)/SDD.

Complex	Interaction position	Frequency (cm^{-1})
PCCFG–I	–	νC = N/3478.48
PCCFCG–I@Pb^{2+}	N–Pb^{2+}	νC=N/542.26

v. Spin density analysis

Spin densities are computed as part of the population analysis. The spin density is the electron density in a molecule with odd numbers of electrons: e.g., radical species, taking into account spin polarization. Spin density is positive (blue in Fig. 4.42 (a)) in areas where an electron is more likely to be found in the α spin state (around Pb in this case) and negative (green in Fig. 4.42 (a)) where an electron is more likely to be found in the β spin state. As the difference of α and β electron densities, it indicates likely regions for unpaired electrons. After adsorption of Pb^{2+} onto PCCFG–I, the MO (Fig. 4.41 and spin density (Fig. 4.42 (a)) shows that there is unpaired elections in N–Pb regions. These indicates that Pb follows bi–dentate or poly–dentate than monodentate during coordination with–N and other atoms of PCCFG–I.

vi. Natural bond orbital analysis

Natural bond orbital (NBO) were calculated by Gaussian 09 with "*pop full NBO"* keywords. NBO analysis was used for the study of the charge transfer occurring within the atom, adjacent atom or more remote atom during the interaction/adsorption processes. The charge transfer calculation were carried out with the DFT/B3PW91–D3/6-31G(d)/SDD level of theory. Potential adsorption sites atoms with NBO charge greater than or equal to –0.5 were selected for NBO analysis (Table 4.17). The calculated NBO (from NBO summary of Gaussian output), before and after Pb^{2+} interactions are presented in Table 4.18 and Table 4.19, respectively. The perturbation energy of PCCFG–I and PCCF-I@Pb^{2+} of atoms of NBO total charge greater than or equal to –0.5, with largest stabilization energy and list stabilization energy, calculated using Eq. (3.30) were presented in Table 4.20 and Table 4.21, respectively. As presented in Table 4.18, the possible adsorption site, nitrogen (N26) of

chitosan, and oxygen (O30) of L–cysteine, and oxygen (O20) of GO of PCCFG–I have a potential for adsorption of heavy metal ions.

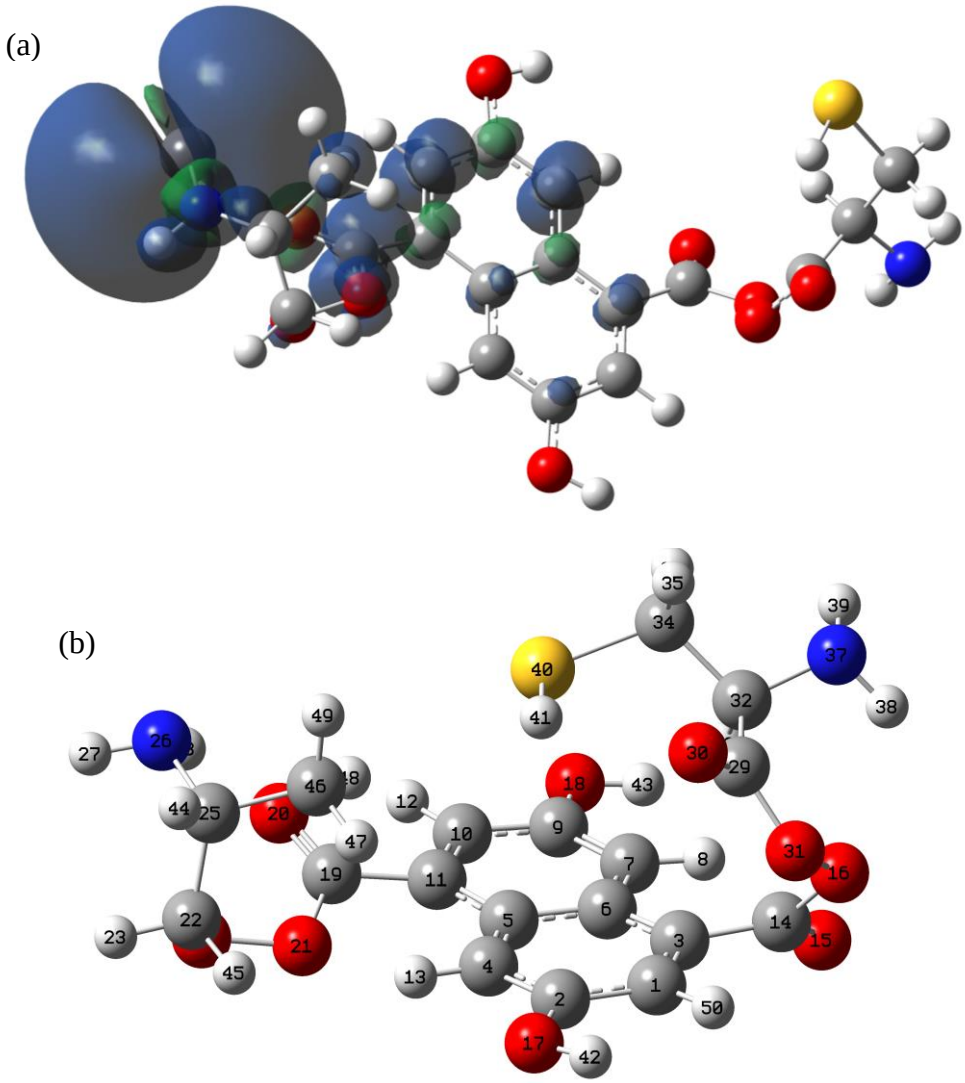

Fig.4. 42 Spin density of PCCFG-I@Pb^{2+} (a); Labels for atoms of optimized PCCFG-I (b)

The oxygen lone pair ($LP(2)O_{20}$) and nitrogen lone pair ($LP(1)N_{26}$) were seen to be the highest–energy Lewis NBO, and to be primarily delocalized into anti-bonds BD^{*}C-C, BD^{*}N-H, BD^{*}C-O, and BD^{*}C-C, BD^{*}C-H, respectively, before adsorption of Pb^{2+}. This region was experienced with high electron density (-ve) as observed from MEP (Fig. 4.39(c)) and low electron occupancy (Fig. 4.40(a)). These two atoms with highest energy (-0.27002 a. u. for O20 and -0.28812 a. u. for N26) indicate the possibility of adsorption site relative to other atoms with lowest energy. At the bottom of table, summary shows that the Lewis NBOs is about 98.104% of the total electron density, with the remaining non–Lewis density found primarily in the valence–shell anti-bonds.

Table 4.17 NBO total charge of PCCFG-I/ DFT/B3PW91–D3/6-31G(d)/SDD.

Labels (Fig. 4.39b)	Atom	NBO charge	Labels (Fig. 4.39b)	Atom	NBO charge
15	O	-0.531	20	O	-0.574
17	O	-0.678	26	N	-0.905
18	O	-0.674	37	N	-0.898

Table 4.18 Lewis and non–Lewis NBO (from NBO Summary) of PCCFG-I/ DFT/B3PW91–D3/6-31G(d)/SDD.

Surface	Lewis NBO	Occupancy (electrons)	Energy (a. u)	Principal Delocalization (non-Lewis NBO)
PCCFG-I	$LP(1)O_{15}$	1.97559	-0.72543	BD^*_{C-C}
	$LP(1)O_{17}$	1.97855	-0.61039	BD^*_{C-C}
	$LP(2)O_{17}$	1.86761	-0.33650	BD^*_{C-C}
	$LP(1)O_{18}$	1.97919	-0.61138	BD^*_{C-O}
	$LP(2)O_{18}$	1.86136	-0.33573	BD^*_{C-C}
	$LP(1)O_{20}$	1.97252	-0.70106	BD^*_{N-H}, BD^*_{C-O}
	$LP(2)O_{20}$	1.83271	-0.27002	BD^*_{N-H}, BD^*_{C-O}
	$LP(1)N_{26}$	1.95073	-0.28812	BD^*_{C-C}, BD^*_{C-H}
	$LP(1)N_{37}$	1.95684	-0.33029	BD^*_{C-C}, BD^*_{C-H}
Total Lewis 225.64006 (98.1044%)				
Valence non-Lewis 3.96270 (1.7229%)				
Rydberg non-Lewis 0.39723 (0.1727%)				

After adsorption of Pb^{2+} onto PCCFG, it was observed that the electron occupancy and energy were changed in $LP(1)N_{26}$ Lewis NBOs (Table 4.19). Transfer of electrons were observed from nitrogen ($LP(2)N_{26}$) to lead (Pb50) [$LP(2)N_{26} \rightarrow LP^*(1)Pb$], and from lead (Pb50) to nitrogen (N26) [$LP(1)Pb_{50} \rightarrow BD^*N_{26}\text{-}H_{27}$, $LP(1)Pb_{50} \rightarrow BD^*C_{25}\text{-}N_{26}$] (Table 4.19). From this, we can infer that there were chemical bonding between lead and nitrogen atoms during orbital over lapping, which shows adsorption of Pb^{2+} onto the PPSgCG hydrogel by chemical means. As observed in Table 4.18 and Table 4.19, the electron occupancy was reduced after Pb^{2+} adsorption onto the PCCFG-I for all atoms. The minimum

electron occupancy observed in PCCFG–I (before Pb^{2+} interaction) was 1.80551 electron were as the maximum electron occupancy was 0.99029 electron after Pb^{2+} adsorption/interaction, which shows electron transfer during orbital overlapping and interaction.

Table 4.19 Lewis and non–Lewis NBO (from NBO summary) of PCCFGI@Pb^{2+}/ DFT/B3PW91–D3/6-31G (d)/SDD.

Surface	Lewis NBO	Occupancy (electrons)	Energy(a. u)	Non-Lewis NBO
PCCFG-I@Pb^{2+}	LP(1)O_{15}	0.98864	-0.72167	BD^{*}C-C
	LP(1)O_{17}	0.98956	-0.62433	BD^{*}C-C
	LP(2)O_{17}	0.93444	-0.33683	BD^{*}C-C
	LP(1)O_{18}	0.98989	-0.61014	BD^{*}C-C
	LP(2)O_{18}	0.93066	-0.33341	BD^{*}C-C
	LP(1)O_{20}	0.97601	-0.70566	BD^{*}N-H, BD^{*}C-O
	LP(2)O_{20}	0.92135	-0.29665	BD^{*}N-H, BD^{*}C-O
	LP(1)N_{26}	0.9168	-0.28387	BD^{*}C-C, BD^{*}C-H
	LP(2)N_{26}	0.85754	-0.31618	LP^{*}(1)Pb, RY^{*}Pb
	LP(1)N_{37}	0.97938	-0.32859	BD^{*}C-C, BD^{*}C-H
	LP(1)Pb50	0.99586	-0.39088	$BD^{*}N_{26}$-H_{27}, $BD^{*}C_{19}$-O_{20}, $BD^{*}C_{25}$-N_{26}

		Total Lewis 112.33392 (97.8806%)		
		Valence non-Lewis 2.23917 (1.9511%)		
		Rydberg non-Lewis 0.19316 (0.1683%)		

vii. Perturbation energy analysis

The highest and the lowest second–order perturbation energy is selected for discussion in this section. In particular, we focus on active adsorption site (-NH_2, -COOH) of PCCFG–I. For PCCFG–I surfaces, the three highest stabilization energy was observed at interacting orbital's LP(2)O15 $\rightarrow$ BD^{*}(1)C_{14}-O_{16}, LP(2)O30 $\rightarrow$ BD^{*}(1)C_{29}-O_{31} and LP(2)O_{20} $\rightarrow$ BD*(1)C_{19}-O_{21} with values of 39.20, 38.10 and 37.55 kcal mol^{-1}, respectively (Table 4.20). The three lowest stabilization energy was observed at interacting orbital's LP(1)O_{15} $\rightarrow$ BD^{*}(1)C_{7}-H_{8},

$LP(1)N_{26} \rightarrow RY^{*}(4)C_{25}$, and $LP(1)N_{37} \rightarrow BD^{*}(1)C_{32}$-$C_{34}$ with values of 0.5, 0.61, and 0.69 kcal mol^{-1}, respectively. The O15, O17, O20, O30, and N26 are atoms with the highest stabilization energy, which is perturbed (unstable) due to reactivity (Louis et al. 2022). Hence, these atoms are susceptible to interactions involving electrophiles which agreed with electrostatic potential (ESP).

After Pb^{2+} adsorption (Pb^{2+} adsorbed onto N26), for PPSgCG-I@Pb^{2+} (Table 4.21), the lower stabilization energy (perturbation energy) was observed in adsorption site (O20 and N26) at interacting orbital's $LP(2)O_{20} \rightarrow LP^{*}(4)Pb_{50}$, $LP(2)N_{26} \rightarrow LP^{*}(4)Pb_{50}$, and $LP(1)O_{20} \rightarrow LP*(3)Pb_{50}$ with values of 0.24, 0.26, and 3,68 kcal mol^{-1}, respectively. These shows decreases in electron density around O22 and N26 after interacted with Pb^{2+}, which shows the transfer of electron from –O and –N atoms to Pb.

Table 4.20 Second Order Perturbation Theory Analysis of Fock Matrix in NBO Basis of PCCFG-I/ DFT/B3PW91–D3/6-31G(d)/SDD. Threshold for printing: 0.50 kcal mol^{-1}

Surface	Donor (i)	Acceptor (j)	E^2(i, j)(kcal mol^{-1})	E(i)–E(j)(a. u)	F(i, j)(a. u)
PCCFG–I	$LP(1)O_{15}$	$BD^{*}(1)C_7$-H_8	0.50	1.18	0.022
	$LP(2)O_{17}$	$BD^{*}(2)C_2$-C_4	28.92	0.35	0.095
	$LP(1)O_{18}$	$BD^{*}(1)C_7$-C_9	6.80	1.19	0.080
	$LP(2)O_{20}$	$BD^{*}(1)$ C_{11}-C_{19}	19.64	0.67	0.105
	$LP(2)O_{20}$	$BD^{*}(1)C_{19}$-O_{21}	37.55	0.60	0.135
	$LP(1)N_{26}$	$BD^{*}(1)$ C_{22}-C_{25}	9.44	0.66	0.070
	$LP(1)N_{26}$	$RY^{*}(4)C_{25}$	0.61	2.26	0.034
	$LP(1)N_{37}$	$BD^{*}(1)C_{32}$-H_{33}	8.16	0.76	0.070
	$LP(1)N_{37}$	$BD^{*}(1)C_{32}$-C_{34}	0.69	0.68	0.019

On the other hand, electron transfer from Pb to –N and –O atoms with interacting orbital's $LP(1)Pb_{50} \rightarrow RY^{*}(4)N_{26}$, $LP(1)Pb_{50} \rightarrow BD^{*}(1)N_{26}$-$H_{27}$, $LP(1)Pb_{50} \rightarrow BD^{*}(2)C_{19} - O_{20}$, and $LP(1)Pb_{50} \rightarrow BD^{*}(1)C_{25}$ - N_{26} with values 0.05, 0.17, 0.29 and 0.63 kcal mol^{-1} stabilization energy, respectively. Overall, the stabilization energy of O15, O17, O20, O30, and N26 atoms were decreased after the adsorption of Pb^{2+} onto PCCFG. For instance, the maximum stabilization energy of O20 ($LP(2)O_{20} \rightarrow BD^{*}(1)C_{19}$ - O_{21}) and N26 ($LP(1)N_{26} \rightarrow BD*(1)C_{22}$-

C_{25}) before interacted with Pb^{2+} were 37.55 and 9.44 kcal mol^{-1}. However, after interaction with Pb^{2+}, the maximum stabilization energy of O20 ($LP(1)O_{20} \rightarrow LP^{*}(3)Pb_{50}$) and N26 ($LP(2)N26 \rightarrow LP^{*}(4)Pb_{50}$) were 3.68 and 0.26 kcal mol^{-1}, respectively. These shows strong interaction and orbital over lapping between Pb^{2+}, oxygen, and nitrogen atoms. Moreover, the oxygen and nitrogen atoms were less perturbat (more stable) after interaction with Pb^{2+}.

Table 4.21 Second Order Perturbation Theory Analysis of Fock Matrix in NBO Basis of PCCFG-I@Pb^{2+}/ DFT/B3PW91–D3/6-31G(d)/SDD. Threshold for printing: 0.25 kcal/mol

Surface	Donor (i)	Acceptor (j)	E^2(i, j)(kcal mol^{-1})	E(i)–E(j)(a. u)	**F(i,**j)(a. u)
PCCFG-I@Pb^{2+}	$LP(2)O_{15}$	$BD^{*}(1)C_{14}$ - O_{16}	19.19	0.56	0.132
	$LP(2)O_{17}$	$BD^{*}(2)C_{2}$ - C_{4}	14.28	0.35	0.094
	$LP(2)O_{18}$	$BD^{*}(2)C_{7}$ - C_{9}	15.60	0.35	0.098
	$LP(2)O_{20}$	$BD^{*}(1)C_{19}$ - O_{21}	14.80	0.63	0.123
	$LP(1)N_{26}$	$BD^{*}(1)C_{22}$ - C_{25}	4.32	0.65	0.069
	$LP(1)N_{26}$	$BD^{*}(1)C_{25}$ - H_{43}	0.28	0.73	0.019
	$LP(1)N_{37}$	$BD^{*}(1)C_{31}$ - H_{32}	3.92	0.77	0.069
	$LP(1)Pb_{50}$	$BD^{*}(2)C_{19}$ – O_{20}	0.29	0.39	0.014
	$LP(1)Pb_{50}$	$BD^{*}(1)C_{25}$ - N_{26}	0.63	0.80	0.028
	$LP(1)Pb_{50}$	$BD^{*}(1)N_{26}$ - H_{27}	0.17	0.89	0.015
	$LP(1)Pb_{50}$	$LP^{*}(2)Pb_{50}$	1.17	0.45	0.031

CHAPTER FIVE

CONCLUSION and RECOMMENDATION

5.1. Conclusion

The synthesized hybrid bio–hydrogels were biodegradable; possess robust regeneration ability for further use, short adsorption processing time and better stability with good adsorption performance towards heavy metals both in single and competitive environment.

The synthesized hybrid bio–hydrogel also shows moderate adsorption performance in sequestration of heavy metals from real wastewater.

The output result from this work reveals high surface area of graphene oxide together with modified/functionalized with L–cysteine and blending with chitosan–grafted starch makes the synthesized hydrogels to possess high adsorption performance. Besides, surface modification of biopolymer materials changes the intrinsic properties such as instability, weak affinity, low degree of swelling, and slow kinetic adsorption time.

Together with kinetic model, the DFT result shows that the metal ions adsorption involves exchange of electrons between the adsorption site (–NH_2, –$CONH_2$, –COOH, –SH) of the hydrogel and the metal ions. The results from EDX also reveal that the metal ions were adsorbed onto the hydrogel via complexation/coordination and ion exchange.

Results from theoretical investigation (DFT calculation) such as Frontier molecular orbital's (FMO) analysis, natural bond orbital (NBO) result, and perturbation energy analysis as well as results from experimental investigation such as FTIR and EDX shows heavy metal adsorption onto the hydrogel were via chemical bonding/covalently bonded.

Overall, synthesized hybrid bio–hydrogel adsorbents possess remarkable adsorption capacity, robust regeneration ability for further use, short adsorption time and fast adsorption kinetics. These analysis and the aforementioned results indicate that the synthesized hybrid bio–hydrogel adsorbent have a potential for the removal of heavy metal ions from real wastewater with fairly losing adsorption capacity after repeatedly regenerated for further use.

5.2. Recommendation

- Based on our findings, we recommend XPS analysis and study the Quantum Theory of Atoms in Molecules (QTAIM) by using DFT and other level of theory to understand deeply the adsorption mechanism of heavy metals.

- Based on our findings, we recommend on future work should be focus on improving the grafting efficiency of biopolymer.

- To know the stability of the hydrogel in continuous flow industrial wastewater treatment, we recommended in future work to studies in fixed–bed column mode.

- To develop the practical application of the PPSgCG, CZVI–CS–PVA, and PCCFG for heavy metal removal, a pilot–scale experimental test is recommended.

- It is recommended to do a thorough cost–benefit analysis for using PPSgCG, CZVI–CS–PVA, and PCCFG hydrogel for heavy metal remediation.

REFERENCES

Abdel-Raouf, M. S., and A. R. M. Abdul-Raheim. 2017a. “Removal of Heavy Metals from Industrial Waste Water by Biomass-Based Materials: A Review. j Pollut Eff Cont 5: 180. Doi: 10.4172/2375-4397.1000180 Page 2 of 13 Volume 5• Issue 1• 1000180 j Pollut Eff Cont, an Open Access Journal Issn: 2375-4397 the Top Si.” *Mercury* 8:15–19.

Abdel-Raouf, M. S., and A. R. M. Abdul-Raheim. 2017b. “Removal of Heavy Metals from Industrial Waste Water by Biomass-Based Materials: A Review.” *J Pollut Effects Control* 5(1):1–13.

Abera, Getnet, Belay Woldeyes, Hundessa Dessalegn Demash, and Garret M. Miyake. 2019. “Comparison of Physicochemical Properties of Indigenous Ethiopian Tuber Crop (Coccinia Abyssinica) Starch with Commercially Available Potato and Wheat Starches.” *International Journal of Biological Macromolecules* 140:43–48.

Afolabi, Felicia Omolara, Paul Musonge, and Babatunde Femi Bakare. 2021. “Application of the Response Surface Methodology in the Removal of Cu2+ and Pb2+ from Aqueous Solutions Using Orange Peels.” *Scientific African* 13:e00931.

Ahamad, Tansir, Mu Naushad, Basheer M. Al-Maswari, and Saad M. Alshehri. 2019. “Fabrication of Highly Porous Adsorbent Derived from Bio-Based Polymer Metal Complex for the Remediation of Water Pollutants.” *Journal of Cleaner Production* 208:1317–26.

Ahmad, Naqhiyah Farhan, Muhammad Afzal Kamboh, Hamid Rashidi Nodeh, Siti Nadiah Binti Abd Halim, and Sharifah Mohamad. 2017. “Synthesis of Piperazine Functionalized Magnetic Sporopollenin: A New Organic-Inorganic Hybrid Material for the Removal of Lead (II) and Arsenic (III) from Aqueous Solution.” *Environmental Science and Pollution Research* 24:21846–58.

Ahmad, Rais, and Anam Mirza. 2018. “Facile One Pot Green Synthesis of Chitosan-Iron Oxide (CS-Fe2O3) Nanocomposite: Removal of Pb (II) and Cd (II) from Synthetic and Industrial Wastewater.” *Journal of Cleaner Production* 186:342–52.

Aksu, Zümriye, and Özlem Tunç. 2005. “Application of Biosorption for Penicillin G Removal: Comparison with Activated Carbon.” *Process Biochemistry* 40(2):831–47.

Alboghbeish, Mousa, Arash Larki, and Seyyed Jafar Saghanezhad. 2022. “Effective Removal of Pb (II) Ions Using Piperazine-Modified Magnetic Graphene Oxide Nanocomposite; Optimization by Response Surface Methodology.” *Scientific Reports* 12(1):9658.

Algureiri, Ahmed H., and Yossor R. Abdulmajeed. 2016. “Removal of Heavy Metals from

Industrial Wastewater by Using RO Membrane." *Iraqi Journal of Chemical and Petroleum Engineering* 17(4):125–36.

Ali, Rehab M., Hesham A. Hamad, Mohamed M. Hussein, and Gihan F. Malash. 2016. "Potential of Using Green Adsorbent of Heavy Metal Removal from Aqueous Solutions: Adsorption Kinetics, Isotherm, Thermodynamic, Mechanism and Economic Analysis." *Ecological Engineering* 91:317–32.

Ali, Shafqat, Zareen Zuhra, Sajjad Ali, Qi Han, Muhammad Ahmad, and Zhongying Wang. 2021. "Ultra-Deep Removal of Pb by Functionality Tuned UiO-66 Framework: A Combined Experimental, Theoretical and HSAB Approach." *Chemosphere* 284:131305.

Alsbaiee, Alaaeddin, Brian J. Smith, Leilei Xiao, Yuhan Ling, Damian E. Helbling, and William R. Dichtel. 2016. "Rapid Removal of Organic Micropollutants from Water by a Porous β-Cyclodextrin Polymer." *Nature* 529(7585):190–94.

APHA, AWWA, WEF. 2023. "Lipps WC, Braun-Howland EB, Baxter TE, Eds. Standard Methods for the Examination of Water and Wastewater." *Washington DC: APHA Press* 24th ed.

Appuhamillage, Gayan A., Danielle R. Berry, Candace E. Benjamin, Michael A. Luzuriaga, John C. Reagan, Jeremiah J. Gassensmith, and Ronald A. Smaldone. 2019. "A Biopolymer-based 3D Printable Hydrogel for Toxic Metal Adsorption from Water." *Polymer International* 68(5):964–71.

Aschale, Minbale, Yilma Sileshi, Mary Kelly-Quinn, and Dereje Hailu. 2015. "Potentially Toxic Trace Element Contamination of the Little Akaki River of Addis Ababa, Ethiopia." *J Nat Sci Res* 5(1):1–13.

Aziz, Hamidi A., Mohd N. Adlan, and Kamar S. Ariffin. 2008. "Heavy Metals (Cd, Pb, Zn, Ni, Cu and Cr (III)) Removal from Water in Malaysia: Post Treatment by High Quality Limestone." *Bioresource Technology* 99(6):1578–83.

Badawi, M. A., N. A. Negm, M. T. H. Abou Kana, H. H. Hefni, and M. M. Abdel Moneem. 2017. "Adsorption of Aluminum and Lead from Wastewater by Chitosan-Tannic Acid Modified Biopolymers: Isotherms, Kinetics, Thermodynamics and Process Mechanism." *International Journal of Biological Macromolecules* 99:465–76.

Bagbi, Y, A. Sarswat, S. Tiwari, D. Mohan, A. Pandey, and R. Solanki Pratima. 2017. "L-Cysteine Stabilized Zero Valent Iron Nanoparticle and Their Application for Remediation of Lead Ions from Water." *Environmental Nanotechnology, Monitoring & Management* 7:34–45.

Bagbi, Yana, Ankur Sarswat, Sachchidanand Tiwari, Dinesh Mohan, Arvind Pandey, and Pratima R. Solanki. 2017. “Synthesis of L-Cysteine Stabilized Zero-Valent Iron (NZVI) Nanoparticles for Lead Remediation from Water.” *Environmental Nanotechnology, Monitoring & Management* 7:34–45.

Bai, Yuan, and Bronisław Bartkiewicz. 2009. “Removal of Cadmium from Wastewater Using Ion Exchange Resin Amberjet 1200H Columns.” *Polish Journal of Environmental Studies* 18(6):1191–95.

Bashir, Arshid, Taniya Manzoor, Lateef Ahmad Malik, Aaliya Qureashi, and Altaf Hussain Pandith. 2020. “Enhanced and Selective Adsorption of Zn (II), Pb (II), Cd (II), and Hg (II) Ions by a Dumbbell-and Flower-Shaped Potato Starch Phosphate Polymer: A Combined Experimental and DFT Calculation Study.” *ACS Omega* 5(10):4853–67.

Basri, Sri Norleha, Norhazlin Zainuddin, Kamaruddin Hashim, and Nor Azah Yusof. 2016. “Preparation and Characterization of Irradiated Carboxymethyl Sago Starch-Acid Hydrogel and Its Application as Metal Scavenger in Aqueous Solution.” *Carbohydrate Polymers* 138:34–40.

Bhatt, Ronak, B. Sreedhar, and P. Padmaja. 2015. “Adsorption of Chromium from Aqueous Solutions Using Crosslinked Chitosan–Diethylenetriaminepentaacetic Acid.” *International Journal of Biological Macromolecules* 74:458–66.

Bhatt, Ronak, B. Sreedhar, and P. Padmaja. 2017. “Chitosan Supramolecularly Cross Linked with Trimesic Acid–Facile Synthesis, Characterization and Evaluation of Adsorption Potential for Chromium (VI).” *International Journal of Biological Macromolecules* 104:1254–66.

Bodagh, Atefe, Hamid Khoshdast, Hakimeh Sharafi, Hossein Shahbani Zahiri, and Kambiz Akbari Noghabi. 2013. “Removal of Cadmium (II) from Aqueous Solution by Ion Flotation Using Rhamnolipid Biosurfactant as an Ion Collector.” *Industrial & Engineering Chemistry Research* 52(10):3910–17.

Boddu, Veera M., Krishnaiah Abburi, Jonathan L. Talbott, and Edgar D. Smith. 2003. “Removal of Hexavalent Chromium from Wastewater Using a New Composite Chitosan Biosorbent.” *Environmental Science & Technology* 37(19):4449–56.

Borsagli, Fernanda Guerra Lima Medeiros, and Alessandro Borsagli. 2019. “Chemically Modified Chitosan Bio-Sorbents for the Competitive Complexation of Heavy Metals Ions: A Potential Model for the Treatment of Wastewaters and Industrial Spills.” *Journal of Polymers and the Environment* 27:1542–56.

BrbootI, Mahmood M., Balasim A. Abid, and Najah M. Al-ShuwaikI. 2011. “Removal of Heavy Metals Using Chemicals Precipitation.” *Eng. Technol. J* 29(3):595–612.

Cancer, International Agency for Research on. 2012a. “A Review of Human Carcinogens: Personal Habits and Indoor Combustions.”

Cancer, International Agency for Research on. 2012b. *Review of Human Carcinogens*. Vol. 100. IARC Monographs on the Evaluat.

Chai, Jeng-Da, and Martin Head-Gordon. 2008. “Long-Range Corrected Hybrid Density Functionals with Damped Atom–Atom Dispersion Corrections.” *Physical Chemistry Chemical Physics* 10(44):6615–20.

Chang, Jeong Ho, Jinwon Kim, and Hyesun Lee. 2017. “PNIPAm Grafted Amino-Functionalized Mesoporous Silica for Thermo-Responsive Chromium Elimination.” *Applied Surface Science* 424:115–21.

Chaudhary, Abdul J., Nimai C. Goswami, and Susan M. Grimes. 2003. “Electrolytic Removal of Hexavalent Chromium from Aqueous Solutions.” *Journal of Chemical Technology & Biotechnology: International Research in Process, Environmental & Clean Technology* 78(8):877–83.

Chauhan, Divya, Jaya Dwivedi, and Nalini Sankararamakrishnan. 2014. “Novel Chitosan/PVA/Zerovalent Iron Biopolymeric Nanofibers with Enhanced Arsenic Removal Applications.” *Environmental Science and Pollution Research* 21:9430–42.

Cheballah, Karima, Amar Sahmoune, Karima Messaoudi, Nadjib Drouiche, and Hakim Lounici. 2015. “Simultaneous Removal of Hexavalent Chromium and COD from Industrial Wastewater by Bipolar Electrocoagulation.” *Chemical Engineering and Processing: Process Intensification* 96:94–99.

Chen, Yan Xiao, Ben He Zhong, and Wei Mao Fang. 2012. “Adsorption Characterization of Lead (II) and Cadmium (II) on Crosslinked Carboxymethyl Starch.” *Journal of Applied Polymer Science* 124(6):5010–20.

Cheremisinoff, Paul N., and Fred Ellerbusch. 1978. “Carbon Adsorption Handbook.” *(No Title)*.

Dahlan, Nuraina Anisa, Anand Kumar Veeramachineni, Steven James Langford, and Janarthanan Pushpamalar. 2017. “Developing of a Magnetite Film of Carboxymethyl Cellulose Grafted Carboxymethyl Polyvinyl Alcohol (CMC-g-CMPVA) for Copper Removal.” *Carbohydrate Polymers* 173:619–30.

Daneshmand, Maryam, Mohammad Outokesh, Ahmad Akbari, Mohammadreza Kosari, and

Ahmad Tayyebi. 2018. “Synthesis of ‘L-Cysteine–Graphene Oxide’ Hybrid by New Methods and Elucidation of Its Uptake Properties for Hg (II) Ion.” *Separation Science and Technology* 53(6):843–55.

Dax, Daniel, María Soledad Chávez, Chunlin Xu, Stefan Willför, Regis Teixeira Mendonça, and Julio Sánchez. 2014. “Cationic Hemicellulose-Based Hydrogels for Arsenic and Chromium Removal from Aqueous Solutions.” *Carbohydrate Polymers* 111:797–805.

Dichiara, Anthony B., Steven J. Weinstein, and Reginald E. Rogers. 2015. “On the Choice of Batch or Fixed Bed Adsorption Processes for Wastewater Treatment.” *Industrial & Engineering Chemistry Research* 54(34):8579–86.

Donner, Mark W., Muhammad Arshad, Aman Ullah, and Tariq Siddique. 2019. “Unravelled Keratin-Derived Biopolymers as Novel Biosorbents for the Simultaneous Removal of Multiple Trace Metals from Industrial Wastewater.” *Science of The Total Environment* 647:1539–46.

Dutta, Kingshuk, and Sirshendu De. 2017. “Aromatic Conjugated Polymers for Removal of Heavy Metal Ions from Wastewater: A Short Review.” *Environmental Science: Water Research & Technology* 3(5):793–805.

Edition, Fourth. 2011. “Guidelines for Drinking-Water Quality.” *WHO Chronicle* 38(4):104–8.

El-Hamshary, Hany, Moustafa M. G. Fouda, Meera Moydeen, and Salem S. Al-Deyab. 2014. “Removal of Heavy Metal Using Poly (N-Vinylimidazole)-Grafted-Carboxymethylated Starch.” *International Journal of Biological Macromolecules* 66:289–94.

Esfahani, Amirhosein Ramazanpour, Ahmad Farrokhian Firouzi, Gholamabbas Sayyad, and Alireza Kiasat. 2013. “Lead Removal from Aqueous Solutions Using Polyacrylicacid-Stabilized Zero-Valent Iron Nanoparticles.” *Research Journal of Environmental and Earth Sciences* 5(9):548–55.

Fang, Zhanqiang, Jinhong Chen, Xinhong Qiu, Xiuqi Qiu, Wen Cheng, and Licai Zhu. 2011. “Effective Removal of Antibiotic Metronidazole from Water by Nanoscale Zero-Valent Iron Particles.” *Desalination* 268(1–3):60–67.

Fatehi, M. H., J. Shayegan, M. Zabihi, and I. Goodarznia. 2017. “Functionalized Magnetic Nanoparticles Supported on Activated Carbon for Adsorption of Pb (II) and Cr (VI) Ions from Saline Solutions.” *Journal of Environmental Chemical Engineering* 5(2):1754–62.

Frisch, A. 2009. “Gaussian 09W Reference.” *Wallingford, USA, 25p* 470.

Ge, Fei, Meng-Meng Li, Hui Ye, and Bao-Xiang Zhao. 2012. “Effective Removal of Heavy

Metal Ions Cd2+, Zn2+, Pb2+, Cu2+ from Aqueous Solution by Polymer-Modified Magnetic Nanoparticles." *Journal of Hazardous Materials* 211:366–72.

Ge, Huacai, Hui Chen, and Shiying Huang. 2012. "Microwave Preparation and Properties of O-crosslinked Maleic Acyl Chitosan Adsorbent for Pb2+ and Cu2+." *Journal of Applied Polymer Science* 125(4):2716–23.

Ghaedi, Abdol Mohammad, Mohammad Panahimehr, Alireza Rayegan Shirazi Nejad, Seyed Javad Hosseini, Azam Vafaei, and Mohammad Mehdi Baneshi. 2018. "Factorial Experimental Design for the Optimization of Highly Selective Adsorption Removal of Lead and Copper Ions Using Metal Organic Framework MOF-2 (Cd)." *Journal of Molecular Liquids* 272:15–26.

Gokila, S., T. Gomathi, P. N. Sudha, and Sukumaran Anil. 2017. "Removal of the Heavy Metal Ion Chromiuim (VI) Using Chitosan and Alginate Nanocomposites." *International Journal of Biological Macromolecules* 104:1459–68.

Gopi, D., S. Nithiya, E. Shinyjoy, D. Rajeswari, and L. Kavitha. 2014. "Carbon Nanotubes/Carboxymethyl Chitosan/Mineralized Hydroxyapatite Composite Coating on Ti-6Al-4V Alloy for Improved Mechanical and Biological Properties." *Industrial & Engineering Chemistry Research* 53(18):7660–69.

Guan, Zhengrong, Li Liu, Lilu He, and Sen Yang. 2011. "Amphiphilic Hollow Carbonaceous Microspheres for the Sorption of Phenol from Water." *Journal of Hazardous Materials* 196:270–77.

Habiba, Umma, Amalina M. Afifi, Areisman Salleh, and Bee Chin Ang. 2017. "Chitosan/(Polyvinyl Alcohol)/Zeolite Electrospun Composite Nanofibrous Membrane for Adsorption of Cr6+, Fe3+ and Ni2+." *Journal of Hazardous Materials* 322:182–94.

Hakiri, R., I. Ameur, S. Abid, and N. Derbel. 2018. "Synthesis, X-Ray Structural, Hirshfeld Surface Analysis, FTIR, MEP and NBO Analysis Using DFT Study of a 4-Chlorobenzylammonium Nitrate (C7ClH9N)+(NO3)–." *Journal of Molecular Structure* 1164:486–92. doi: https://doi.org/10.1016/j.molstruc.2018.03.068.

Hayati, Bagher, Afshin Maleki, Farhood Najafi, Hiua Daraei, Fardin Gharibi, and Gordon McKay. 2017. "Super High Removal Capacities of Heavy Metals (Pb2+ and Cu2+) Using CNT Dendrimer." *Journal of Hazardous Materials* 336:146–57.

He, Jing, Yangcheng Lu, and Guangsheng Luo. 2014. "Ca (II) Imprinted Chitosan Microspheres: An Effective and Green Adsorbent for the Removal of Cu (II), Cd (II) and Pb (II) from Aqueous Solutions." *Chemical Engineering Journal* 244:202–8.

Hizhnyi, Yuriy, Sergii Nedilko, Viktor Borysiuk, and Andrii Shyichuk. 2017. “Ab Initio Computational Study of Chromate Molecular Anion Adsorption on the Surfaces of Pristine and B-or N-Doped Carbon Nanotubes and Graphene.” *Nanoscale Research Letters* 12(1):1–9.

Hohenberg, Pierre, and Walter Kohn. 1964. “Inhomogeneous Electron Gas.” *Physical Review* 136(3B):B864.

Hokkanen, Sanna, Eveliina Repo, and Mika Sillanpää. 2013. “Removal of Heavy Metals from Aqueous Solutions by Succinic Anhydride Modified Mercerized Nanocellulose.” *Chemical Engineering Journal* 223:40–47.

Horzum, Nesrin, Mustafa M. Demir, Muath Nairat, and Talal Shahwan. 2013. “Chitosan Fiber-Supported Zero-Valent Iron Nanoparticles as a Novel Sorbent for Sequestration of Inorganic Arsenic.” *RSC Advances* 3(21):7828–37.

Hu, Zhao-Hong, Ahmed Mohamed Omer, Xiao-kun Ouyang, and Di Yu. 2018. “Fabrication of Carboxylated Cellulose Nanocrystal/Sodium Alginate Hydrogel Adsorbents for Adsorption of Pb (II) from Aqueous Solution.” *International Journal of Biological Macromolecules* 108:149–57.

Huang, Huayu, Yang Wang, Yubin Zhang, Zhiying Niu, and Xinli Li. 2020. “Amino-Functionalized Graphene Oxide for Cr (VI), Cu (II), Pb (II) and Cd (II) Removal from Industrial Wastewater.” *Open Chemistry* 18(1):97–107.

Huang, Ting, Yao-wen Shao, Qian Zhang, Yu-fan Deng, Zhi-xuan Liang, Fu-zhi Guo, Peng-chao Li, and Yong Wang. 2019. “Chitosan-Cross-Linked Graphene Oxide/Carboxymethyl Cellulose Aerogel Globules with High Structure Stability in Liquid and Extremely High Adsorption Ability.” *ACS Sustainable Chemistry & Engineering* 7(9):8775–88.

Ifthikar, Jerosha, Xiang Jiao, Audrey Ngambia, Ting Wang, Aimal Khan, Ali Jawad, Qiang Xue, Lei Liu, and Zhuqi Chen. 2018. “Facile One-Pot Synthesis of Sustainable Carboxymethyl Chitosan–Sewage Sludge Biochar for Effective Heavy Metal Chelation and Regeneration.” *Bioresource Technology* 262:22–31.

Jamali, Abbas, Alireza Azhdari Tehrani, Farzaneh Shemirani, and Ali Morsali. 2016. “Lanthanide Metal–Organic Frameworks as Selective Microporous Materials for Adsorption of Heavy Metal Ions.” *Dalton Transactions* 45(22):9193–9200.

Javidparvar, Ali Asghar, Reza Naderi, and Bahram Ramezanzadeh. 2020. “L-Cysteine Reduced/Functionalized Graphene Oxide Application as a Smart/Control Release

Nanocarrier of Sustainable Cerium Ions for Epoxy Coating Anti-Corrosion Properties Improvement." *Journal of Hazardous Materials* 389:122135.

Kahu, S. S., A. Shekhawat, D. Saravanan, and R. M. Jugade. 2016. "Two Fold Modified Chitosan for Enhanced Adsorption of Hexavalent Chromium from Simulated Wastewater and Industrial Effluents." *Carbohydrate Polymers* 146:264–73. doi: 10.1016/J.CARBPOL.2016.03.041.

Kalidhasan, S., A. Santhana Krishna Kumar, Vidya Rajesh, and N. Rajesh. 2013. "Enhanced Adsorption of Hexavalent Chromium Arising out of an Admirable Interaction between a Synthetic Polymer and an Ionic Liquid." *Chemical Engineering Journal* 222:454–63.

Kan, Lina, Qiaojiao Zhao, Jiaqi Hu, Yanwen Wu, and Jie Ouyang. 2017. "Synthesis and Physicochemical Properties of Carboxymethyl Chestnut Starch." *Journal of Food Processing and Preservation* 41(6):e13229.

Karnib, Mona, Ahmad Kabbani, Hanafy Holail, and Zakia Olama. 2014. "Heavy Metals Removal Using Activated Carbon, Silica and Silica Activated Carbon Composite." *Energy Procedia* 50:113–20.

Katsoyiannis, Ioannis A., Thomas Ruettimann, and Stephan J. Hug. 2008. "PH Dependence of Fenton Reagent Generation and As (III) Oxidation and Removal by Corrosion of Zero Valent Iron in Aerated Water." *Environmental Science & Technology* 42(19):7424–30.

Kim, Seol Ah, Seralathan Kamala-Kannan, Kui-Jae Lee, Yool-Jin Park, Patrick J. Shea, Wang-Hyu Lee, Hyung-Moo Kim, and Byung-Taek Oh. 2013. "Removal of Pb (II) from Aqueous Solution by a Zeolite–Nanoscale Zero-Valent Iron Composite." *Chemical Engineering Journal* 217:54–60.

Kustov, Leonid M., Elena D. Finashina, Elena V Shuvalova, Olga P. Tkachenko, and Olga A. Kirichenko. 2011. "Pd–Fe Nanoparticles Stabilized by Chitosan Derivatives for Perchloroethene Dechlorination." *Environment International* 37(6):1044–52.

Lagergren, Stan. 1898. "Zur Theorie Der Sogenannten Adsorption Geloster Stoffe." *Kungliga Svenska Vetenskapsakademiens. Handlingar* 24:1–39.

Lalmi, Afaf, Kamel-Eddine Bouhidel, Basma Sahraoui, and Chams el Houda Anfif. 2018. "Removal of Lead from Polluted Waters Using Ion Exchange Resin with Ca (NO3) 2 for Elution." *Hydrometallurgy* 178:287–93.

Langmuir, Irving. 1918. "The Adsorption of Gases on Plane Surfaces of Glass, Mica and Platinum." *Journal of the American Chemical Society* 40(9):1361–1403.

Lanthong, P., R. Nuisin, and S. Kiatkamjornwong. 2006. "Graft Copolymerization,

Characterization, and Degradation of Cassava Starch-g-Acrylamide/Itaconic Acid Superabsorbents." *Carbohydrate Polymers* 66(2):229–45.

Lee, Ju-Wook, Hoon Choi, Un-Ki Hwang, Ju-Chan Kang, Yue Jai Kang, Kwang Il Kim, and Jun-Hwan Kim. 2019. "Toxic Effects of Lead Exposure on Bioaccumulation, Oxidative Stress, Neurotoxicity, and Immune Responses in Fish: A Review." *Environmental Toxicology and Pharmacology* 68:101–8.

Leng, Yang. 2009. *Materials Characterization: Introduction to Microscopic and Spectroscopic Methods*. John Wiley & Sons.

Li, Guoliang, Zongshan Zhao, Jiyan Liu, and Guibin Jiang. 2011. "Effective Heavy Metal Removal from Aqueous Systems by Thiol Functionalized Magnetic Mesoporous Silica." *Journal of Hazardous Materials* 192(1):277–83.

Li, Li, Lanfeng Liao, Yaping Ding, and Hongyan Zeng. 2017. "Dithizone-Etched CdTe Nanoparticles-Based Fluorescence Sensor for the off–on Detection of Cadmium Ion in Aqueous Media." *RSC Advances* 7(17):10361–68.

Li, Luzhong, Zhu Wang, Piming Ma, Huiyu Bai, Weifu Dong, and Mingqing Chen. 2015. "Preparation of Polyvinyl Alcohol/Chitosan Hydrogel Compounded with Graphene Oxide to Enhance the Adsorption Properties for Cu (II) in Aqueous Solution." *Journal of Polymer Research* 22:1–10.

Li, Qing, Zheng Wang, Dong-Mei Fang, Hai-yun Qu, Yan Zhu, Hui-jun Zou, Yi-rui Chen, Yi-Ping Du, and Hui-lian Hu. 2014. "Preparation, Characterization, and Highly Effective Mercury Adsorption of L-Cysteine-Functionalized Mesoporous Silica." *New Journal of Chemistry* 38(1):248–54.

Li, Ting, Xiaojin Liu, Luzhong Li, Yang Wang, Piming Ma, Mingqing Chen, and Weifu Dong. 2019. "Polydopamine-Functionalized Graphene Oxide Compounded with Polyvinyl Alcohol/Chitosan Hydrogels on the Recyclable Adsorption of Cu (II), Pb (II) and Cd (II) from Aqueous Solution." *Journal of Polymer Research* 26:1–12.

Li, Xiao-Min, Zheng-Zong Wu, Bao Zhang, Yi Pan, Ran Meng, and Han-Qing Chen. 2019. "Fabrication of Chitosan Hydrochloride and Carboxymethyl Starch Complex Nanogels as Potential Delivery Vehicles for Curcumin." *Food Chemistry* 293:197–203.

Li, Yan, Tianbao Qiu, and Xiaoyan Xu. 2013. "Preparation of Lead-Ion Imprinted Crosslinked Electro-Spun Chitosan Nanofiber Mats and Application in Lead Ions Removal from Aqueous Solutions." *European Polymer Journal* 49(6):1487–94.

Li, Yanxiang, Lixia Cao, Lei Li, and Chuanfang Yang. 2015. "In Situ Growing Directional

Spindle TiO2 Nanocrystals on Cellulose Fibers for Enhanced Pb2+ Adsorption from Water." *Journal of Hazardous Materials* 289:140–48.

Liang, Rui-hong, Ya Li, Li Huang, Xue-dong Wang, Xiao-xue Hu, Cheng-mei Liu, Ming-shun Chen, and Jun Chen. 2020. "Pb2+ Adsorption by Ethylenediamine-Modified Pectins and Their Adsorption Mechanisms." *Carbohydrate Polymers* 234:115911.

Lin, Xiaoju, Gaoling Wei, Xiaoliang Liang, Jing Liu, Lingya Ma, and Jianxi Zhu. 2021. "The Competitive Adsorption of Chromate and Sulfate on Ni-Substituted Magnetite Surfaces: An ATR-FTIR Study." *Minerals* 11(1):88.

Liu, Botao, Azmatullah Khan, Ki-Hyun Kim, Deepak Kukkar, and Ming Zhang. 2020. "The Adsorptive Removal of Lead Ions in Aquatic Media: Performance Comparison between Advanced Functional Materials and Conventional Materials." *Critical Reviews in Environmental Science and Technology* 50(23):2441–83.

Liu, Jiwei, Jianguo Jiang, Aikelaimu Aihemaiti, Yuan Meng, Meng Yang, Yiwen Xu, Yuchen Gao, Quan Zou, and Xuejing Chen. 2019. "Removal of Phosphate from Aqueous Solution Using MgO-Modified Magnetic Biochar Derived from Anaerobic Digestion Residue." *Journal of Environmental Management* 250:109438.

Liu, Lihua, Jun Wu, Xin Li, and Yulin Ling. 2013. "Synthesis of Poly (Dimethyldiallylammonium Chloride-Co-Acrylamide)-Graft-Triethylenetetramine–Dithiocarbamate and Its Removal Performance and Mechanism of Action towards Heavy Metal Ions." *Separation and Purification Technology* 103:92–100.

Liu, Weikang, Liang Yang, Shihao Xu, Yao Chen, Bianhua Liu, Zhong Li, and Changlong Jiang. 2018. "Efficient Removal of Hexavalent Chromium from Water by an Adsorption–Reduction Mechanism with Sandwiched Nanocomposites." *RSC Advances* 8(27):15087–93.

Liu, Yu, Bao-Hang Han, and Yun-Ti Chen. 2002. "Molecular Recognition and Complexation Thermodynamics of Dye Guest Molecules by Modified Cyclodextrins and Calixarenesulfonates." *The Journal of Physical Chemistry B* 106(18):4678–87.

Liu, Zeyu, Tian Lu, and Qinxue Chen. 2021. "Vibrational Spectra and Molecular Vibrational Behaviors of All-Carboatomic Rings, Cyclo [18] Carbon and Its Analogues." *Chemistry–An Asian Journal* 16(1):56–63.

Loría-Bastarrachea, M. I., W. Herrera-Kao, J. V Cauich-Rodríguez, J. M. Cervantes-Uc, H. Vázquez-Torres, and A. Ávila-Ortega. 2011. "A TG/FTIR Study on the Thermal Degradation of Poly (Vinyl Pyrrolidone)." *Journal of Thermal Analysis and Calorimetry*

104(2):737–42.

Louis, Hitler, Ernest E. Ekereke, Bartholomew B. Isang, Alexander I. Ikeuba, Ismail O. Amodu, Terkumbur E. Gber, Aniekan E. Owen, Adedapo S. Adeyinka, and Ernest C. Agwamba. 2022. "Assessing the Performance of Al12N12 and Al12P12 Nanostructured Materials for Alkali Metal Ion (Li, Na, K) Batteries." *ACS Omega* 7(50):46183–202. doi: 10.1021/acsomega.2c04319.

Luo, Huiyuan, Fuping Dong, Qian Wang, Yihang Li, and Yuzhu Xiong. 2021. "Construction of Porous Starch-Based Hydrogel via Regulating the Ratio of Amylopectin/Amylose for Enhanced Water-Retention." *Molecules* 26(13):3999.

Luo, Jingqi, Chuanjie Fan, Zhi Xiao, Tianshu Sun, and Xiaodong Zhou. 2019. "Novel Graphene Oxide/Carboxymethyl Chitosan Aerogels via Vacuum-Assisted Self-Assembly for Heavy Metal Adsorption Capacity." *Colloids and Surfaces A: Physicochemical and Engineering Aspects* 578:123584.

Ma, Jianhong, Guiyin Zhou, Lin Chu, Yutang Liu, Chengbin Liu, Shenglian Luo, and Yuanfeng Wei. 2017. "Efficient Removal of Heavy Metal Ions with an EDTA Functionalized Chitosan/Polyacrylamide Double Network Hydrogel." *ACS Sustainable Chemistry & Engineering* 5(1):843–51.

La Mantia, Francesco Paolo, and Antonino Valenza. 1994. "Thermo-mechanical Degradation of Polymer Blends." *Die Angewandte Makromolekulare Chemie: Applied Macromolecular Chemistry and Physics* 216(1):45–65.

Manzoor, Kaiser, Mudasir Ahmad, Suhail Ahmad, and Saiqa Ikram. 2019. "Removal of Pb (Ii) and Cd (Ii) from Wastewater Using Arginine Cross-Linked Chitosan–Carboxymethyl Cellulose Adsorbents as Green Adsorbent." *RSC Advances* 9(14):7890–7902.

Marcano, Daniela C., Dmitry V Kosynkin, Jacob M. Berlin, Alexander Sinitskii, Zhengzong Sun, Alexander Slesarev, Lawrence B. Alemany, Wei Lu, and James M. Tour. 2010. "Improved Synthesis of Graphene Oxide." *ACS Nano* 4(8):4806–14.

Meena, Amanda H., and Yuji Arai. 2016. "Effects of Common Groundwater Ions on Chromate Removal by Magnetite: Importance of Chromate Adsorption." *Geochemical Transactions* 17:1–13.

Miao, Yue-E., Ruiyu Wang, Dan Chen, Zhenyan Liu, and Tianxi Liu. 2012. "Electrospun Self-Standing Membrane of Hierarchical SiO2@ γ-AlOOH (Boehmite) Core/Sheath Fibers for Water Remediation." *ACS Applied Materials & Interfaces* 4(10):5353–59.

Milenković, Mila, Aleksandra Mišović, Dragana Jovanović, Ana Popović Bijelić, Gabriele Ciasca, Sabrina Romanò, Aurelio Bonasera, Marija Mojsin, Jelena Pejić, and Milena Stevanović. 2021. "Facile Synthesis of L-Cysteine Functionalized Graphene Quantum Dots as a Bioimaging and Photosensitive Agent." *Nanomaterials* 11(8):1879.

Mondal, Naba Kumar, and Samarpita Chakraborty. 2020. "Adsorption of Cr (VI) from Aqueous Solution on Graphene Oxide (GO) Prepared from Graphite: Equilibrium, Kinetic and Thermodynamic Studies." *Applied Water Science* 10:1–10.

Moradi, Atefeh, Peyman Najafi Moghadam, Reza Hasanzadeh, and Mika Sillanpää. 2017. "Chelating Magnetic Nanocomposite for the Rapid Removal of Pb (II) Ions from Aqueous Solutions: Characterization, Kinetic, Isotherm and Thermodynamic Studies." *RSC Advances* 7(1):433–48.

Mukhopadhyay, Biswajit, Jon Sundquist, and Rodney J. Schmitz. 2007. "Removal of Cr (VI) from Cr-Contaminated Groundwater through Electrochemical Addition of Fe (II)." *Journal of Environmental Management* 82(1):66–76.

Muralikrishna, S., K. Sureshkumar, Thomas S. Varley, Doddahalli H. Nagaraju, and Thippeswamy Ramakrishnappa. 2014. "In Situ Reduction and Functionalization of Graphene Oxide with L-Cysteine for Simultaneous Electrochemical Determination of Cadmium (II), Lead (II), Copper (II), and Mercury (II) Ions." *Analytical Methods* 6(21):8698–8705.

Musa, H., Y. Musa, and M. Suleiman. 2019. "Synthesis and Characterization of Starch-Graft-Acrylamide Hydrogel for Oral Drug Delivery." *Nigerian Journal of Basic and Applied Sciences* 27(2):16–21.

Nasseh, Negin, Lobat Taghavi, Behnam Barikbin, and Ali Reza Harifi-Mood. 2017. "The Removal of Cr (VI) from Aqueous Solution by Almond Green Hull Waste Material: Kinetic and Equilibrium Studies." *Journal of Water Reuse and Desalination* 7(4):449–60.

Nekouei, Rasoul Khayyam, Farshid Pahlevani, Mohammad Assefi, Samane Maroufi, and Veena Sahajwalla. 2019. "Selective Isolation of Heavy Metals from Spent Electronic Waste Solution by Macroporous Ion-Exchange Resins." *Journal of Hazardous Materials* 371:389–96.

Nuengmatcha, Prawit, Ratana Mahachai, and Saksit Chanthai. 2015. "Adsorption of Functionalized Thiol-Graphene Oxide for Removal of Mercury from Aqueous Solution." *Asian Journal of Chemistry* 27(11):4167.

Ogawa, Kozo, Kunio Oka, and Toshifumi Yui. 1993. “X-Ray Study of Chitosan-Transition Metal Complexes.” *Chemistry of Materials* 5(5):726–28.

Pandey, Sadanand, and James Ramontja. 2016. “Guar Gum-Grafted Poly (Acrylonitrile)-Templated Silica Xerogel: Nanoengineered Material for Lead Ion Removal.” *Journal of Analytical Science and Technology* 7:1–15.

Park, Donghee, Chi Kyu Ahn, Young Mi Kim, Yeoung-Sang Yun, and Jong Moon Park. 2008. “Enhanced Abiotic Reduction of Cr (VI) in a Soil Slurry System by Natural Biomaterial Addition.” *Journal of Hazardous Materials* 160(2–3):422–27.

Pathak, Vaibhav. 2018. “Effect of Starch-Based Hydrogel on Early Growth of Corn.”

Paulino, Alexandre T., Laurence A. Belfiore, Lauro T. Kubota, Edvani C. Muniz, Vitor C. Almeida, and Elias B. Tambourgi. 2011. “Effect of Magnetite on the Adsorption Behavior of Pb (II), Cd (II), and Cu (II) in Chitosan-Based Hydrogels.” *Desalination* 275(1–3):187–96.

Pawlukojć, A., J. Leciejewicz, A. J. Ramirez-Cuesta, and J. Nowicka-Scheibe. 2005. “L-Cysteine: Neutron Spectroscopy, Raman, IR and Ab Initio Study.” *Spectrochimica Acta Part A: Molecular and Biomolecular Spectroscopy* 61(11–12):2474–81.

Pei, Guangpeng, Yuen Zhu, Junguo Wen, Yanxi Pei, and Hua Li. 2020. “Vinegar Residue Supported Nanoscale Zero-Valent Iron: Remediation of Hexavalent Chromium in Soil.” *Environmental Pollution* 256:113407.

Peng, Weijun, Luping Chang, Peiya Li, Guihong Han, Yukun Huang, and Yijun Cao. 2019. “An Overview on the Surfactants Used in Ion Flotation.” *Journal of Molecular Liquids* 286:110955.

Perez, Talita, Daniel Pasquini, Alexandre de Faria Lima, Eliane Vieira Rosa, Marcelo Henrique Sousa, Daniel Alves Cerqueira, and Luis Carlos de Morais. 2019. “Efficient Removal of Lead Ions from Water by Magnetic Nanosorbents Based on Manganese Ferrite Nanoparticles Capped with Thin Layers of Modified Biopolymers.” *Journal of Environmental Chemical Engineering* 7(1):102892.

Pooresmaeil, Malihe, and Hassan Namazi. 2020. “Application of Polysaccharide-Based Hydrogels for Water Treatments.” Pp. 411–55 in *Hydrogels based on natural polymers*. Elsevier.

Pour, Zahra Sekhavat, and Mousa Ghaemy. 2015. “Removal of Dyes and Heavy Metal Ions from Water by Magnetic Hydrogel Adsorbents Based on Poly (Vinyl Alcohol)/Carboxymethyl Starch-g-Poly (Vinyl Imidazole).” *RSC Advances*

5(79):64106–18.

Prakash, N., and S. Arungalai Vendan. 2016. “Biodegradable Polymer Based Ternary Blends for Removal of Trace Metals from Simulated Industrial Wastewater.” *International Journal of Biological Macromolecules* 83:198–208.

Preethi, Jayaram, Subbaiah Muthu Prabhu, and Sankaran Meenakshi. 2017. “Effective Adsorption of Hexavalent Chromium Using Biopolymer Assisted Oxyhydroxide Materials from Aqueous Solution.” *Reactive and Functional Polymers* 117:16–24.

Qian, Linbo, Xiao Shang, Bo Zhang, Wenying Zhang, Anqi Su, Yun Chen, Da Ouyang, Lu Han, Jingchun Yan, and Mengfang Chen. 2019. “Enhanced Removal of Cr (VI) by Silicon Rich Biochar-Supported Nanoscale Zero-Valent Iron.” *Chemosphere* 215:739–45.

Radwan, Mohamed A., and Ahmed K. Salama. 2006. “Market Basket Survey for Some Heavy Metals in Egyptian Fruits and Vegetables.” *Food and Chemical Toxicology* 44(8):1273–78.

Raghi, K. R., D. R. Sherin, M. J. Saumya, P. S. Arun, V. N. Sobha, and T. K. Manojkumar. 2018. “Computational Study of Molecular Electrostatic Potential, Docking and Dynamics Simulations of Gallic Acid Derivatives as ABL Inhibitors.” *Computational Biology and Chemistry* 74:239–46. doi: https://doi.org/10.1016/j.compbiolchem.2018.04.001.

Rao, Vijayalaxmi, P. Latha, P. V Ashokan, and M. H. Shridhar. 1999. “Thermal Degradation of Poly(N-Vinylpyrrolidone)–Poly(Vinyl Alcohol) Blends.” *Polymer Journal* 31(10):887–89. doi: 10.1295/polymj.31.887.

Ren, Genkuan, Xinlong Wang, Penghui Huang, Benhe Zhong, Zhiye Zhang, Lin Yang, and Xiushan Yang. 2017. “Chromium (VI) Adsorption from Wastewater Using Porous Magnetite Nanoparticles Prepared from Titanium Residue by a Novel Solid-Phase Reduction Method.” *Science of the Total Environment* 607:900–910.

Ren, Yueming, Xizhu Wei, and Milin Zhang. 2008. “Adsorption Character for Removal Cu (II) by Magnetic Cu (II) Ion Imprinted Composite Adsorbent.” *Journal of Hazardous Materials* 158(1):14–22.

Ribeiro, Igor Hernandes Santos, Davi Texeira Reis, and Douglas Henrique Pereira. 2019. “A DFT-Based Analysis of Adsorption of Cd2+, Cr3+, Cu2+, Hg2+, Pb2+, and Zn2+, on Vanillin Monomer: A Study of the Removal of Metal Ions from Effluents.” *Journal of Molecular Modeling* 25(9):267.

Rodrigues, M. A. S., Franco Dani Rico Amado, J. L. N. Xavier, K. F. Streit, A. M. Bernardes, and J. Zoppas Ferreira. 2008. "Application of Photoelectrochemical–Electrodialysis Treatment for the Recovery and Reuse of Water from Tannery Effluents." *Journal of Cleaner Production* 16(5):605–11.

Sadeghi, Mohammad, and Fatemeh Soleimani. 2012. "Synthesis of PH-Sensitive Hydrogel Based on Starch-Polyacrylate Superabsorbent."

Sahraei, Razieh, Zahra Sekhavat Pour, and Mousa Ghaemy. 2017. "Novel Magnetic Bio-Sorbent Hydrogel Adsorbents Based on Modified Gum Tragacanth/Graphene Oxide: Removal of Heavy Metals and Dyes from Water." *Journal of Cleaner Production* 142:2973–84.

Sanchez-Hachair, Arnaud, and Annette Hofmann. 2018. "Hexavalent Chromium Quantification in Solution: Comparing Direct UV–Visible Spectrometry with 1, 5-Diphenylcarbazide Colorimetry." *Comptes Rendus Chimie* 21(9):890–96.

Sandoval, Claudia, Cristian Castro, Ligia Gargallo, Deodato Radic, and Juan Freire. 2005. "Specific Interactions in Blends Containing Chitosan and Functionalized Polymers. Molecular Dynamics Simulations." *Polymer* 46(23):10437–42.

Setty, C. Mallikarjuna, Anand S. Deshmukh, and Aravind M. Badiger. 2014. "Hydrolyzed Polyacrylamide Grafted Maize Starch Based Microadsorbents: Application in PH Responsive Drug Delivery." *International Journal of Biological Macromolecules* 70:1–9.

Shaker, Medhat A., and Amr A. Yakout. 2016. "Optimization, Isotherm, Kinetic and Thermodynamic Studies of Pb (II) Ions Adsorption onto N-Maleated Chitosan-Immobilized TiO2 Nanoparticles from Aqueous Media." *Spectrochimica Acta Part A: Molecular and Biomolecular Spectroscopy* 154:145–56.

Shrestha, Rakesh, Sagar Ban, Sijan Devkota, Sudip Sharma, Rajendra Joshi, Arjun Prasad Tiwari, Hak Yong Kim, and Mahesh Kumar Joshi. 2021. "Technological Trends in Heavy Metals Removal from Industrial Wastewater: A Review." *Journal of Environmental Chemical Engineering* 9(4):105688.

Singh, Shrawan K., Walter Z. Tang, and Georgio Tachiev. 2013. "Fenton Treatment of Landfill Leachate under Different COD Loading Factors." *Waste Management* 33(10):2116–22. doi: https://doi.org/10.1016/j.wasman.2013.06.019.

Smara, Abdelaziz, Rachid Delimi, Christiane Poinsignon, and Jacqueline Sandeaux. 2005. "Electroextraction of Heavy Metals from Diluted Solutions by a Process Combining

Ion-Exchange Resins and Membranes." *Separation and Purification Technology* 44(3):271–77.

Spagnol, Cristiane, Francisco H. A. Rodrigues, Antonio G. B. Pereira, André R. Fajardo, Adley F. Rubira, and Edvani C. Muniz. 2012. "Superabsorbent Hydrogel Nanocomposites Based on Starch-g-Poly (Sodium Acrylate) Matrix Filled with Cellulose Nanowhiskers." *Cellulose* 19:1225–37.

Suwalsky, M., R. Castro, F. Villena, and C. P. Sotomayor. 2008. "Cr (III) Exerts Stronger Structural Effects than Cr (VI) on the Human Erythrocyte Membrane and Molecular Models." *Journal of Inorganic Biochemistry* 102(4):842–49.

T. H. Dunning Jr. and P. J. Hay. 1977. "In Modern Theoretical Chemistry." Ed. H. F.:1–28.

Taghizadeh, Mohammad Taghi, and Narges Sabouri. 2013. "Biodegradation Behaviors and Water Adsorption of Poly (Vinyl Alcohol)/Starch/Carboxymethyl Cellulose/Clay Nanocomposites." *International Nano Letters* 3:1–8.

Tahmasebi, Elham. 2020. "Insights into the Adsorption Mechanism of Al30 Polyoxocations-Modified Graphene Oxide Nanosheets for Efficient Removal of Phosphate, Chromate and Selenate Oxyanions: A Comparative Study." *Journal of Molecular Liquids* 299:112111.

Tan, K. L., and B. H. Hameed. 2017. "Insight into the Adsorption Kinetics Models for the Removal of Contaminants from Aqueous Solutions." *Journal of the Taiwan Institute of Chemical Engineers* 74:25–48.

Tang, Xuejiao, Lan Gan, Yuxin Duan, Yanmei Sun, Yifan Zhang, and Zhidan Zhang. 2017. "A Novel Cd2+-Imprinted Chitosan-Based Composite Membrane for Cd2+ Removal from Aqueous Solution." *Materials Letters* 198:121–23.

Taseidifar, Mojtaba, Fatemeh Makavipour, Richard M. Pashley, and A. F. M. Mokhlesur Rahman. 2017. "Removal of Heavy Metal Ions from Water Using Ion Flotation." *Environmental Technology & Innovation* 8:182–90.

Town, Raewyn M., and Montserrat Filella. 2002. "Implications of Natural Organic Matter Binding Heterogeneity on Understanding Lead (II) Complexation in Aquatic Systems." *Science of the Total Environment* 300(1–3):143–54.

Turan, Eylem, Serkan Demirci, and Tuncer Caykara. 2009. "Preparation of Polyacrylamide Hydrogels at Various Charge Densities by Postmodification." *Journal of Applied Polymer Science* 111(1):108–13.

Unuabonah, E. I., K. O. Adebowale, and B. I. Olu-Owolabi. 2007. "Kinetic and

Thermodynamic Studies of the Adsorption of Lead (II) Ions onto Phosphate-Modified Kaolinite Clay." *Journal of Hazardous Materials* 144(1–2):386–95.

Valentín-Reyes, J., R. B. García-Reyes, A. García-González, E. Soto-Regalado, and F. Cerino-Córdova. 2019. "Adsorption Mechanisms of Hexavalent Chromium from Aqueous Solutions on Modified Activated Carbons." *Journal of Environmental Management* 236:815–22.

Vellingiri, Kowsalya, Ya-Xin Deng, Ki-Hyun Kim, Jheng-Jie Jiang, Taejin Kim, Jin Shang, Wha-Seung Ahn, Deepak Kukkar, and Danil W. Boukhvalov. 2018. "Amine-Functionalized Metal–Organic Frameworks and Covalent Organic Polymers as Potential Sorbents for Removal of Formaldehyde in Aqueous Phase: Experimental versus Theoretical Study." *ACS Applied Materials & Interfaces* 11(1):1426–39.

Wang, Jianlong, and Xuan Guo. 2020. "Adsorption Kinetic Models: Physical Meanings, Applications, and Solving Methods." *Journal of Hazardous Materials* 390:122156.

Wang, Jianlong, and Shuting Zhuang. 2017. "Removal of Various Pollutants from Water and Wastewater by Modified Chitosan Adsorbents." *Critical Reviews in Environmental Science and Technology* 47(23):2331–86.

Wang, Lawrence K., Yung-Tse Hung, and Nazih K. Shammas. 2005. *Physicochemical Treatment Processes*. Vol. 3. Springer.

Wang, Xiangxue, Zhongshan Chen, and Shubing Yang. 2015. "Application of Graphene Oxides for the Removal of Pb (II) Ions from Aqueous Solutions: Experimental and DFT Calculation." *Journal of Molecular Liquids* 211:957–64.

Wei, Xiuzhen, Xin Kong, Songxue Wang, Hai Xiang, Jiade Wang, and Jinyuan Chen. 2013. "Removal of Heavy Metals from Electroplating Wastewater by Thin-Film Composite Nanofiltration Hollow-Fiber Membranes." *Industrial & Engineering Chemistry Research* 52(49):17583–90.

Wu, Ruiping. 2019. "Removal of Heavy Metal Ions from Industrial Wastewater Based on Chemical Precipitation Method." *Ekoloji Dergisi* (107).

Wu, Shu-Ping, Xiang-Zi Dai, Jia-Rui Kan, Fang-Di Shilong, and Mai-Yong Zhu. 2017. "Fabrication of Carboxymethyl Chitosan–Hemicellulose Resin for Adsorptive Removal of Heavy Metals from Wastewater." *Chinese Chemical Letters* 28(3):625–32.

Xia, Zhiyong, Lance Baird, Natasha Zimmerman, and Matthew Yeager. 2017. "Heavy Metal Ion Removal by Thiol Functionalized Aluminum Oxide Hydroxide Nanowhiskers." *Applied Surface Science* 416:565–73.

Yap, Pei Lay, Yow Loo Auyoong, Kamrul Hassan, Farzaneh Farivar, Diana N. H. Tran, Jun Ma, and Dusan Losic. 2020. “Multithiol Functionalized Graphene Bio-Sponge via Photoinitiated Thiol-Ene Click Chemistry for Efficient Heavy Metal Ions Adsorption.” *Chemical Engineering Journal* 395:124965.

Yin, Na, Ke Wang, Lizhen Wang, and Zongqun Li. 2016. “Amino-Functionalized MOFs Combining Ceramic Membrane Ultrafiltration for Pb (II) Removal.” *Chemical Engineering Journal* 306:619–28.

Yu, Caixia, Zhichao Shao, and Hongwei Hou. 2017. “A Functionalized Metal–Organic Framework Decorated with O− Groups Showing Excellent Performance for Lead (II) Removal from Aqueous Solution.” *Chemical Science* 8(11):7611–19.

Yu, Jie, Jidong Zheng, Quanfang Lu, Shuxiu Yang, Xiaomei Zhang, Xing Wang, and Wu Yang. 2016. “Selective Adsorption and Reusability Behavior for Pb 2+ and Cd 2+ on Chitosan/Poly (Ethylene Glycol)/Poly (Acrylic Acid) Adsorbent Prepared by Glow-Discharge Electrolysis Plasma.” *Colloid and Polymer Science* 294:1585–98.

Yuan, Zhihua, Xiaoxia Cheng, Lubin Zhong, Renxiang Wu, and Yuming Zheng. 2019. “Preparation, Characterization and Performance of an Electrospun Carbon Nanofiber Mat Applied in Hexavalent Chromium Removal from Aqueous Solution.” *Journal of Environmental Sciences* 77:75–84.

Yuvaraja, Gutha, Yixiong Pang, Di-Yun Chen, Ling-Jun Kong, Sajid Mehmood, Munagapati Venkata Subbaiah, Devineni Subba Rao, Chandra Mouli Pavuluri, Jet-Chau Wen, and Guda Mallikarjuna Reddy. 2019. “Modification of Chitosan Macromolecule and Its Mechanism for the Removal of Pb (II) Ions from Aqueous Environment.” *International Journal of Biological Macromolecules* 136:177–88.

Zhang, Cheng, Jiehe Sui, Jing Li, Yilun Tang, and Wei Cai. 2012. “Efficient Removal of Heavy Metal Ions by Thiol-Functionalized Superparamagnetic Carbon Nanotubes.” *Chemical Engineering Journal* 210:45–52.

Zhang, Dan, Lan Wang, Hehua Zeng, Peng Yan, Jing Nie, Virender K. Sharma, and Chuanyi Wang. 2019. “A Three-Dimensional Macroporous Network Structured Chitosan/Cellulose Biocomposite Sponge for Rapid and Selective Removal of Mercury (II) Ions from Aqueous Solution.” *Chemical Engineering Journal* 363:192–202.

Zhang, Haifeng, Qifeng Dang, Chengsheng Liu, Dongsu Cha, Zhenzhen Yu, Wenjing Zhu, and Bing Fan. 2017. “Uptake of Pb (II) and Cd (II) on Chitosan Microsphere Surface Successively Grafted by Methyl Acrylate and Diethylenetriamine.” *ACS Applied*

Materials & Interfaces 9(12):11144–55.

Zhang, Jinmiao, Zhenhu Xiong, Chen Li, and Chunsheng Wu. 2016. "Exploring a Thiol-Functionalized MOF for Elimination of Lead and Cadmium from Aqueous Solution." *Journal of Molecular Liquids* 221:43–50.

Zhang, Runyuan, Nuanqin Zhang, and Zhanqiang Fang. 2018. "In Situ Remediation of Hexavalent Chromium Contaminated Soil by CMC-Stabilized Nanoscale Zero-Valent Iron Composited with Biochar." *Water Science and Technology* 77(6):1622–31.

Zhang, Sam, Lin Li, and Ashok Kumar. 2008. *Materials Characterization Techniques*. CRC press.

Zhang, Xin, Shen Lin, Zuliang Chen, Mallavarapu Megharaj, and Ravendra Naidu. 2011. "Kaolinite-Supported Nanoscale Zero-Valent Iron for Removal of Pb2+ from Aqueous Solution: Reactivity, Characterization and Mechanism." *Water Research* 45(11):3481–88.

Zhao, Feiping, Eveliina Repo, Dulin Yin, and Mika E. T. Sillanpää. 2013. "Adsorption of Cd (II) and Pb (II) by a Novel EGTA-Modified Chitosan Material: Kinetics and Isotherms." *Journal of Colloid and Interface Science* 409:174–82.

Zhao, Feiping, Walter Z. Tang, Dongbo Zhao, Yong Meng, Dulin Yin, and Mika Sillanpää. 2014. "Adsorption Kinetics, Isotherms and Mechanisms of Cd (II), Pb (II), Co (II) and Ni (II) by a Modified Magnetic Polyacrylamide Microcomposite Adsorbent." *Journal of Water Process Engineering* 4:47–57.

Zhao, Jiling, Chen Wang, Shixing Wang, and Yang Zhou. 2020. "Experimental and DFT Study of Selective Adsorption Mechanisms of Pb (II) by UiO-66-NH2 Modified with 1, 8-Dihydroxyanthraquinone." *Journal of Industrial and Engineering Chemistry* 83:111–22.

Zhitkovich, Anatoly. 2005. "Importance of Chromium− DNA Adducts in Mutagenicity and Toxicity of Chromium (VI)." *Chemical Research in Toxicology* 1(18):3–11.

Zhou, Ke, Yaochi Liu, Zhaoguang Yang, Ting Xie, Houzhi Liu, and Chubin Zhong. 2016. "Adsorptive Removal of Heavy Metals by a Bio-Based Polymeric Material PAO-CI from Wastewater." *Journal of the Taiwan Institute of Chemical Engineers* 61:342–50.

Zhu, Yehua, Jun Hu, and Jianlong Wang. 2014. "Removal of Co2+ from Radioactive Wastewater by Polyvinyl Alcohol (PVA)/Chitosan Magnetic Composite." *Progress in Nuclear Energy* 71:172–78.

Annexes

Annex 1| Calibration curve

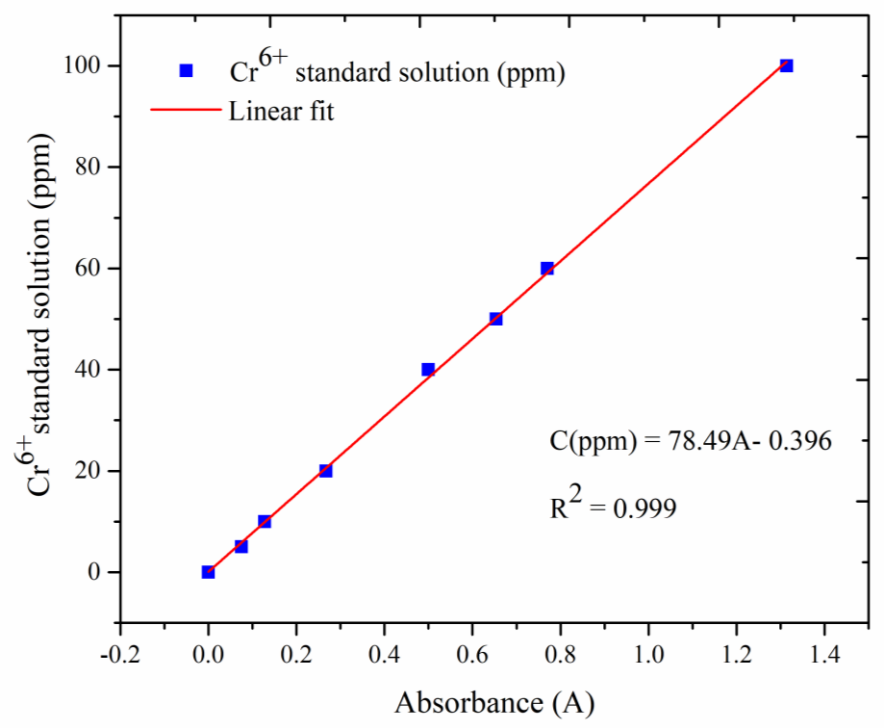

Annex 2| Grafted starch synthesis (lab images and Schematic diagram).

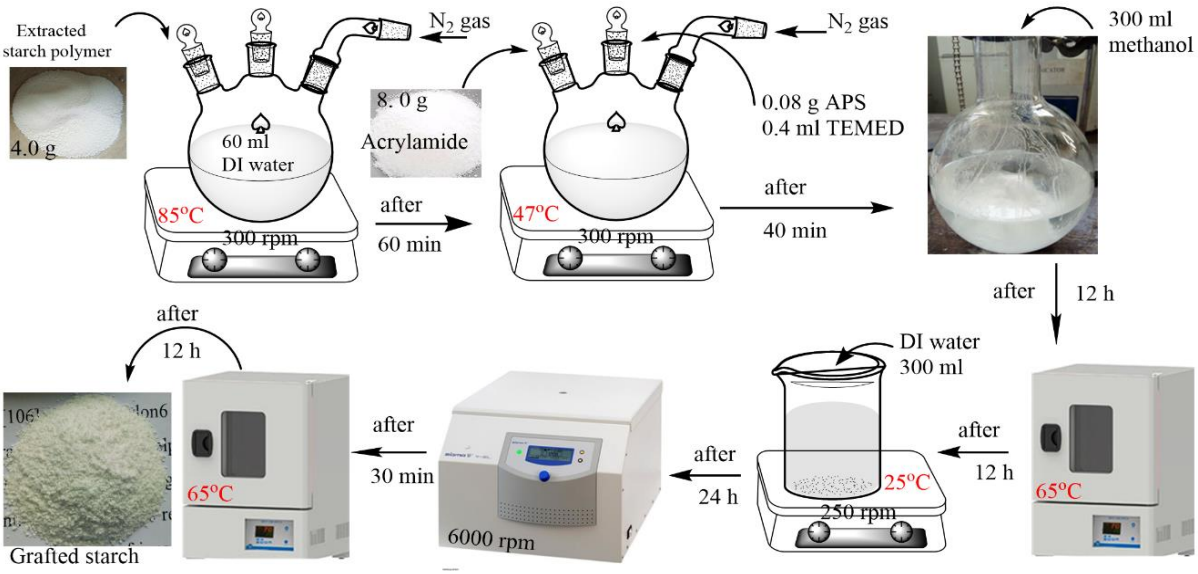

Annex 3| Graphene oxide synthesis by improved Hummer's method.

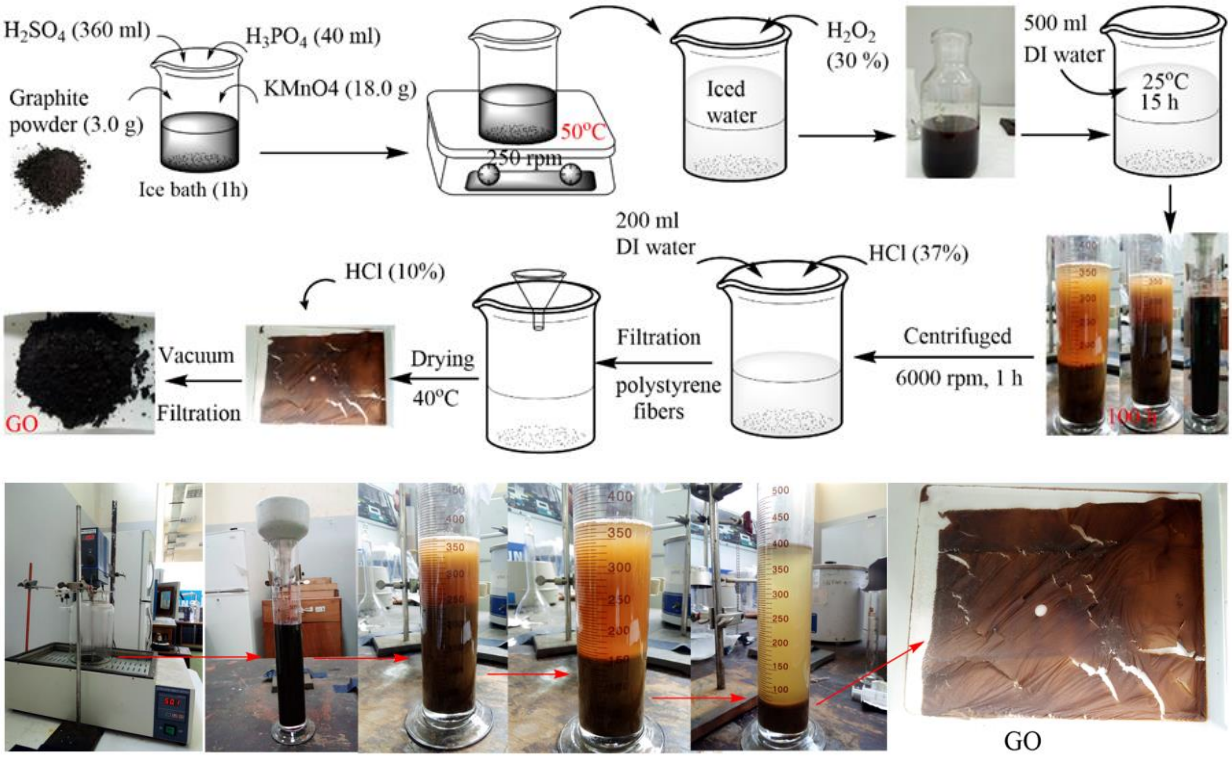

Annex 4| Graphene oxide functionalization with L-cysteine

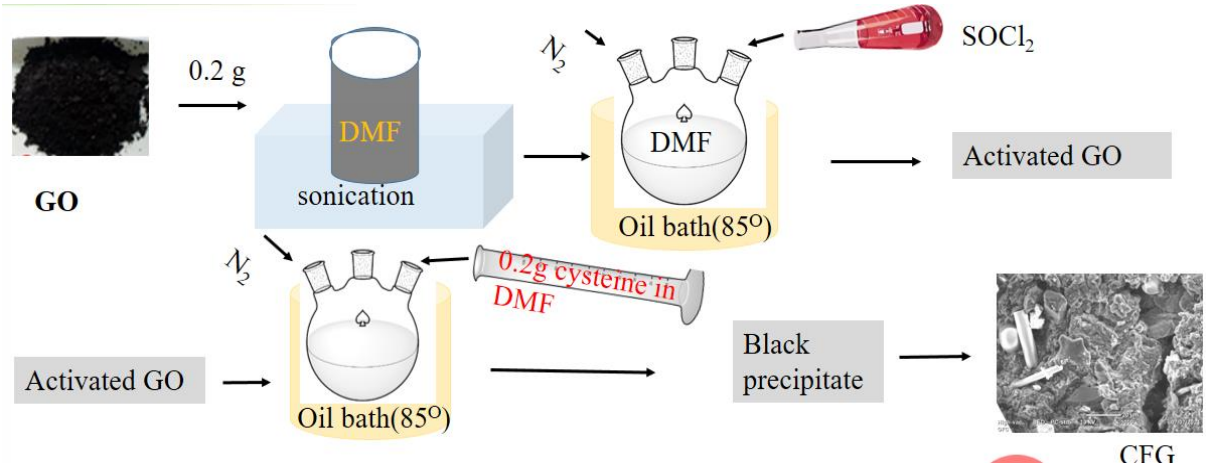

Annex 5| PPSgCG hydrogel synthesis

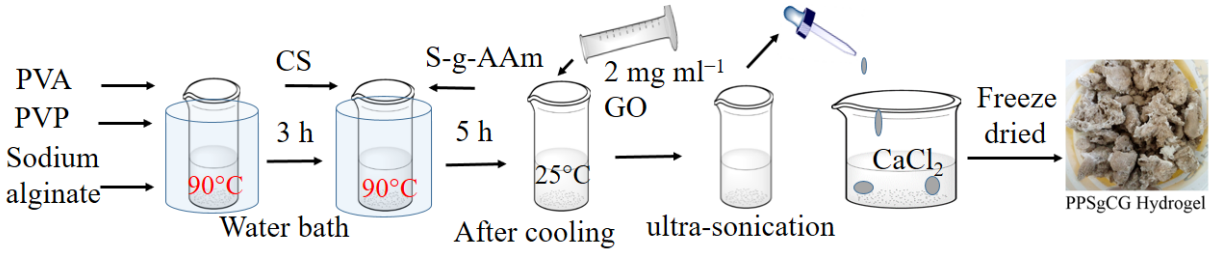

Annex 6| PCCFG hydrogel synthesis

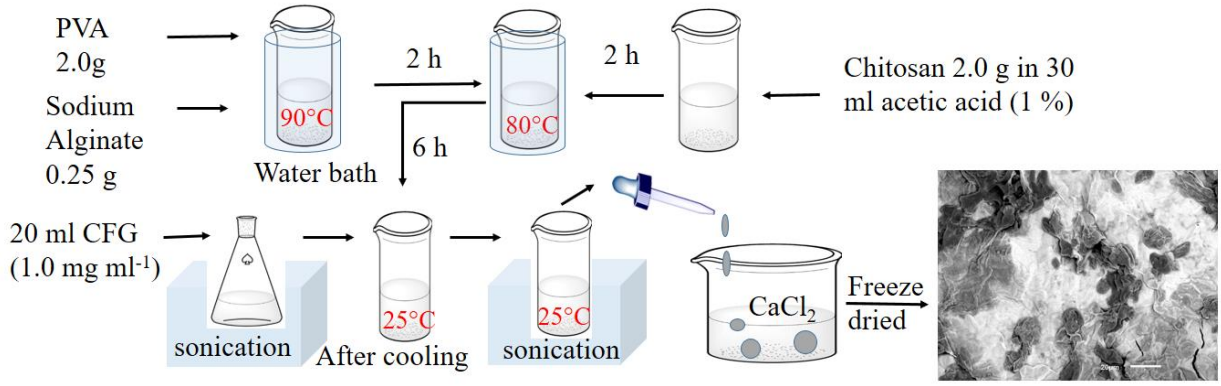

Annex 7| CZVI – CS – PVA hydrogel synthesis

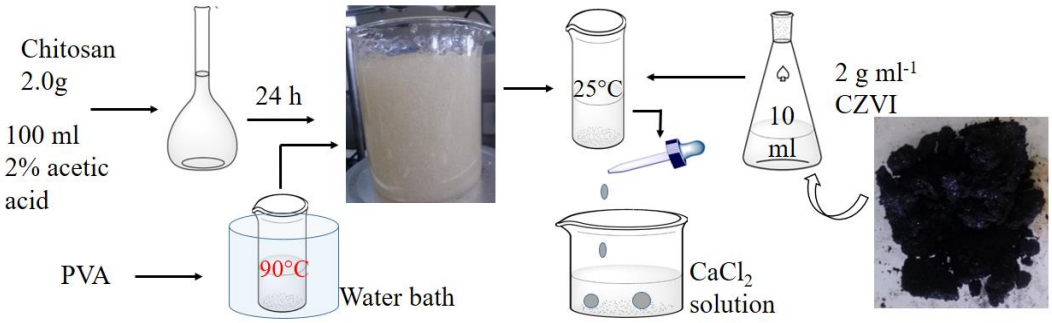

Annex 8| Optimization–frequency calculation of PPSgCG–I: showing convergence/DFT/B3PW91–D3/6-31G(d).

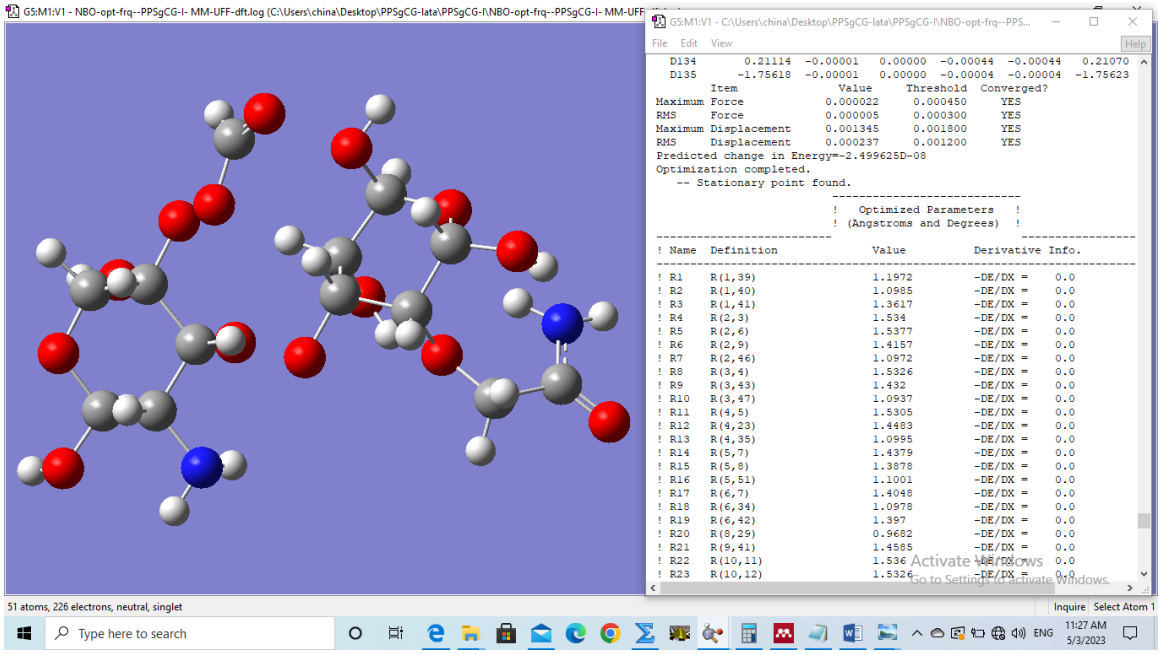

Annex 9| Optimization–frequency calculation of PPSgCG–I: showing +ve frequency/DFT/B3PW91–D3/6-31G(d).

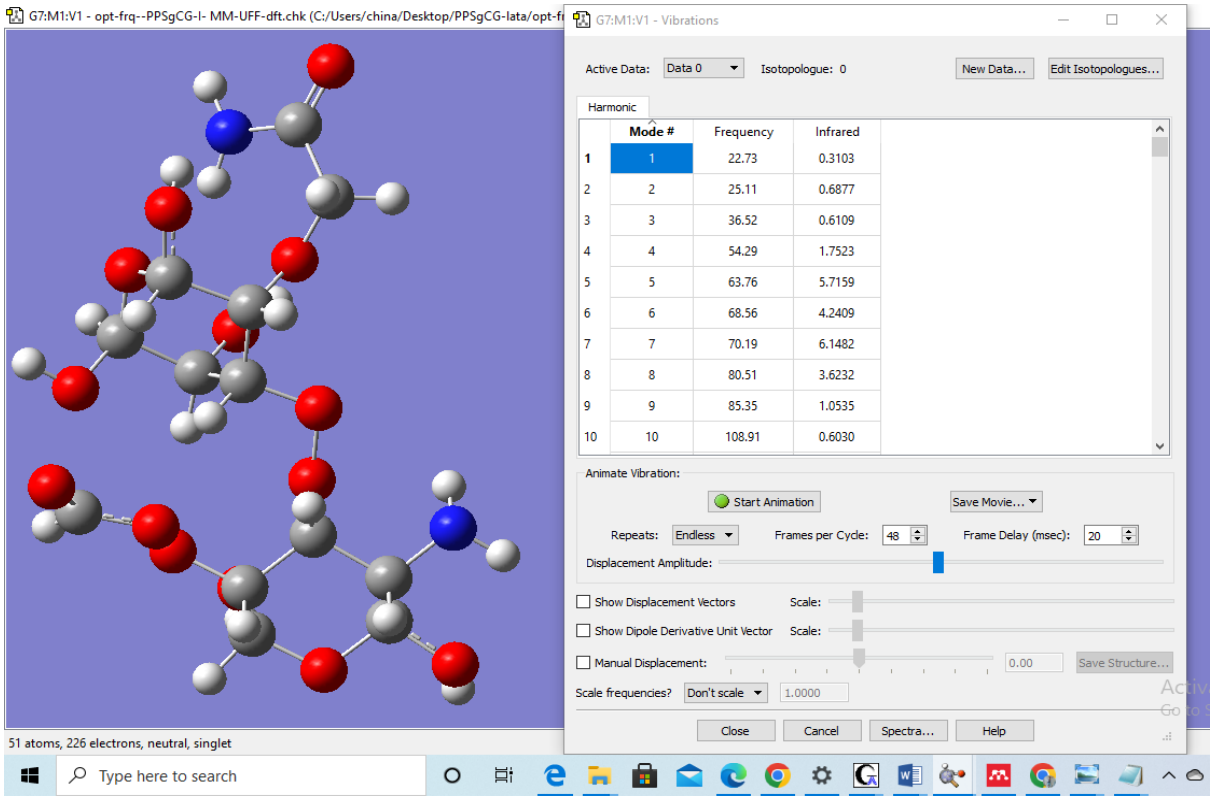

Annex 10| Bond length (Å) of converged PPSgCG–I/ DFT/B3PW91–D3/6-31G(d)/SDD.

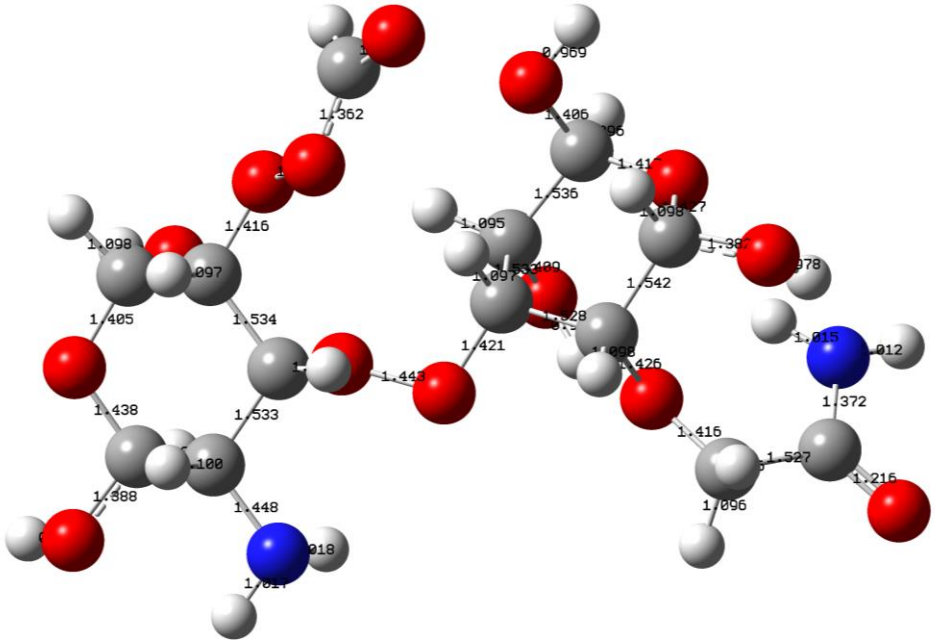

Annex 11| Bond length (Å) of converged PPSgCG–I@Cr^{6+}/ DFT/B3PW91–D3/6-31G(d)/SDD.

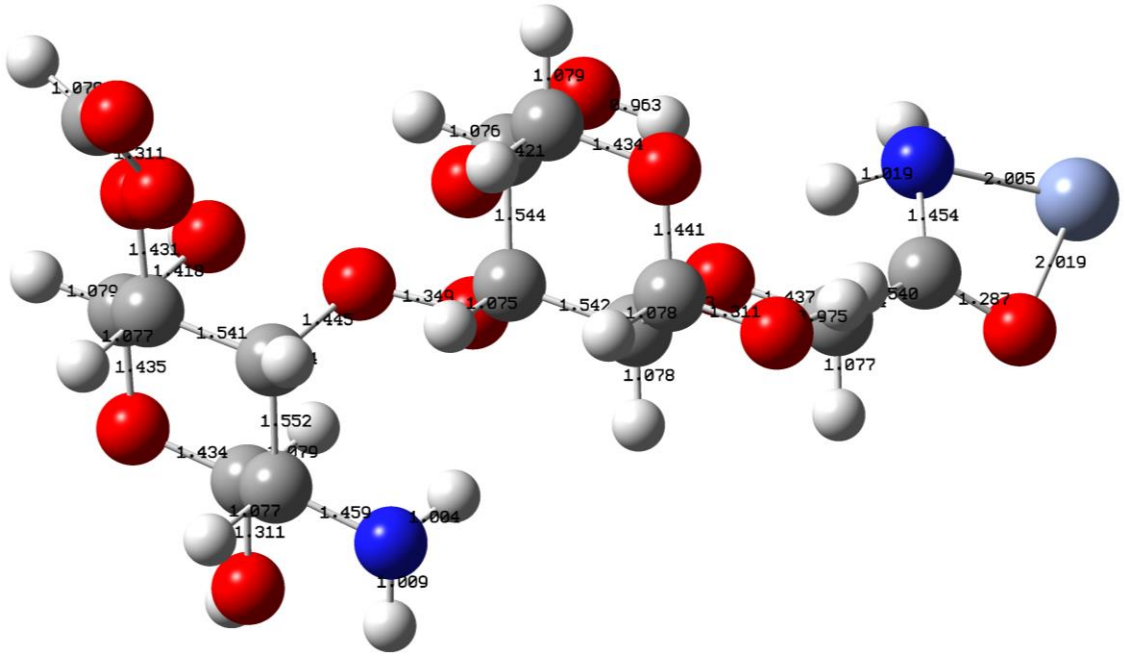

Annex 12| HOMO (with orbital energy) of PPSgCG–I/DFT/wB97XD/6-311+G(d,p)

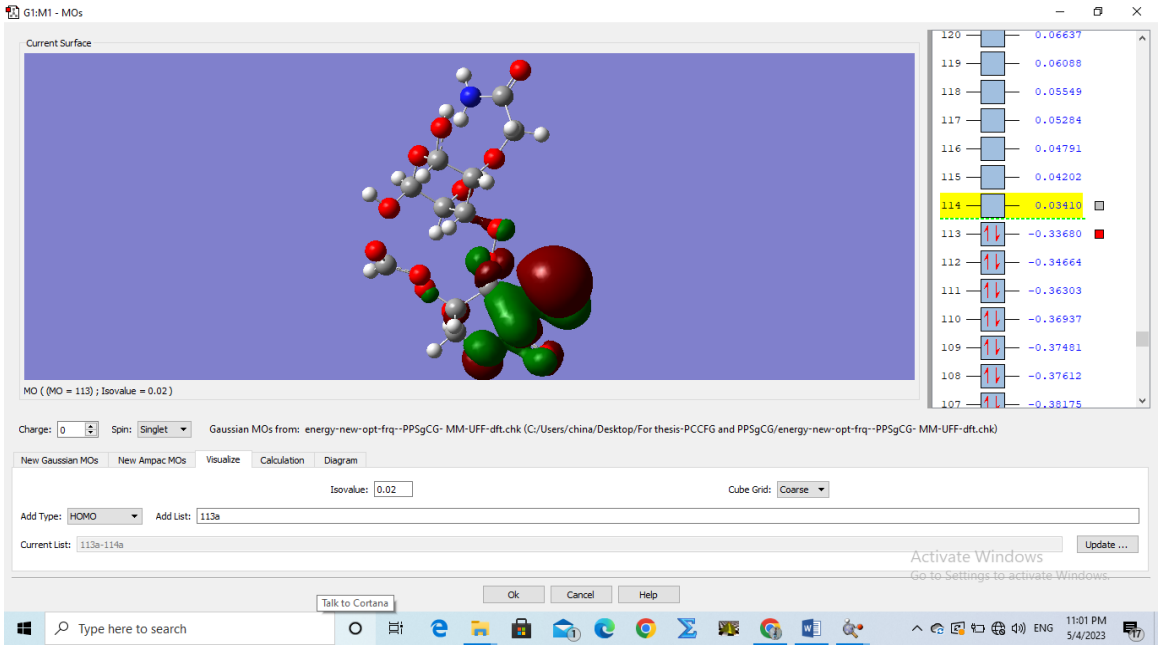

Annex 13| LUMO (with orbital energy) of PPSgCG–I/DFT/wB97XD/6-311+G(d,p)

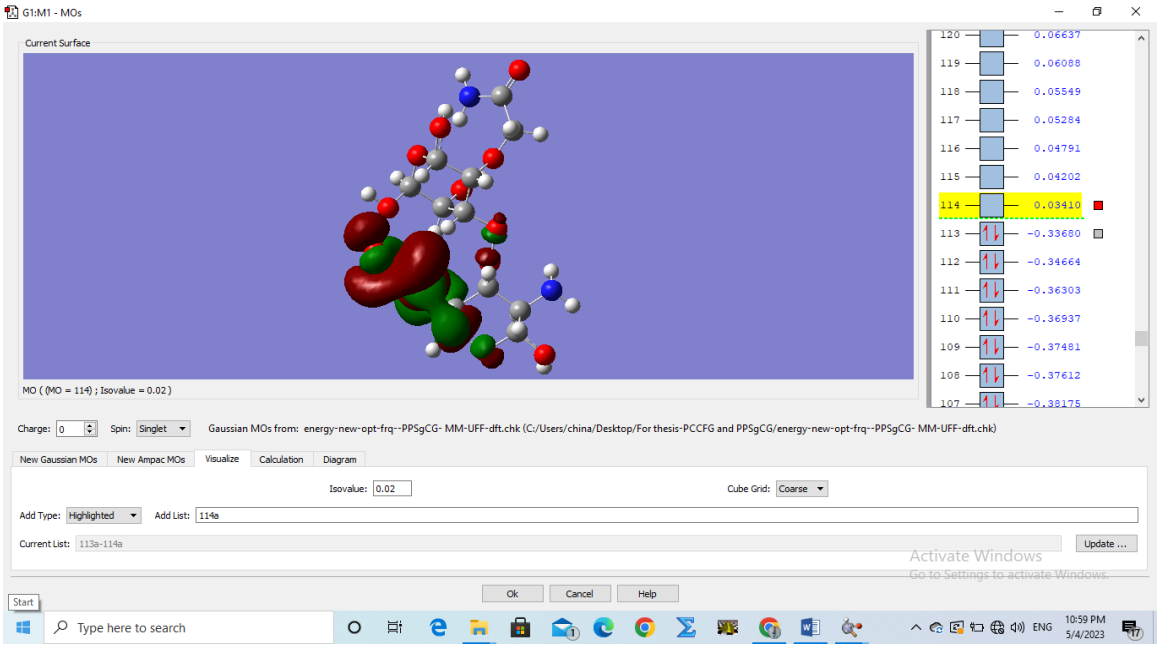

Annex 14| IR (from frequency calculation) of PPSgCG–I/ DFT/B3PW91–D3/6-31G(d)/SDD.

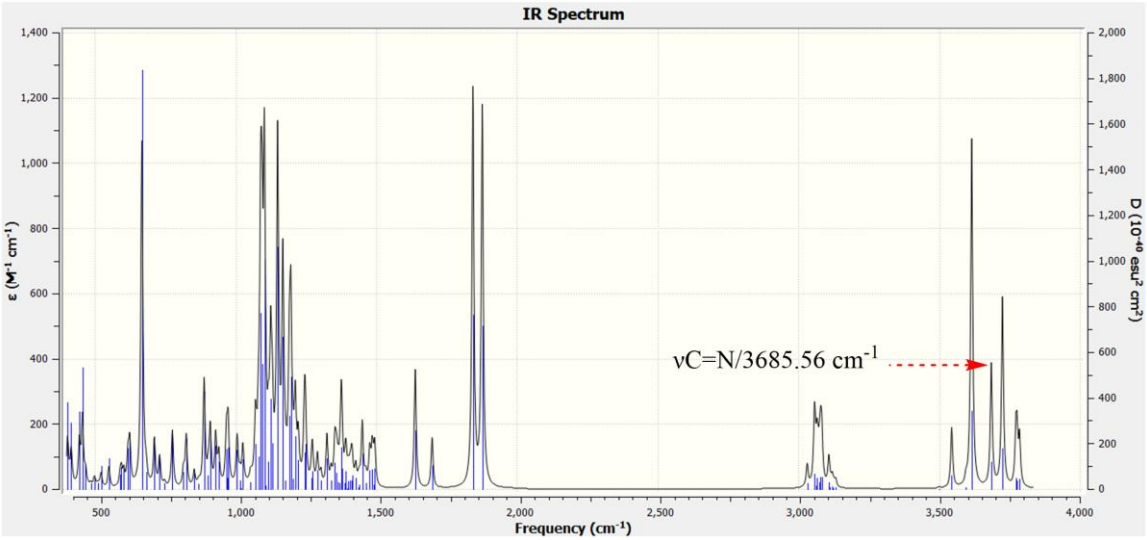

Annex 15| IR of converged PPSgCG–I@Cr^{6+}/ DFT/B3PW91–D3/6-31G(d)/SDD.

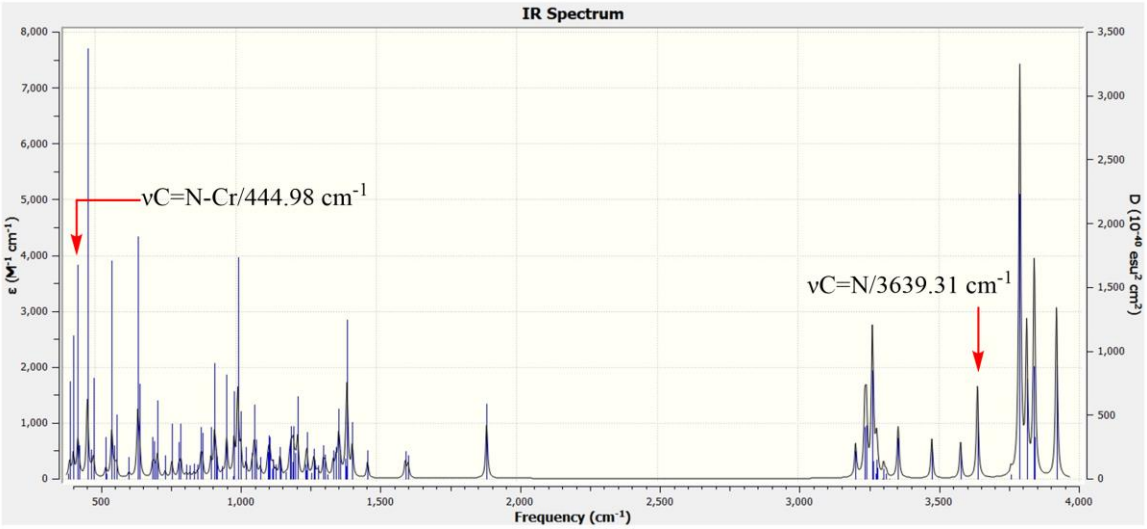

Annex 12| Total NBO charge of PPSgCG–I/ DFT/B3PW91–D3/6–31G(d).

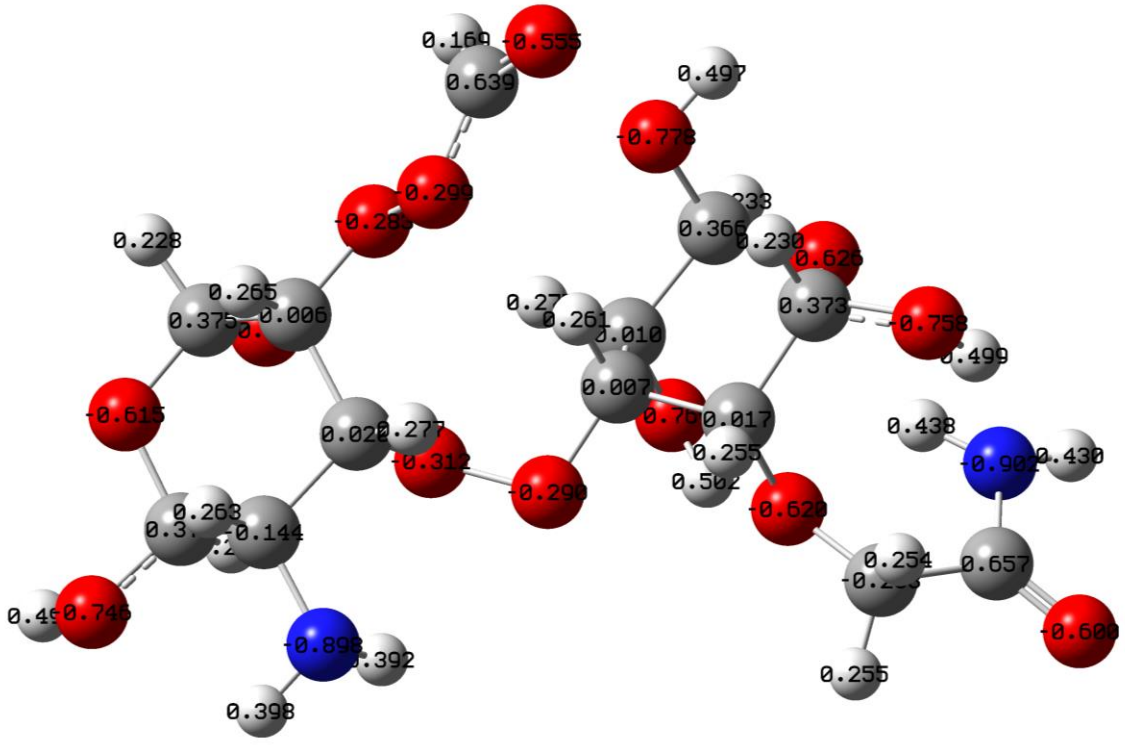

Annex 18| Optimization – frequency calculation of PCCFG–I: showing convergence criteria/DFT/B3PW91–D3/6-31G(d).

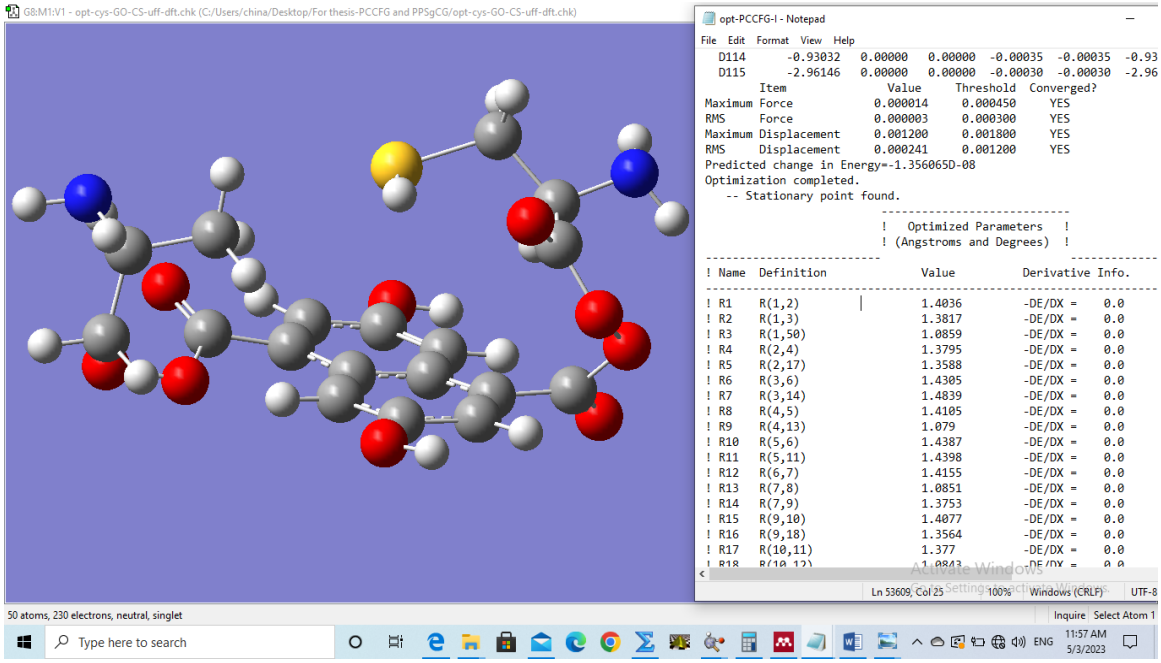

Annex 19| Bond length (Å) of optimized PCCFG–I/DFT/B3PW91–D3/6-31G(d).

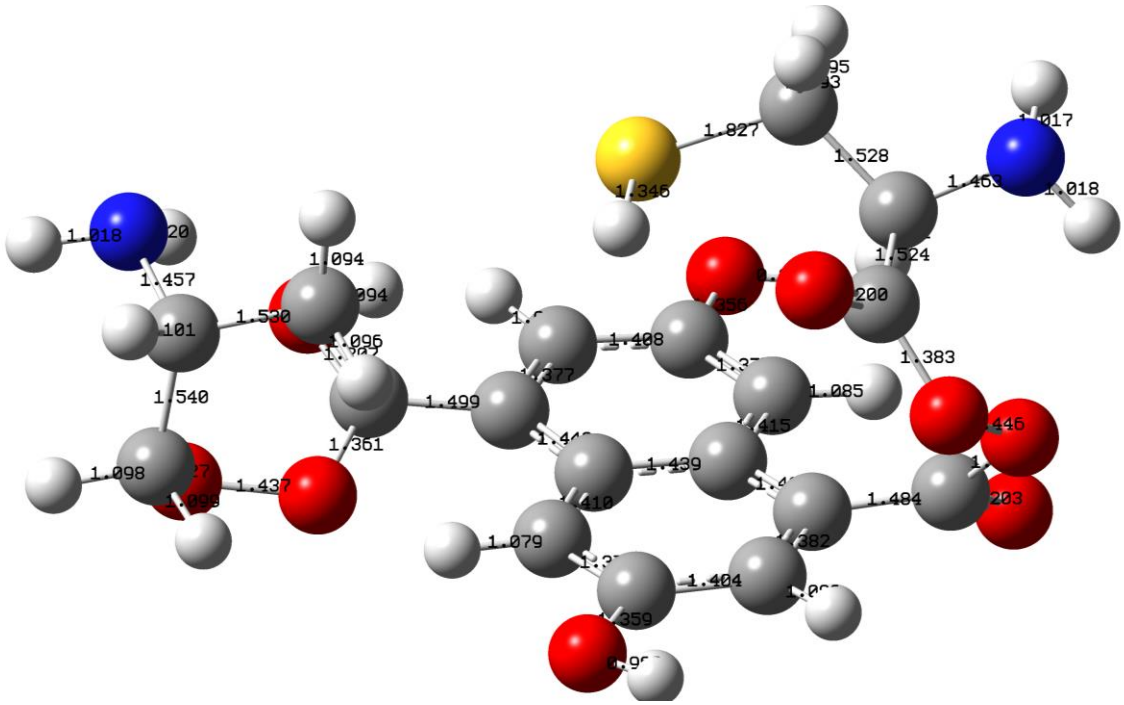

Annex 20| Bond length (Å) of optimized PCCFG–I@Pb^{2+}/DFT/B3PW91–D3/6-31G(d).

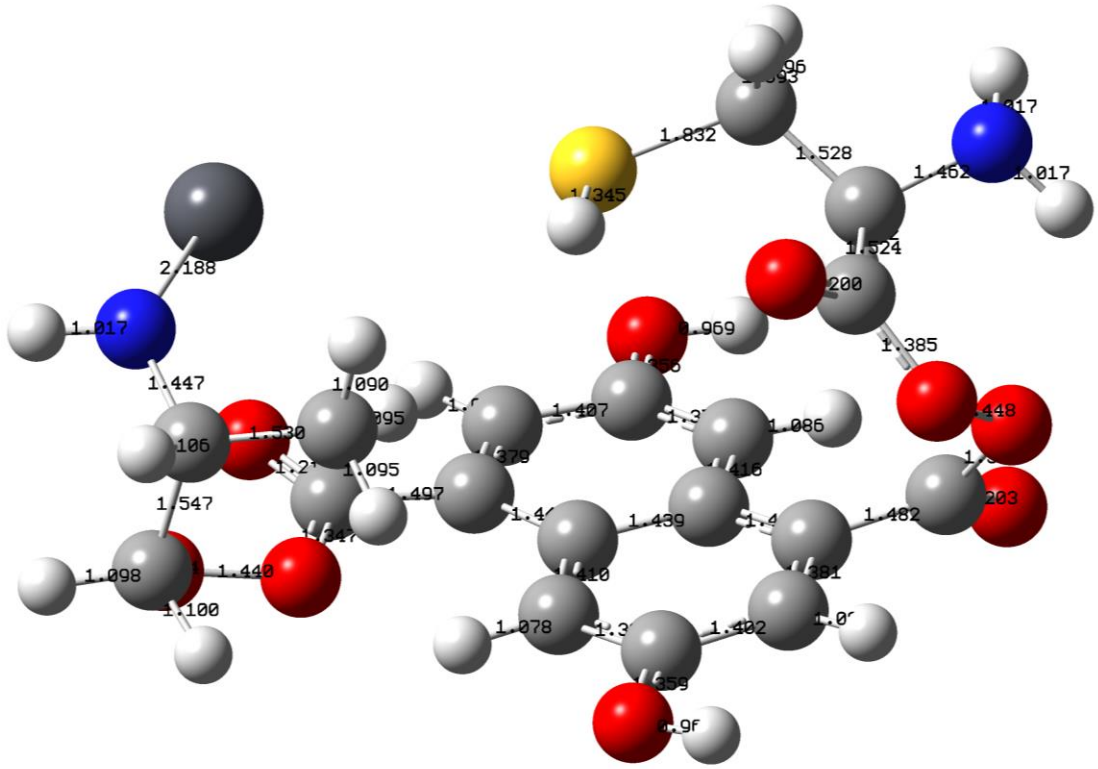

Annex 21| HOMO (with orbital energy) of PCCFG–I/DFT/wB97XD/6-311+G(d,p)

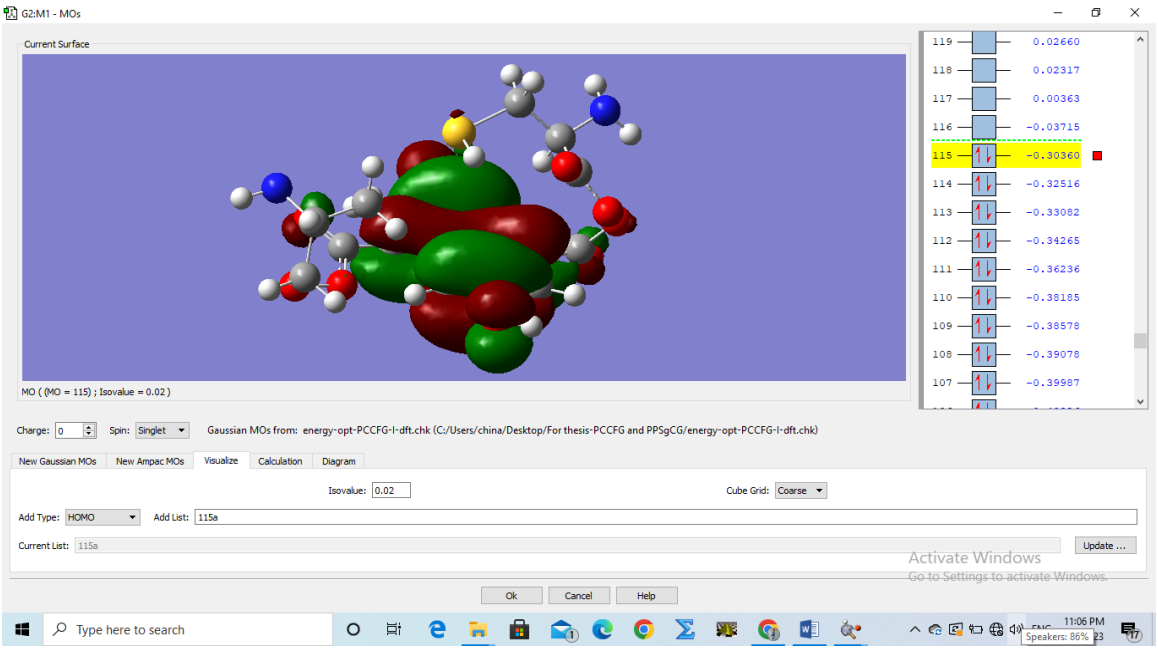

Annex 22|LUMO (with orbital energy) of PCCFG–I/DFT/wB97XD/6-311+G(d,p)

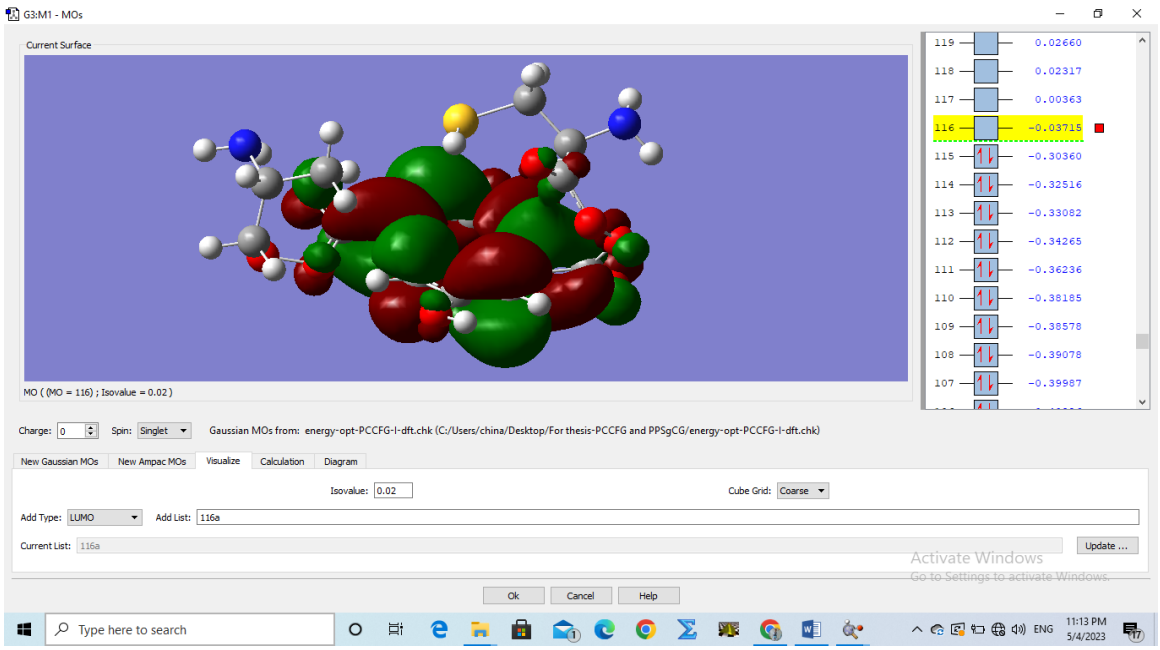

Annex 23| Frequency of converged PCCFG–I/ DFT/B3PW91–D3/6-31G(d)/SDD

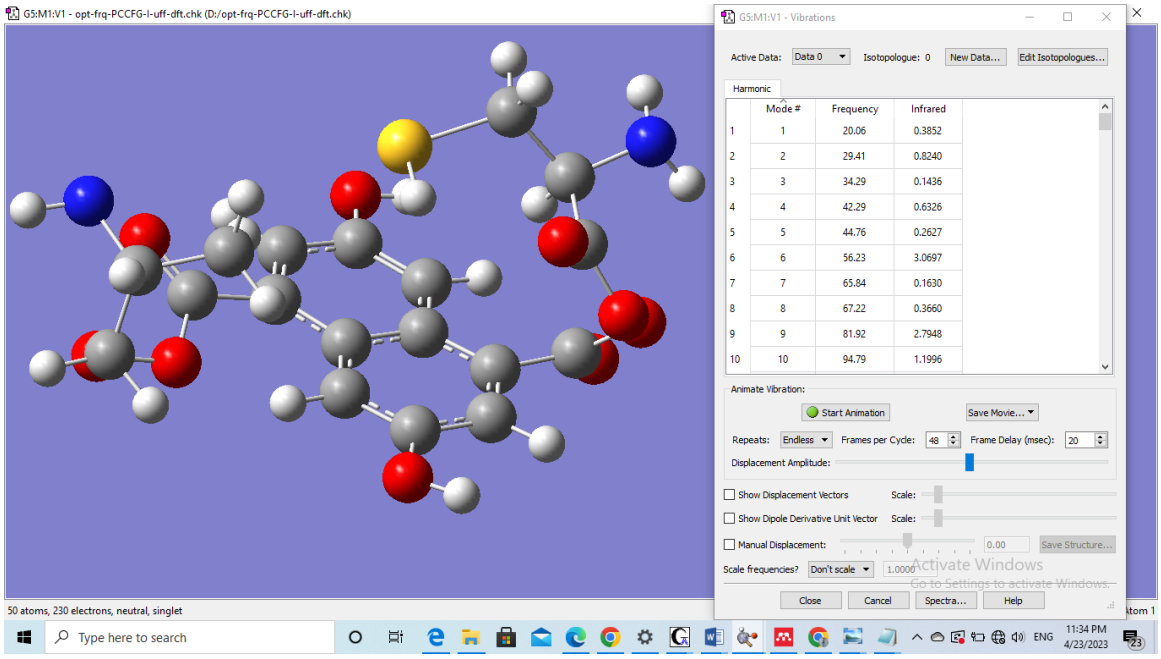

Annex 24| IR (from frequency calculation) of PCCFG–I/ DFT/B3PW91–D3/6-31G(d)/SDD

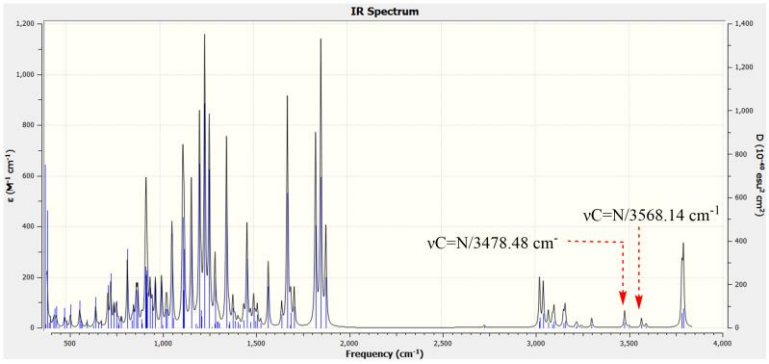

Annex 25| Optimization – frequency calculation of PCCFG–I@Pb^{2+}:

Showing convergence criteria/DFT/B3PW91–D3/6-31G(d)/SDD.

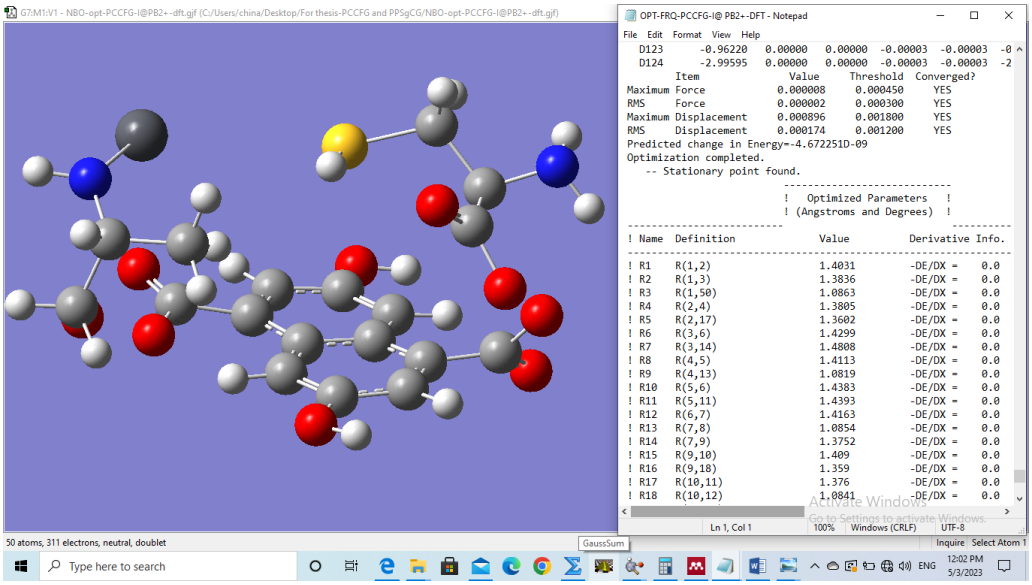

Annex 26| Frequency of converged PCCFG–I@Pb^{2+}/ DFT/B3PW91–D3/6-31G(d)/SDD.

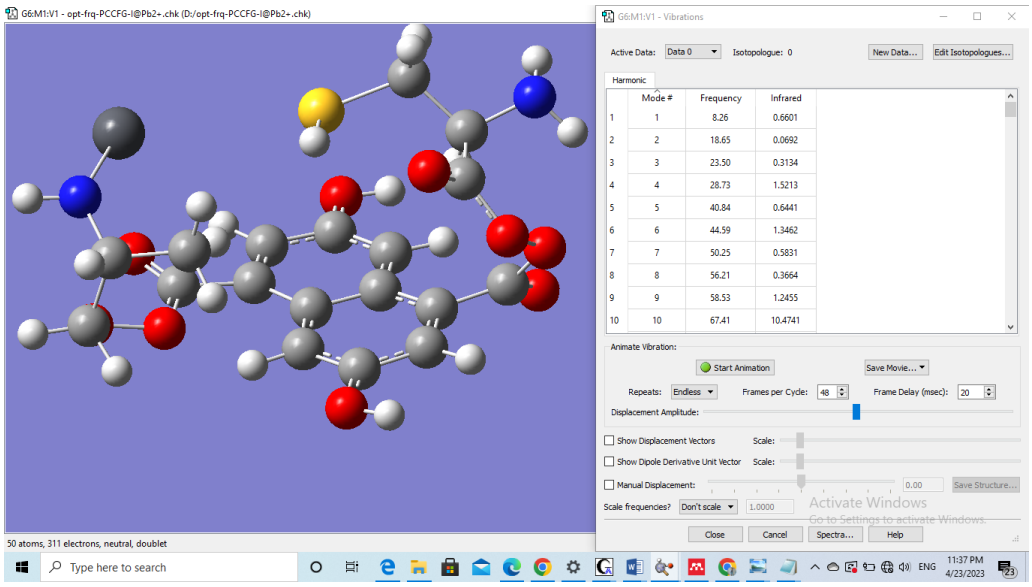

Publications

SEPARATION SCIENCE AND TECHNOLOGY
2023, VOL. 58, NO. 2, 241–256
https://doi.org/10.1080/01496395.2022.2106441

Taylor & Francis
Taylor & Francis Group

Check for updates

Adsorption of Cr (VI) ion from aqueous solution on acrylamide – grafted starch (Coccinia abyssinicca) – PVA/PVP/chitosan/graphene oxide blended hydrogel: isotherms, kinetics, and thermodynamics studies

Endalu Lemma, Zebene Kiflie, and Shimelis Kebede Kassahun

School of Chemical and Bio-Engineering, Environmental Engineering Chair, Addis Ababa Institute of Technology, Addis Ababa University, Addis Ababa, Ethiopia

ABSTRACT

Adsorption-based research toward biodegradable polymers has received much attention in recent years due to environmental concerns. Polysaccharides in this domain are interesting starting materials for the preparation of novel adsorbents. In this work, novel type of biopolymer-based hybrid hydrogel (HH) was designed for removal of Cr (VI) ion from aqueous solution. Polyvinyl alcohol (PVA), polyvinylpyrrolidone (PVP), acrylamide-grafted native starch (*Coccinia abyssinica*) (ST-g-AAm), chitosan (CS), and graphene oxide (GO) were used to prepare PVA/PVP/ST-g-AAm/CS/GO HH. Physiochemical properties of freeze-dried hydrogel were characterized by Fourier transform infrared spectroscopy, scanning electron microscopy, thermogravimetric analysis, and swelling tests. Adsorptions of Cr (VI) ion onto the hydrogel as functions of initial Cr (VI) ion concentration, pH, time, hydrogel dose, and temperature have been studied. The adsorption data agree with Langmuir isotherm at 25°C and follow pseudo-second-order kinetic model at pH of 2. The maximum adsorption capacity of the hydrogel was 93 mg g^{-1}. The obtained negative standard Gibb's free energy (ΔG° = − 1.120 kJ mol^{-1}) and negative enthalpy (ΔH° = − 2.360 kJ mol^{-1}) reveal the spontaneity and exothermic nature of Cr (VI) ion adsorption. Moreover, the adsorption thermodynamics shows enthalpically favoring host–guest complexion along with decrease in entropy.

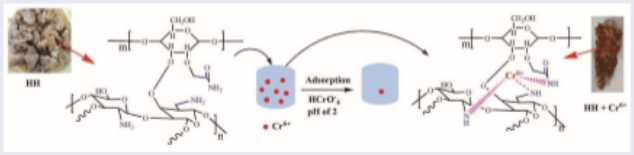

ARTICLE HISTORY
Received 29 April 2022
Accepted 22 July 2022

KEYWORDS
Adsorbent; adsorption; Cr (VI) ion removal; hybrid hydrogel; polysaccharides; pristine starch grafting

DOI: 10.1002/ren.21754

RESEARCH ARTICLE

WILEY

Adsorption of Pb^{2+} and Cd^{2+} on the L-cysteine-functionalized graphene oxide/chitosan/polyvinyl alcohol hydrogel: Kinetic, isotherm, and thermodynamic study

Leta Lemma | Zebene Kiflie | Shimelis K. Kassahun

School of Chemical and Bio-Engineering, Environmental Engineering Chair, Addis Ababa Institute of Technology, Addis Ababa University, Addis Ababa, Ethiopia

Correspondence
Zebene Kiflie, School of Chemical and Bio-Engineering, Environmental Engineering Chair, Addis Ababa Institute of Technology, Addis Ababa University, P.O. Box 385, King George VI St, Addis Ababa, Ethiopia.
Email: zebene.kiflie@aau.edu.et and kifliez@gmail.com

Abstract

In this study, Polyvinyl alcohol-chitosan-cysteine-functionalized graphene oxide (PCCFG) hydrogel was synthesized from L-cysteine-functionalized graphene oxide (CFG), chitosan (CS), and polyvinyl alcohol (PVA). The hydrogel was characterized by Fourier transform infrared spectroscopy, scanning electron microscopy, and energy-dispersive X-ray spectroscopy and employed for decontamination for lead ion (Pb^{2+}) and cadmium ion (Cd^{2+}) from aqueous solution. The effects of initial metal ion concentration, hydrogel dose, pH, time, and temperature were studied. The experimental data were well described by a pseudo-second-order kinetic model and Langmuir isotherm with maximum adsorption capacities of 250 and 192 mg g^{-1} at 25°C for Pb^{2+} and Cd^{2+}, respectively. The adsorption capacity of the PCCFG hydrogel increased with the increase in temperature. The value of ΔG° was negative, which shows the spontaneity of the reaction (electron exchange or ion exchange) between the metal ion and electron-rich atoms (–N, –S, –O). The positive ΔH° shows that the adsorption reaction consumes energy and the positive ΔS° shows the strong affinity of PCCFG toward the Pb^{2+} and Cd^{2+} ions. Pb^{2+} had better affinity and less spontaneity than Cd^{2+}. The results show that the coexistence of Pb^{2+}, Cd^{2+}, and Cu^{2+} in the solution inhibits the adsorption capacity of PCCFG.